Towards CO_2 Emission Monitoring with Passive Air- and Space-Borne Sensors

Jonas Simon Wilzewski

München 2021

Towards CO_2 Emission Monitoring with Passive Air- and Space-Borne Sensors

Jonas Simon Wilzewski

Dissertation
an der Fakultät für Physik
der Ludwig–Maximilians–Universität
München

vorgelegt von
Jonas Simon Wilzewski
aus Frankfurt am Main

München, den 6. Mai 2021

Erstgutachter: Prof. Dr. Bernhard Mayer
Zweitgutachter: Prof. Dr. André Butz
Tag der mündlichen Prüfung: 7. Juli 2021

Contents

Spectroscopy is an almost magical technique.
It amazes me still. CARL SAGAN, COSMOS

Disclaimer

Parts of the content presented in this thesis have been published in the following article:

Wilzewski, J. S., Roiger, A., Strandgren, J., Landgraf, J., Feist, D. G., Velazco, V. A., Deutscher, N. M., Morino, I., Ohyama, H., Té, Y., Kivi, R., Warneke, T., Notholt, J., Dubey, M., Sussmann, R., Rettinger, M., Hase, F., Shiomi, K., and Butz, A.: Spectral sizing of a coarse-spectral-resolution satellite sensor for XCO2, Atmos. Meas. Tech., 13, 731–745, https://doi.org/10.5194/amt-13-731-2020, 2020.

Abstract

Coal-fueled power plants are responsible for 30 % of anthropogenic carbon dioxide (CO_2) emissions and can therefore be considered important drivers of climate warming. The 2015 Paris Climate Accord has established a global stock take mechanism, which will assess the progress of global carbon emission reduction policies in five-yearly tallies of worldwide emissions. However, there exists no independent monitoring network, which could verify such stock takes. Remote sensing of atmospheric CO_2 concentrations from air- and space-borne sensors could provide the means of monitoring localized carbon sources, if their ground sampling distance is sufficiently fine (i.e. below the kilometer scale). Increased spatial resolution can be achieved at the expense of decreasing the spectral resolution of the instrument, which in turn complicates CO_2 retrieval techniques due to the reduced information content of the spectra. The present thesis aims to add to the methodology of remote CO_2 monitoring approaches by studying the compromise between spectral and spatial resolution with CO_2 retrievals from three different sensors.

First, the trade-off between coarse spectral resolution and retrieval performance is discussed for a hypothetical imaging spectrometer which could reach a spatial resolution of $\sim 50 \times 50$ m^2 by measuring backscattered sunlight in the short wave infrared spectral range at a resolution of $\Delta\lambda \sim 1$ nm. To this end, measurements of the Greenhouse gases Observing SATellite (GOSAT) at $\Delta\lambda = 0.1$ nm are artificially degraded to coarser spectral resolutions to emulate the proposed sensor. CO_2 column retrievals are carried out with the native and degraded spectra and the results are compared with each other, while data from the ground based Total Carbon Column Observing Network (TCCON) serve as independent reference data. This study identifies suitable retrieval windows in the short wave infrared spectral range and a favorable spectral resolution for a CO_2 monitoring mission.

Second, CO_2 column retrievals are carried out with measurements of the air-borne AVIRIS-NG sensor at a spectral resolution of $\Delta\lambda = 5$ nm. This case study identifies advantageous CO_2 retrieval configurations, which minimize correlations between retrieval parameters, near two coal-fired power plants. A bias correction method is proposed for the retrievals and a plume mask is applied to the retrieved CO_2 enhancements to separate the CO_2 emission signal from the atmospheric background. Emission rates of the two facilities are calculated under consideration of the local wind speed, compared to a public inventory and discussed in terms of their uncertainties.

Third, CO_2 retrievals are extended to spectral resolutions on the order of $\Delta\lambda \sim 10$ nm

by analyzing spectra of the specMACS imager near a small power plant. Retrieval effects that hamper the detection of the source signal are discussed.

Zusammenfassung

Kohlekraftwerke verursachen 30 % der gesamten anthropogenen Kohlenstoffdioxid (CO_2) Emissionen und werden daher als wesentliche Faktoren für die Erwärmung des Erdklimas betrachtet. Das Pariser Klimaabkommen von 2015 sieht einen globalen, fünfjährlichen Bilanzierungsmechanismus vor, in dem der Fortschritt globaler CO_2 Emissionsreduktionsziele bewertet wird. Allerdings existiert kein unabhängiges Netzwerk zur Überwachung von CO_2 Emissionen, das die Emissionsbilanzen der Staaten verifizieren könnte. Eine Möglichkeit zur Überwachung von Kohlekraftwerken stellt die passive Fernerkundung atmosphärischen Kohlenstoffdioxids mit Flugzeug- und Satellitensensoren dar. Zu diesem Zweck werden Instrumente benötigt, die eine feine räumliche Bodenauflösung realisieren (Abtastung der Erdoberfläche in Abständen unter 1 km), beispielsweise indem sie auf eine hohe spektrale Auflösung des Spektrometers verzichten. Der Verlust spektraler Information stellt jedoch eine Herausforderung für die Ableitung der CO_2 Konzentration dar. Diese Arbeit adressiert den Kompromiss zwischen spektraler und räumlicher Auflösung in drei Fallstudien, in denen CO_2 Konzentrationen aus Messungen drei verschiedener Sensoren berechnet werden.

Zunächst wird ein hypothetischer Satellitensensor mit einer Bodenauflösung von $\sim 50 \times 50$ m^2 untersucht, der von der Erde zurückgestreutes Sonnenlicht im kurzwelligen Infrarot Spektralbereich bei einer spektralen Auflösung von $\Delta\lambda \sim 1$ nm misst. Dabei werden Messungen des Greenhouse gases Observing SATellite (GOSAT) bei $\Delta\lambda = 0.1$ nm spektral degradiert, um die reduzierte Spektralauflösung des vorgeschlagenen Instruments zu imitieren. Die Ableitung der Säulenkonzentration des CO_2 geschieht unter Verwendung der nativen und der degradierten Spektren und die Berechnungen der CO_2 Konzentrationen werden miteinander verglichen. Ebenso wird ein Vergleich mit dem unabhängigen, stationären Total Carbon Column Observing Netzwerk (TCCON) angestellt, so dass der Zusammenhang zwischen spektraler Auflösung und Performanz der CO_2 Berechnung untersucht werden kann. Auf diese Art werden geeignete Spektralfenster im kurzwelligen Infrarot identifiziert, die die Ableitung der CO_2 Konzentration ermöglichen, und es lässt sich eine favorisierte spektrale Auflösung für eine zukünftige CO_2 Emissions-Monitoring Mission bestimmen.

Dann werden CO_2 Säulenkonzentrationen aus Messungen eines Flugzeugspektrometers mit einer Auflösung von $\Delta\lambda = 5$ nm abgeleitet. Diese Fallstudie zeigt vorteilhafte Konfigurationen der CO_2 Inversion auf, welche Korrelationen zwischen der berechneten CO_2

Konzentration, der Bodenalbedo und der Wasserdampfsäule minimieren. In der Anwendung auf Überflüge von zwei Kohlekraftwerken wird eine a posteriori Korrektur Methode für die CO_2 Berechnung entwickelt und die Abgasfahne wird mit einem Filter vom atmosphärischen Hintergrund getrennt. Unter Einbeziehung der lokalen Windgeschwindigkeit lassen sich so die Emissionsraten der beiden Anlagen abschätzen und mit öffentlichen Emissionsinventaren vergleichen.

Schließlich wird die Methodik der CO_2 Fernerkundung auf das abbildende Spektrometer specMACS mit $\Delta\lambda \sim 10$ nm angewendet und das Emissionssignal eines kleinen Kraftwerks untersucht. Effekte, die die Detektion der CO_2 Abgasfahne verhindern, werden diskutiert.

Chapter 1

Introduction

Carbon dioxide (CO_2) warms the atmosphere of Earth through its absorption of long-wave radiation. Ever since the industrial revolution anthropogenic CO_2 emissions to the atmosphere have significantly enhanced carbon dioxide concentrations in the air, thereby altering the temperature of the planet. The burning of coal in power plants presently accounts for 30 % of all human CO_2 emissions (International Energy Agency, 2021). Although most nations in the world recognize this man-made climate change as a major challenge an independent monitoring network which could deliver information on climate policy performance is yet to be created (Ciais et al., 2014). In the case of power plant emissions it is currently standard practice to adopt emission tallies from the very companies that own the facilities into national emission reports. The 2015 Paris Climate Accord, in which the global community aims to keep global warming below 2° K above preindustrial levels, calls for the establishment of five-yearly global stock takes that will asses the impact of global climate policies. The present work is motivated by the lack of independent carbon emission monitoring and verification and it pursues the development of remote sensing methods which are suited to quantify CO_2 emissions from localized sources.

This thesis focuses on CO_2 monitoring methods based on Earth-observing space- and air-borne sensors. Remote sensing of atmospheric carbon dioxide concentrations from these platforms relies on the measurement of a spectrum of light. Figure 1.1 illustrates a spectrum of radiation as it arrives at the sensor. This is a simplified model of a spectrum in a broad spectral range before it enters the optics of the instrument, i.e. an atmospheric transmittance calculation at zenith/nadir viewing angle at infinite spectral resolution. The atmospheric composition was chosen to be representative of that of Earth by including the seven most prominent absorbing molecules of our atmosphere: H_2O, CO_2, O_3, N_2O, CO, CH_4 and O_2. Concentrations of these seven species were selected according to their natural occurrence in the atmosphere. The spectral range modeled here reflects the spectral range that is most interesting from a remote sensing perspective for there are many atmospheric "windows", i.e. spectral ranges which are not opaque and which provide information on the molecules that absorb there.

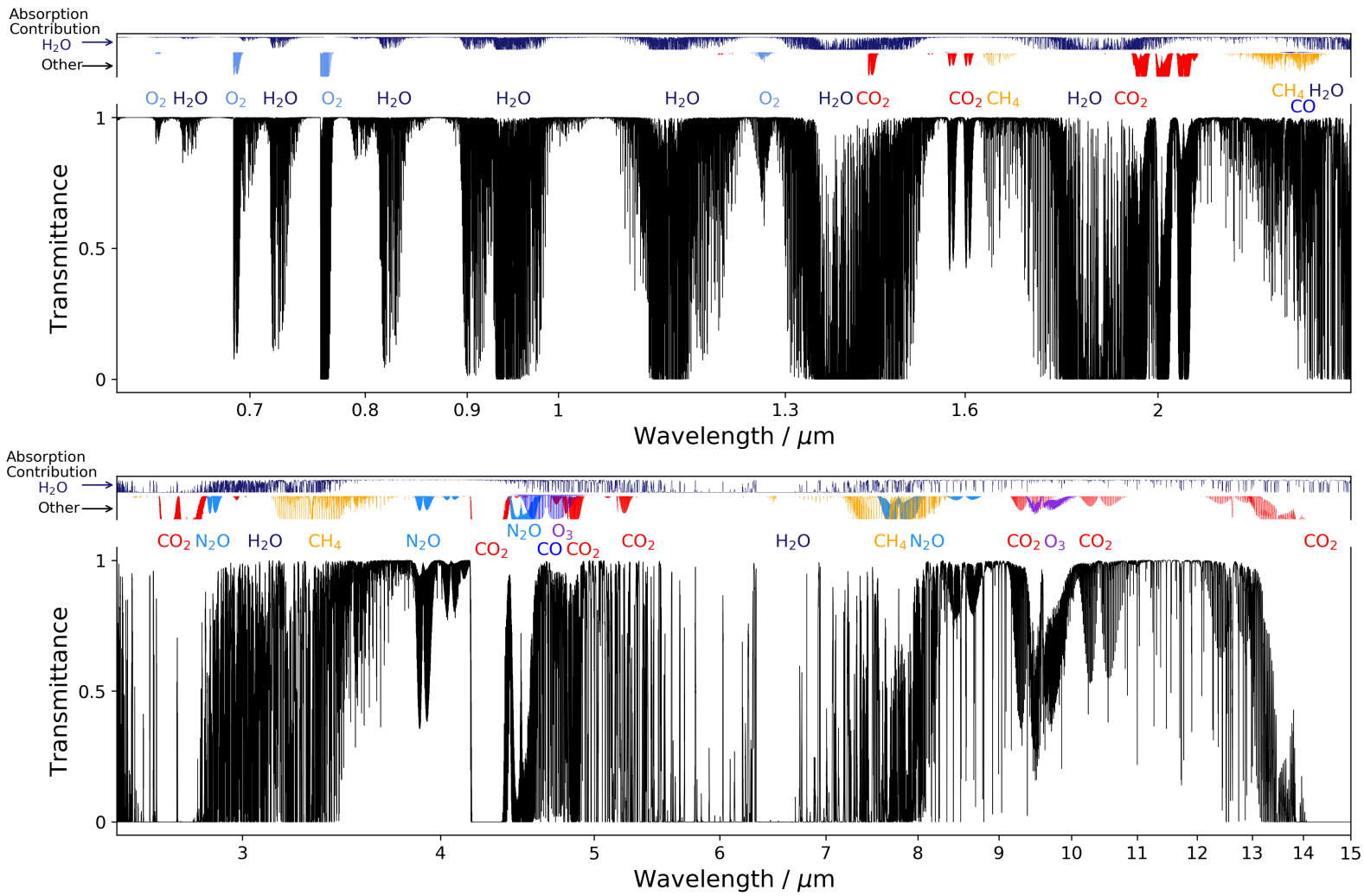

Figure 1.1: Simulated zenith transmittance through an exponential atmosphere between 0.6 and 15 μm at infinite spectral resolution. The small panels on top of each transmittance plot indicate the species contributing to the absorption (separated for water vapor and other species). This simplified spectrum includes the seven most important absorbing molecules of the atmosphere of Earth: H_2O, CO_2, O_3, N_2O, CO, CH_4 and O_2. Molecular cross sections are calculated with HAPI (Gordon et al., 2017, Kochanov et al., 2016).

The measurement process convolves the spectrum shown in Fig. 1.1 to a coarser spectral resolution, $\Delta\lambda > 0$ nm, which is a sensor-specific process. In this thesis sensors that span three orders of magnitude in spectral resolution space will be discussed; from $\Delta\lambda = 0.1$ nm to $\Delta\lambda \sim 10$ nm. Spectrometers that measure at high spectral resolution require longer measurement integration times than coarse-spectral-resolution instruments with comparable optics in order for the recorded signal to sufficiently exceed the measurement noise. The size of the ground area over which the instrument collects radiation is therefore typically related to the spectral resolution. Qualitatively this means high spectral resolution requires long integration which causes a large ground area due to the rapid movement of air- and space-borne platforms. Conversely, coarse spectral resolution can enable rather small ground pixels.

To monitor power plant emissions or other localized carbon dioxide sources with passive air- or space-borne instruments it is critical to enable spectral measurements, which provide not only high accuracy and precision in retrieved column-averaged dry-air mole fractions of CO_2 (XCO_2) but also high spatiotemporal sampling, so that they could potentially serve as a gauge for climate action plans and emission reduction objectives proposed by governments around the world. High spatial sampling limits the ground swath of remote sensing instruments, but spatial coverage could be enhanced to the global scale by deploying satellite sensors in a fleet, which would ultimately necessitate an uncomplicated design of the sensor.

Over the course of the last three decades the CO_2 remote sensing community has developed a number of space-borne instruments, which have gradually approached ever-smaller ground pixel sizes at the cost of reduced spectral resolving power (i.e. wavelength, λ, divided by full width at half maximum, $\Delta\lambda$, of the sensor's spectral response function). First worldwide space-borne XCO_2 concentration measurements were explored by the SCanning Imaging Absorption SpectroMeter for Atmospheric CHartographY mission, SCIAMACHY (e.g. Burrows et al., 1995, Reuter et al., 2010, Schneising et al., 2013), which had ground pixels of $\sim$60$\times$30 km^2 (Bovensmann et al., 1999). The Greenhouse Gases Observing Satellite (GOSAT) accomplished finer ground resolution (at $\frac{\lambda}{\Delta\lambda} > 20,000$) with a 10.5 km diameter ground footprint (Kuze et al., 2009, 2016) and the Orbiting Carbon Observatory (OCO-2 with $\frac{\lambda}{\Delta\lambda} > 20,000$) later achieved 1.3$\times$2.3 km^2 ground resolution (Crisp et al., 2008, 2017). Likewise, the TanSat mission has followed the OCO-2 approach (Yang et al., 2018) and the OCO-2 concept has been implemented on the International Space Station as OCO-3 (Eldering et al., 2019).

Observations of natural processes of the terrestrial carbon cycle (Chatterjee et al., 2017, Guerlet et al., 2013a, Liu et al., 2017, Parazoo et al., 2013) and anthropogenic emission signals (Hakkarainen et al., 2016) have been carried out with GOSAT and OCO-2. Both sensors, as well as OCO-3, have been shown to capture urban CO_2 emission patterns, for instance in the Los Angeles basin (Eldering et al., 2017, Kiel et al., 2021, Kort et al., 2012, Schwandner et al., 2017). Furthermore, emissions from individual power stations have been resolved in OCO-2 imagery by Nassar et al. (2017). The power of imaging remote sensing has subsequently been recognized as a promising concept for future missions addressing

localized carbon dioxide emissions. The CarbonSat mission (Bovensmann et al., 2010) and its successor, the CO2M mission (Sierk et al., 2019), are examples of future XCO_2 imaging sensors – with CarbonSat (at $\frac{\lambda}{\Delta\lambda} > 4,000$) a former candidate for a European CO_2 monitoring mission (e.g. Broquet et al., 2018, Pillai et al., 2016, Reuter et al., 2019) and CO2M (ground resolution: 4 km^2, $\frac{\lambda}{\Delta\lambda} > 6,000$) intended for launch in 2025/26 by the European Space Agency (Kuhlmann et al., 2020, Wu et al., 2020).

A common design aspect of all of the above mentioned sensors is their spectral measurement configuration, which includes the oxygen (O_2) A-band at ∼0.76 μm in the near infrared (NIR) as well as the CO_2 absorption bands in the short wave infrared at 1.6 (SWIR-1) and 2.0 μm (SWIR-2). In the case of typical GOSAT retrievals this spectral set-up allows for estimates of XCO_2 and aerosol scattering parameters from these bands.

Further, it has been established that methane (CH_4) hot-spots can be detected from space at even lower spectral resolutions ($\frac{\lambda}{\Delta\lambda} < 1,000$) with sensors that resolve the surface of the Earth with a ground sampling distance of 30 m and which only employ one absorption band near 2.35 μm (Thompson et al., 2016). Aircraft spectrometers that operate at similar resolving powers can reach even smaller ground pixel sizes and may serve to quantify methane emissions (Dennison et al., 2013, Krings et al., 2018, Thorpe et al., 2016a,b). It has been proposed by Dennison et al. (2013) that a single-band satellite spectrometer with resolving power $\frac{\lambda}{\Delta\lambda} \approx 200$ centered on the SWIR-2 spectral range (at 2.0 μm, i.e. FWHM= $\Delta\lambda = 10$ nm) would be able to reach ground resolutions of 60×60 m^2. Spectral measurements near 2 μm with the AVIRIS-NG instrument ($\Delta\lambda = 10$ nm) have showcased CO_2 emission quantification ability for point source plumes (Thorpe et al., 2017). Thorpe et al. (2016b) argued that, for quantitative methane retrievals, the most favorable trade-off between spectral resolution and ground pixel size may be a spectrometer design with $\frac{\lambda}{\Delta\lambda} \approx 2,000$, i.e. a spectral resolution of 1 nm. As methane presents similar remote sensing challenges as CO_2 it is worthwhile applying these recent developments to CO_2 spectrometer concepts, while the specific implementation of such approaches is investigated in this work.

This thesis adds to the discourse on CO_2 emission monitoring methods in three individual case studies, which aim to analyze the effect of coarse spectral resolution on XCO_2 retrieval performance.

Firstly, an opportunity for a new spectral sensor design, which could resolve XCO_2 on scales of $\sim 50 \times 50$ m^2 when deployed in space, will be investigated. In this case study (chapter 4.1) GOSAT spectra are utilized for a CO_2 retrieval sensitivity study in resolving power space – by convolving the measurements from $\frac{\lambda}{\Delta\lambda} > 20,000$ to $\frac{\lambda}{\Delta\lambda} < 2,000$ – to determine a favorable spectral sizing for a potential future satellite sensor. Retrievals in the SWIR-1 and SWIR-2 spectral ranges are compared and target spectral resolutions are recommended. The second case study of this thesis (ch. 4.2) employs power plant observations of the AVIRIS-NG aircraft sensor at $\frac{\lambda}{\Delta\lambda} = 400$ to analyze CO_2 monitoring capabilities from actual spectrometer imagery. Aircraft sensors serve to examine remote sensing challenges in advance of satellite missions as versatile and less expensive options. Advantageous retrieval configurations based on an analysis of test spectra selected from a background region over various surface materials will be discussed. A posterior XCO_2

correction method is proposed and flux rate quantification techniques suited for these measurements are applied. Thirdly and lastly, XCO_2 power plant signals are examined in measurements of the specMACS aircraft sensor, which has $\frac{\lambda}{\Delta\lambda} \sim 200$ (ch. 4.3).

An overview of the physical background of CO_2 remote sensing is provided in chapter 2 and an introduction to the data sets and methods of this work is given in chapter 3, followed by the three case studies in chapter 4. Finally, chapter 5 holds the conclusions drawn from this work as well as an outlook on future developments in CO_2 monitoring methods with passive sensors.

Chapter 2

From Radiation to Carbon Dioxide Concentrations

The goal of this chapter is to contextualize the research question introduced above within the framework of physics. An overview of the science behind the process chain of passive trace gas remote sensing, from radiation to concentrations of atmospheric species will be given here.

This introduction will include the fundamental principles of absorption, emission and scattering of radiation in the atmosphere (section 2.1) as well as the concept of measuring spectral properties of radiation (section 2.2). The process of modeling such observations will subsequently be introduced in section 2.3. Finally, the basic approach of retrieving an atmospheric variable from the measurement by making use of the model and its derivatives will be presented (section 2.4).

The following sections cover standard textbook material and therefore not all statements in this chapter are backed up with references. Instead, the books by Goldstein et al. (2006), Hansen and Travis (1974), Liou (1980), Paus (2007), Petty (2006), Rodgers (2008), van de Hulst (1981), Wallace and Hobbs (2006), Zdunkowski et al. (2007), which inspired this chapter, represent starting points for further reading.

2.1 Interaction of Radiation with the Atmosphere

Radiation is the primary source of energy in the atmosphere of Earth. Both shortwave radiation from the sun ($\sim 0.2 - 3.5$ μm) and longwave radiation from the Earth and the atmosphere itself ($\sim 3.5 - 100$ μm) are the drivers of a plethora of atmospheric phenomena. It is quite fascinating that the interaction of radiation with the constituents of our atmosphere (atoms, molecules, particles) can be described by just three fundamental processes: absorption, emission and scattering (see for instance Zdunkowski et al., 2007, ch. 1.6). The purpose of this section is to give an overview of these important forms of interaction. While the following discussion focuses on the interaction of radiation with molecules, the

same principles generally apply when considering the interaction with atoms.

2.1.1 Absorption and Emission

Molecules exist in states of discrete energies with regard to their electronic, vibrational and rotational configuration. Each state, ψ, with energy, E, is ultimately a solution to the Schrödinger equation

$$H\psi = E\psi \tag{2.1}$$

where the Hamiltonian, H, is the sum of the quantum mechanical operators of kinetic and potential energy of the molecule. Although equation 2.1 cannot be derived from a higher principle, similarly discontinuous energy "states" can be observed for vibrating objects in classical physics. When the complicated intra-atomic potential of a conceptual/hypothetical molecule is approximated, classically, as the potential of coupled harmonic oscillators with coupling strengths, k, and vibrating masses, m, one finds resonant energies at $E \sim \sqrt{k/m}$ for the vibrations of the molecule (Goldstein et al., 2006, ch. 6.4). Qualitatively, this is also observed in real molecules[1], although actual molecular Hamiltonians are, of course, much more complicated. The above discussion foreshadows the idea that resonance phenomena are the key to generating transitions between different energy states of a molecule, which can generally occur through either kinetic or radiative processes.

Kinetically, collisions of the molecule with its surrounding can both increase and decrease the energy of the system such that the molecule transitions to a higher or lower energy state, respectively. While this kinetic pathway plays a very important role in restoring local thermodynamic equilibrium[2] in (the lower parts of) our atmosphere, the next paragraphs will deal primarily with the radiative pathways of *absorption* and *emission*, because they cause the signals that can be used to detect molecules remotely.

Basic Concepts Radiatively, a molecule can be transferred into a higher energy state when exposed to an external radiation field that delivers the amount of energy needed to bridge the gap between the discrete states of the system. This process is known as *absorption*, i.e. the incident photon is absorbed by the molecule. Once excited to a higher energy state, there are two radiative processes which can relax the molecule to a lower state: *spontaneous* and *stimulated emission*. Both processes include the re-radiation of a photon with energy equivalent to the transition energy. The direction of the emitted radiation is random for spontaneous emission and identical to the direction of incident photons in the case of stimulated emission. Excited states are never stable in quantum physics, i.e.

[1] As an example from the atmosphere: the anti-symmetric stretch vibration of CO_2 occurs at $\lambda = 4.26\ \mu m$. If one of the oxygen atoms is replaced by a more massive sulfur atom, the resulting carbonyle sulfide molecule, OCS, is still linear and also double bonded. However, its anti-symmetric stretch is found at $\lambda = 4.85\ \mu m$, qualitatively demonstrating that the increased mass leads to resonance at decreased energies.

[2] Local thermodynamic equilibrium means that the local group of molecules populates the energy states, E_i, according to a Boltzmann distribution: $N_i \sim exp(-\frac{E_i}{kT})$

even without collisions there is a probability for a spontaneous transition to a lower level. Hence, it is a matter of when an emission occurs, which can be predicted theoretically through transition probability coefficients derived by Einstein (e.g. Rothman et al., 1987). In essence, one can show that the probability for a molecule to undergo spontaneous emission is proportional to the third power of the transition energy. Stimulated emission, on the other hand, is triggered by incoming radiation. As for absorption, the external photon must have an energy that resonates with the energy gap between upper and lower state of the molecule to induce the transition/the emission. Stimulated emission does not play a significant role in the atmosphere of Earth.

Despite the many processes involved on the molecular scale, radiative energy is finally conserved, i.e. emission and absorption processes are balanced out exactly in our atmosphere (Kirchhoff's law). Yet, as the air gets thinner above the stratosphere (> 50 km), the equilibrating effect of collisions is lost and the door opens to a world where molecules start behaving in ways that will be left to experts of non local thermodynamic equilibrium to write about. Here, a first step is made towards the application of remote sensing by discussing which absorption and emission processes occur and how these manifest themselves as spectral lines and bands.

Allowed Transitions and Spectral Lines Just like the wave functions of a harmonic oscillator, energy states of a molecule, ψ, can be either symmetric or antisymmetric under symmetry operations (e.g. inversion, nucleus exchange, etc.). A transition between the states ψ_1 and ψ_2 is only *allowed*, i.e. it can only occur, if the external radiation field can couple to the electric (or magnetic) molecular dipole moment, η. The relative strength of this coupling is described by the transition dipole moment, $\langle p \rangle$, between these states defined by the volume integral

$$\langle p \rangle = \int \psi_1 \eta \psi_2 dV. \tag{2.2}$$

As a scalar, observable quantity, the transition dipole moment must be totally symmetric under any kind of symmetry operation. In the absence of a permanent electric dipole moment (like H_2O), whether or not certain transitions are *allowed* depends on the symmetries of the wavefunctions and the dipole moment in eq. 2.2[3]. As a result, there are *forbidden* transitions, e.g. vibrations which are theoretically possible, but which cannot be excited in nature ($\langle p \rangle = 0$). One prominent example is the CO_2 transition from the vibrational ground state into the symmetric stretch vibration, which is a vibrational mode in which both oxygen atoms move away/towards the carbon atom simultaneously. Fundamentally, it is the vanishing transition dipole moment, which prohibits this transition. But intuitively, the symmetric stretch does not create a dipole moment within a linear, triatomic molecule, to which incident radiation could couple. This also explains

[3]To illustrate this idea, consider dipole oscillation occurring along a given axis of the molecule, as a linear (antisymmetric) function, i.e. $\eta(t) \sim e \cdot z(t)$ (e being the oscillating charge and z the distance along the oscillation axis). The transition moment then vanishes for all combinations of vibrations ψ_1 and ψ_2 where these functions have the same symmetry under inversion.

why diatomic molecules like the dominant constituents of our atmosphere, N_2 and O_2, do not absorb through vibrations (or rotations): their vibrations have no electronic dipole moment. Diatomics can only be excited into a rotation or vibration, if interactions with the surrounding molecules become strong enough to temporarily induce a dipole (*collision induced absorption*, CIA).

Now that the concepts of absorption and emission are introduced as resonant dipole coupling events between the molecule and an external radiation field, it should be emphasized that – although the energy for a transition is theoretically expected at a single energy value – in reality one observes transitions as *spectral lines* with a finite width. Spectral lines cannot have a vanishing width, ΔE, because that would mean that the lifetime of the initial state of the transition, Δt, becomes infinitely long, according to Heisenberg's theorem

$$\Delta E \Delta t \geq \hbar. \tag{2.3}$$

As the transition is taking place, the lifetime of the initial state becomes finite, which calls for a finite width of the transition energy. This natural broadening, however, is of no relevance in the atmosphere where the width, and more generally, the shape of the resulting spectral line depend on the pressure and temperature of the environment, but also on the atmospheric species that surround the molecule (through collisions). Two dominant mechanisms responsible for a broadening of spectral lines can be identified in our atmosphere: 1) Collisional broadening, where collisions stochastically distort the molecular energy levels through electromagnetic interaction and thus increase the width of the observed spectral line and 2) Doppler broadening, where spectral lines are broadened due to the thermal motion of molecules in low pressure (i.e. high altitude) environments, which results in Doppler shifts of the transition energy. Collisional broadening produces significantly broader line wings than Doppler broadening and the spectroscopic community has therefore introduced line shape functions that account for both processes. For rotational-vibrational transitions, the Hartmann-Tran-Profile (HTP, Tennyson et al. (2014)) is the standard description of the shape of spectral lines to date. It captures a number of collisional line shape effects that primarily play a role at very high spectral resolution and at intermediate pressure levels, where the line shape transitions from the collisional to the Doppler regime. In this thesis, a simplification of the HTP will be used for many applications, the Voigt profile (for details see Humlicek, 1982):

$$f(\lambda, m, p, T) \sim \underbrace{\sqrt{\frac{m}{T}} e^{-\left(\lambda^2 \frac{m}{T}\right)}}_{\text{Gaussian}} \circledast \underbrace{\frac{\gamma(p,T)}{\left(\lambda - \delta(p,T)\right)^2 + \gamma(p,T)^2}}_{\text{Lorentzian}} \tag{2.4}$$

The line shape function, f, in eq. 2.4 is the convolution of the Gaussian and Lorentzian line shapes associated with Doppler and collisional broadening, respectively. For a given wavelength, λ, away from the line center at $\lambda = 0$, the line shape is influenced by the mass of the molecule, m, as well as by the state of the atmosphere (pressure, p, temperature, T). The pressure broadened half width, γ, as well as the pressure shift correction to the

line position, δ, can be calculated for a combination of pressure and temperature from spectroscopic parameters compiled in databases like HITRAN (Gordon et al., 2017).

A final line shape effect that will be taken into account separately in this thesis is *line mixing*. This is a phenomenon that occurs in high pressure environments between overlapping rotational-vibrational lines of a molecule and it is essentially a mix of radiative and kinetic state changes. For example, in addition of undergoing a transition between two states ψ_1 and ψ_2 through emission or absorption, the molecule can be transferred to a neighboring transition $\psi_{1,neighbor}$ through a collision, undergo the transition $\psi_{1,neighbor}$ to $\psi_{2,neighbor}$ there and then transfer back to ψ_2 through a collision. As a result, both spectral lines are skewed towards their mutual center.

When the line shape, f, is known, one can introduce the *absorption/emission coefficient*, β_{abs}, which is a monochromatic quantity at wavelength λ_0 that indicates how much radiation is depleted from the incident field by a single absorption process (or conversely added by emission) and it is given by

$$\beta_{abs}(\lambda_0, p, T) = S(T) \cdot f(\lambda_0, p, T) \tag{2.5}$$

with $S(T)$ the spectral line intensity which is tabulated in databases (Rothman et al., 1987). The unit of β_{abs} is $1/(\text{molecule}\cdot\text{cm}^{-2})$ and the coefficient will be needed in section 2.3 to propagate radiation through an absorbing medium. The absorption coefficient can be normalized to units of 1/cm by multiplying eq. 2.5 by the number of absorbing molecules per unit gas volume. Molecular absorption cross sections, σ_{abs} are derived by multiplying absorption coefficients with the corresponding molecular mixing ratio.

Before closing this section on absorption and emission processes, the spectral structures of the CO_2 molecule that will be required throughout this thesis to derive concentrations of carbon dioxide are introduced.

Spectral Bands of CO_2 near 1.6 and 2.0 μm In general, vibrational transitions of a molecule occur under simultaneous change in rotational state, E_{rot}, (while the electronic state remains unchanged) and one therefore commonly refers to rotational-vibrational transition *bands*. These are sets of spectral lines that appear in close proximity of each other; the individual line strengths being governed by the population of the respective rotational and vibrational levels (with selection rules derived from equation 2.2) and the magnitude of the transition dipole moment. Typical energies needed to excite such transitions are in the infrared spectral range (IR, $\sim 1 - 15$ μm)[4].

In this thesis, rotational-vibrational absorption bands of carbon dioxide will be used constantly to derive CO_2 concentrations. CO_2 has three fundamental vibrations: the forbidden symmetric stretch, "ν_1", the bending mode, "ν_2", and the antisymmetric stretch,

[4]At greater radiative energies (visible (VIS, $\sim 400 - 700$ nm) or ultraviolet (UV, $\sim 200 - 300$ nm) or at even higher energies) molecules can be excited to change electronic state, or the radiation may also disassociate the atoms of the molecule. Beyond the IR, purely rotational absorption bands can be excited in the far infrared (FIR, $> 15\mu$m).

"ν_3". The strong rotational-vibrational bands observed near 1.6 and 2.0 μm each form through linear combinations of the ν_1 and ν_3 band ($2\nu_1 + \nu_3$ near 2 μm and $3\nu_1 + \nu_3$ near 1.6 μm). The reason why there are so many bands of CO_2 associated with these vibrations is an accidental resonance between the ν_1 vibration and the first overtone of the ν_2 band (Rothman and Young, 1981), i.e. the ν_1 band occurs at twice the energy of the ν_2 band. As a result of this coincidence, the energy level of the $2\nu_1 + \nu_3$ band near 2.0 μm, for example, can be reached through three combinations of vibrational modes which all have roughly the same energy and are therefore in resonance with each other: $2\nu_1 + \nu_3, 4\nu_2 + \nu_3$ and $\nu_1 + 2\nu_2 + \nu_3$, which appear as three CO_2 absorption bands. The wave functions of these vibrations are linear combinations of the unperturbed states.

2.1.2 Scattering

Much like during absorption or emission, atmospheric constituents that scatter radiation interact with the oscillating electromagnetic field of the incident radiation. The mechanism of scattering can generally be understood as the generation of a secondary electromagnetic wave sent out from a particle whose charges oscillate at the frequency of the incident radiation field (*elastic* scattering) or at a shifted frequency (*inelastic* scattering). A plethora of scattering phenomena exist that strongly depend on the size, composition (charge distribution, refractive index) and shape of the particle, the distance to other scattering particles and the wavelength of the incoming radiation. This thesis will focus on elastic scattering effects that play a significant role for solar and terrestrial radiation in the atmosphere of Earth, namely processes where the size parameter, a, of the scattering particle with radius r at wavelength λ

$$a = \frac{2\pi r}{\lambda} \tag{2.6}$$

is on the order $10^{-3} < a < 10^3$.

The lower boundary condition reflects the requirement for scattering to occur, i.e. wavelengths too great (frequencies too low) cannot force dipole oscillations in small particles (e.g. radio waves do not even scatter off rain drops). The motivation for the choice of the upper bound will become clearer in section 2.3. Briefly, scattering scenarios with $a > 10^3$ are typically so complex in our atmosphere, that they make passive trace gas remote sensing too complicated. Inelastic scattering events primarily occur in the UV-VIS spectral range in the terrestrial atmosphere and thus they are neglected in this discussion, as is the scattering of radiation at the surface of the Earth. For the purpose of this thesis it will be sufficient to approximate surface scattering by isotropic backscattering as will be explained in section 2.3.

The following introduction is condensed significantly with regard to the mathematical framework to favor qualitative aspects of scattering phenomena over mathematical rigor. Scattering events are represented here by scalar functions, although the full description of polarized radiation in the Stokes-Müller formalism would involve a generalization to four dimensional vector calculus (see for instance Zdunkowski et al., 2007, ch. 10).

Rayleigh Scattering The scattering regime defined by size parameters in the range $10^{-3} < a < 10^{-1}$ is known as the Rayleigh regime. When the incident wavelength is much greater than the extent of the particle, the amplitude of the electronic part of the alternating radiation field forces the electrons of the scattering particle to follow its frequency, inducing a dipole with subsequent coherent reradiation of radiation (the scattered wave is in phase with the incident wave). The ability of radiation to force charges of a particle into oscillation is generally a function of the refractive index of the particle, which in turn is a function of wavelength. In the present regime of small particles, the refractive index can be assumed to increase with the number of bound electrons of the particle, but this generalization is no longer valid in the aerosol scattering regime. It can be shown that the Rayleigh scattering cross section, σ_R, which indicates how much radiative energy is lost from the incident direction after the scattering event, strongly depends on particle radius, r, and wavelength, λ (Petty, 2006):

$$\sigma_R \sim \frac{r^6}{\lambda^4} \tag{2.7}$$

The strong wavelength dependence is responsible for the blue color of the sky, as Rayleigh scattering is much more effective towards smaller wavelengths and the smallest wavelength the human eye is sensitive to is blue. A scattering coefficient, β_R (in units of 1/cm), can be obtained by multiplying the scattering cross section with the number of scattering molecules/particles per unit gas volume.

Rayleigh scattering as a dipole radiation phenomenon creates polarized radiation, even though the radiation coming from the sun is not polarized. According to the characteristic dipole radiation, reradition of unpolarized light in a dipole scattering event occurs predominantly orthogonally to the dipole axis. As a consequence, Rayleigh scattering is not isotropic, since less light is scattered towards 90°(where the radiation is polarized orthogonally to the incident direction), but it is symmetric with regard to backward and forward scattering. The angular distribution of scattered radiation, the so called *phase function*, $p(\Theta)$, is given by

$$p(\Theta) = \frac{3}{4}\left(1 + \cos(\Theta)^2\right) \tag{2.8}$$

where the angle Θ is the angle between incident and scattered radiation. The phase function is displayed as a function of the scattering angle, Θ, in Fig. 2.1 (dashed line).

Aerosol scattering Whereas Rayleigh scattering of solar and terrestrial radiation occurs for molecules and atoms in the atmosphere of Earth, bigger particles lead to more complex scattering characteristics. Specifically, aerosols – small particles such as dust, sea salt, pollen and many others – fall into a range of size parameters that covers $10^{-1} < a < 10^3$. In this scattering regime, clearly, incident radiation will cause all sorts of oscillations (electric/magnetic dipole or multi-pole oscillations) within the particle, causing interference

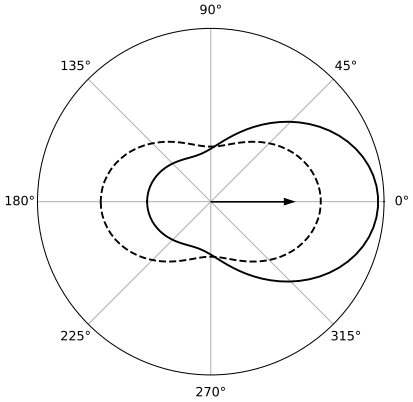

Figure 2.1: Phase functions of Rayleigh (dashed line) and Mie (solid line) scattering at $a = 0.05$ and $a = 1$, respectively. The arrow shows the direction of the incident radiation. The phase functions were taken from Prahl (2020).

between many incoherently scattered and polarized electromagnetic waves.[5] Consequently, scattering characteristics of aerosols are much more complex than what is observed in the Rayleigh regime. For homogeneous, spherical particles, Mie theory allows the computation of the far field of the scattered radiation. Evidently, due to the assumption of spherical particles, the relative angle between incident and outgoing radiation, Θ, fully determines the spatial/geometric distribution of the scattered wave. The analytical expression of the Mie phase function is, however, very complex. In practice, the phase function in the size parameter range $10^{-1} < a < 10^3$ must therefore be approximated numerically in some way (see section 2.3). Fig. 2.1 shows the (approximated) phase function of an idealized aerosol at $a = 1$ (solid line), which is heavily antisymmetric with a large fraction of radiation scattered into a forward direction. Generally, the greater a value of a is reached, forward scattering becomes even more dominating for aerosol scattering in the Mie approximation and one eventually observes a peak at zero degree scattering, which increases in magnitude with a. At $a = 10^3$, the value of the phase function for forward and backward scattering angles are finally orders of magnitude apart.

An interesting result of Mie calculations is that the scattering cross section of aerosols, σ_M, as a function of the size parameter and its refractive index, m, contains a dampened oscillation behavior caused by interference of radiation from the many oscillators within the particle (van de Hulst, 1981). Thus, one can expect that certain combinations of size and refractive index will lead to constructive interference and increased scattering. Yet, such maxima are not observed in the atmosphere, because aerosols in the atmosphere appear at many different sizes, the scattering signals of which are mixed together in observations,

[5] Aerosol particles can also absorb radiation, if their refractive index has a non-vanishing imaginary part (van de Hulst, 1981, ch. 14.1), as for example black carbon. Aerosol absorption is largely neglected in this work, since many natural aerosols are non-absorbing (see section 3.1.2 for details).

effectively smoothing out interference patterns expected for a single particle scattering event. To derive aerosol properties from radiative, atmospheric measurements, one therefore has to choose parameters that sufficiently characterize the aerosol distribution (see section 3.1.2). The scattering cross section of aerosols additionally depends on wavelength through the size parameter and the refractive index (which can depend strongly on wavelength). However, in contrast to scattering in the Rayleigh regime, aerosols and small water droplets tend to have similar scattering cross sections across orders of magnitude in wavelength space.

In the limit of $a \sim 10^{-1}$, Mie theory scattering cross sections converge towards the Rayleigh expression, while at $a \sim 10^{3}$ Mie scattering characteristics converge towards those obtained with *geometric optics* calculations (essentially ray tracing through homogeneous spheres, characterized by massive forward-scattering peaks).

2.2 From Radiation to Spectra

Turning broadband solar or terrestrial radiation into a wavelength dependent observation – a *spectrum* – is the key step in most atmospheric passive remote sensing applications. In this thesis, radiation will be measured in units of W $m^{-2}sr^{-1}nm^{-1}$, which is known as *spectral radiance*, I_λ. This quantity specifies the energy, dQ, that passed through an area, dA, orthogonal to the viewing direction in solid angle, $d\Omega$, per time, dt, and wavelength interval, $d\lambda$.

$$I_\lambda = \frac{dQ}{dA\ d\Omega\ dt\ d\lambda} \tag{2.9}$$

An integration over the wavelength axis yields the *radiance*, I, in units of W $m^{-2}sr^{-1}$ and an additional integration of solid angles (taking the solar zenith angle into account) gives the *flux* or *irradiance*, F, in W m^{-2}.

This section will introduce the principles of measuring spectral radiances with the examples of grating spectrometers and Fourier Transform Spectrometers (FTS) and imaging spectrometers, because such measurement data will be used later in chapter 4. This section also aims at giving the reader a perspective on how radiative energy can be converted to electric energy in the detector of a spectrometer and how these electronic signals are finally converted into physically meaningful radiative quantities (sections 2.2.2, 2.2.3).

2.2.1 Spectrometers

Spectrometers are interferometers that split up a beam of incident light, for instance with a dispersive element such as a prism or a grating. An *optical path difference* (OPD) is introduced into the different parts of the beams which subsequently leads to an interference pattern in wavelength space: the desired measurement of a radiance spectrum, I_λ. While radiation incident on the spectrometer can be thought of as being at "infinite spectral resolution" (i.e. each spectral line has a width that is solely governed by the processes described

in section 2.1.1), every spectrometer introduces an instrument specific spectral resolution, $\Delta\lambda$, which expresses the smallest distance between two spectral lines at which these lines can still be resolved individually. The quantity $\Delta\lambda$ is the width of the *spectral response function* (SRF) of a spectrometer, which is the instrument's response to a monochromatic radiation input. Hence, the spectrometer measurement can be thought of as a convolution of the incident radiation with the spectral response function of the instrument.

Because this thesis revolves around spectral measurements at spectral resolutions across orders of magnitude, the following discussion of basic spectrometer types will focus on their interferometric mechanisms and the typical shape of their spectral response functions.

Fourier Transform Spectrometers

The Fourier Transform Spectrometer is a special case of an interferometer in the sense that it splits the incident beam into only two parts, which then recombine. Inherently, this special property assures a high throughput of the spectrometer, because all incident (broadband) radiation participates in the interference process. By splitting up the incident light beam and directing each half onto a mirror before recombining the beam, Fourier Transform Spectrometers borrow their build from Michelson interferometers. Linear motion of one or both mirrors leads to path length differences which in turn cause interference of the radiation with itself upon recombination. Path length differences can also be created by replacing the mirrors by cube-corner-mirrors and moving both in a rotary motion (see chapter 3.2). The signal of recombined radiation as a function of optical path difference (OPD) of the two beams is referred to as an *interferogram*. The spectrum as a function of wavenumber, $\nu = 10^4/\lambda$ (λ in nm and ν in cm^{-1}), can be recovered from the interferogram by means of Fourier transformation:

$$\widetilde{S}(\nu) = \int_{-\infty}^{\infty} I(x) \cdot e^{-2i\pi\nu x}\, dx \tag{2.10}$$

where $\widetilde{S}(\nu) \equiv \frac{1}{2}\left[S(\nu) + S(-\nu)\right]$ is a two-sided, symmetric spectrum in wavenumber space and $I(x)$ is the interferogram in OPD space (unit of x is meter, and x is measured via interference signals from a monochromatic reference light source). Conversely, one can transform a measured spectrum, $S(\nu)$, back into an interferogram. Eq. 2.10 is an idealization in several aspects: in reality, the integral will be evaluated as a sum, in which dx will not be infinitesimally small and the optical path difference, x, cannot reach infinity in the lab. These limitations have important implications.

Firstly, the sampling of the interferogram in OPD space, dx, has to be sufficiently small, because it determines the number of samples in the spectrum, N, through $N = \frac{2L}{dx}$, where L is the length of the interferogram along the optical path difference axis ($-L \leq x \leq L$). In fact, when a spectrum shall be measured in the spectral range $\nu < \nu_{max}$, dx must be chosen according to

$$\frac{1}{dx} > 2\nu_{max} \tag{2.11}$$

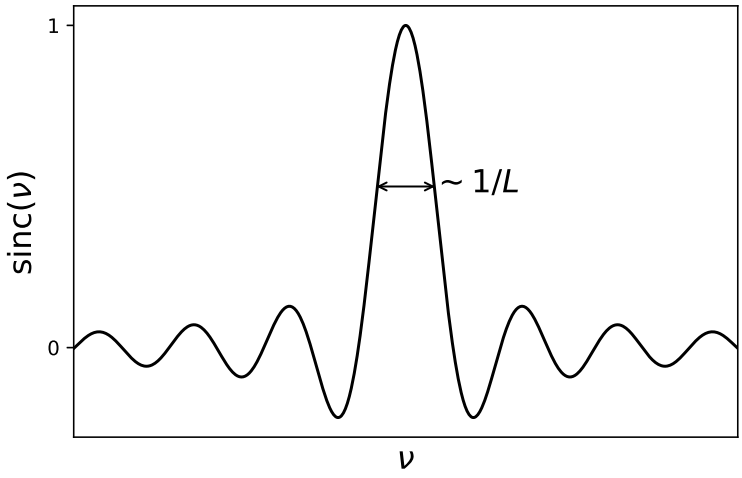

Figure 2.2: The sinc function dominates the shape of FTS spectral response function. Its full width half maximum (FWHM) goes with $\sim \frac{1}{L}$, with L the maximum optical path difference of the measurement.

in order to avoid artefacts from the convolution process in the measured spectrum $S(\nu)$ (an effect known as *aliasing*).

Secondly, the limitation $|x| < \infty$ means that the interferogram is cut off at a certain value of optical path difference, x, during the measurement. Mathematically this can be expressed as a multiplication of the interferogram by a boxcar function. Due to the Fourier transform theorem, this operation is equivalent to a convolution of the spectrum with the Fourier transform of the boxcar in wavelength space. The Fourier transform of the boxcar function is the sinc function, shown in Fig. 2.2. Its FWHM is proportional to $\frac{1}{L}$, with L being the maximum OPD value.

As a consequence, the spectral response function of an FTS can be approximated as

$$\mathrm{SRF} \sim \Pi_a \circledast \mathrm{sinc} \circledast \Pi_d \tag{2.12}$$

The boxcar function Π_d reflects the cut-off of the beam, which occurs at the detector behind the spectrometer (the *field stop*), while Π_a is a result of divergent, off-axis light beams introduced by the finite size of the *aperture stop* at the spectrometer entrance. This is, of course, a qualitative discussion that leaves out many optical effects that contribute to the shape of the SRF (e.g. misalignment of the moving mirror, effects of additional mirrors, collimating elements, etc.).

The dominating term for the spectral response of a Fourier transform spectrometer is the sinc term in eq. 2.12, i.e. typical spectral response functions behave like a sinc. As a consequence, the FWHM (the spectral resolution $\Delta\lambda$) of the instrument is critically driven by the length of the interferogram, L. High spectral resolution implies large optical path

differences, meaning that the moving mirror must be moved far along the optical axis of the system. Some FTS systems (like the ones introduced in section 3.5) therefore have $L \sim 2$ m. While the possibility to reach very narrow spectral response functions is a great advantage of FTS technology, its realization through large instruments with moving parts can be challenging for field deployment in atmospheric science. On the other hand, the circular shape of the aperture is an additional advantage in FTS systems, as the input flux to the instrument is proportional to (aperture radius)^2 instead of linear in slit width. The spectral range of an FTS is only limited by the detector spectral range, so that one spectrometer may be used to carry out measurements in a large spectral range. However, photon noise increases with broader spectral coverage, so that some Earth-observing FTS instruments restrict coverage to narrow bands. Since a monochromatic light source is used as a reference to measure OPD in the sensor, Fourier transform spectrometers provide their own wavelength calibrations, which is another major benefit (although re-calibration of the wavelength axis is often necessary at very high resolving powers $\lambda/\Delta\lambda > 20,000$). Finally, Fourier transform spectrometers only need one detector unit, which is another benefit.

Grating Spectrometers

In comparison to a FTS, grating spectrometers have a smaller spectral range and they typically cannot match the resolving power ($\lambda/\Delta\lambda$) of an FTS, but they are usually more compact and more robust due to the lack of moving parts. A grating causes interference of the incident light. Upon interaction with the grating structure, which contains N grating lines, the incident beam is split up into many parts, which recombine and interfere after transmission through (or reflection off) the grating. Different orders of diffraction can be observed behind the grating (see Fig. 2.3 and also Paus (2007, ch. 52.4)), but constructive interference only occus if the order, m, of diffraction is not zero (i.e. no spectrum is observed at $m = 0$). The presence of neighboring orders of diffraction limits the spectral range a grating spectrometer can possess, because the spectra will eventually overlap with each other. To remedy the fact that a lot of energy is lost in unnecessary diffraction orders, the grating lines can be shaped such that they focus more radiation into a desired diffraction order (*blazed gratings*). As a rule, for a beam incident orthogonally on the grating, spectral observations are expected at angles θ, which satisfy the interference condition

$$D \cdot \sin(\theta) = m \cdot \lambda, \tag{2.13}$$

where D is the lattice constant (typically on the order of a few micrometers) of the grating and λ the wavelength. It should be emphasized that as a result of equation 2.13, gratings deflect red light towards larger angles than blue light (the opposite is true for prisms). Also, the smaller the lattice constant (the higher the density of slits on the grating) the farther apart the maximums of interference will appear from each other. One

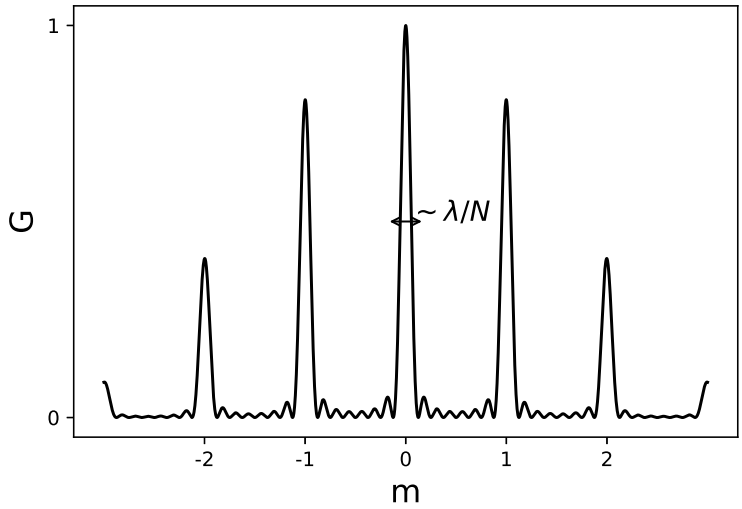

Figure 2.3: Diffraction pattern of a grating as a function of diffraction order, m. The FWHM of a grating strongly depends the number of grating lines, N.

can show, that the diffraction pattern, G, has a shape proportional to

$$G \sim \left(\frac{\sin(N\phi)}{N \sin(\phi)} \right)^2 \tag{2.14}$$

with N the number of lines on the grating and $\phi \sim D \cdot \sin(\theta)/\lambda$ (Paus, 2007). A qualitative plot of a diffraction pattern is shown in Fig. 2.3. The FWHM is found to be inversely proportional to the number of grating lines, i.e. the finer the grating, the higher the spectral resolution: $\Delta\lambda \sim \frac{\lambda}{N}$. Similar to the spectral response of the FTS, the spectral response of a grating can be approximated as a convolution of the diffraction pattern, G, with the boxcar functions representing the entrance slit, Π_a, and the detector, Π_d (Mouroulis and Green, 2018):

$$\text{SRF} \sim \Pi_a \circledast G \circledast \Pi_d. \tag{2.15}$$

Since more optical elements for collimation and focusing of the light beam are present in the spectrometer, the SRF typically originates from even more boxcar-like convolution operations. It turns out that, as a result, many grating spectrometers have response functions similar to a Gaussian (or "super Gaussian") shape (Beirle et al., 2017). Finally, it should be noted that many detector elements are needed to capture the spectral information of the grating.

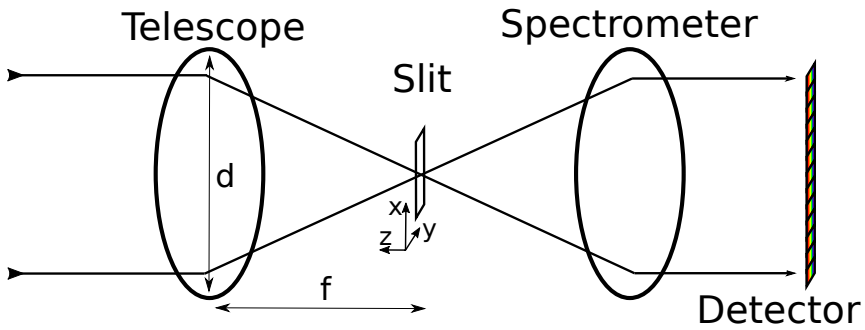

Figure 2.4: Sketch of a push-broom imaging spectrometer with rectangular slit. The smaller the ratio of focal length, f, and aperture, d, of the telescope the more light can be collected by the sensor. Behind the slit, the light is guided through dispersive elements onto the detector. Spectra are expanded along the y-axis, which is also the direction of motion of the entire system. Spatial information is collected along the length of the split in x-direction.

Push Broom Imaging Spectrometers

Push broom imaging spectrometers do not only collect spectral information of radiation incident on the instrument, but they simultaneously collect spatial information of the at-aperture radiation field along a spatial line. The general principle is illustrated in Fig. 2.4. The sensor has four critical components along the instrument axis z: a telescope with aperture diameter, d, a slit in the x-y-plane at distance f from the aperture, a spectrometer and a detector array parallel to the slit.

The telescope is needed to direct sufficient radiation collected from the desired viewing angle into the instrument. While many technical realizations of telescopes exist, an intuition about the quality of any telescope can be gained from the ratio of focal length and aperture diameter $\frac{f}{d}$, which is commonly referred to as "F number". Optical systems with low F number are called "*fast optics*", as exposures with sufficient signal can be realized in shorter time[6]. The slit of the instrument serves to constrain the radiation field to a dimension that will later fit onto the detector. It is oriented perpendicular to the incident light (in the xy-plane in Fig. 2.4). The spectrometer subsequently disperses the radiation in y-direction and propagates the spatial components in x-direction towards the detector. Spatial and spectral information is recorded at the same time by mapping the field of view onto a two-dimensional set of detectors, also known as a *focal plane array* (see section 2.2.2).

A single measurement results in one image that looks like a line. When the sensor is moved along the y-axis and the measurement process is continuously repeated, one can essentially map the at-aperture radiation field along both the spectral and spatial axis.

The spectral response functions of push broom imaging instruments generally depend

[6] A small F number of two (notation f/2) collects four times as many photons as a f/4 telescope (aperture area varies with d^2).

on the implementation of the spectrometer. Yet, the majority of push broom instruments are based on grating spectrometers so that a typical SRF behaves like the SRF of a grating (see previous paragraphs).

A detailed review of imaging spectrometer design has been presented by Mouroulis and Green (2018) and Jia et al. (2020) give an overview of established push broom imaging instruments.

2.2.2 Detectors and Spectral Noise

Following the previous discussion of how radiation can be dispersed in a spectrometer, this section introduces the concept of how that signal is actually recorded and why the measurement is noisy.

Once radiation with radiance I has been dispersed to a spectral resolution of $\Delta\lambda$ and focused in the optics of the sensor, it hits the detector with a signal, S, for a duration of t_{int}

$$S \sim I \cdot \Delta\lambda \cdot t_{int} + \sigma_{tot} \tag{2.16}$$

where σ_{tot} is the total measurement noise (see for instance Strandgren et al. (2020)). Measurement noise arises from a variety of effects. On the one hand, the amount of photons, N, received by the instrument is inherently a noisy quantity, with signal shot noise, $\sigma_{ss} \sim \sqrt{N}$. On the other hand, measurement noise is typically driven by the detector.

The detector consists of a semi-conductor material with band gaps between valence and conduction bands small enough to be excited by the incident radiation[7]. This process is very similar to the molecular absorption process described in section 2.1.1. The excitation then creates a photo current, the contributing electrons of which are temporarily "stored" in a potential well (a capacitor) for the duration of the measurement integration. The number of electrons can then be read out and it can be related directly to the number of photons absorbed by the semi-conductor. The read out process goes along with an amplification of the signal, which can be adjusted according to the relative intensity of incident radiation. In practice, noise is introduced into the measurement signal through a number of detector related effects, some of which are listed below:

- Semi-conductor materials provide a photo current even in the absence of an absorption process. This current, known as *dark current*, is caused by random thermal current generation in the semi-conductor material.

- The semi-conductor will receive radiation even if the aperture of the instrument is closed, because of thermal background radiation from the various parts of the spectrometer. This introduces a thermal background noise.

[7]Only a few materials, like silicon (Si), mercury cadmium telluride (HgCdTe) and indium gallium arsenide (InGaAs), are suited for measurements of UV-VIS-IR radiation.

- The process of reading the charge accumulated in the capacitor over the course of the measurement introduces another (small) source of noise, due to noise in the read-out amplifier.

The dark current noise, σ_{dc}, and the thermal background noise, σ_{tb}, can both be reduced by cooling of the detector (and instrument), while read-out noise, σ_{ro}, is constant in temperature and cannot be avoided. Since $\sigma_{dc} \sim \sqrt{N}$ (like σ_{ss}), it can be shown that noise as a function of signal can be approximated as (Li et al., 2016):

$$\sigma_{tot}(N) \sim \sqrt{N + \sigma_{ro}^2} \tag{2.17}$$

Although this is an oversimplified description of noise characteristics of a spectral measurement where many more effects typically need to be taken into acount, it explains the overall observation in the lab: At low signal levels ($N \to 0$), the total noise is dominated by the read-out term $\sigma_{tot} \sim \sigma_{ro}$, while at high signal levels ($N < \infty$), total measurement noise follows $\sigma_{tot} \sim \sqrt{N} \sim \sqrt{S}$. Finally, eq. 2.17 is no longer valid when $N \to \infty$, because detector saturation conditions are reached and σ_{tot} becomes highly non-linear in signal-space, mostly making such measurements useless for the purposes of atmospheric science.

The combination of many detector elements into a two-dimensional focal plane array finally enables imaging spectroscopy as described in the previous chapter. An overview of focal plane array characteristics and applications can be found for example in Mackay (1986).

Up to here, the signal, S, in eq. 2.16 was given in units of *digital numbers*, i.e. the number of electrons counted by the detector. In the next section the general idea of converting digital numbers into physically meaningful variables will be discussed.

2.2.3 Sensor Characterization

A critical step in the processing chain of spectral data is the conversion of digital units (the detector measurement, see above) into radiometric units. Regardless of the spectrometer type, a common radiometric calibration approach is to reference the signal measured by the detector to a standard radiometer. These are low-radiance-uncertainty light sources – like the sun, the moon, or artificial standards in the laboratory (e.g. Eppeldauer et al., 2009, Taubert et al., 2013). The radiance standard, I_{ref}, in units of W $\mathrm{sr}^{-1}\mathrm{nm}^{-1}\mathrm{m}^{-2}$ can be related to the detector measurement, S (from eq. 2.16), as

$$I_{ref} = t_{int} \cdot R \cdot S \tag{2.18}$$

with t_{int} the integration time and R the calibration coefficient in units of radiance per time and digital numbers. When the calibration coefficients have been determined in an experiment, they can be applied to future measurements of the same sensor to convert digital numbers to radiances. Eq. 2.18 is a simplification of the actual calibration procedure,

because the signal, S, is generally a function of temperature (see section 2.2.2). Additionally, the detector signal may depend non-linearly on the at-aperture-radiance, I (see eq. 2.16). However, the specific corrections applied to eq. 2.18 in the real world depend on the problem and they vary in complexity.

As explained in section 2.2.1 a defining property of any spectrometer is its spectral response function (SRF), because it convolves the incident "infinite-spectral-resolution" radiation to a coarser spectral resolution, $\Delta\lambda$ (see eq. 2.16). The shape of the SRF was shown to be a function of the effects of entrance aperture, dispersive elements and the detector on the propagation of radiation through the sensor. As a result, the SRF must be determined experimentally so that the detector signal, S, can be characterized. The level of experimental detail, which is required to correctly measure a sensor's instrumental response function in the lab goes beyond the scope of this thesis. Here, merely a qualitative idea will be given with respect to how these experiments are usually designed .

In the case of Fourier Transform Spectrometers, one conducts measurements of spectral lines that are thinner in width than the spectral response of the instrument (e.g. narrow lines in the Doppler broadening regime), because the SRF will then dominate the line shape. The SRF can subsequently be calculated from the measured spectrum by adjusting a low number of model parameters (e.g. Hase et al., 1999). Alternatively, a monochromatic signal from a laser can be used to characterize the SRF.

In the case of a grating spectrometer each detector pixel is illuminated with monochromatic radiation that is varied over the spectral range of the detector pixel (e.g. Baumgartner, 2019). This provides a detailed measurement of the SRF and allows for a derivation of the center wavelength of the spectral pixel. For an imaging spectrometer, the instrument's response must be characterized both in the spectral dimension (same approach as for a grating) and in the spatial dimension. Spatially, calibration is carried out by moving the image of a point source across each detector pixel for the designated along and across track scan direction, while registering the sensor response (see for example Baumgartner et al. (2012)).

2.3 Radiative Transfer

The processes that control the measurements of spectral radiances in the atmosphere of Earth have been introduced in the previous sections – from fundamental physical mechanisms to instrument related effects on the measurement. In the following paragraphs, the framework used to model the measurement process will be introduced with a focus on the Earth-observing viewing geometry in the solar spectral range that is central to trace gas observations in this work. To this end – and as in section 2.1.2 – polarization effects will be neglected here, i.e. unpolarized (spectral) radiances and scattering events will be treated as scalars and scalar functions, respectively. Effects of three-dimensional radiative transfer and the spherical shell shape of the atmosphere will also be neglected. The interested reader may find the full treatment of vector radiative transfer for example in Zdunkowski

et al. (2007, ch. 10) or Hasekamp and Landgraf (2002) and Landgraf et al. (2001), more information on 3D radiative transfer for example in Mayer (2009) and a starting point for radiative transfer in a spherical-shell atmosphere in Dahlback and Stamnes (1991).

Radiative Transfer Equation To model spectral measurements in the atmosphere of Earth, one must consider the transfer of radiation through the atmosphere from source to sensor. In this thesis the source is the sun and the sensor is an Earth-observing passive spectrometer (which convolves the at-aperture radiance with the SRF). As long as the zenith angle of incident sunlight is sufficiently small, i.e. $\theta_0 < 70°$(see for instance Dave and Mateer (1967)), one can treat the atmosphere as a plane-parallel volume. This assumption makes the formulation of the transfer equation possible in a standard cartesian coordinate system. When a beam of sunlight is observed under a viewing zenith angle θ and an azimuth angle φ through the atmosphere along a path $ds = dz/cos(\theta) \equiv dz/\mu$, its radiance, I, will be depleted through absorption and (out-) scattering, while some radiance will be added by (in-) scattering from different beams, resulting in a total change in radiance, $dI/ds = \mu dI/dz$ (see Fig. 2.5). Thermal (black body) emission of the atmosphere is generally also added to the beam, but will be neglected in this introduction, because the remote sensing instruments in this thesis do not measure in the thermal spectral range where atmospheric emission matters ($\sim 3.5 < \lambda < 100$ μm). Hence, the radiative transfer equation for at-aperture radiance in the solar spectral range can be summarized by

$$\mu \frac{dI}{dz} = \mu \left(\underbrace{\frac{dI_{\text{abs}}}{dz} + \frac{dI_{\text{out-scat}}}{dz}}_{\text{extinction}} + \underbrace{\frac{dI_{\text{in-scat}}}{dz}}_{\text{source } J'} \right) = -\beta_{\text{ext}} I + J' \tag{2.19}$$

where the subscripts refer to absorption, out-scattering and in-scattering. The combination of absorption and out-scattering processes on the right-hand-side of eq. 2.19 is defined through an extinction coefficient

$$\frac{dI_{\text{abs}}}{dz} + \frac{dI_{\text{out-scat}}}{dz} = -\beta_{\text{abs}} I - \beta_{\text{scat}} I \equiv -\beta_{\text{ext}} I \tag{2.20}$$

with the absorption coefficient, β_{abs}, which was introduced in eq. 2.5 and the scattering coefficient $\beta_{\text{scat}} = \beta_R + \beta_M$ the sum of Rayleigh and aerosol (Mie) scattering cross sections introduced in section 2.1.2.

The increase in radiance due to in-scattering from the direction (θ', φ') into the sensor viewing direction (θ, φ) (the source term in eq. 2.19) is what makes radiative transfer a challenge. In-scattering can occur from every direction in space and therefore one needs to account for all solid angles and evaluate the scattering phase function for each of these possibilities. This is a problem that cannot be solved analytically and it becomes even more challenging when clouds are introduced into the atmosphere (remember the complexity of scattering phase functions of large particles). For this reason, clouds are left out of this introduction entirely – and in trace gas remote sensing one tries to avoid clouds in almost

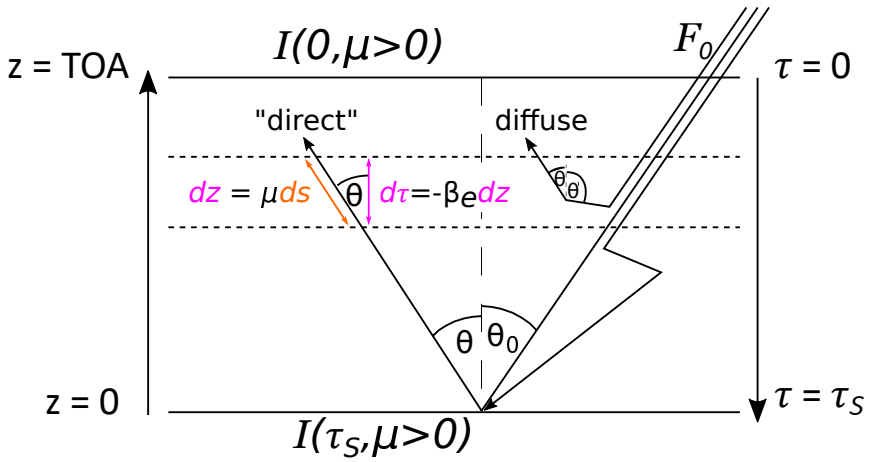

Figure 2.5: Sketch of radiative transfer through a two-dimensional, plane-parallel atmosphere visualizing the upwelling radiance at viewing zenith angle θ ($\mu = \cos(\theta)$), $I(0, \mu > 0)$, presented in eq. 2.24. There are two contributions – "direct" radiation reflected at the surface and attenuated by extinction processes in each atmospheric layer $d\tau$ and an exemplary "diffuse" light path. Solar radiation with flux F_0 is incident at the top under zenith angle θ_0.

all situations. While Rayleigh and Mie phase functions for individual scattering events are azimuth-symmetric, the source J' in eq. 2.19 must be expressed by integrating the scattering phase function over all zenith and azimuth angles as

$$J' \equiv \mu \frac{dI_{\text{in-scat}}}{dz} = \frac{\beta_{\text{scat}}}{4\pi} \int_0^{2\pi} \int_{-1}^{1} p(\mu, \varphi; \mu', \varphi') I(\mu', \varphi') d\mu' d\varphi' \tag{2.21}$$

where $p(\mu, \varphi; \mu', \varphi')$ is the scattering phase function for a scattering event from any direction (μ', φ') into the viewing direction (μ, φ) – as introduced in section 2.1.2.

Solution of the Radiative Transfer Equation for Upwelling Radiance Due to the complexity of the scattering phase function eq. 2.19 does not possess an analytical solution. Here, a general expression for upwelling radiance will be derived, i.e. $\mu > 0$, as observed by an Earth-observing instrument (see Fig. 2.5). To this end, one can consider the atmosphere as one or more homogeneous layers that all have a similar optical path, $d\tau$, where $\tau(z)$ is defined as

$$\tau(z) = -\int_z^{\text{TOA}} \beta_{\text{ext}}(z') dz'. \tag{2.22}$$

The optical depth or optical thickness, τ, is a vertical axis of the atmosphere, which indicates the downward increasing amount of extinction (see Fig. 2.5). Using $d\tau = -\beta_{\text{ext}} \mu ds = -\beta_{\text{ext}} dz$ and $J = J'/\beta_{\text{ext}}$ one can simplify the radiative transfer equation 2.19 to

$$\mu \frac{dI}{d\tau} = I - J. \tag{2.23}$$

A formal solution of the transfer equation can be achieved after multiplication with the *transmittance*, $T = e^{-\tau/\mu}$, so that eq. 2.23 can be integrated over the atmosphere, for example from top to surface, $\tau = 0$ to $\tau = \tau_S$ (Liou, 1980, ch. 1.4.4). While radiative transfer models typically propagate radiances between many closely neighboring layers in optical depth space, the following is a simplification to identify the most critical contribution to the radiance measurements that this thesis deals with. One can show for upwelling radiance at TOA ($\tau = 0$) and direction $\mu > 0$ (see Fig. 2.5):

$$I(0, \mu > 0) = \underbrace{I(\tau_S, \mu > 0) e^{-\tau_S/\mu}}_{\text{“direct”}} + \underbrace{\frac{1}{\mu} \int_0^{\tau_S} J \cdot e^{-(\tau')/\mu} d\tau'}_{\text{diffuse}} . \tag{2.24}$$

As one would assume intuitively, radiance at the top of the atmosphere (at the sensor) consists of two separate contributions: a “direct” and a diffuse term. The “direct” term originates from radiance reflected at the surface under the specific viewing direction, $I(\tau_S, \mu > 0)$, and attenuated by the transmittance (strictly speaking this contribution is therefore a single-scattering contribution). The diffuse term contains scattered radiation from all levels in the atmosphere, which are all attenuated by the respective transmittances. For the reflected radiance, one can show similarly that $I(\tau_S, \mu > 0)$ contains direct radiance from the sun (attenuated by transmittance) plus diffuse contributions. The fact that one can separate direct and diffuse terms in radiative transfer also separates viewing geometries in passive remote sensing. Whenever a sensor is oriented towards the source – for example a ground based spectrometer oriented towards the sun – the diffuse term can safely be neglected, because the magnitude of the direct term is so much greater (as long as the target source is the brightest source in the system). Transfer calculations become much easier in such cases, but, on the other hand, any information about aerosols is lost.

Scattering of radiation at the surface of the Earth usually involves absorption, i.e. certain wavelengths are absorbed and scattering occurs anisotropically (and often with altered polarization state) into the atmosphere. Yet, lacking alternatives, for downward-looking trace gas remote sensing instruments, which only view the scene from one specific azimuthal angle, the reflectivity of the surface in the shortwave spectral range is approximated by a single value, which is referred to as the *surface albedo*, $a = a(\lambda)$. The albedo is essentially the probability for a reflection to occur (i.e. $a = 1$: full reflection towards the sensor) under the assumption that the surface reflects isotropically (as a “Lambertian” reflector).

Many approximations have been proposed to handle the diffuse radiation term in eq. 2.24. Most of these approaches somehow approximate the diffuse radiation field $I(\mu')$ and the phase function $p(\mu', \mu)$, that make up the diffuse source term, $J = J(I, p)$ (see eq. 2.21). Simple choices include setting $I(\mu) = I(\mu > 0) + I(\mu < 0) = \text{const.}$ (*two stream approximation*) or $I(\mu) = I_0 + \mu I_1$ (*Eddington approximation*). Under such assumptions, the phase function can either be represented by a few parameters or one can expand the phase function into a series of Legendre polynomials.

In the next paragraph a short introduction to a specific technique will be given to solve the radiative transfer equation which may help to gain more of an intuition about diffuse

radiation.

Successive-Orders-of-Scattering-Approach In this approximation the azimuth dimension shall be neglected for simplicity and the source term of diffuse radiation in eq. 2.24 is treated as a sum of distinct *orders of scattering*, J_n, i.e.

$$J(\tau, \mu) = \Sigma_{n=1}^{\infty} J_n(\tau, \mu) \tag{2.25}$$

where the index n is the order of scattering; $n = 1, 2, ...$ meaning that the beam is scattered once, twice, etc. on its path to the sensor. In this approximation, one can show (Liou, 1980, ch. 6.2.1) that the diffuse upwelling radiance field at scattering order n can likewise be calculated as a sum of scattering orders. When the solar flux, F_0 (at TOA), and the solar zenith angle, μ_0, are known, it is straightforward to obtain the direct transmittance towards the ground at optical depth τ': $I_0 = \pi F_0 e^{-\tau'/\mu_0} \delta(\mu' - \mu_0)$. All diffuse source terms in eq. 2.25 are then defined by the recursive relationships

$$J_{n+1} = \frac{\omega}{2\pi} \int_{-1}^{1} p(\mu', \mu) I_n(\mu') d\mu' \tag{2.26}$$

$$I_{n \geq 1} = \frac{1}{\mu} \int_{0}^{\tau_S} J_n \cdot e^{-(\tau')/\mu} d\tau' \tag{2.27}$$

with $\omega = \beta_{\text{scat}}/\beta_{\text{ext}}$ the so called *single scattering albedo* ($0 \leq \omega \leq 1$). Depending on the value of ω, i.e. depending on the atmospheric composition[8], high order terms can effectively be neglected in eq. 2.25, because, as one can see from the recursion formulas, $I_n \sim \omega^n$. Thus, one can determine an order N at which the sum in eq. 2.25 can be truncated and one also typically replaces the integrations over μ and τ in eqs. 2.26, 2.27 by a sum over a certain number of layers and directions (referred to as "streams" in the literature).

The steps outlined above enable modelling of (spectral) radiances at the top of the atmosphere through radiative transfer calculations. The specific details of the radiative transfer model, as employed in this thesis, will be presented in chapter 3.1. In the following and last section of this chapter, it will be shown how the transfer model can be combined with measurements to *retrieve* information about the atmospheric state (e.g. CO_2 concentrations).

[8]The single scattering albedo is a function of wavelength, so that it may vary strongly even within individual spectral lines. For example, one can typically expect ω to be lower towards absorption line centers (where absorption increases) and greater in the line wings, which means that the radiative path through the atmosphere is generally shorter at the line center than in the wings.

2.4 From Spectra to CO_2 Concentrations

The previous sections have shown that measurements of spectral radiances in the atmosphere of Earth contain a lot of information about a number of processes. To *retrieve* an atmospheric state variable – like the profile of CO_2 concentration – from the measurement, one tries to compare the measured radiance spectrum to a simulated spectrum from a radiative transfer model (with variable CO_2) and tune the desired model parameters such that the difference between measurement and model is on the order of (or smaller than) the measurement noise. However, achieving agreement between measurement and model can be ambiguous, especially for Earth-observing spectrometers, where, for example, variations in a spectral absorption feature can be caused by several atmospheric species with overlapping absorption lines, by changes in the lightpath due to aerosol scattering or by the reflection properties of the surface or even by artifacts of the spectrometer. As a result, CO_2 retrievals rely on statistical methods, many of which have been described by Rodgers (2008). In the following, an introduction to the specific approach used in this work will be given.

The remote sensing problem The goal of remote sensing in this thesis is to derive n characteristic quantities of the atmosphere (trace gas concentrations, surface albedo, etc.), assembled in a vector $\vec{\mathbf{x}}$ from a spectral measurement, $\vec{\mathbf{y}}$, with spectral dimension m and a forward (radiative transfer) model, $\vec{\mathbf{F}}$, through the relationship

$$\vec{\mathbf{y}} = \vec{\mathbf{F}}(\vec{\mathbf{x}}) + \vec{\boldsymbol{\sigma}}. \tag{2.28}$$

At this point, the vector $\vec{\boldsymbol{\sigma}}$ in eq. 2.28 only contains the total measurement noise from eq. 2.17, but it will be expanded later to also accommodate errors of the model. By linearizing $\vec{\mathbf{F}}$ around some initial state $\vec{\mathbf{x}}_0$ by means of Taylor expansion one can rewrite eq. 2.28 as

$$\vec{\mathbf{y}} \approx \vec{\mathbf{F}}(\vec{\mathbf{x}_0}) + \mathbf{K}(\vec{\mathbf{x}} - \vec{\mathbf{x}_0}) + \vec{\boldsymbol{\sigma}} \tag{2.29}$$

$$\Rightarrow \tilde{\vec{\mathbf{y}}} = \mathbf{K}\vec{\mathbf{x}} + \vec{\boldsymbol{\sigma}} \tag{2.30}$$

with $\tilde{\vec{\mathbf{y}}} = \vec{\mathbf{y}} - \vec{\mathbf{F}}(\vec{\mathbf{x}_0}) + \mathbf{K}\vec{\mathbf{x}}_0$. The $m \times n$ matrix $\mathbf{K}_{ij} = \frac{\delta \vec{\mathbf{F}}_i(\vec{\mathbf{x}})}{\delta \vec{\mathbf{x}}_j}$ is known as the *Jacobian* or *weighting function matrix*. It is a measure of the sensitivity of the observed radiance at spectral index i to changes in the respective state vector element x_j. The Jacobian can be obtained numerically by calculating the derivatives of the transfer model, $\vec{\mathbf{F}}$, with respect to state vector parameters, or analytically through adjoint perturbation theory borrowed from neutron transport calculations in nuclear reactors, which will be discussed briefly in chapter 3.1.2. Formally, eq. 2.28 has now been simplified into a linear algebra problem, where the solution $\vec{\mathbf{x}}$ can be found by inverting the Jacobian matrix. However, this *inversion* is often not straight forward.

In the case of atmospheric sounding, the Jacobian usually cannot be inverted analytically, because it is almost never a square matrix, i.e. mostly $m > n$. In addition, it is not

possible to reduce typical Jacobians into to an $n \times n$ shape – which could then be inverted – because the rows of $\mathbf{K}$, $\vec{\mathbf{K}}_i$, are not linearly independent (which means that they contain redundant or inconsistent information, e.g. due to measurement noise). In the present case, eq. 2.28 is the kind of problem that is *ill-posed* in the sense that it is simultaneously *over-* and *under-determined*. It is over-determined since more measurements are available than state vector entries to solve for and it is under-determined, because some components of the actual state of the atmosphere cannot be captured adequately by the measurement. For example, a satellite measurement of upwelling radiation intrinsically does not contain much information about the vertical structure of trace gas profiles, because of the observing geometry. The next paragraph will explain why such under-determined retrieval problems can occur from a linear algebra point of view.

Singular Vector Decomposition of the Jacobian Mathematically, under-determination of the remote sensing problem manifests itself in vanishing *singular values* for some entries of the Jacobian (see Rodgers (2008, ch. 2.2.2)). According to Rodgers (2008, Appendix A.4), a singular vector decomposition is a sort of eigenvalue problem constructed for an arbitrary $m \times n$ matrix, $\mathbf{K}$, which can be decomposed into the singular vectors $\mathbf{U}$ and $\mathbf{V}$ and a matrix $\mathbf{\Lambda}$ through

$$\mathbf{K}_{m\times n} = \mathbf{U}_{m\times n}\mathbf{\Lambda}_{n\times n}\mathbf{V}^T_{n\times n}. \tag{2.31}$$

The dimensions of the vectors and matrices are indicated as subscripts above. Such a singular vector decomposition (SVD) can generally be used to solve eq. 2.30 numerically, via the *pseudo inverse* Jacobian $\mathbf{K}^\dagger = \mathbf{V}\mathbf{\Lambda}^{-1}\mathbf{U}^T$.The matrix $\mathbf{\Lambda}$ is of special interest, because it is a diagonal matrix that contains the singular values, λ_i, of the Jacobian, which can be sorted such that the λ_i become smaller with increasing index i (see for instance Borsdorff et al. (2014)). As a consequence, equation 2.30 can be shown to decompose into a sum over the singular values of $\mathbf{K}$:

$$\tilde{\vec{\mathbf{y}}} = \Sigma_{i=1}^{n}\lambda_i \left(\vec{\mathbf{v}}_i^T \vec{\mathbf{x}}\right) \vec{\mathbf{u}}_i + \vec{\boldsymbol{\sigma}} \tag{2.32}$$

where the vectors $\vec{\mathbf{u}}_i$, $\vec{\mathbf{v}}_i$ are the column vectors of the singular vectors $\mathbf{U}$ and $\mathbf{V}$, respectively. Contributions with high indices i impact the measurement, $\tilde{\vec{\mathbf{y}}}$, much less than the first few contributions, i.e. $\lambda_{i\to n} \to 0$. Additionally, after inversion with $\mathbf{K}^\dagger$ (and truncation of the sum in eq. 2.32) the state vector can be shown to be proportional to $\vec{\mathbf{x}} \sim \mathbf{\Lambda}^{-1}\vec{\boldsymbol{\sigma}}$ (Rodgers, 2008, ch. 6.3). This means that when there are vanishing singular values λ_i, the SVD inversion produces results that are nothing more but amplified noise. Such state vector components are said to be within the *null space* of $\mathbf{K}$ – their values are not accessible in the measurement data. While there are many statistical techniques that stabilize the inversion with respect to variables that are hard to extract from the measurement (Rodgers, 2008), the next section focuses on a *regularized* retrieval variant, which reduces the noise that propagates into some components of the state vector.

Twomey-Phillips-Tikhonov Regularization The idea behind statistical inversion approaches for eq. 2.30 is to make use of some prior information that is available before the measurement is even made. For instance, when inverting CO_2 concentrations, it is safe to assume that the value of CO_2 in the atmosphere must lie between zero and positive infinity. From the range of possible values, one *a priori* value can be chosen for each state vector entry to form the a prior state vector $\vec{\mathbf{x}}_a$. Twomey, Phillips and Tikhonov have proposed to find the state vector, $\vec{\mathbf{x}}$, by minimizing the following cost function (Phillips, 1962, Twomey, 1963).

$$\chi^2 = (\vec{\mathbf{x}} - \vec{\mathbf{x}}_a)^T \gamma \mathbf{W} (\vec{\mathbf{x}} - \vec{\mathbf{x}}_a) + \left(\vec{\mathbf{y}} - \vec{\mathbf{F}}(\vec{\mathbf{x}})\right)^T \mathbf{S}_{\boldsymbol{\sigma}}^{-1} \left(\vec{\mathbf{y}} - \vec{\mathbf{F}}(\vec{\mathbf{x}})\right) \tag{2.33}$$

The scalar γ is the *regularization parameter* and $\mathbf{W}$ is the *regularization matrix* and there can in general be various γ to scale subentities of $\mathbf{W}$. Setting γ to zero reduces eq. 2.33 to a classic least squares solution; weighted with the measurement error covariance matrix $\mathbf{S}_{\boldsymbol{\sigma}}$ that contains the square of the measurement noise contributions on the diagonal. This right-hand-side term introduces the measurement noise into the retrieval and will eventually cause unphysical results, as discussed above, if sensitivity to some state vector variable is very low. These are the situations, when it is favorable to constrain the result to the prior value. The smoothing operator $\mathbf{W}$ that mediates the difference between retrieval result and the prior can be chosen freely, but for simplicity I'll assume $\mathbf{W} = \mathbb{1}$ here. As γ is increased towards higher values, the a priori information contributes more and more to the retrieved state vector. By evaluating $d/d\vec{\mathbf{x}}\ \chi^2 = 0$, the minimum of eq. 2.33 is found for

$$\implies \vec{\mathbf{x}} = \vec{\mathbf{x}}_a + \underbrace{(K^T \mathbf{S}_{\mathbf{y}}^{-1} K + \gamma \mathbf{W})^{-1} K^T \mathbf{S}_{\mathbf{y}}^{-1}}_{\mathbf{G}} (\vec{\mathbf{y}} - \vec{\mathbf{F}}(\vec{\mathbf{x}}_a)). \tag{2.34}$$

The above equation can be summarized simply as

$$\vec{\mathbf{x}} = \vec{\mathbf{x}}_a + \mathbf{G}(\vec{\mathbf{y}} - \vec{\mathbf{F}}(\vec{\mathbf{x}}_a)). \tag{2.35}$$

The difficulty in any regularized retrieval approach is to find appropriate values of γ for those state vector elements that shall be regularized in the retrieval. Ideally, γ should smooth the retrieval result, but still allow for a physical interpretation of the inversion beyond the prior information. In chapter 4.1, Fig. 4.4 shows how a regularization can be realized and how suitable regularization parameters are chosen in this work. Another approach of constraining the regularization parameters is presented in Hansen (1992), Hansen and O'Leary (1993).

The formal solution of the remote sensing problem has been found in eq. 2.35 by taking the derivative of the cost function with respect to the state vector. As a result, eq. 2.35 will produce the correct result for a problem, that is linear in state vector space, yet the regularization was introduced precisely because the forward model is not linear with respect to some state vector components (that lie in the near-null space of the Jacobian). Thus, the retrieved state vector $\vec{\mathbf{x}}$ has to be found iteratively, with repeated updates to

the *gain matrix*, $\mathbf{G}$, which dominates the iteration step direction (see chapter 3.1.3). Some iterative methods for the minimization of the cost function, which differ primarily in their computational efficiency and their ability to reach convergence when unfavorable starting points are chosen, are summarized in Rodgers (2008, ch. 5).

The regularized state vector found in eq. 2.35 is only an approximation of the true state of the atmosphere. In the next paragraph, retrieval error characterization will provide the limits within which retrieval results are valid.

Retrieval Error One can characterize the deviation of the estimated state vector $\vec{\mathbf{x}}$ from the true state, $\vec{\mathbf{x}}_{\text{true}}$ by accounting for both measurement and forward model error terms $\vec{\boldsymbol{\sigma}}_M, \vec{\boldsymbol{\sigma}}_F$ in eq. 2.28 :

$$\vec{\mathbf{y}} = \vec{\mathbf{F}}(\vec{\mathbf{x}}_{\text{true}}) + \vec{\boldsymbol{\sigma}}_M + \vec{\boldsymbol{\sigma}}_F \tag{2.36}$$

$$\approx \vec{\mathbf{F}}(\vec{\mathbf{x}}_a) + K(\vec{\mathbf{x}}_{\text{true}} - \vec{\mathbf{x}}_a) + \vec{\boldsymbol{\sigma}}_M + \vec{\boldsymbol{\sigma}}_F \tag{2.37}$$

Two kinds of errors in the forward model can be distinguished: those that arise from simplifications in radiative transfer modeling (see section 2.3) and those that arise from uncertainty in auxiliary parameters used by the model; for example, spectroscopic parameters. While actual modeling errors must typically be assessed in simulation studies and comparisons with more sophisticated models (Butz et al., 2009), errors of auxiliary parameters may be more readily available. Substituting eq. 2.37 into eq. 2.35, the error of the retrieved state $\vec{\mathbf{x}}$ can be quantified as a deviation from the true state (Rodgers, 2008, ch. 3):

$$\vec{\mathbf{x}} - \vec{\mathbf{x}}_{\text{true}} = (\mathbf{A} - 1)(\vec{\mathbf{x}}_{\text{true}} - \vec{\mathbf{x}}_a) + \mathbf{G}\vec{\boldsymbol{\sigma}}_M + \mathbf{G}\vec{\boldsymbol{\sigma}}_F \tag{2.38}$$

The matrix $\mathbf{A} = \mathbf{GK}$ is known as the *averaging kernel* and the three error contributions on the right-hand-side are referred to as *smoothing error*, *noise error* and *forward model error*. Diagonal entries of the averaging kernel can be understood as the *Degree of Freedom for Signal*, DFS, of the corresponding state vector entry. The DFS of each retrieval variable indicates the information content of the measurement with respect to that variable, i.e. DFS close to zero means the variable is not well constrained by the measurement. To interpret eq. 2.38 consider solving for the retrieved state $\vec{\mathbf{x}}$:

$$\vec{\mathbf{x}} = \mathbf{A}\vec{\mathbf{x}}_{\text{true}} + (1 - \mathbf{A})\vec{\mathbf{x}}_a + \mathbf{G}\vec{\boldsymbol{\sigma}}_M + \mathbf{G}\vec{\boldsymbol{\sigma}}_F \tag{2.39}$$

The inversion can thus be understood as a smoothing operation of the real atmospheric state, where the ability to carry over true information from the atmosphere into the state vector is characterized by the averaging kernel (see also Rodgers and Connor (2003)). The component of the true atmosphere, that is not picked up into the retrieval (because the measurement is insensitive to it) is replaced by prior information, $(1 - \mathbf{A})\vec{\mathbf{x}}_a$. Finally, the gain matrix propagates the measurement noise and forward model errors into the retrieval.

Chapter 3

Methods and Data

This chapter introduces the methods and datasets that are at the core of this work. The central algorithm, with which most of the analyses of this thesis have been carried out, is the *RemoTeC* retrieval code, presented in section 3.1. It has been applied to a range of datasets including measurements of the TANSO-FTS on board of the GOSAT satellite (section 3.2), and the AVIRIS-NG (section 3.3) and specMACS (section 3.4) imagers. Additionally, the TCCON dataset has been used for validation purposes and will be introduced in section 3.5.

3.1 The RemoTeC Retrieval Algorithm

The RemoTeC retrieval algorithm (e.g. Butz et al., 2009, Guerlet et al., 2013b) is a software that consists of two components: a radiative transfer model (Hasekamp and Landgraf, 2002, Landgraf et al., 2001, Schepers et al., 2014) and a regularization based inversion algorithm (e.g. Butz et al., 2010, 2011). The code can be used to retrieve atmospheric state variables – like trace gas abundances – from radiance spectra measured by earth-observing instruments. Technical details of the retrieval method will be presented in the following sections 3.1.1, 3.1.2 and 3.1.3, while section 3.1.4 finally gives an overview of previous applications of the algorithm.

3.1.1 Auxiliary Data

Several auxiliary datasets need to be merged in a preprocessing step to operate the retrieval code. These include gridded meteorological data for the observation scene such as vertical pressure, temperature and humidity profiles, as well as surface pressure and surface winds, which are obtained from weather reanalyses from the European Centre for Medium-Range Weather Forecasts (ECMWF), see Berrisford et al. (2011), Copernicus Climate Change Service (C3S) (2017), Hersbach et al. (2020)). The reanalysis data are interpolated to the ground footprint of the sounding taking into account ground elevation

data from the Shuttle Radar Topography Mission (SRTM) digital elevation model (Hennig et al., 2001). In addition, the initial guess for the vertical distribution of carbon dioxide is approximated by the 2011 CarbonTracker model (Peters et al., 2007). Further input parameters to the algorithm are a high spectral resolution solar reference spectrum (Sneep et al., 2015) and zenith and azimuth angles defining the solar position and the viewing geometry.

3.1.2 Radiative Transfer Model

The radiative transfer model solves eq. 2.23 by splitting the plane-parallel model atmosphere obtained from the preprocessing procedure into 36 barometrically equidistant layers. Each layer is split up once more to calculate molecular absorption cross sections, σ_{abs} (as in eq. 2.5), on a pressure and temperature grid with higher resolution. The values of the absorption cross sections are then interpolated to the center of each layer of the transfer model. To solve the radiative transfer equation, the diffuse radiation field is discretized into 16 zenith angle streams (compare chapter 2.3, page 26). Further, the scattering phase function is expanded into Legendre polynomial series with regard to azimuth angles (see Hasekamp and Landgraf, 2002).

Molecular cross sections The calculation of the molecular absorption cross sections is carried out in a *line-by-line* fashion, where every spectral line tabulated in the HITRAN database (Gordon et al., 2017, Rothman et al., 2009) is used to infer σ_{abs} for a given molecule at very high spectral resolution ($\Delta\lambda < 0.05$ nm). In this work, the line shape function used to determine σ_{abs} depends on the application. For retrievals at coarse spectral resolution and for atmospheric species that interfere with the CO_2 spectrum (e.g. H_2O), the Voigt profile (eq. 2.4) offers sufficient performance. When retrieving CO_2 concentrations at high spectral resolution, spectral line mixing (see page 11) can be accounted for through a more sophisticated line shape profile from Lamouroux et al. (2010). Collision induced absorption (CIA) features of oxygen are modeled with a software from Tran and Hartmann (2008). Line-by-line calculations are carried out in advance of the retrieval to save computational effort.

Aerosol cross sections Scattering and absorption cross sections, $\sigma_{aer,scat}$ and $\sigma_{aer,abs}$, of spherical aerosols as well as their phase functions are taken from a look-up-table by Dubovik et al. (2006). These crucial aerosol optical properties can be extracted from the look-up-table when the total column number density of aerosols, N_{aer}, the size distribution $n_{aer}(r)$ and the real and imaginary parts of the aerosol refractive index $m = m_r - i \cdot m_i$ are known (recall $\sigma_{aer,abs} \sim m_i$, van de Hulst (1981, ch. 14.1)). In the present work, the refractive index is fixed at $m = 1.4 - i \cdot 0.003$ across all wavelengths[1] so that the aerosol

[1]This choice of refractive index leads to negligible absorption for small spherical particles (van de Hulst, 1981, ch. 14.1) and m is similar to values expected, for example, for Saharan sand aerosol particles in the SWIR spectral range (compare ARIA Database, University of Oxford, 2020).

total column and the size distribution are the only free variables.

Aerosol Parameterizations To simplify and stabilize the retrieval, the size distribution of aerosols is assumed to follow a power-law (Butz et al., 2009, Fig. 2):

$$n_{aer}(r) = \begin{cases} A & r \leq r_1 \\ A\ (r/r_1)^{\alpha} & r_1 < r \leq r_2 \\ 0 & r > r_2 \end{cases} \tag{3.1}$$

with A a normalization parameter, the limiting particle radii are $r_1 = 0.1$ μm and $r_2 = 10$ μm and the exponent α a single retrieval parameter characterizing the size distribution. Calculation of aerosol optical depth in a given layer of the model can be carried out according to eq. 2.22 when a further assumption about the vertical profile of aerosol particles is made. The RemoTeC algorithm uses a Gaussian parameterization of the height profile $h(z)$:

$$h(z) = B\ \exp\left(-\frac{4\ \ln 2 (z - z_{aer})^2}{w_{aer}(z_{aer})^2}\right) \tag{3.2}$$

where B is a normalization parameter and the width, w_{aer}, about the center height of the aerosol layer, z_{aer}, is fixed to 2,000 m. RemoTeC retrieves N_{aer}, α and z_{aer} from radiance measurements to approximate aerosol optical properties. The vertical aerosol optical depth of each model layer k, $\tau_{aer,k}$, is finally given by the product of aerosol cross sections with the aerosol profile function

$$\tau_{aer,k} = (\tau_{aer,abs} + \tau_{aer,scat}) \cdot h(z_k)\Delta z_k. \tag{3.3}$$

The modeling of aerosol scattering effects described by eqs. 3.1 to 3.3 must be regarded as an *effective* aerosol parameterization. The RemoTeC aerosol model neglects non-spherical particle shapes and the variability in real-world aerosol size and height distributions is not represented in eqs. 3.1 and 3.2. Thin (sub-visual) cirrus clouds are also not considered in the particle scattering forward model, yet Butz et al. (2009) and Guerlet et al. (2013b) showed that the model has some capability to account even for cirrus scattering. The effective aerosol retrieval can be thought of as an attempt to generate knowledge about light path changes by minimizing any spectral residuals that remain after fitting the trace gas concentrations. At the same time the aerosol parameterization ensures convergence of the inversion algorithm, because information content on aerosol scattering properties is limited in the measurements that RemoTeC is typically applied to (see section 3.1.3).

Analytical Calculation of Jacobians Apart from its ability to simultaneously adjust aerosol and trace gas properties as discussed above, another key quality of the RemoTeC algorithm is its analytical treatment of the Jacobian matrix, $\mathbf{K}$ (see eq. 2.30). Instead of calculating the derivatives of the forward model with respect to the state vector variables numerically (which is computationally expensive), the derivatives can be obtained

analytically as described in Hasekamp and Landgraf (2002), Landgraf et al. (2001, and references therein). In summary, there exists an *adjoint* formulation of the radiative transfer equation (2.23), which propagates the *adjoint radiance*, I^+, from the sensor backwards to the source. Mathematically, this is equivalent to changing the sign of the streaming term $\mu\frac{dI}{d\tau} \Rightarrow -\mu\frac{dI^+}{d\tau}$ in the transfer model and reversing all scattering events in the source term (see eq. 2.21) of the transfer model by reverting the direction of scattering in the phase function: $p(\mu' \rightarrow \mu) \Rightarrow p(\mu' \leftarrow \mu)$. Conceptually, the information about an atmospheric state, $\vec{\mathbf{x}}$, contained in the (forward) modeled at-sensor-radiance, I, is equivalently contained in the (backward) modeled adjoint radiance, I^+, at the top of the atmosphere at the point of entry of incident solar radiation. These two mathematically equivalent expressions of how radiation is propagated through the atmosphere are both descriptions of the model $\mathbf{F}(\vec{\mathbf{x}})$. In first order perturbation theory one can then show that the derivatives of the model are given by an integral over $I^+ \cdot I$ over solid angles and optical depth which can be solved analytically. Hence, the Jacobian can be caluclated in a computationally fast manner by solving the forward and backward formulations of the radiative transfer equation and a final integration. For a full introduction to adjoint radiative transfer see Zdunkowski et al. (2007, ch. 5, eq. 5.66).

3.1.3 Inversion Strategy

Regularization Set-Up Throughout this work, the RemoTeC retrieval algorithm is operated with a Twomey-Phillips-Tikhonov regularization method (see chapter 2.4) with respect to the three effective aerosol parameters N_{aer}, α, z_{aer} (eqs. 3.1,3.2) and sometimes also with respect to CO_2 column concentrations, XCO_2. Specifically, the inversion algorithm solves eq. 2.34 with a smoothing operator, $\mathbf{W}$, that is chosen as the first squared difference operator (Rodgers, 2008) for the CO_2 inversion, which is given by

$$\mathbf{W} = \begin{pmatrix} 1 & -1 & 0 & 0 & 0 & 0 \\ -1 & 2 & -1 & 0 & 0 & 0 \\ 0 & -1 & 2 & -1 & 0 & 0 \\ 0 & 0 & -1 & 2 & -1 & 0 \\ 0 & 0 & 0 & -1 & 2 & -1 \\ 0 & 0 & 0 & 0 & -1 & 1 \end{pmatrix} \tag{3.4}$$

for order six. The inversion of aerosol parameters uses the unity matrix as regularization matrix $\mathbf{W}$. The regularization parameters γ for trace gas concentrations and aerosol parameters are selected according to the application, i.e. some measurements may contain more information about these state vector variables than others[2]. A discussion of effects of variable regularization strengths for aerosol parameters is given in chapter 4.1, Fig. 4.4.

[2]The average value for degrees of freedom for the three aerosol parameters for GOSAT measurements is near DFS$\sim$ 2.5 Guerlet et al. (2013b)

Iterative Method The solution for the state vector $\vec{\mathbf{x}}$ is approached iteratively with a Gauss-Newton with reduced step-size method (Rodgers, 2008, ch. 5.3), which adjusts the iteration step size, $\Delta\vec{\mathbf{x}}$, after each step. The basic idea is to find the state vector $\vec{\mathbf{x}}$ by applying a dampening in the iteration step towards the solution through a parameter λ according to

$$\vec{\mathbf{x}}_{i+1} = \vec{\mathbf{x}}_i + \frac{1}{1+\lambda_i}\Delta\vec{\mathbf{x}}_i. \tag{3.5}$$

The step size, $\Delta\vec{\mathbf{x}}_i$, can be constructed from the first and second derivatives of the cost function χ^2 (eq. 2.33). As a result the step direction is given by the gain matrix, $\mathbf{G}$ (eq. 2.35), and the magnitude of the step depends on the difference between the model and the measurement as well as the (regularized) difference between the current state, $\vec{\mathbf{x}}_i$ and the prior state (for details see Rodgers, 2008, eq. 5.8). In the first iteration (when $\vec{\mathbf{x}}_0$ would be the initial guess, derived from a prior), $\lambda_0 = 10$ is chosen so that $\Delta\vec{\mathbf{x}}_0$ is significantly constrained. In each iteration thereafter, the value of the residuals, χ^2, is compared to the value of χ^2 of the previous iteration. If the residuals have increased by more than 10%, the iteration is reapeated with a step size λ_{i+1} that is further reduced by multiplying $\lambda_{i+1} = \lambda_i \times 2.5$. In the rest of cases the dampening parameter is divided by two to increase the step size in order to approach the solution, $\lambda_{i+1} = \lambda_i/2$. RemoTeC considers the inversion to have "properly converged" in iteration step n only if the parameter λ_n finally approaches zero ($\lambda_n < 0.05$).

The reduced step size method described above is only used in RemoTeC for retrievals that attempt to calculate all three effective aerosol parameters, since these are the cases with the most complex χ^2 surfaces. In all other cases, the step size is only constrained in the first step of the solver.

3.1.4 Algorithm Legacy

Its flexibility with regard to state vector configuration and the selection of spectral retrieval windows has enabled adaptation of RemoTeC for retrievals of methane and carbon dioxide column concentrations (XCO_2, XCH_4) from a number of satellite sensors over the past decade. These efforts include – among others – XCO_2 retrievals (Buchwitz et al., 2017, Butz et al., 2011, Guerlet et al., 2013b) from GOSAT measurements (Butz et al. (2011), Kuze et al. (2009, 2016), see also section 3.2) and XCO_2 retrievals (Wu et al., 2018, 2019) from the OCO-2 satellite (Crisp et al., 2008, 2017). The operational ESA XCH_4 product from Sentinel-5 Precursor/TROPOMI (Veefkind et al., 2012) is also based on RemoTeC retrievals (Butz et al., 2012, Hu et al., 2016, 2018, Lorente et al., 2020). RemoTeC retrieval results have been used in several studies to inversely infer sources (and sinks) of carbon dioxide (Basu et al., 2013, 2014, Guerlet et al., 2013a, Reuter et al., 2014, Takagi et al., 2014) and methane (Varon et al., 2019, Zhang et al., 2020).

The algorithm has also been employed to carry out radiative transfer simulations to study the expected retrieval performances of proposed satellite instruments (Butz et al., 2015, Strandgren et al., 2020). RemoTeC can further be utilized to retrieve chlorophyll

fluorescence signals of vegetation from solar backscatter measurements (Schepers et al., 2014).

Typical RemoTeC state vector variables common to most of the retrievals mentioned above are: **a)** 12-layer vertical profile of trace gas number densities **b)** H_2O total column number density **c)** three effective aerosol parameters N_{aer}, α, z_{aer} **d)** a polynomial describing the ground albedo in every retrieval window (typically of second order) and **e)** spectral shifts in every retrieval window. The trace gas total columns are then calculated by dividing the respective sum of the retrieval sub-layer number densities (total column number density, denoted $[CO_2]$) by the dry air mass ($[O_2]$), derived from the auxiliary ECMWF and SRTM data according to $\mathrm{XCO_2} = 0.2095 \cdot [CO_2]/[O_2]$ (Wunch et al., 2011a).

3.2 The TANSO-FTS Spectrometer aboard GOSAT

The Greenhouse gases Observing SATellite (GOSAT) was launched in 2009 with the primary goal to measure global CO_2 and CH_4 column concentrations (Kuze et al., 2009, 2016, Nakajima et al., 2017). GOSAT is the platform carrying the Thermal And Near infrared Sensor for carbon Observations (TANSO) Fourier Transform Spectrometer and the Cloud and Aerosol Imager (CAI) on a sun-synchronous, near-Earth orbit. While the CAI instrument (Ishida et al., 2011) mainly serves to identify clear-sky scenes[3], the measurements of the TANSO-FTS sensor are of particular interest for this thesis. In the following paragraphs, the instrument properties, its radiometric calibration, observation strategy and the scientific highlights that TANSO measurements have brought forward will be discussed briefly. The attributes of TANSO presented here, and more detailed descriptions of all instrument related issues, can be found in Kuze et al. (2009, 2011, 2014, 2016).

The Instrument Because space-borne sensors experience a lot of mechanical stress during launch and operation, it is favorable to adapt the design of Fourier transform spectrometers for satellite applications. Instead of a linear movement of one of the mirrors, the TANSO-FTS relies on a rotary pendulum motion of two cube-corner-mirrors making the measurement process less sensitive to vibrations or shocks (see Jaacks and Rippel (1989) for a description of such sensors). The mirrors are aligned with each other and the TANSO-FTS can reach a maximum optical path difference of ± 2.5 cm with mirror movements on the scale of only ~ 6 mm (Kuze et al., 2009), i.e. the interferogram ($I(x)$ in eq. 2.10) is fully two-sided. One interferogram is measured by a one-way motion of the pendulum from one turning point to the other. Interferograms are sampled according to eq. 2.11 to enable slight over-sampling of the recorded spectra with a sampling ratio of 1.2 in the SWIR bands. This means that the SRF is greater than the spectral sampling interval by a factor of 1.2. The SWIR spectra are measured at very high resolving powers of $\lambda/\Delta\lambda > 20,000$ (see Table 3.1). TANSO observations comprise upwelling spectral radiances between $0.75 - 0.78$ μm (O_2 A-band), $1.56 - 1.72$ μm (SWIR-1), $1.92 - 2.08$ μm (SWIR-2) and also in the long-wave

[3]The CAI sensor can also be used to derive a *normalized difference vegetation index* (Liu et al., 2011).

Pointing	±35° across-track ±20° along-track			
Aperture	6.8 cm			
Maximum OPD	±2.5 cm			
Integration Time	4 sec			
	O_2 A-band	**SWIR-1**	**SWIR-2**	**TIR**
Spectral Range / μm	$0.75 - 0.78$	$1.56 - 1.72$	$1.92 - 2.08$	$5.5 - 14.3$
Detector(s)	2× Si	2× InGaAs	2× InGaAs	HgCdTe
FWHM / nm	<0.1	<0.1	<0.1	1.4

Table 3.1: Key specifications of the TANSO-FTS system; adapted from Kuze et al. (2009). The short-wave bands measure two polarization directions and thus require two detectors each.

spectral range between $5.5 - 14.3$ μm (TIR). The high spectral resolution at correspondingly high values of Signal-to-Noise-Ratio (SNR[4]$= S/\sigma >$ 300, compare eqs. 2.16, 2.17) is accomplished through long integration times; typically $t_{int} = 4$ sec and a large aperture diameter of 6.8 cm. Shorter exposure times are feasible as well and the SNR is also controlled through three detector read-out-amplifier *gain* settings, which can be adjusted according to the brightness of the observation scene (recall chapter 2.2.2). GOSAT measures the three short-wave bands in two perpendicular polarization states, so that two detectors are necessary for each of these bands. Measurements of polarization states are possible due to the polarization sensitive zinc selenide beam splitter. The detectors are based on typical semi-conductor materials with band gaps in the range of VIS-IR photon energies, such as silicon (Si), indium gallium arsenide (InGaAs) and mercury cadmium telluride (HgCdTe). Total (unpolarized) spectral radiances, I_λ, can be obtained by averaging the spectra recorded for the two polarization planes (O'Brien et al., 2013). The entire optical system is temperature controlled to minimize any detrimental thermal expansion of optical components.

The sensors aboard GOSAT have been monitored with regard to their geometric, spectroscopic and radiometric performance throughout the mission. In the next paragraph, some detail on the radiometric characterization procedures will be given to provide a real-world example of the calibration strategy discussed in chapter 2.2.3.

Radiometric Calibration The TANSO sensor has been characterized radiometrically before launch according to the procedure described in chapter 2.2.3, eq. 2.18, i.e. the measured signal has been referenced to a standard radiation source (Kuze et al., 2009). Absolute radiometric accuracy of the short-wave bands of the TANSO-FTS before launch was within 3% (Kuze et al., 2014). The corresponding calibration coefficients are contin-

[4]for a reference scene with albedo 0.3 and solar zenith angle SZA= 30°(Crisp et al., 2012)

ually being monitored through in-flight calibrations of the two GOSAT sensors. In case of the short-wave bands of the TANSO-FTS, the signal is referenced to direct solar radiation once a month and the spectral response functions are monitored using a custom on-board laser. The TIR spectra are referenced to an on-board standard black body and observations of deep space. CAI measurements are calibrated by looking at the lunar surface. Additionally, vicarious calibration activities are necessary, because of degradation of the on-board calibration components (diffuser plates, etc.). Extensive TANSO calibration campaigns have been carried out at the Railroad Valley playa (Kuze et al., 2011, 2014), where the surface reflectance and the state of the atmosphere above the TANSO footprint can be characterized very well. Differences between recorded spectra and radiative transfer models can hence give insights into the degradation of the radiometric calibration of the sensor. The radiometric calibration of the TANSO sensor has been very stable since an initial degradation in the first two years of operation (Kuze et al., 2016).

Observation Strategy GOSAT observes the Earth with the help of a pointing mirror system that can be operated in *nominal*, *glint* or *target* observation mode. The pointing mirrors can move within an angular range of ±35° in the across-track and ±20° in the along-track direction with respect to the orbit of the satellite. In nominal mode over land, GOSAT collects five (before summer 2010) or three (since summer 2010) separate across track measurements over a swath width of roughly 800 km, each measurement with a circular ground pixel diameter of 10.5 km at the sub-satellite point, while off-nadir soundings have larger and elliptical ground pixels (Crisp et al., 2012, Kuze et al., 2011). Above the oceans, which reflect so little SWIR radiation that trace gas retrievals are not possible, TANSO-FTS targets the bright spot of specular reflection (glint) on the ocean surface in its so called glint mode. Due to the sun-satellite geometry, glint observations are limited by the along-track pointing ability of the system so that glint can only be observed at ±20° around the sub-solar latitude (compare Table 3.1). Near sites of interest – mega cities, volcanoes, ground reference stations, etc. – target mode data acquisition allows for high density measurements of these locations employing forward-motion-compensation of the satellite and/or reduced integration times. The glint and target pointing modes described here are only operated when the satellite is on the day side of Earth, while the nominal mode can also be used for TIR band observations on the night side. The orbit of GOSAT has a three-day revisit cycle of all nominal ground locations (over 3,000 individual footprints) and the observations occur at around 13:00 hours local time to allow for low solar zenith angles (SZA).

Scientific Applications The GOSAT mission – still operational in 2021 – can be considered one of the path finding satellite missions in remote sensing of carbon dioxide and methane from space. Its successes have inspired follow-up missions such as GOSAT-2 (Suto et al., 2021), which was launched in 2018, and GOSAT-GW (WMO, 2020), expected for 2023. Some applications of TANSO-FTS measurements are highlighted here.

The scientific advances that GOSAT has driven are mainly based on the three short-

wave bands of the TANSO sensor. Generally, the rationale behind this choice of spectral windows is to have access to CO_2 and CH_4 absorption bands in the SWIR-1 and SWIR-2 bands, while the O_2 A-band contains information about the atmospheric light path. These measurements have enabled accurate XCO_2 and XCH_4 inversions that capture, for instance, natural, seasonal cycles of these gases (see Jiang et al., 2021, Lindqvist et al., 2015, Parker et al., 2020, and references therein), or emissions from strong anthropogenic sources (Kort et al., 2012, Kuze et al., 2020). TANSO-FTS short-wave measurements have been employed to conduct inversions of sources and sinks of CO_2 and CH_4 on global, continental and national scales (Baray et al., 2021, Basu et al., 2013, Miller et al., 2019, Turner et al., 2015). Moreover, GOSAT data have helped constrain large process-based fluxes of the terrestrial carbon cycle, such as wetland CH_4 emissions (Pandey et al., 2017) or even global photosynthetic activity (Frankenberg et al., 2011).

The TIR spectral window of the TANSO sensor is a special feature of the GOSAT mission, as telluric emission spectra can be used to infer information about the vertical distribution of trace gases (CO_2, CH_4, O_3, NH_3), because the averaging kernels peak in the upper troposphere or lower stratosphere (de Lange and Landgraf, 2018, Saitoh et al., 2016, Someya et al., 2020). In principle, these TIR spectra could be used synergistically with the SWIR spectral bands to retrieve several CO_2 sub-columns or layers (Herbin et al., 2013, Kulawik et al., 2017, Worden et al., 2015), however such retrievals have not been implemented operationally. Since the combination of the SWIR spectral windows is sufficient to constrain CO_2 total columns, the TIR measurements are neglected in the present work.

Dataset for this Work Backscattered radiances of the level 1B (L1B) data version 201.202 were utilized in this thesis and the GOSAT data record was filtered for cloud-free, quality screened soundings over land to save computational costs. The data set has been produced by the algorithm configuration used in Butz et al. (2011) in native GOSAT RemoTeC retrievals within the framework of the Climate Change Initiative of the European Space Agency (ESA) (Buchwitz et al., 2017), which can be accessed at `http://www.esa-ghg-cci.org`. This collection of GOSAT spectra in the period from April 1, 2009 to December 31, 2016 consists of 469,689 L1B soundings.

3.3 The Air-Borne AVIRIS-NG Sensor

The Next Generation Airborne Visible Infrared Spectrometer (AVIRIS-NG) instrument is a push broom imaging spectrometer (see page 20) developed for a wide range of terrestrial ecosystem science (Bender et al., 2010, Hamlin et al., 2011). It is the successor of the well-established AVIRIS instrument (Chrien et al., 1990, Green et al., 1998), which serves as an air-borne demonstrator for the *HyspIRI* mission (e.g. Lee et al., 2015) and which has also inspired similar sensors, for instance the *VSWIR* instrument of the Airborne Taxonomic Mapping System (Asner et al., 2012) or the Airborne Methane Plume Spectrometer (Thorpe et al., 2016b).

The Instrument AVIRIS-NG observes upwelling spectral radiances across most of the solar spectrum between $380-2,510$ nm at a spectral resolution of ~ 5 nm. With a spectral sampling ratio of $1-1.5$, these measurements are conducted on a single HgCdTe detector with 425 spectral pixels (Chapman et al., 2019). AVIRIS-NG has an across-track field

Field of view (across-track)	36°
Spatial pixels	600
F-number	f/3
Spectral range / nm	$380-2,510$
Detector	HgCdTe
FWHM / nm	~ 5
Spectral sampling / nm	~ 5

Table 3.2: Key specifications of the AVIRIS-NG sensor system.

of view of 36° and standard data products contain 600 spatial elements (see Table 3.2), each with an instantaneous field of view of 1 mrad^2. Ground sampling distance is, for example, 10 m for an aircraft altitude of 10 km and exposure times are usually on the order of 10 milliseconds. The sensor has a 9 mm aperture resulting in a f/3 optics that enables observations with high signal-to-noise ratios, e.g. SNR$\sim 200-400$ (Cusworth et al., 2019). The instrument is enclosed in a vacuum-container and equipped with an active temperature control to stabilize environmental conditions. Fig. 3.1 illustrates a typical AVIRIS-NG measurement.

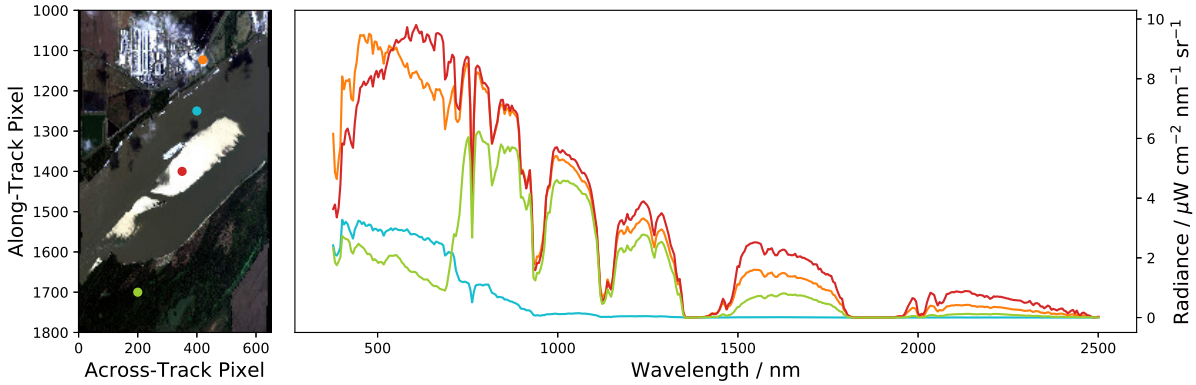

Figure 3.1: Illustration of an AVIRIS-NG measurement near New Madrid, MO, USA. Left: RGB image of the scene. Right: Selected spectra from four color-coded spatial pixels containing spectra of sand (red), cloud (orange), vegetation (green) and water (cyan).

Characterization Radiometric and spectral calibration of AVIRIS-NG is carried out before each research flight and additionally during the flight at the end of each flight line. The characterization procedures have been described by Chapman et al. (2019). While

the initial (lab) characterizations of AVIRIS-NG are comparable to the calibration efforts of specMACS (see ch. 3.4), acquiring boresight and in-flight radiometric and spectral responses has the added value of monitoring the stability of calibration parameters determined in the lab (i.e. SRF shape and FWHM, radiometric calibration coefficients). Thompson et al. (2018a) demonstrated an in-scene spectral response validation method that exploits the absorption features of the O_2 A-band to correct the SRF for stray light effects. Further, AVIRIS-NG is equipped with on-board calibration sources to enable radiometric and spectral characterization during operation. It has been shown that the properties of the sensor characterization remain very stable, both in terms of radiometric and spectral accuracy, over a period of several years (Chapman et al., 2019). The SRF for the AVIRIS-NG data used in this thesis is Gaussian and homogeneous over the spatial dimension of the detector, i.e. all spatial pixels exhibit the same spectral response, which varies across the wavelength axis by less than ± 5 %. Absolute radiometric accuracy of the sensor is 95% (Green, 2012).

Scientific Applications Due to its successes in many different areas of Earth system science, the AVIRIS-NG sensor has had a large impact on the development of imaging spectrometers. AVIRIS-NG has previously been used to study methane emissions (Ayasse et al., 2018, 2019, Borchardt et al., 2021, Cusworth et al., 2020, Duren et al., 2019, Foote et al., 2020, Frankenberg et al., 2016, Krautwurst et al., 2017, Thompson et al., 2015, 2016, Thorpe et al., 2013, 2017, 2020, Zhang et al., 2017) and also carbon dioxide emissions (Deschamps et al., 2011, Marion et al., 2004, Raychaudhuri et al., 2019, Thorpe et al., 2017). Other applications include atmospheric correction (Thompson et al., 2018b), remote sensing of aerosols (Mauceri et al., 2019), lithological mapping (Tripathi et al., 2020) and many more.

Dataset for this Work The flightlines *ang20190621t200919* and *ang20150420t181345* are analyzed in chapter 4.2.4. The former was obtained on June 21, 2019, at a solar elevation of 72° and it contains the "Four Corners Power Plant" near Farmington, NM, USA. The latter dataset is the flight that was analyzed by Thorpe et al. (2017) to retrieve CO_2 concentrations near the "San Juan Generating Station", which is located roughly 20 km north of the Four Corners facility. These spectra were recorded on April 20, 2015, at a solar elevation of 61°. The two datasets were obtained at above-ground sensor altitudes of 2.7 km (Four Corners) and 1.1 km (San Juan), so that the ground sampling distances are 2.7 m and 1.1 m, respectively, for these flights. Noise vectors for AVIRIS-NG measurements were not available at the time of publication of this thesis.

3.4 The Air-Borne specMACS Sensor

The spectrometer of the Munich Aerosol and Cloud Scanner (specMACS) is a combination of two push broom imaging spectrometers that primarily serve the study of cloud physics. It has been deployed in various viewing geometries – as a ground-based sensor or on board of the German research aircraft HALO (Ewald et al., 2016, Stevens et al., 2019).

The Instrument specMACS consists of two complementary sensors in the VNIR ($\sim 400 - 1,000$ nm) and SWIR ($\sim 1,000 - 2,500$ nm) spectral ranges. In the airborne configuration of the system, the two sensors are aligned such that their fields of views overlap for a mutual field of view of 32°, which is somewhat smaller than the individual fields of view of each sensor (see Table 3.3). Different detectors are deployed in the two sensors – a fact that leads to differences in radiometric accuracy and differences in spatial and spectral resolution of the instruments. The VNIR focal plane array does not require cooling, but the SWIR HgCdTe detector must be operated at 200 K. While both sensors have comparable optics with f/2.4 and f/2.1 in the VNIR and SWIR, respectively, the VNIR sensor has a significantly higher spectral resolution than the SWIR sensor (3.1 vs. 10.3 nm on average). The average spectral (over-) sampling ratios of the two cameras are 3.9 in the VNIR and 1.6 in the SWIR. Many updates to the specMACS system have been implemeted over the last years. Among these are an enclosure to enable operation of specMACS in non-pressurized areas of an aircraft and the addition of two cameras sensitive to different polarzation states of incident radiation. An overview of the key sensor parameters is given in Table 3.3.

	VNIR	SWIR
Field of view (across-track)	32.7°	35.5°
Spatial pixels	1,312	320
F-number	f/2.4	f/2.1
Spectral range / nm	$417 - 1,016$	$1,015 - 2,496$
Detector	Si	HgCdTe
FWHM / nm	$2.2 - 6.0$	$7.1 - 19.6$
Spectral sampling / nm	$0.6 - 1.0$	$5.2 - 6.9$

Table 3.3: Key specifications of the specMACS sensor system, comprising a VNIR and a SWIR sensor.

The field of view of an individual detector pixel, the *instantaneous field of view*, is 1.4×2.0 mrad^2 and 3.8×1.8 mrad^2 for the VNIR and SWIR detectors. At a flight altitude of 10 km above ground, this translates into nadir pixel sizes of 14×20 m^2 and 38×18 m^2, respectively. Integration times for both sensors are typically on the order of a few milliseconds.

Characterization The instrument has been characterized by Ewald et al. (2016) who found the SRF in the VNIR to be non-Gaussian, while the Gaussian approximation fits well with the SWIR sensor. However, large variations in FWHM are expected across the spectrum and across the spatial domain of the sensor (see Fig. 3.2). The CO_2 absorption bands in the short wave-infrared are sampled with quite different spectral resolution by the sensor. While the average spectral resolution in the SWIR-2 (1960 – 2130 nm) is 8.5 nm across all spatial pixels, the average in the SWIR-1 range ($1,540 - 1,640$ nm) is 12.4 nm.

A major difference between the VNIR and SWIR sensors with regard to their radiometric performance is the stability of their respective dark current levels (σ_{dc}, see chapter 2.2.2). Ewald et al. (2016) showed that large drifts in the SWIR dark current can occur during air-borne operation of specMACS, while the VNIR dark current is stable. These variations depend both on temperature and integration time, making in-flight dark current measurements as well as temperature control of the entire camera crucial in order to be able to calibrate the detector reading to absolute spectral radiances. Radiometric uncertainties on the order of $< 5\%$ remain in the VNIR band for a well-lit scene, while accuracy in the SWIR is highly wavelength dependent. At the spectral bands of CO_2 absorbtion near 1.6 μm and 2.0 μm the absolute radiometric accuracy is better than 10%, although other spectral ranges are associated with uncertainties as high as 50% (Ewald et al., 2016, Fig. 22).

specMACS has been characterized only once in 2016, and since no in-flight calibration has been developed yet, no information about the stability of its calibration is available.

Scientific Applications Typical applications of specMACS deal with the derivation of macroscopic cloud parameters, such as their geometry (Kölling et al., 2019), or with retrievals of cloud microphysical parameters (Ewald et al., 2019, Höppler et al., 2020, Jäkel et al., 2017, Zinner et al., 2019). The present study is the first attempt to use the broad spectral range of specMACS to retrieve trace gas information.

Dataset for this Work Due to a sparse cloud-free data set, only few archived scenes could be identified, which contain a stronger localized source. One such data set was recorded on September 27, 2016, during a transfer flight of the North Atlantic Waveguide and Downstream Impact Experiment campaign (NAWDEX, Schäfler et al. (2018)), when specMACS observed the city of Andernach, Germany, and an adjacent power plant from an altitude of ~ 12.6 km above ground at a solar elevation of 65.5°. XCO_2 retrievals from this flight scene will be discussed in chapter 4.3. Measurement noise vectors were not available for this study, but typical SNR values[5] in the SWIR-1 spectral range can be expected to be above SNR > 100, with average SNR at 127 across the flight track and 73 % of all scenes having SNR > 100. The noise level is proportional to $\sigma_{\text{tot}} \sim \sqrt{S}$ (see eq. 2.17 and find

[5]SNR calculated as the value of the $1,560$ nm signal (continuum radiance close to the SWIR-1 bands) devided by the standard deviation of the signal in the neighboring opaque water vapor band between $1,827 - 1,936$ nm.

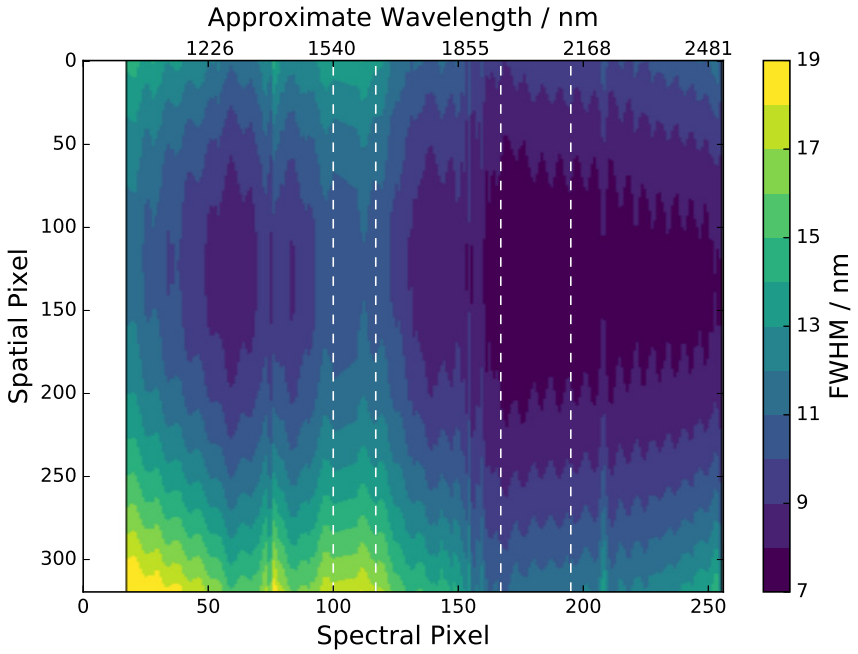

Figure 3.2: Visualization of the FWHM of the specMACS sensor across the SWIR detector array. The CO_2 absorption bands in SWIR-1 and SWIR-2 are located between the dashed lines, where the average FWHM is 12.4 nm and 8.5 nm, respectively. The top axis shows the center wavelengths along the central spatial detector row (number 160).

details in Ewald et al. (2016), Fig. 13), i.e. the darker the surface the lower is the SNR.

3.5 The Ground Based TCCON Network

The Total Carbon Column Observing Network (TCCON) is a global network of ground based FTS instruments that routinely measure direct solar absorption spectra between 0.7 and 2.6 μm (Kiel et al., 2019, Messerschmidt et al., 2011, Wunch et al., 2011a,b) at spectral resolutions below $\Delta\lambda = 0.01$ nm. Their measurements are used to infer column concentrations of a number of molecules in the (clear-sky) atmosphere of Earth, such as O_2, CO_2, CH_4, CO, HF and others. As the impact of scattering on direct solar radiation is negligible (e.g. Oshchepkov et al., 2013), such measurements enable the determination of carbon dioxide column concentrations with high precision and accuracy, both better than 0.3% of XCO_2 (Messerschmidt et al., 2011). The present study uses measurements from 24 TCCON stations around the world from the "GGG2014" data product (available at https://tccondata.org). An overview of the data sets employed in this work can be found in Table B.1 in appendix B.

Column concentrations reported by TCCON are calibrated with respect to World

Meteorological Organization (WMO) standards (Messerschmidt et al., 2011, Zhao and Tans, 2006). This provides an absolute calibration of XCO_2 data across the network and a traceable link to standardized in-situ CO_2 measurement networks (e.g. ICOS , `https://www.icos-cp.eu/`).

Due to the operational continuity, standardized instrumentation, data processing and calibration, the record of the TCCON network has become a valuable source for validation studies of satellite instruments targeting XCO_2.

In recent years, new FTS technology has enabled similarly high accuracy in measuring trace gas columns with much smaller ground-based spectrometers, which may become an addition to the TCCON network in the future (Frey et al., 2019, Knapp et al., 2021, Luther et al., 2019).

Chapter 4

Results

In this chapter three case studies are presented which are carried out with the RemoTeC retrieval algorithm. Its application to the measurement data introduced in the previous chapter will be discussed with regard to the challenges and possibilities offered by coarse-spectral-resolution sensors. First, section 4.1 discusses which spectral resolution and spectral window would be favorable for a satellite sensor targeting localized XCO_2 enhancements. Second, section 4.2 explores power plant XCO_2 retrievals from the AVIRIS-NG sensor and lastly, section 4.3 analyzes XCO_2 retrievals from specMACS measurements near a small power plant.

4.1 Spectral Sizing of a Coarse-Spectral-Resolution Satellite Sensor

Substantial parts of the text in this section as well as many figures are adopted from the Atmospheric Measurement Techniques article published by the author of this thesis (Wilzewski et al., 2020).

From an XCO_2 retrieval perspective, the present chapter explores the margins available in the spectral resolution of CO_2 absorption band measurements with the aim of enhancing ground resolution and facilitating a single-band sensor configuration, which may allow for such sensors to be deployed in a fleet of low-cost satellites. Fig. 4.1 schematically depicts the key advantage of a hypothetical 50×50 m^2 ground resolution spectrometer over a sensor with km-scale resolution for point-source monitoring. Satellite sensor ground pixels which capture only a part of the source plume average the plume enhancement with the local background concentration. In case of the example in Fig. 4.1, this produces a maximum enhancement of 3 ppm for the satellite sensor with 2×2 km^2 ground resolution, whereas reduced ground pixel sizes of 50×50 m^2 yields a maximum enhancement of 12 ppm at 2 km downwind distance, as well as a higher sampling rate of the plume with over 10 pixels along

the plume cross-section. This augmented performance can be understood as larger fractions of each (smaller) pixel being occupied by plume enhancements. With increased downwind distance from the source, per-pixel enhancements become comparable for the two sensors, but the increased spatial sampling of the fine ground resolution sensor would still allow to observe the plume in many ground pixels. Thus, a fine-ground-resolution sensor poses less stringent per-pixel precision requirements and offers the possibility of recording the plume shape at higher detail. One design aspect for passive sensors with high ground resolution is to gather a sufficient amount of backscattered photons in each of the small spatial pixels, which is generally more challenging at finer the ground sampling distances. A typical approach to increase the light throughput of the system is to coarsen the spectral resolution. Finer spatial resolution is also accompanied by narrower swath widths, so that global monitoring of localized CO_2 sources surely requires a fleet of sensors, ideally with a simple, single-band spectral set-up instead of the expensive, full spectral coverage provided by existing missions.

In this chapter, the performance of a hypothetical coarse-spectral-resolution spectrometer will be assessed that only covers one spectral band. Specifically, the following sections will appraise a sensor concept which is based on either the 1.6 (SWIR-1) or the 2.0 μm (SWIR-2) CO_2 absorption bands at resolving powers approximately between the AVIRIS-NG and CarbonSat concepts (i.e. $700 < \frac{\lambda}{\Delta\lambda} < 10,000$). Galli et al. (2014) proposed an avenue towards the envisioned performance tests by convolving high-spectral-resolution GOSAT soundings down to resolving powers of $\frac{\lambda}{\Delta\lambda} \approx 3,000$ and retrieving XCO_2 with the common 3-band configuration (NIR, SWIR-1, SWIR-2). Their study concluded that, when validated with ground truth, reduced spectral resolution retrievals typically lead to increased systematic and statistical XCO_2 errors. Here, the approach of Galli et al. (2014) is being followed, but taken beyond the range of resolving powers discussed there and retrievals are limited to a single spectral band. In terms of single-band XCO_2 measurements, Wu et al. (2019) have demonstrated that when restricting OCO-2 retrievals to one band (and leaving spectral resolution untouched), XCO_2 retrieval precision and accuracy suffer virtually no degradation in comparison to the full spectral configuration.

The methodological approach of spectrally degrading GOSAT soundings in the SWIR-1 or SWIR-2 bands is introduced in section 4.1.1. Section 4.1.2 summarizes the findings regarding various coarse-spectral-resolution XCO_2 retrievals by comparing the results with ground-truth from the Total Carbon Column Observing Network (TCCON). Favorable target spectral resolutions are identified and subsequently evaluated on a global scale with respect to "native" GOSAT retrievals in section 4.1.3. GOSAT soundings of the Los Angeles mega-city are also investigated in an attempt to apply the SWIR retrievals to a true anthropogenic XCO_2 gradient. However, this gradient appears to be unresolved even in native GOSAT retrievals as opposed to previous reports and therefore this path was not pursued any further (see appendix A).

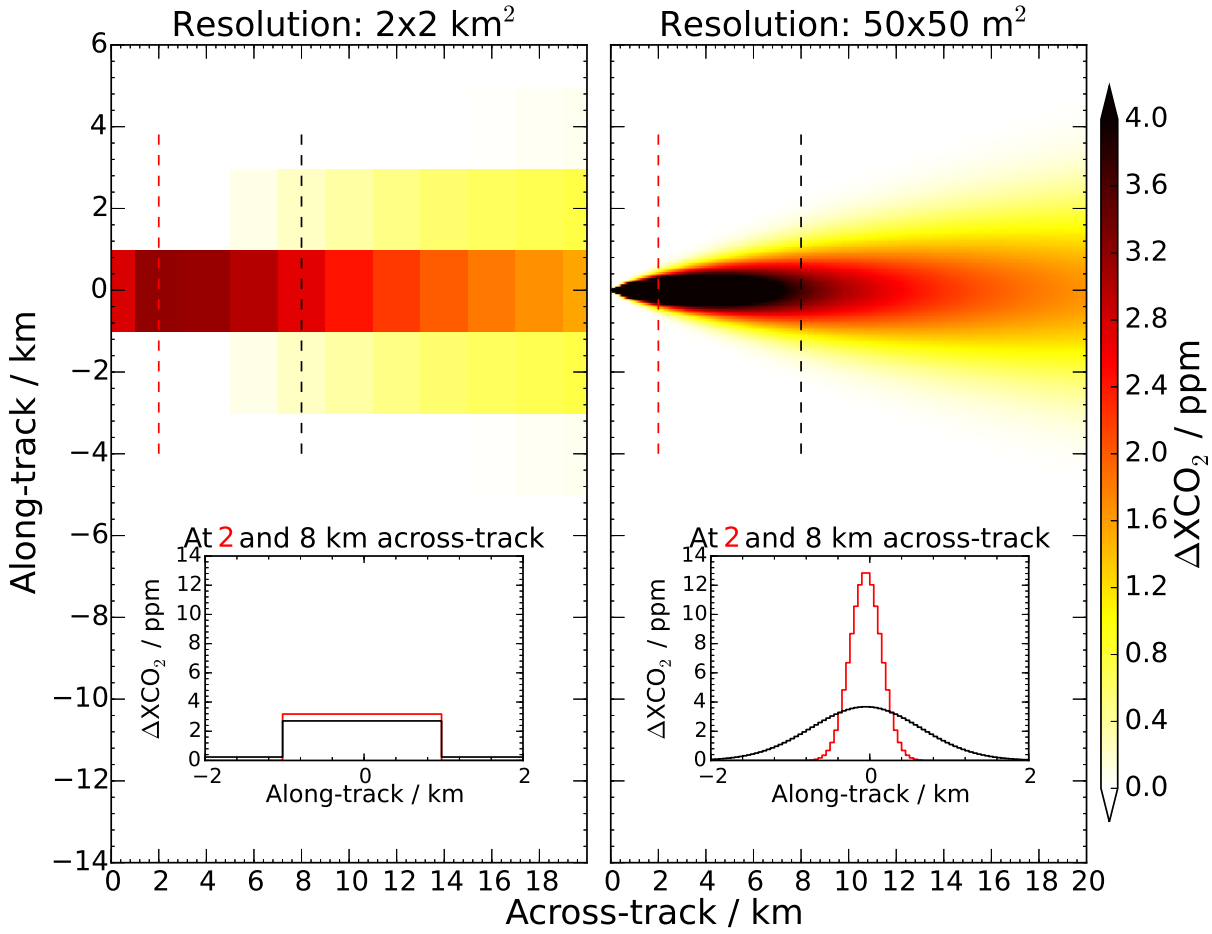

Figure 4.1: Schematic, noise-free XCO_2 enhancements (ΔXCO_2) of a Gaussian plume emanating from a power plant with a flux of 12.3 $MtCO_2$ y^{-1} (Guifford-Pasquill stability class C, wind from left to right; source located at the origin; sensor motion from bottom to top, sampling occurs left to right) as observed by hypothetical satellite instrument with 2×2 km^2 ground pixels (left), and 50×50 m^2 ground pixels (right). Inset plots indicate ΔXCO_2 recorded by the sensors at 2 km (red) and 8 km (black) downwind of the source along the plume cross section (dashed lines). Figure adopted from Wilzewski et al. (2020).

4.1.1 Spectral Degradation of GOSAT Measurements

With its broad spectral coverage in the SWIR-1 and SWIR-2 spectral ranges, GOSAT is especially suited for the present study, as opposed to other sensors (e.g. OCO-2), because the wide bandpass of the instrument permits a relatively free choice of the retrieval windows. The wide spectral windows observed by GOSAT (except for the TIR-band) are shown in Fig. 4.2. To imitate a coarse-resolution sensor, a Gaussian convolution of variable FWHM was applied to the native GOSAT spectra. The same convolution was also assigned to the noise of the native GOSAT spectra, i.e. no additional noise was included here. By setting

the noise of the coarse-resolution spectrometer to the convolved noise of the native spectra, this work focuses on the sole effect of decreasing the spectral resolution. Of course, extra noise must be expected for a hypothetical small-ground-pixel sensor. However, adding the noise calculated from a detailed instrument model (as discussed in Strandgren et al. (2020)) would introduce another artificial feature to the analysis. Here, those conditions will be studied under which the noise of the detector is in essence negligible, as commonly found for GOSAT (where errors are typically governed by systematic patterns, like spectroscopic errors, uncertain scattering effects, etc.). Systematic sources of error will be addressed in sections 4.1.2 and 4.1.3 by correlating retrieval results with geophysical parameters. Figure 4.2 visualizes the convolution approach in comparison to the native GOSAT spectra for hypothetical resolving powers of 1,200 (blue line) and 1,600 (red line) in SWIR-1 and SWIR-2, respectively. A 256 spectral pixel focal plane array was assumed for the proposed sensor.

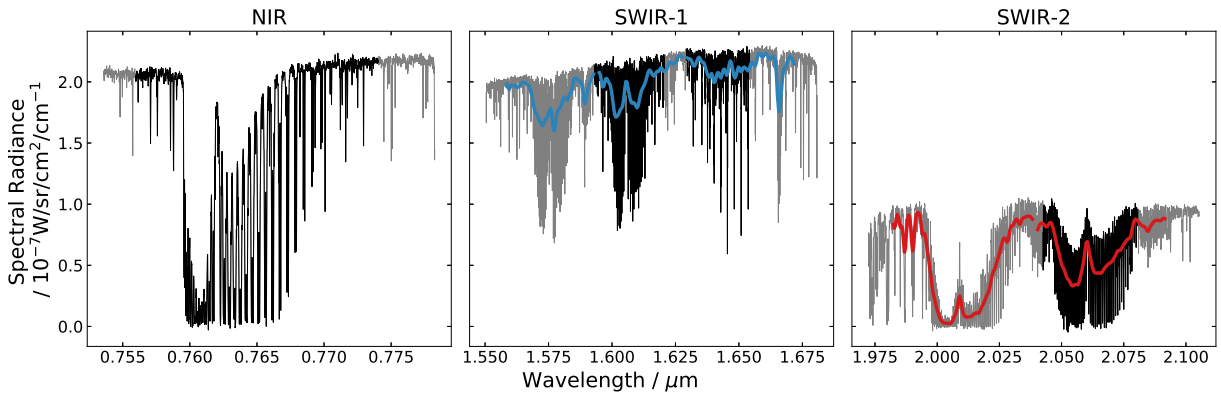

Figure 4.2: Observed GOSAT spectrum of the radiance backscattered in the NIR, SWIR-1 and SWIR-2 spectral ranges (left to right) depicted in grey with respective GOSAT retrieval windows shown in bold black. Measurements after Gaussian convolution at resolving powers of $\sim$ 1,200 (SWIR-1) and $\sim$ 1,600 (SWIR-2) are illustrated in bold blue and bold red, respectively. Figure adopted from Wilzewski et al. (2020).

Native and degraded GOSAT spectra were analyzed with the RemoTeC retrieval software (Butz et al., 2009, 2011, Guerlet et al., 2013b). The retrieval configuration for GOSAT measurements at native spectral resolution is the so called full-physics ("native" GOSAT) retrieval, where RemoTeC takes into account four spectral windows in the NIR, SWIR-1 and SWIR-2 spectra ranges (see Table 4.1 and Fig. 4.2) and inverts the measurements for XCO_2, XCH_4 simultaneously with surface albedo and spectral shifts as well as three particle scattering parameters (compare chapter 3.1). This native GOSAT set-up corresponds to the standard retrieval which is operated for ESA's climate change initiative (e.g. Buchwitz et al. (2017)).

To emulate a single-band spectrometer, either of the SWIR spectral ranges were used alone at coarse spectral resolution, and XCO_2 (as well as XCH_4 in SWIR-1) and spectral shift and surface albedo parameters were retrieved. The convolution of the modeled, coarse-

resolution spectra was carried out in analogy to the standard retrieval procedure: Firstly, RemoTeC models spectra at native GOSAT spectral resolution and subsequently mimics the proposed low-spectral-resolution spectra by means of a Gaussian convolution. While the spectrally degraded SWIR-1 retrievals also fit H_2O and XCH_4, they do not take particle scattering into account (Rayleigh scattering is incorporated). As such, the low-resolution SWIR-1 retrievals are basically transmittance computations along the geometric lightpath, which are hereafter denominated non-scattering retrievals. Sensitivity studies suggest that coarse-resolution SWIR-1 retrievals of atmospheric scattering parameters deteriorate XCO_2 retrieval performance (with regard to the non-scattering retrieval) and that they exhibit low information content for aerosols. In the SWIR-2, XCO_2 was retrieved simultaneously

	Coarse spectral resolution sensor		native GOSAT
	SWIR-1	SWIR-2	
Spectral Windows Used / nm	1.559 - 1.593 1.595 - 1.628 1.630- 1.672	1.982 - 2.038 2.040 - 2.092	0.7741 - 0.7560 1.593 - 1.621 1.629 - 1.654 2.042 - 2.081
FWHM / cm^{-1}	0.75 . . . **5.1** . . . 8.0	0.75 . . . **3.1** . . . 7.0	0.24
FWHM / nm	0.20 . . . **1.37** . . . 2.15	0.31 . . . **1.29** . . . 2.90	0.1
approx. Resolving Power	8,100. . . **1,200**. . . 760	6,500. . . **1,600**. . . 700	> 20,000

Table 4.1: GOSAT retrieval windows at native and coarse spectral resolution. For the different retrieval configurations, the spectral resolution that was identified for subsequent analyses is given in bold font (see section 4.1.2). Table adopted from Wilzewski et al. (2020).

with XH_2O. Furthermore, by applying the standard Phillipps-Tikhonov regularization of RemoTeC (e.g. Butz et al. (2012) and see chapter 3.1), three standard, effective particle parameters were retrieved from the SWIR-2. A regularization strength was identified which yielded an average of 0.38 degrees of freedom (DFS) for aerosols (DFS $\gtrapprox$1.5 are usually observed in native GOSAT retrievals). In spite of this low value for aerosol DFS, the performance of these "scattering" retrievals was significantly enhanced in comparison to the non-scattering fits. As the GOSAT spectra are convolved to lower spectral resolutions, the average degrees of freedom for particles decreases as well (e.g. from 0.45 at a resolving power of 6,500 to 0.32 at a resolving power of 700). While altering the DFS available for the effective aerosol fit may impact the convergence rate of the retrieval algorithm, more than 75 % of all retrievals converge at any given FWHM that was considered in this study. More details about the choice of suitable particle scattering regularization parameters is provided in the following section (ch. 4.1.2). Note, that although the SWIR-1 and SWIR-2

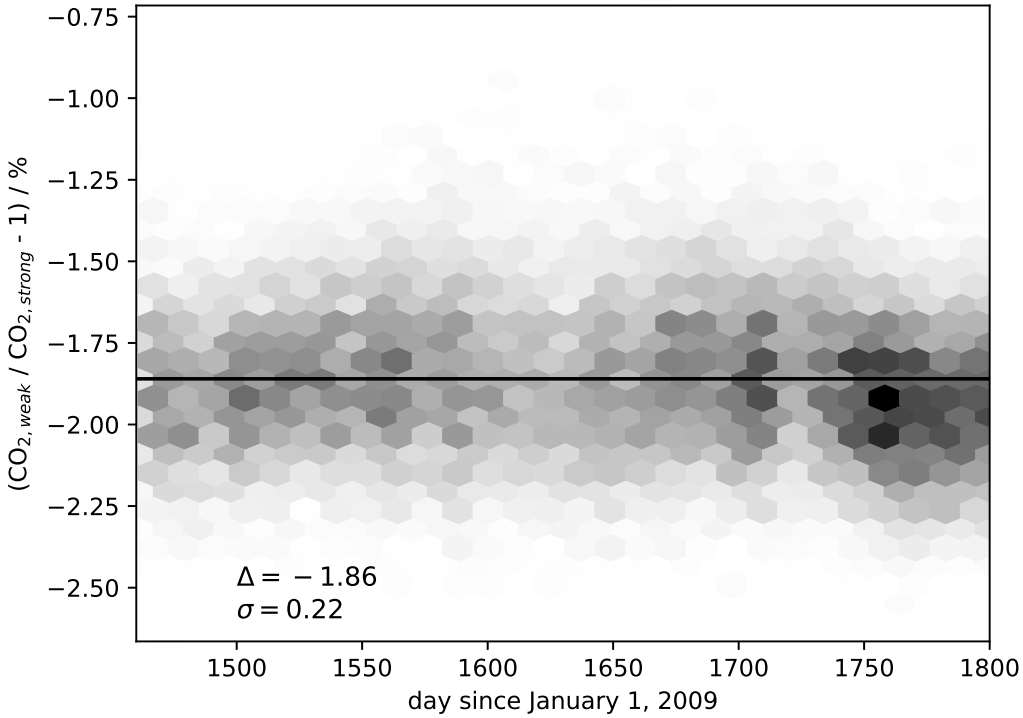

Figure 4.3: The scaling factor for the strong CO_2 band near 2.01 μm was derived from a set of aerosol and cloud free GOSAT spectra. The figure shows how the ratio of CO_2 derived from the two bands (at native spectral resolution) varies over the course of 2013. The mean (Δ) and standard deviation (σ) are noted on the lower left.

retrievals use separate sub-windows to fit each CO_2 band, only one XCO_2 value is retrieved from each spectral range by coupling XCO_2 between the sub-windows.

Table 4.1 lists and Fig. 4.2 shows the definitions of the spectral retrieval windows. These spectral boundaries were used throughout this work when convolving spectra to various values of FWHM. Both coarse-spectral-resolution SWIR retrieval configurations include two CO_2 absorption bands to maximize CO_2 information content at low spectral resolution, while native GOSAT retrievals only utilize one of the CO_2 bands in each SWIR spectral range to save computational costs and because the extra bands would introduce largely redundant information. Yet, the boundaries of the selected spectral windows may need to be refined in the future, when the sensor design is more advanced in terms of a noise model, etc.. The retrieval windows for coarse resolution spectra encompass optically (almost) transparent spectral ranges, which serve to characterize the surface albedo. Retrieval performance was observed to profit significantly from spectral windows that did *not* "cut off" parts of CO_2 absorption bands, in order to preserve as much spectral information about CO_2 absorption as possible (not shown here).

FWHM / nm	native	0.3	0.4	0.5	0.6	0.7	0.8	1.2	1.3	1.7	2.1	2.5	3.0
scaling factor	0.9814	0.9843	0.9864	0.9867	0.9863	0.9859	0.9856	0.9837	0.9834	0.9838	0.9847	0.9867	0.9859

Table 4.2: Scaling factors for the strong CO_2 band cross sections (HITRAN08) at different spectral resolutions derived with the upper-edge method (Butz et al., 2013).

As discussed in chapter 3.1.1, the dry airmass for each sounding was determined from the average surface pressure of a meteorological reanalysis (ERA-Interim) and a digital elevation model (SRTM). Retrieval errors that originate from erroneous satellite pointing (which in turn incurs errors in the airmass calculation) are one element of the total error declared for the TCCON validation sites (section 4.1.2).

CO_2 absorption cross sections from the HITRAN08 spectroscopic database (Rothman et al., 2009) are known to introduce small offsets in XCO_2 retrievals when the SWIR-1 and SWIR-2 bands are used separately. Butz et al. (2013) found that XCO_2 retrievals from the 2.06 μm and 2.01 μm absorption bands produced inconsistent results, which could be corrected by scaling the cross sections of the 2.01 μm band. Here, their study is reiterated and extended to extend it to the longer measurement period employed here and to derive the necessary scaling parameter (which generally may depend on the resolving power of the convolved spectra). Butz et al. (2013) proposed the "upper-edge" method, in which ocean-glint scenes free of aerosols and clouds are used for non-scattering retrievals in the 2.01 μm and the 2.06 μm bands separately. The mean ratio of the retrieved XCO_2 distributions can be interpreted as the scaling factor, which equals 0.981 ± 0.002 at native GOSAT spectral resolution (i.e. the 2.01 μm cross sections require scaling by 0.981). Fig. 4.3 illustrates the derivation of the scaling factor from the upper-edge ensemble for the year 2013, comprising 22,000 GOSAT glint soundings. Scaling factors were derived on a sub-set of available GOSAT spectra to save computational resources. It appears that the XCO_2 offset and standard deviation found here generally agree with the results of Butz et al. (2013) who estimated the scaling factor to be 0.978 ± 0.007. Fig. 4.3 hints at a slight seasonality in the XCO_2 offset between the two SWIR-2 bands, which will not be investigated further in this work. Butz et al. (2013) found no systematic temporal patterns over a course of three years in their analysis of relative differences between individual CO_2 bands, but they discuss possible variability induced by the seasonally changing glint spot observation pattern of GOSAT. This study follows the approach of Butz et al. (2013) and assumes that temporal variability plays no role in the correction of HITRAN08 cross-sections the strong CO_2 band. Correspondingly, an appropriate scaling factor is calculated at every spectral degradation selected in this study to reveal the impact of the convolution procedure on the coarse-resolution spectra. These factors were found to vary on the sub-permil level from the correction factor at native GOSAT spectral resolution. A complete list of scaling factors is given in Table 4.2.

4.1.2 Validation with the TCCON Network

As explained in section 4.1.1, XCO_2 retrievals were operated on a global set of cloud-free GOSAT measurements for both, the native as well as the coarse-spectral-resolution SWIR configurations. The SWIR-1 and SWIR-2 configurations were carried out at a range of values of the FWHM of the Gaussian SRF which is used to degrade the native GOSAT spectra by means of convolution. Additionally, both retrieval configurations were analyzed in terms of convergence rate and the effects of adjusting effective aerosol parameters with variable regularization set-ups of the Philips Tikhonov scheme of RemoTeC. A state-of-the-art full-physics reference retrieval was conducted on the same data set at native GOSAT resolution using the typical three-band configuration (from NIR to SWIR). The SWIR-1 and SWIR-2 retrieval runs at coarse spectral resolutions serve as test cases for a possible future spectrometer with single-band coverage and low resolving power. Retrieved XCO_2 values are evaluated through comparisons to measurements of the ground-based TCCON network (Kiel et al., 2019, Messerschmidt et al., 2011, Wunch et al., 2011a,b). A GOSAT sounding is considered colocated with a TCCON station, if the satellite sounding occurred within a 5° radius with respect to latitude/longitude of the respective ground station. In such a case, the GOSAT XCO_2 retrieval is validated against the average TCCON XCO_2 recording within $\pm$ 2 hours of the GOSAT sounding time.

XCO_2 retrieval precision is usually measured as the standard deviation of the differences ("scatter") between TCCON and GOSAT. Figure 4.4 illustrates the parameter space spanned by the constraining metrics scatter, convergence, aerosol DFS for both the SWIR-1 and SWIR-2 spectral ranges for various resolving powers (color code). Interestingly, the two SWIR windows display very different behaviors when the strength of the regularization is increased (i.e. the value of DFS for aerosol is decreased). This is a scenario, when the retrieval is similar to a non-scattering retrieval, essentially setting the aerosol parameters to values that are very close to the aerosol prior. In the SWIR-1, lower DFS for the aerosol retrieval generally translates into improved retrieval performance with regard to TCCON. This is an indication that the loss of spectral resolution has a severe impact on the availability of aerosol information in the spectra, which makes a non-scattering retrieval the most obvious choice for this spectral range. The non-scattering retrieval has a performance with respect to TCCON that is very similar to the highly regularized aerosol retrieval, but due to its simple state vector the time needed for the retrieval is much shorter. Conversely, the SWIR-2 XCO_2 retrieval can be improved when some aerosol information is retrieved. The right-hand side panel of Fig. 4.4 shows that at intermediate regularization strengths, i.e. in the range between 0.3 and 1.0 degrees of freedom for the three aerosol parameters, XCO_2 retrieval scatter around TCCON drops by a few tenths of ppm. This pattern is especially pronounced at high resolving powers, which shows that spectral resolutions closer to the native spectral resolution of GOSAT are more sensitive to aerosol scattering properties in the SWIR-2. This trend is only reversed at very low resolving powers, when the aerosol information finally seems to vanish from the coarsely resolved spectra. A common feature of the SWIR spectral ranges is that the percentage of spectra that can be analyzed successfully is decreased when more DFS are allowed for the aerosol retrieval.

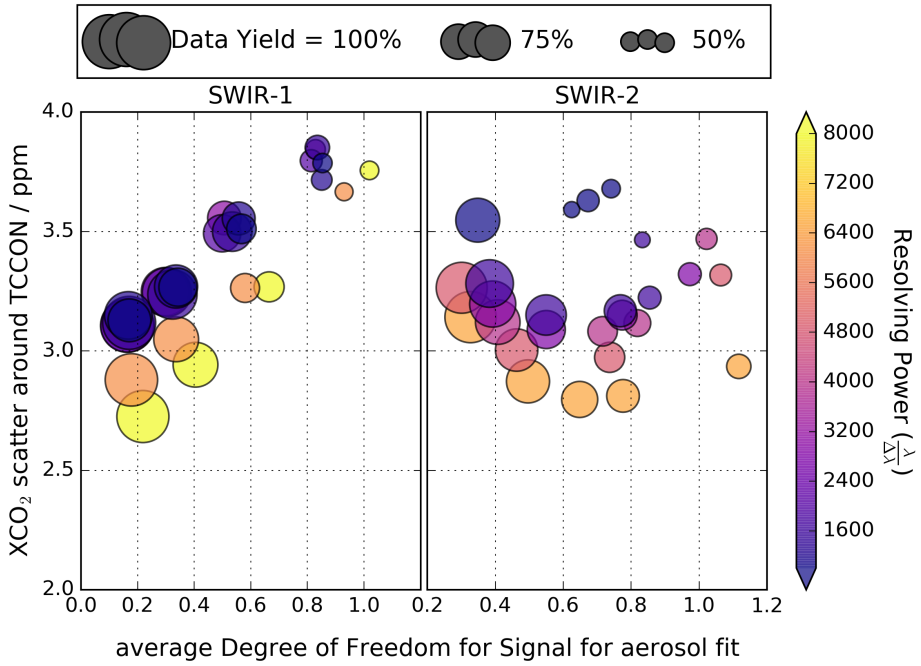

Figure 4.4: Analysis of retrieval sensitivity as a function of scatter around TCCON, aerosol degrees of freedom, resolving power (color coded) and data yield (i.e. convergence rate; proportional to symbol size). In the SWIR-1 (left), there is little sensitivity for scattering parameters with increased data yield and decreased XCO_2 scatter for low DFS aerosol. In the SWIR-2 (right), an effective aerosol fit with low DFS aerosol helps to decrease XCO_2 scatter with only moderate losses in data yield, especially for high resolving powers.

This observation can be expected from the above considerations: when little information about aerosol scattering is available in the measurement, a retrieval of particle scattering parameters will be increasingly difficult, because the inverse problem is strongly ill-posed. In the following, the non-scattering SWIR-1 retrieval and the SWIR-2 retrieval with average DFS for aerosol at 0.38 are selected for all further analyses. Figure 4.5 illustrates that lower resolving powers entail greater overall scatter for these retrievals, while there exists some margin for the selection of spectral resolution in the SWIR-1 band. The figure also implies that the scatter around TCCON stabilizes temporarily at a "plateau" in resolving power space located right beyond the spectral resolution needed to discriminate between neighboring CO_2 absorption lines in the SWIR-1 (the critical resolving powers are ∼3,300 in SWIR-1 and ∼2,700 in SWIR-2; see dotted vertical lines in Fig. 4.5). As the convolution operation combines individual spectral lines into a wider spectral shape, the non-scattering SWIR-1 retrieval maintains a rather stable scatter around TCCON for another 1,000 resolving powers. SWIR-2 retrievals exhibit gradually enhanced scatter around TCCON (without a "plateau" pattern) as the resolving power is decreased (bold red line

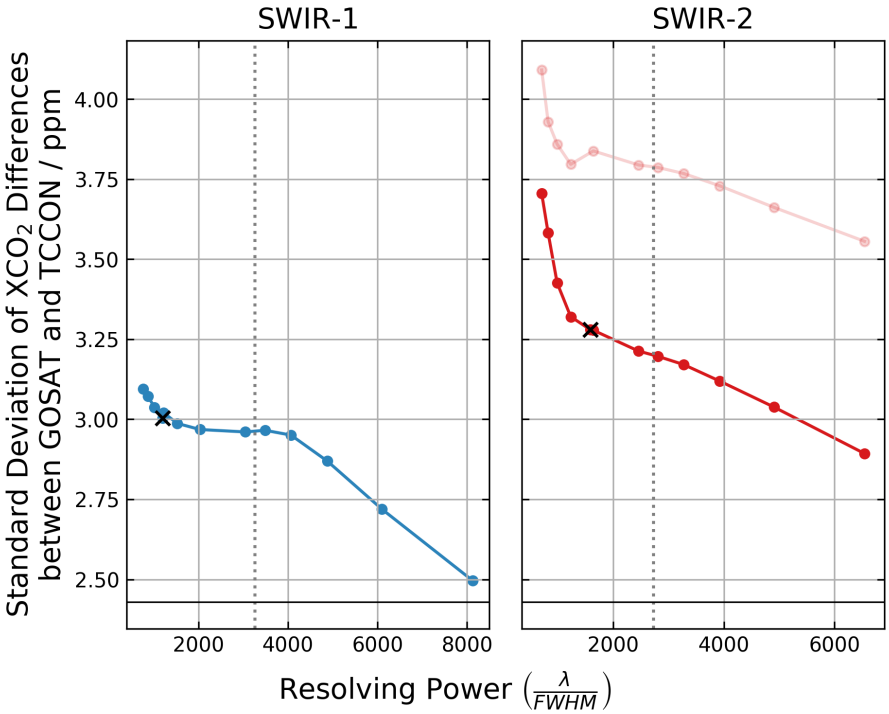

Figure 4.5: XCO_2 retrieval standard deviation for SWIR-1 (left) and SWIR-2 (right) retrievals colocated with TCCON measurements shown as a function of resolving power. The faint red line illustrates the standard deviation for a non-scattering SWIR-2 retrieval. Dotted lines indicate the resolving powers at which individual spectral lines become visually inseparable in the degraded spectra. The scatter of the native GOSAT retrieval around TCCON is shown as a black horizontal line. The × signifies the resolving power examined in the rest of this chapter. Figure adopted from Wilzewski et al. (2020).

in Fig. 4.5). In a sensitivity study without the effective aerosol retrieval in the SWIR-2 spectral range (i.e. employing the same non-scattering set-up in the SWIR-2 as in the SWIR-1), SWIR-2 retrieval scatter with respect to TCCON was significantly amplified (light red curve in Fig. 4.5). This points to advantageous retrieval performance when the effective aerosol retrieval is turned on, although DFS for the particle retrievals is low. The present investigation is in broad agreement with the works by Galli et al. (2014) and Wu et al. (2020) who also observed enhanced retrieval scatter as spectral resolution became degraded to lower levels, although the current analysis exceeds the spectral resolution range studied by these previous research designs. In this respect, this thesis actually examines the usage of a hyperspectral imager, whereas the above mentioned studies are still in the regime of conventional spectrometers.

The scatter with respect to TCCON is the key variable to constrain the spectral resolution of the hypothetical satellite sensor, because the spectrometer will be designed to resolve local scale XCO_2 augmentations. Thus, resolving powers above the ones which

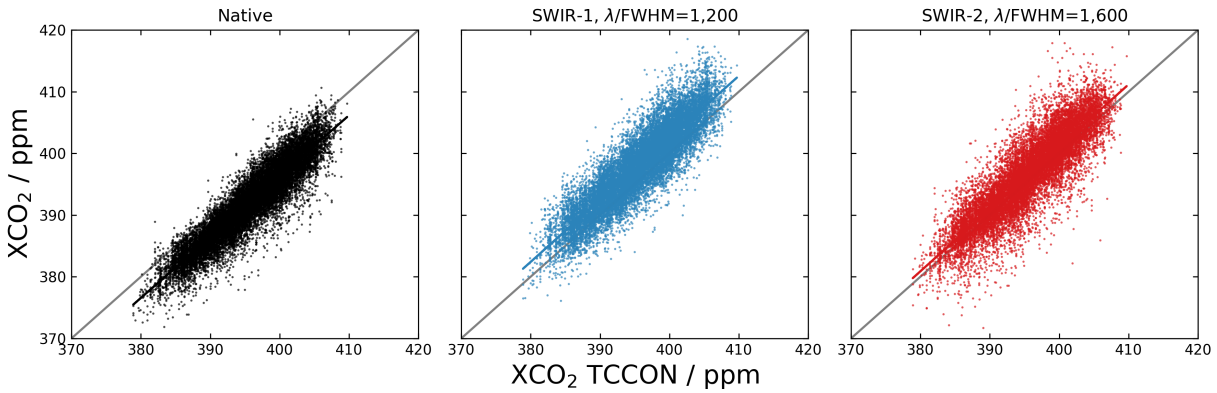

Figure 4.6: XCO_2 retrievals from GOSAT correlated with colocated TCCON measurements. Left to right: native GOSAT, SWIR-1 and SWIR-2 retrievals. Resolving powers in the SWIR-1 and SWIR-2 are 1,200 and 1,600, respectively. Grey lines: 1:1 correlation. Linear fits to the data sets are shown as colored lines. The scatter around TCCON measures 2.43 ppm (native, consider e.g. Guerlet et al. (2013b)), 3.00 ppm (SWIR-1) and 3.28 ppm (SWIR-2). Figure adopted from Wilzewski et al. (2020).

introduce a sharp increase in XCO_2 scatter in Fig. 4.5 appear reasonable choices. Since a 256 spectral pixel sensor with a spectral sampling ratio of three is envisaged for the future spectrometer, this technical constraint narrows down the possible spectral resolution of the sensor. Hence, target resolving powers of 1,200 and 1,600 in SWIR-1 and SWIR-2 (denoted with a $\times$ in Fig. 4.5) can be identified, which will image the entire spectrum onto the detector and allow for only moderate increases in XCO_2 retrieval scatter. Figure 4.6 illustrates the correlation of the SWIR-1, SWIR-2 and native GOSAT XCO_2 retrievals with respect to colocated TCCON measurements for the defined target spectral resolutions. The standard deviations around the ground truth, TCCON, reach 2.43 ppm (native), 3.00 ppm (SWIR-1) and 3.28 ppm (SWIR-2). The three retrieval configurations produce distinct mean differences ("biases") with regard to TCCON (no bias correction was applied to the retrievals). However, as the goal of these measurements is to record concentration gradients to enable emission estimates on local scales, the presence of an absolute bias is not critical. Biases of satellite derived XCO_2 products are commonly observed and it is common practice to correct for such offsets by scaling the retrieval to match the ground benchmark measurements.

Figure 4.7 examines the biases per TCCON ground station for the SWIR-1 and SWIR-2 retrievals at resolving powers of 1,200 and 1,600, respectively. Such station-by-station biases are often analyzed in terms of their collective standard deviation ("bias variability"), which is then interpreted as a measure for regional systematic errors. These regional-scale spurious gradients hamper the assessment of sources and sinks on a regional scale. The proposed retrieval configurations exhibit only minor enhancements in TCCON bias variability – from 0.94 ppm for native GOSAT increased to 0.99 ppm and 0.97 ppm in SWIR-1 and SWIR-2 retrievals, respectively. XCO_2 retrieval standard deviations by TCCON station

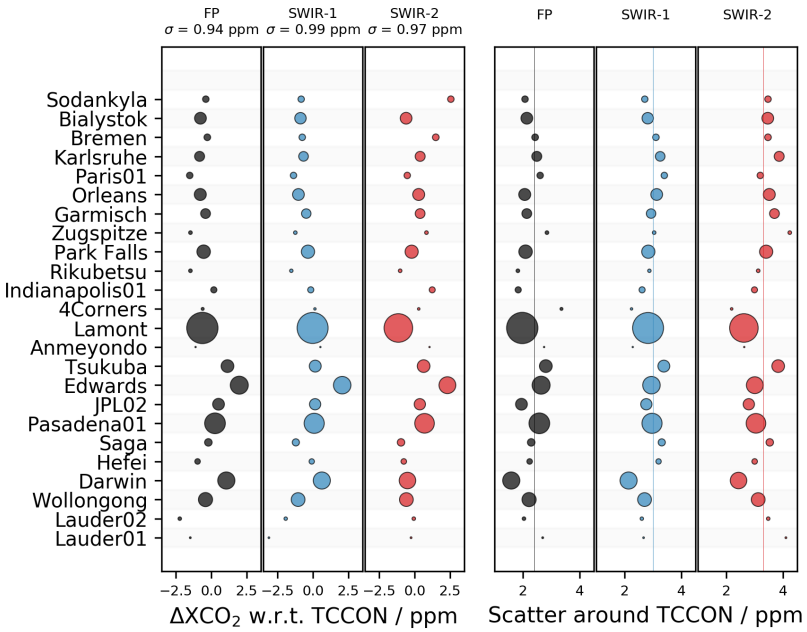

Figure 4.7: Illustration of retrieval performances at individual TCCON sites, ordered north to south. The marker size is proportional to the number of colocated GOSAT spectra at each site. Left: Site-by-site average differences between TCCON and the native, SWIR-1 and SWIR-2 retrievals (black, blue and red, respectively). The standard deviation of average differences among the stations, σ, totals 0.94 ppm (native), 0.99 ppm (SWIR-1) and 0.97 ppm (SWIR-2). Right: Scatter about TCCON per station for the native, SWIR-1, and SWIR-2 configurations. Vertical lines indicate the mean standard deviations (native: 2.43 ppm, SWIR-1: 3.00 ppm, SWIR-2: 3.28 ppm). Figure adopted from Wilzewski et al. (2020).

are also shown in Figure 4.7. A detailed overview of the retrieval performance at individual TCCON sites is provided in Table B.2 in appendix B.

Since the aim of the proposed retrievals is to resolve gradients on a local scale, regional-scale variability is not a top priority here. In fact, retrieval error correlation induced by parameters which fluctuate on the local scale are more instructive.

To determine spurious correlations of the retrieved XCO_2 on geophysical parameters that fluctuate on the local scale, several parameter dependencies of GOSAT-TCCON differences were analyzed, namely surface albedo, scattering optical thickness (SOT) and the three effective aerosol parameters z_{par}, N_{par}, and α_{par} defining particle layer height, particle number density and particle size. Surface albedo values refer to albedo at 0.774 μm for native GOSAT, albedo at 1.600 μm for the SWIR-1 configuration, and SWIR-2 albedo at 2.099 μm. Particle scattering parameters are adopted from the native GOSAT retrievals, because the SWIR-1 retrievals do not adjust the particle parameters and because

the SWIR-2 retrievals display little DFS. GOSAT-TCCON biases in the SWIR-2 retrievals appear not to correlate significantly with surface albedo, while small dependencies of the biases (R> 0.1) with respect to albedo are observed in the native and SWIR-1 configurations. As the SWIR-1 retrieval does not account for aerosol scattering, it seems reasonable that GOSAT-TCCON offsets correlate with surface albedo, since surface reflectance strongly influences the effect of scattering with regard to the direct lightpath. However, SWIR-1 departures from TCCON are only weakly dependent on SOT, aerosol size and aerosol layer height (R< 0.1), while minor error correlations are found with respect to aerosol number density near TCCON stations (R=0.11). SWIR-2 retrieval errors appear to correlate especially with the particle layer height (R< −0.3), although SWIR-2 retrievals adjust this parameter in the inversion process. Yet, the high regularization of the SWIR-2 retrieval strongly limits the aerosol parameter space in which the algorithm converges to a narrow range near the scattering parameter a priori (α_{par}=3.5, τ=0.1, z_{par}=3000 m – a standard choice for RemoTeC GOSAT retrievals). As a consequence, remaining correlations

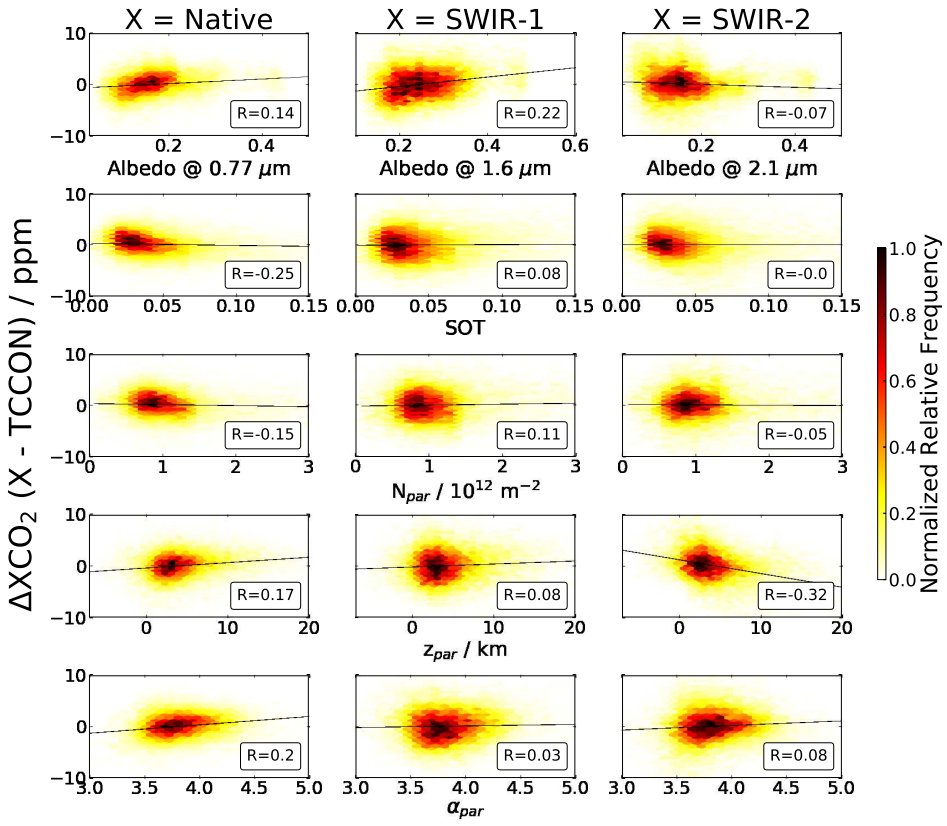

Figure 4.8: Correlation of TCCON-GOSAT differences for some geophysical parameters for native (left), SWIR-1 (center) and SWIR-2 (right) retrievals. Pearson's correlation coefficient R is given in the lower right corner of every subplot. Linear fits shown as solid lines. Relative occurrence of data points is visualized through the color-map. Figure adopted from Wilzewski et al. (2020).

with aerosol scattering parameters in the SWIR-2 retrieval are not particularly large. An examination of the impact of the particle scattering parameters on the SWIR-2 XCO_2 retrieval performance indicated that only a moderate sensitivity to the aerosol priors exists, although there is a de-facto sensitivity which is actually quite large. Altering aerosol optical depth by a factor of two or one half, for example, implies only minor changes in the retrieval standard deviation with respect to TCCON (+0.22 ppm and −0.08 ppm, respectively). Varying the aerosol layer height priors to z_{par}=5000 m or z_{par}=1000 m raised the scatter around TCCON by +0.43 ppm and +0.04 ppm, respectively. Likewise, XCO_2 standard deviation around TCCON varies by −0.05 ppm and +0.22 ppm if the prior α_{par} is adjusted to 5.0 and 3.0, respectively. SWIR-2 retrieval errors around TCCON stations do not depend strongly on SOT, aerosol size parameter and number density. Small correlations with all aerosol parameters are consistently found for native GOSAT retrievals. Additional analyses (not shown here) found that SWIR-1 (and not SWIR-2) retrievals also exhibit correlations with $|R| > 0.1$ with other geophysical variables such as the water vapor column (R=0.21) and the slant airmass of the geometric lightpath (R=-0.17).

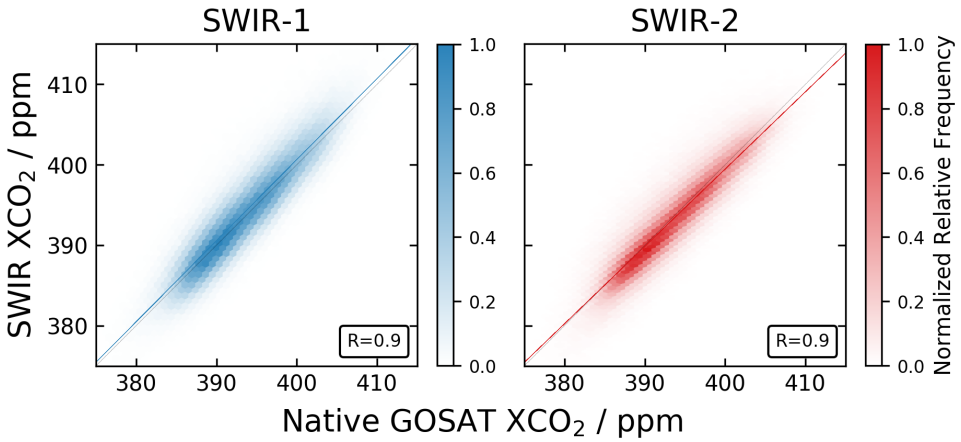

Figure 4.9: Global XCO_2 retrievals of the SWIR-1 (left) and SWIR-2 (right) configurations versus the equivalent native GOSAT retrievals. Linear fits shown as colored lines, 1:1 correlation displayed as grey line. Standard deviations of 2.85 ppm and to 2.69 ppm are found for SWIR-1 and SWIR-2, respectively. Correlation coefficients shown in the lower right corners. Relative occurrence of data points is visualized through the color-maps. Figure adopted from Wilzewski et al. (2020).

4.1.3 Global Evaluation with Native GOSAT Retrievals

Native GOSAT retrievals offer an opportunity to evaluate the proposed coarse-resolution configurations at resolving powers of 1,200 and 1,600 in the SWIR-1 and SWIR-2, respectively, on the global scale. Here, the biases determined in the previous TCCON analysis were subtracted from all XCO_2 retrivals (i.e -3.6 ppm, 2.49 ppm and 1.04 ppm for the

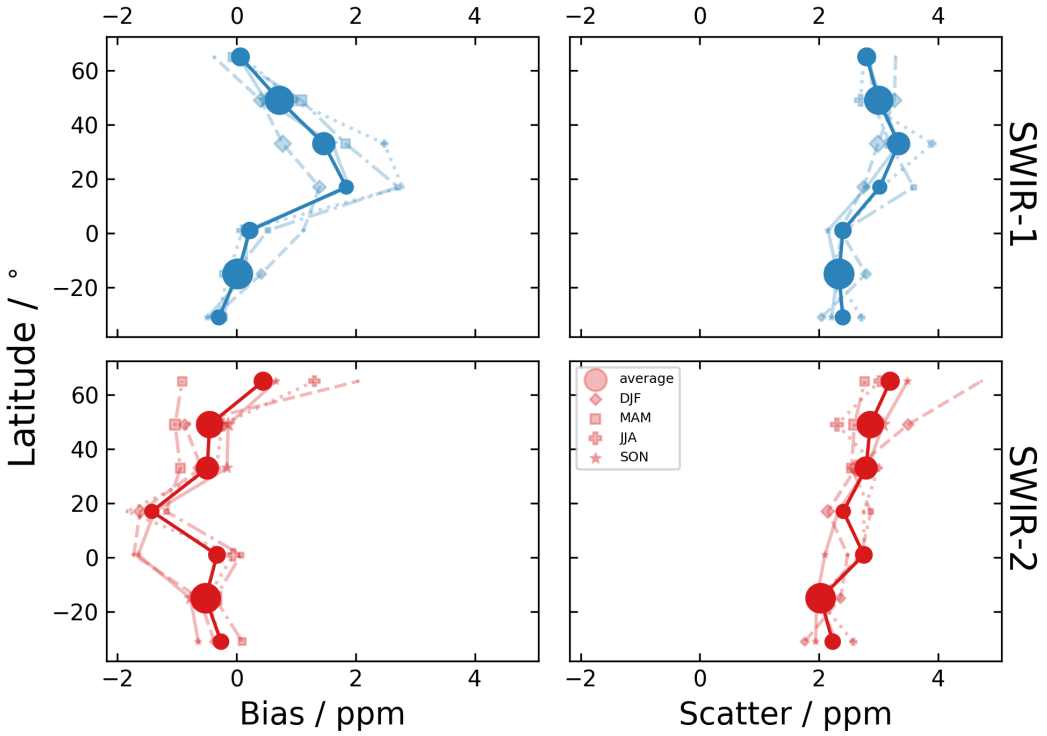

Figure 4.10: Bias and scatter of SWIR-1 (top row) and SWIR-2 (bottom row) with respect to global native GOSAT XCO_2 over land (resolved in 16° bins). Mean bias and scatter indicated by bold circles; seasonal fluctuations displayed for boreal fall (SON, stars), winter (DJF, diamonds), spring (MAM, squares) and summer (JJA, plus). The relative number of GOSAT observations over land in the corresponding latitudinal bin is symbolized by marker size. Figure adopted from Wilzewski et al. (2020).

native, SWIR-1 and SWIR-2 configurations, respectively).

The correlations of the SWIR-1 and SWIR-2 retrievals with the native GOSAT configuration are illustrated in Fig. 4.9. Standard deviations of the differences with respect to native GOSAT ("scatter") amount to 2.85 ppm and 2.69 ppm for SWIR-1 and SWIR-2, respectively, and correlation coefficients for the two SWIR retrievals are 0.90. Despite the subtraction of the overall TCCON biases from the coarse-resolution runs, non-vanishing mean differences ("bias") remain in the global analysis with native GOSAT reference retrievals. The present analysis contains many more spectra than the TCCON study of the previous chapter (even glint spectra) and the observed biases are presumably a result of the uneven distribution of TCCON stations around the globe. Figure 4.10 shows bias and scatter of the SWIR retrievals for the four seasons and resolved in geographic latitude. The upper panels of Figure 4.10 indicate that SWIR-1 bias and scatter are both increased in the northern hemisphere. Across all seasons, SWIR-1 bias and scatter reach top average values at 1.93 ppm and 3.34 ppm, respectively, between 20 and 30° N, i.e. at the location of the large deserts of Earth. Deserts are typically bright surfaces and their dust aerosols

may influence the SWIR-1 retrievals, which neglect scattering by particles. A meridional gradient for scatter as well as an unclear pattern for bias are observed in the lower panels of Fig. 4.10 for the SWIR-2 configuration. Mean SWIR-2 scatter ranges between 3.20 ppm at 65° N and 2.03 ppm at 15° S. The bias appears to imply that SWIR-2 retrievals underestimate the native GOSAT XCO_2 near the desert latitudes (20° N) and overestimate the CO_2 column in higher latitudes (60° N). No clear correlation with the seasons is detectable, while seasonal variations generally exhibit the annual average patterns. Maps of the differences between the native GOSAT configuration and the two SWIR set-ups are shown in Figure 4.11, where these differences are averaged on 1×1° pixels for the entire record of GOSAT observations between 2009 and 2016. The world maps depict the general observations of the zonal means in Fig. 4.10. throughout the high albedo regions of the Sahara, central Asia, and tentatively in central Australia, SWIR-1 retrievals exaggerate XCO_2 in comparison to the native GOSAT retrievals. SWIR-2 produces higher CO_2 columns than native GOSAT in the high latitudes and in Amazonia, whereas mixed patters are found over the deserts.

Fig. 4.12 analyzes correlations of the retrieval differences with selected geophysical parameters in analogy to the examination carried out for TCCON (section 4.1.2, Fig. 4.8). The most relevant correlations are observed for those geophysical parameters which govern the scattering regime, i.e. number density of aerosols (N_{par}), center height of the particle layer (z_{par}), the power-law parameter for the aerosol size distribution (α_{par}), surface albedo and SOT. Correlations to aerosol scattering parameters are shown for the respective parameters derived from native GOSAT retrievals. In general, both SWIR retrievals exhibit more significant parameter correlations than what has been observed in the evaluation with colocated TCCON spectra. Correlation coefficients, R, on the order of 0.2-0.3 are typical, while the peak correlation coefficient of the SWIR-2 configuration is found at 0.5 for the XCO_2 bias as a function of the number density of aerosol, N_{par}. This relatively large correlation occurs although the SWIR-2 retrieval adjusts particle parameters with some freedom (DFS=0.38 on average). Performing a non-scattering SWIR-2 retrieval (not shown here) yielded substantially inferior retrieval performance (compare also Fig. 4.5) due to correlations with, for example, the slant airmass and the water vapor column.

To put the retrieved RemoTeC aerosol parameters into context, retrieved scattering optical thickness from GOSAT measurements were compared with colocated aerosol robotic network (AERONET) aerosol optical depth (AOD) Level 2.0 data (Giles et al., 2019). Only converged full physics retrievals of GOSAT soundings that were obtained within one hour of an AERONET measurement and within a radius of 0.1° around the respective AERONET station were considered. Globally, this resulted in 8,834 matched measurements between 2009 and 2016. Since AERONET does not provide aerosol optical depth at the O_2 A-band, where it is retrieved in RemoTeC/GOSAT, the AOD measured at 500 nm was extrapolated to 760 nm with the Angstrom coefficient for the spectral range 500-870 nm

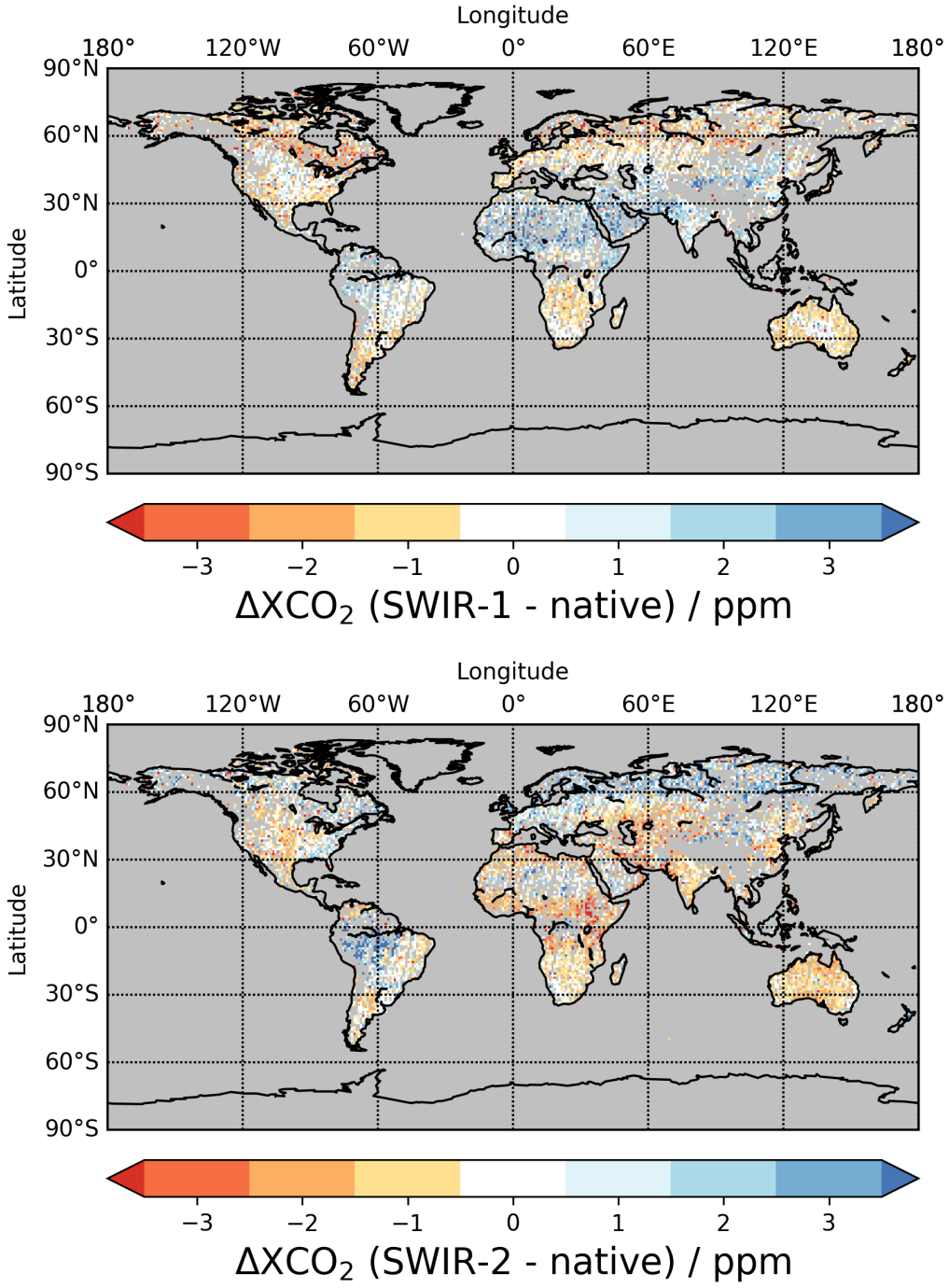

Figure 4.11: World map of native GOSAT-SWIR-1 (top) and SWIR-2 (bottom) XCO_2 differences averaged on $1\times1^\circ$ pixels and over eight years of GOSAT measurements. The global average biases over land of 0.45 ppm (SWIR-1) and 0.03 ppm (SWIR-2) were removed in the graphs. Figures adopted from Wilzewski et al. (2020).

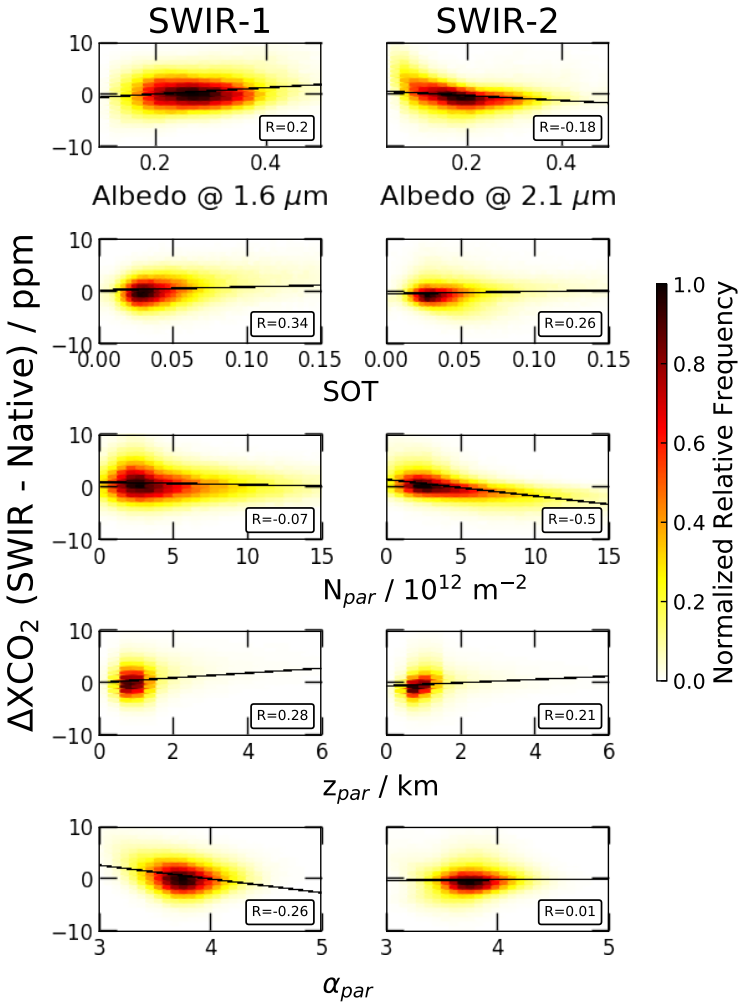

Figure 4.12: SWIR-1 (left) and SWIR-2 (right) retrieval differences with respect to native GOSAT for selected geophysical parameters. R denotes Pearson's correlation coefficient and is listed in each subplot corner. The black line indicates a linear fit to the data. Relative occurrence of data points is visualized through the color-map. Figure adopted from Wilzewski et al. (2020).

that is part of the AERONET L2.0 data set[1]. The agreement between AERONET and RemoTeC in terms of scattering optical depth (SOT) is small. RemoTeC, in its full-physics configuration, seems to underestimate aerosol optical depth systematically, which may be

[1]The Angstrom coefficient is the parameter, α, of a power law to transform aerosol optical depth (AOD) from wavelength λ_1 to wavelength λ_2:

$$AOD_{\lambda_2} = AOD_{\lambda_1} \cdot \left(\frac{\lambda_2}{\lambda_1}\right)^{\alpha}$$

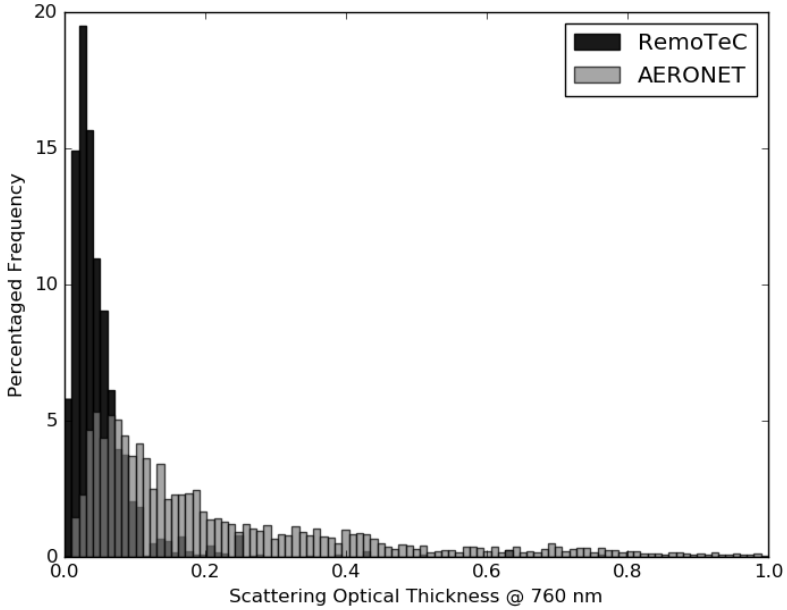

Figure 4.13: Comparison of scattering optical thickness from native GOSAT/RemoTeC and the AERONET reference network. 8,834 AERONET measurements between 2009 and 2016 were taken within ±1 h and a radius of 0.1° of the GOSAT sounding.

an effect of the simplified aerosol forward model of the algorithm (see ch. 3.1). Figure 4.13 illustrates that the range of SOT values retrieved from GOSAT with RemoTeC is far less dynamic than the AERONET reference measurements.

Although previous analyses do not strictly favor one of the SWIR bands, Fig. 4.14 illustrates that SNR considerations tend to favor the SWIR-2 set-up. The noise error shown in Fig. 4.14 corresponds to the GOSAT radiance noise propagated through the RemoTeC algorithm with Gaussian error propagation. Likely because of the presence of stronger absorption lines in the SWIR-2, the SWIR-1 noise errors were found to be greater than the SWIR-2 errors by a factor of 2.9 on average. Strandgren et al. (2020) generally confirmed this tendency in a simulation study using a realistic noise model for the proposed instrument and they recommended the SWIR-2 spectral range in terms of acquiring sufficient SNR.

In summary, the above study has shown that the resolving power of the suggested CO_2 monitoring sensor should not be selected below a resolving power of 1,000 where retrieval scatter around TCCON worsened substantially. Especially the SWIR-2 spectral range showed promising performance at a spectral resolution of 1.3 nm (resolving power of 1,600) with moderate scatter around TCCON and potential for low noise errors. While this spectral range and can be recommended at the specified resolving power, the impact of aerosol scattering should be studied thoroughly in a follow-up analysis, which would

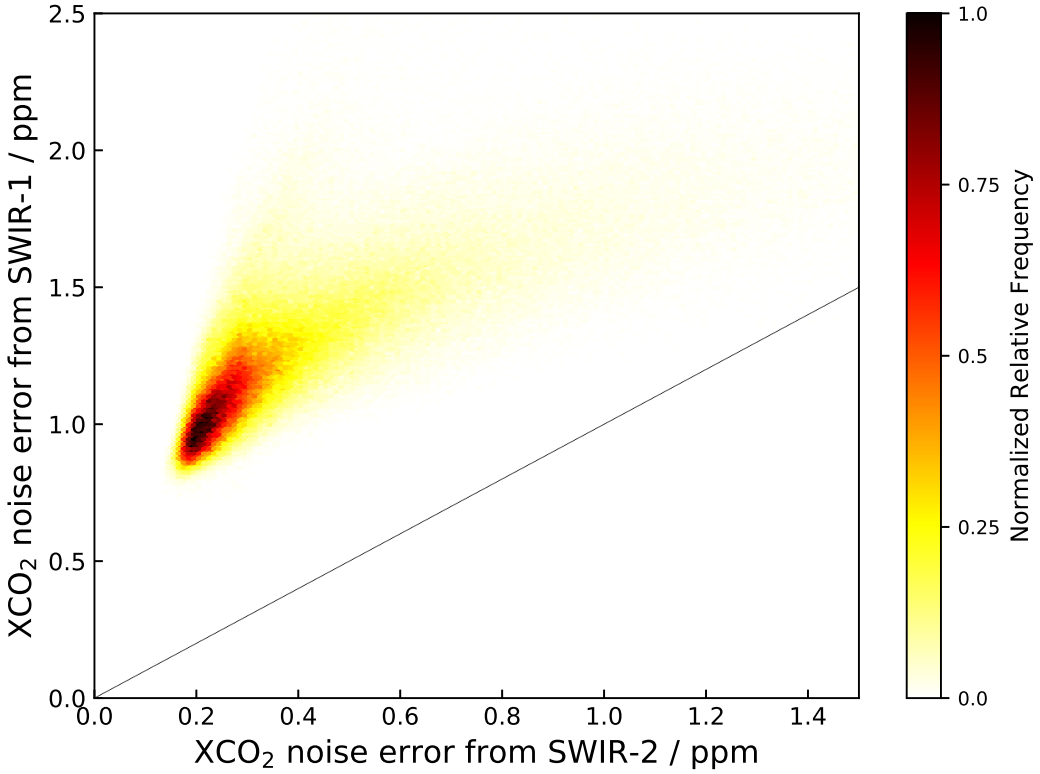

Figure 4.14: SWIR-1 (y-axis) and SWIR-2 (x-axis) XCO_2 noise errors. The 1:1 correlation is depicted as a grey line. Relative occurrence of data points is visualized through the color-map. Figure adopted from Wilzewski et al. (2020).

address, for instance, typical aerosol loads of power plant exhaust air. The importance of aerosol contamination for local plume investigations must be addressed, since XCO_2 retrievals at the above mentioned spectral resolving power were shown to have limited sensitivity to changes in the atmospheric lightpath.

4.2 Power Plant CO_2 Emission Rates Retrieved from Air-Borne AVIRIS-NG Measurements

In this chapter AVIRIS-NG overflights of power plants are investigated to study CO_2 monitoring capabilities with this sensor in combination with the RemoTeC retrieval algorithm. The chapter is structured as follows. Firstly, an overview of previous trace gas retrieval studies based on AVIRIS-NG measurements is given (section 4.2.1). Secondly, an ensemble of test spectra is selected in section 4.2.2 to test various retrieval configurations (section 4.2.3). The most favorable retrieval set-up is utilized in section 4.2.4 to derive the CO_2 fields near two power plants. Posterior bias correction methods are discussed in section 4.2.5 and the flux inversion is finally conducted in section 4.2.6.

4.2.1 AVIRIS-NG Retrieval Approach

The AVIRIS-NG sensor, introduced in chapter 3.3, has been used extensively to detect and quantify methane emissions from localized sources through a number of retrieval approaches. These approaches, which could generally be applied to CO_2 as well, differ primarily with regard to their representation of radiative transfer physics and their computational speed.

One of the most basic trace gas retrieval approaches for AVIRIS-NG, the *continuum interpolated band ratio* (CIBR) method, was described by Bruegge et al. (1990) and Thompson et al. (2015). The CIBR method associates trace gas concentration with the relative depth of an absorption band – a fast but low-accuracy retrieval.

Another trace gas retrieval method, the *residual radiance* method, has been presented by Roberts et al. (2010) and Zhang et al. (2017). They approximate the surface albedo and carry out radiative transfer calculations with background trace gas concentrations (taken from a standard atmosphere or appropriate field measurements). By comparing the model to the measurement, information about trace gas enhancements can be extracted from the remaining spectral residuals in a spectral range where the respective trace gas absorption overwhelms other species. While also being quite fast, this method suffers from errors introduced, for instance, by assuming a constant spectral albedo.

Matched filter algorithms are quite advanced, yet computationally inexpensive retrieval methods that were developed by Funk et al. (2001) and subsequently improved, for example, by Manolakis et al. (2006), Manolakis et al. (2009) and Foote et al. (2020). The general idea of the matched filter method is to compare measured spectra with modeled spectra that are constructed through a multiplication of the trace gas concentration with a spectral target signature. This target signature can be the methane or carbon dioxide absorption spectrum or the respective Jacobian vector, which has to be calculated only once for each flight altitude and viewing geometry. Matched filter techniques have proved to be computationally efficient and sensitive to small emission sources and the method is subject to on-going developments that address e.g. low albedo scenes (Ayasse et al., 2019, Foote

et al., 2020). However, matched filter methods do not account for atmospheric parameters that are spatially variable within a single observation scene, for instance concentrations of interfering absorbing species (e.g. H_2O).

To this end, physics based retrieval algorithms have been developed for AVIRIS-NG, namely the *Iterative Maximum A Posteriori Differential Optical Absorption Spectroscopy* (IMAP-DOAS) code (Frankenberg et al., 2005, Thorpe et al., 2014) and the *Weighting Function Modified Differential Optical Absorption Spectroscopy* (WFM-DOAS) algorithm (Buchwitz et al., 2000, Krings et al., 2011). The original idea of the DOAS technique (Platt and Stutz, 2008) is to remove the broad-band spectral background from a measurement of weak absorption features so that only the spectral signals caused by the absorbing species remain and the key assumption of DOAS is that the absorption optical depth is small ($\tau < 0.01$). This can be achieved by fitting and subtracting a low-order polynomial to and from the spectrum in order to eliminate the background (comprising the solar spectrum, scattering effects, surface reflectance signals, etc.). A differential spectrum remains that can be evaluated for trace gas concentrations when the absorption cross-sections and the SRF of the sensor are known. The IMAP-DOAS algorithm is a non-scattering radiative transfer scheme that adjusts concentrations of strongly absorbing trace gases (CH_4, H_2O, CO_2, ...) in several atmospheric retrieval layers, thereby taking the pressure and temperature dependence of spectral lines into account. The IMAP-DOAS method has been used by Thorpe et al. (2017) to quantify CO_2 emissions from a power plant with AVIRIS-NG imagery. The WFM-DOAS algorithm similarly employs a radiative transfer model that updates the trace gas concentrations depending on the respective height-resolved Jacobians (i.e. weighting functions).

A common finding of most of the AVIRIS-NG trace gas retrieval approaches described above, for example Borchardt et al. (2021), is the challenge of separating molecular absorption features from surface albedo features. Ayasse et al. (2018) have carried out simulations of methane retrievals that show that there are thresholds in surface reflectance below which methane retrievals essentially become dominated by noise. It has been demonstrated by Dennison et al. (2013) and Thorpe et al. (2017) that similar challenges arise in CO_2 retrievals.

This chapter is about the application of the RemoTeC algorithm (chapter 3.1) to AVIRIS-NG measurements with the goal to retrieve carbon dioxide point source emission rates. Although a full-physics based retrieval is used here for AVIRIS-NG, the results of chapter 4.1 have made it clear that the coarse spectral resolution of AVIRIS-NG will essentially remove information about aerosol scattering from the spectra. Consequently, RemoTeC will be operated in its non-scattering configuration, assuming the geometric lightpath. To constrain an optimal retrieval configuration with regard to spectral window and state vector selection, different retrieval configurations are applied to an ensemble of background spectra in the following sections.

4.2.2 An Ensemble of Test Spectra

The large spectral range of AVIRIS-NG offers the possibility to retrieve CO_2 concentrations from both the SWIR-1 and the SWIR-2 spectral range. In order to determine which spectral range(s) support stable and accurate retrieval performance, retrievals were carried out with a test dataset to provide benchmark background spectra and also to save computational resources. Here, an ensemble of test spectra was selected from the AVIRIS-NG flight line *ang20190621t200919*. These measurements were obtained under clear-sky conditions near the *APS Four Corners* power plant in the desert of the Colorado Plateau in New Mexico, USA. This facility operates on coal from a nearby mine and had an estimated emission of 7.71 $MtCO_2y^{-1}$ in 2018 (EPA, 2020). Only spectra obtained upwind of the facility were considered here so that they do not contain the CO_2 exhaust plume from the stack. Essentially, the underlying idea is to collect spectra which all have identical trace gas column concentrations. In total the ensemble is comprised of $1,369$ spectra collected

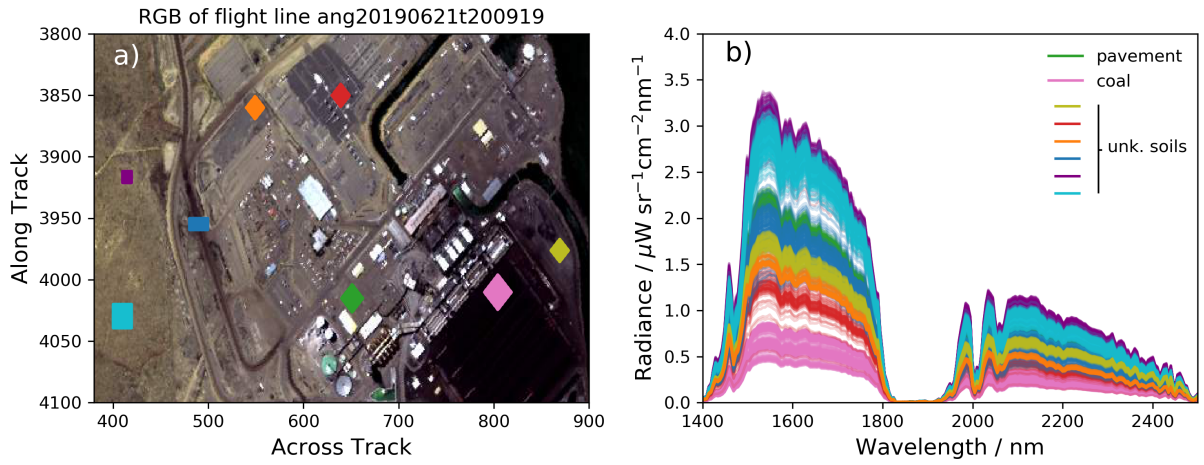

Figure 4.15: Spectra for the test ensemble were selected from eight individual areas. a) RGB-image of the selected flight line with colored rectangles indicating the origin of the test spectra. b) Overview of the ensemble in the spectral range $1.4 - 2.5$ μm; colors match the rectangles in a). Green and pink spectra have been identified as observations of pavement and coal, respectively, while the other colors represent unknown soil types.

over an area of ~ 1 km^2 and should allow to study most challenges that may arise in the retrieval, because they cover a range of various surface types and different radiance levels. Elevation differences of up to 20 m exist between some scenes within the test-ensemble, but geocoding errors are expected to be on the sub-pixel scale (Chapman et al., 2019), where one ground pixel has $\sim 2.7 \times 2.7$ m^2. Thus, CO_2 retrieval differences between ensemble spectra are not expected to be driven by uncertainty in ground elevation. The ensemble was selected from eight individual, rectangular areas (as indicated in Fig. 4.15) with a mean and median spectral radiance of 0.7 $\mu Wsr^{-1}cm^{-2}nm^{-1}$ at $2,100$ nm. Surface materials of two rectangular areas (pavement of a parking lot and a coal deposit) were determined

from visual inspection of Google Earth imagery. The darkest test spectra with radiances below 0.2 μWsr^{-1}cm^{-2}nm^{-1} at 2,100 nm were chosen from the coal deposit, while the brightest scenes come from what is probably barren desert soil. Five other unknown soil kinds are represented in the ensemble and some observations were explicitly excluded, for instance, water surfaces or pixels dominated by shadow as well as spectra measured above metallic roofing materials. The latter turned out to be so bright, possibly due to glint, that the sensor reached saturation conditions. Spectra above dark ground pixels notoriously present some of the most challenging scenes in trace gas remote sensing, i.e. spectra recorded above water surfaces are mostly too dark for meaningful retrievals (e.g. Ayasse et al., 2018) and pixels containing shadow have non-geometric light paths. The rationale behind this choice of test spectra is to cover a wide dynamic range of the sensor, which is representative of the downwind scenes expected on the Colorado Plateau. Fig. 4.15 shows that the test spectra span a nearly continuous range of at-sensor radiances near the CO_2 bands in the short-wave infrared.

4.2.3 Comparison of Retrieval Configurations

In this section, the ensemble of background spectra defined above was treated as a test bed to conduct carbon dioxide retrieval studies with the RemoTeC algorithm. This approach allows for a rigorous comparison of different retrieval configurations with regard to their performance with the test spectra, so that various retrieval set-ups can be compared in terms of statistical metrics. The retrieval procedures analyzed here explore the obvious question for the choice of spectral retrieval windows. Specifically, the test configurations can be categorized into two kinds: CO_2 retrievals that solely use one of the two SWIR spectral ranges (near either 1.6 μm, page 72, or near 2.0 μm, page 75) and retrievals that use both, the SWIR-1 and the SWIR-2, spectral ranges with the absorber amounts of CO_2 (and H_2O) either coupled or separated (page 81). While it is clear from first principles of retrieval theory that more spectral information on a given absorbing species should result in an improved fit, this chapter aims to test this idea quantitatively. In addition, oxygen retrievals from the absorption bands near 0.76 and 1.27 μm were examined in an effort to improve knowledge about the atmospheric light path (page 84). A retrieval will be considered favorable here when spectral residuals, correlations between state vector entries and scatter in CO_2 (and H_2O) concentrations are all low and a high fraction of retrievals converge. XCO_2 and XH_2O columns are obtained by dividing the column number densities of these species by the air number density calculated from prior meteorology.

CO_2 retrieved from the SWIR-1

The SWIR-1 spectral range ($\sim 1,540 - 1,640$ nm) is dominated by two weak carbon dioxide absorption bands and interfering water vapor absorption signals. Hence, all retrieval configurations tested in the SWIR-1 fitted the total column number densities of these two species. In addition, a spectral shift parameter and the degree of the polynomial fitted to

the baseline (to derive the albedo) was adjusted in the fit (2=line fit, 3=parabola fit). The test set-ups included retrievals with spectral windows that covered just one of the two CO_2 bands near 1.6 μm ($1,550-1,597$ nm and $1,585-1,639$ nm) and other retrievals that covered both bands simultaneously ($1,538-1,639$ nm and $1,550-1,634$ nm). Retrievals were conducted with variable off-band spectral margins and a summary of nine retrieval tests is illustrated in Fig. 4.16. Three general observations can be deduced from this test.

Firstly, the retrieval convergence rate in the SWIR-1 spectral band is low for most selections of spectral windows (67 % convergence on average across the nine retrieval tests shown in Fig. 4.16). Convergence is lowest at below 50 % on average when both CO_2 absorption bands are contained in only one spectral window (colums 3-6 in Fig. 4.16). Fitting the two bands individually or separately in a coupled fit increases the convergence rate to over 80 %. This finding can partly be explained by large spectral residuals that were observed for the majority of these fits; see Fig. 4.17. The residual structures were persistent, even when different spectroscopic databases (i.e. HITRAN08, HITRAN16) were used. As the magnitude of the residuals is quite large, these features may hint at instrumental issues between $1,540$ and $1,570$ nm, as well as between $1,590$ and $1,615$ nm. Spectral residuals could be significantly reduced when the two CO_2 absorption bands were fitted separately with baseline polynomials of degree three (see the set-up in the last column in Fig. 4.16, last row in Fig. 4.17). In such a set-up, both XCO_2 and XH_2O are coupled between the two retrieval windows. By uncoupling either or both of these state vector entries, convergence of the retrieval was decreased.

Secondly, the choice of the baseline polynomial has a significant impact on the mean values of XCO_2 and XH_2O in these tests. For instance, CO_2 average values change by ± 6 % on average when changing the baseline representation from a linear to a quadratic fit. Altering the polynomial degree while keeping the state vector and spectral window unchanged also impacts the convergence rate and also the distribution of retrieved albedo values. Root mean square differences ($\mathrm{RMS}=\Sigma_{\mathrm{pixels}}((y_{meas}-y_{mod})^2/N_y)^{1/2}$) between the measurement and the forward model are likewise affected by changes in the baseline fit. This observation suggests that surface reflectance, CO_2 and H_2O absorption features are not entirely separable in the retrieval.

Thirdly, both water vapor and carbon dioxide columns retrieved from the SWIR-1 have large standard deviations amounting to 54 % and 6 % of the respective means of XH_2O and XCO_2 on average.

In summary, the SWIR-1 cannot be regarded an ideal spectral range for CO_2 retrievals from AVIRIS-NG, as was similarly concluded by Borchardt et al. (2021) (for CH_4 retrievals from the SWIR-1). Thorpe et al. (2017) have also omitted the 1.6 μm range for CO_2 retrievals. It may be possible that some of the retrieval issues described above are caused simply by a combination of the coarse spectral resolution of AVIRIS-NG and the lack of strong CO_2 absorption signals near 1.6 μm that have high contrast above the spectral continuum. The most favorable retrieval set-up in terms of low spectral residuals and high convergence rate is the configuration where CO_2 and H_2O are retrieved from individual spectral windows each covering one of the two CO_2 bands ($1,550-1,597$ nm and $1,585-$

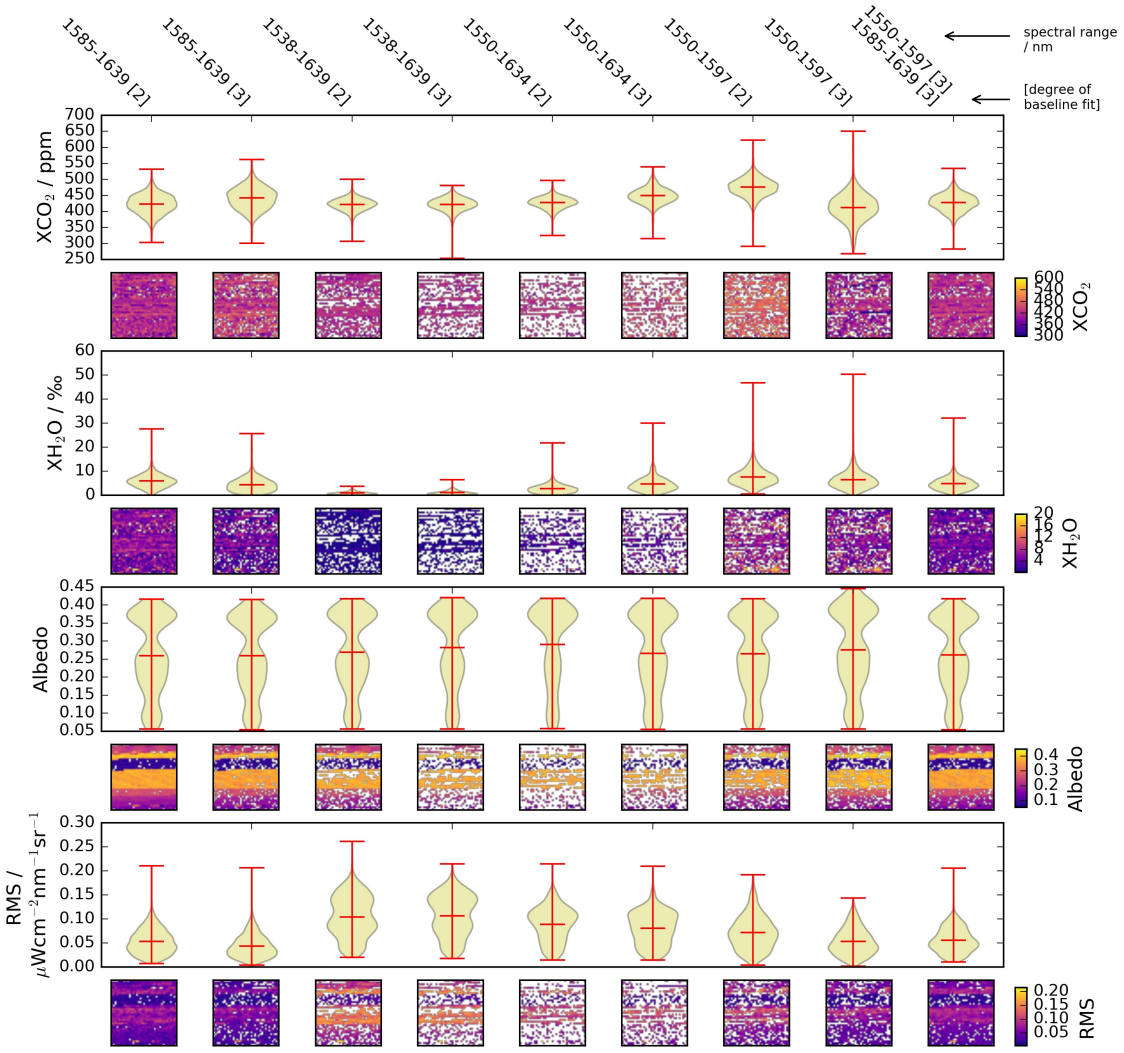

Figure 4.16: Tests of retrieval configurations in the 1.6 μm range. Each column represents a retrieval configuration labeled on the top of the figure (indicating spectral range and polynomial power of the baseline fit). The last column of the Figure shows a retrieval configuration, where two spectral windows were combined and CO_2 and H_2O were coupled in the fit. The colored squares show images of retrieval variables (the test ensemble contains $1,369 = 37{\times}37$ spectra). White dots represent spectra that did not converge in the fit. The violin plots show distributions of critical retrieval parameters. From top to bottom: XCO_2, XH_2O, albedo (at the longwave limit of the respective spectral window), RMS. Note that albedo and RMS do not only depend on the retrieval configuration, but foremost on the radiance in the respective spectral window.

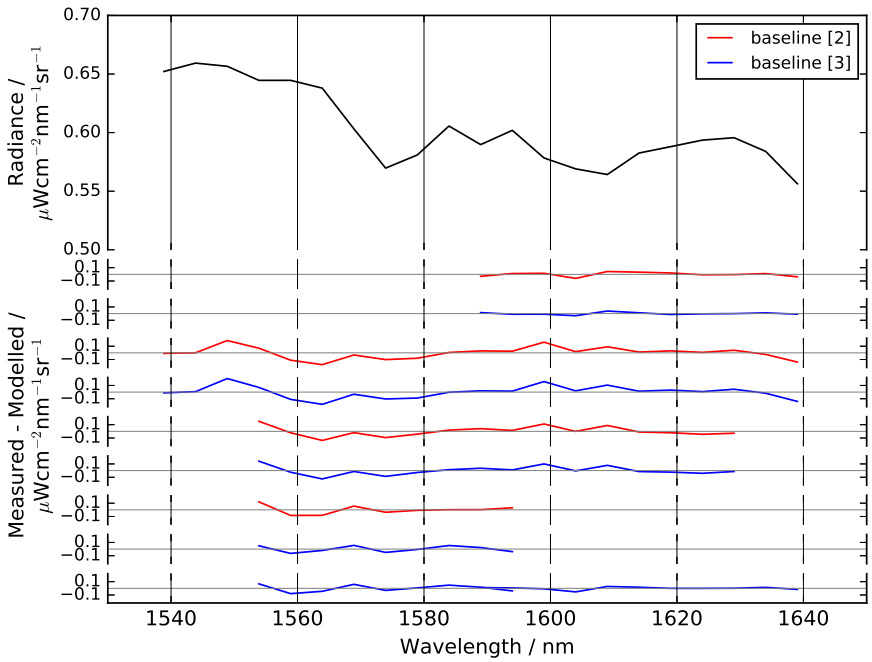

Figure 4.17: Averaged residuals of all test spectra that converged for various retrieval configurations in the SWIR-1. Top: Example spectrum from the test ensemble. Narrow panels: averaged residuals color coded for retrievals where a second order polynomial (red) or third order polynomial (blue) was used for the baseline fit. Residuals for a coupled retrieval from two windows shown in the last row.

1,639 nm). All retrievals reveal relatively high scatter in XCO_2 and XH_2O.

CO_2 retrieved from the SWIR-2

The SWIR-2 spectral range ($\sim 1,960 - 2,140$ nm) contains two CO_2 absorption bands. Water vapor absorption occurs throughout the band, and an opaque water vapor band limits the SWIR-2 spectral range at $\sim 1,900$ nm. As in the SWIR-1 band, the group of retrievals tested here all adjust XCO_2, XH_2O, spectral shift and a baseline polynomial to the measurements. In comparison to the SWIR-1 performance tests, several aspects of retrieval performance are enhanced in the SWIR-2 experiments. All AVIRIS-NG SWIR-2 spectra converged in the present retrieval study and retrieval tests in the SWIR-2 spectral range consistently exhibited significantly lower standard deviations in the retrieved XCO_2 and XH_2O fields at 2 % and 10 % of the respective means on average. Fig. 4.18 gives an overview of some retrieval configurations tested with the ensemble of background spectra.

As in the SWIR-1 tests, XCO_2, XH_2O and albedo are not fully separable in AVIRIS-NG retrievals in the SWIR-2 spectral range. Changes in the fit of the spectral baseline

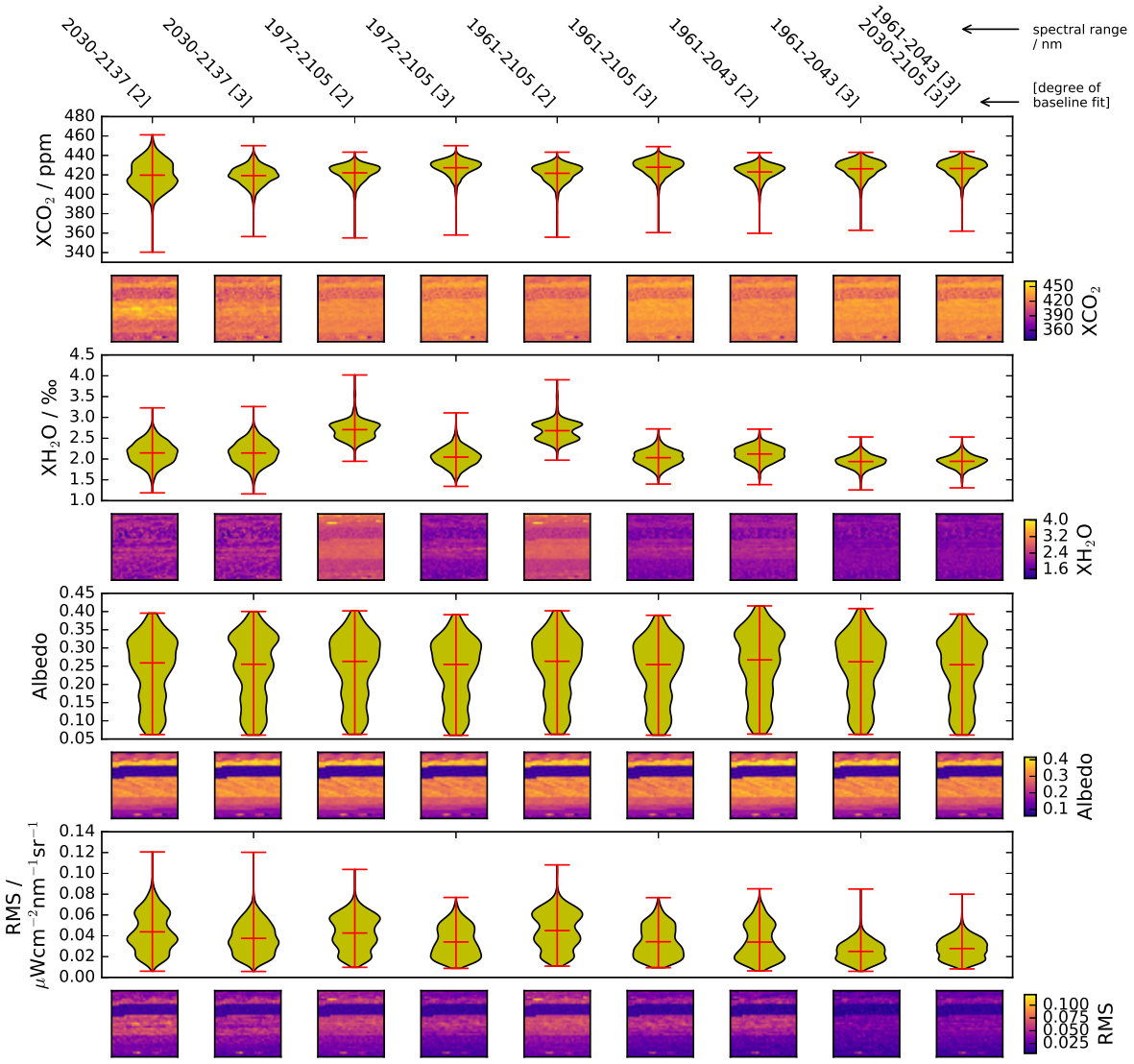

Figure 4.18: Tests of various retrieval configurations in the 2.0 μm range. Figure set-up as in Fig. 4.16. As in the SWIR-1 tests, XCO_2, XH_2O and albedo are not fully separable in AVIRIS-NG retrievals in the SWIR-2 spectral range. The last column represents the retrieval deemed most favorable due to low standard deviation in the trace gas distributions and low spectral residuals.

directly impact the shape and mean values of retrieved XCO_2 and XH_2O distributions. The interdependence of state vector variables is especially pronounced in retrievals that consider both CO_2 bands in one spectral window. Columns three to six in Fig. 4.18 show that these retrievals lead to large shifts in XH_2O distributions. This effect was also

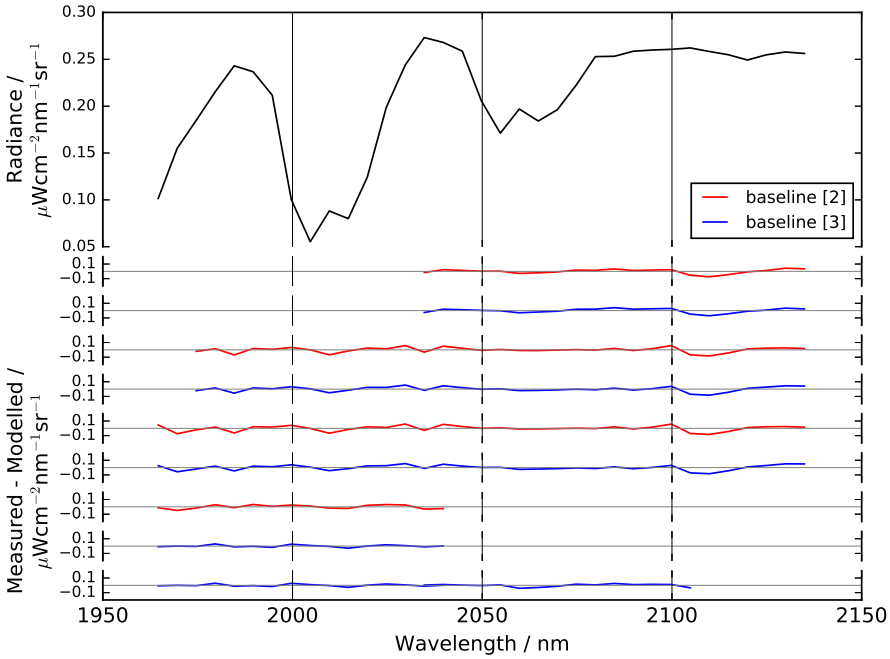

Figure 4.19: Averaged residuals for various retrieval configurations in the SWIR-2 region. Top: Example spectrum from the test ensemble. Narrow panels: averaged residuals color coded for retrievals, where a second order polynomial (red) or third order polynomial (blue) was used for the baseline fit. Residuals for a coupled retrieval from two windows shown in the last row.

observed for the retrieval windows $1,972 - 2,105$ nm and $1,961 - 2,105$ nm, which are not displayed here. At the same time average correlation coefficients of XH_2O w.r.t albedo increased to $R = 0.50$ in the two-band set-ups while $R = 0.34$ in retrieval configurations that only covered one of the CO_2 bands. These tests suggest that SWIR-2 retrievals profit from splitting the spectral range into two retrieval windows.

XCO_2 retrievals are stable within ± 1 % of the total column (419 ppm<XCO_2 <427 ppm), but they correlate clearly with the ground albedo of the test ensemble tile (second row in Fig. 4.18, average correlation coefficient $R = 0.68$).

Changing the degree of the baseline polynomial also had an effect on the spectral residuals. The last row in Fig. 4.18 illustrates that using three polynomial coefficients systematically decreased residuals across the different test cases. Apparently, including more of the longwave water vapor absorption into the retrieval window (beyond $2,110$ nm to $2,137$ nm considered here) is a driver of spectral residuals in the SWIR-2, as can also be observed in Fig. 4.19. These residuals are independent of using the HITRAN08 or HITRAN16 spectroscopic databases as input. However, short retrieval windows covering only the longwave SWIR-2 band (e.g. $2,030 - 2,105$ nm) are not favorable for XCO_2 re-

trievals if *not* combined with a coupled retrieval window near the strong CO_2 band, because further tests revealed that such single-window configurations shift the XCO_2 distribution retrieved from this spectral window by up to ±4 %. Therefore, reduced spectral residuals and favorable retrieval performance can be achieved by coupling the $1,961 - 2,043$ nm and $2,030 - 2,137$ nm bands (last row in Fig. 4.19, last column in Fig. 4.18). Note that the retrieval window only covering the strong CO_2 band near 2.0 μm has very similar overall retrieval performance. However, because large amounts of CO_2 absorption signals are beneficial from a physics point of view, the configuration including the weak band is considered more favorable.

Concluding, the SWIR-2 spectral range shows promising performance with regard to XCO_2 retrievals with full convergence and low XCO_2 scatter, supporting the findings of Thorpe et al. (2017) who retrieved XCO_2 between $1,904 - 2,099$ nm and Borchardt et al. (2021) who only used the weak SWIR-2 band at $2,040 - 2,100$ nm. The above analysis has shown that the specific choice of spectral retrieval windows significantly impacts the water vapor column retrieval. This observation supports the idea that retrievals from weak absorption features (H_2O beyond $2,000$ nm) intrinsically interfere more with the baseline fit – they are harder to distinguish from surface reflectance features. As a consequence, favorable SWIR-2 retrievals use two coupled retrieval windows ($1,961 - 2,043$ nm and $2,030 - 2,137$ nm) with a quadratic polynomial adjusted to the spectral background to reduce residuals. To improve the XH_2O retrieval, a third retrieval window was introduced near the strong water vapor absorption band that separates the SWIR-1 and SWIR-2 spectral ranges in the following paragraph. This dedicated water vapor retrieval window can be used to enhance stable, low-scatter XH_2O retrievals by coupling to the SWIR spectral windows.

Dedicated H_2O retrieval window

To better constrain background XH_2O concentrations, different retrieval configurations were tested in the $1.7 - 1.9$ μm spectral range – in the wing of a strong water vapor band where absorption by other atmospheric species can be neglected. Fig. 4.20 gives an overview of a range of retrieval tests conducted here. As before, the state vector is comprised of the trace gas column, a spectral shift parameter and a polynomial to adjust the spectral baseline and the prior water vapor concentration was obtained from ERA5 reanalysis data.

While the retrieved XH_2O fields in the SWIR-1,2 spectral ranges had average standard deviations of 2.48‰ and 0.19‰, respectively, the present XH_2O fits suggest that the background spectra have narrower XH_2O distributions (average scatter across the ten tests is 0.11‰). Moreover, the tests indicate that the value of the atmospheric water vapor background is near 2.28 ± 0.04‰, i.e. slightly larger than in the SWIR-2 retrievals (e.g. 1.94 ± 0.15‰ in the coupled SWIR-2 test). Such enhanced XH_2O values were also observed in test retrievals near 1.3 μm and 1.5 μm (not shown in Fig. 4.20). In light of the large amount of (strong) water vapor absorption lines available near 1.8 μm and

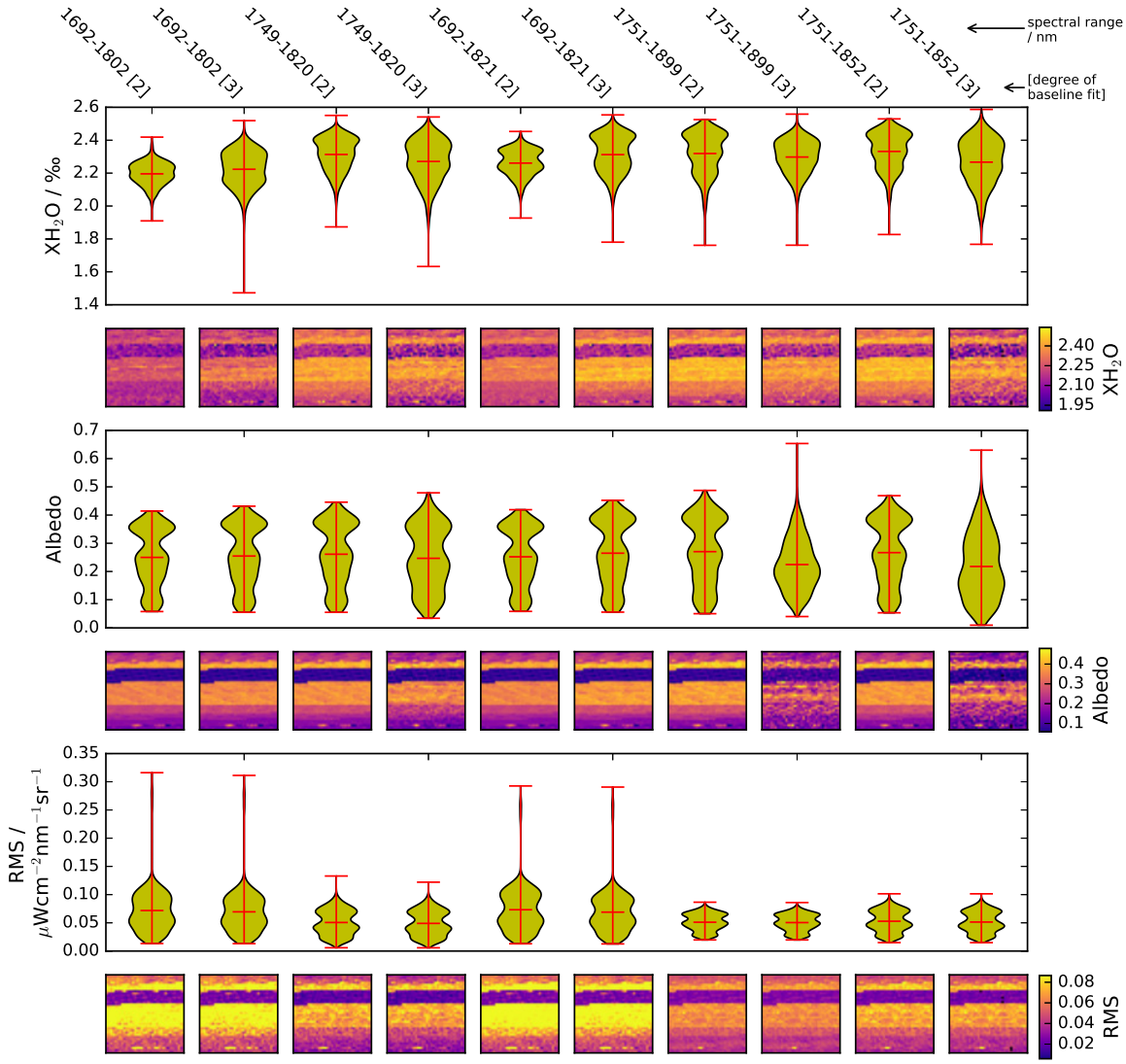

Figure 4.20: Tests of various retrieval configurations in the edge of the water vapor band near 1.8 μm. Figure set-up as in Fig. 4.16. The most favorable set-up, which did not produce large spectral residuals, captured the ground reflectance well and also had a reduced XH_2O standard deviation is the third column, i.e. $1,749 - 1,820$ nm [2].

specifically due to the low retrieval scatter, this spectral range can therefore be considered advantageous to retrieve the H_2O column.

Many retrieval configurations have similar performance regarding the XH_2O retrieval, but they differ substantially with respect to spectral residuals and retrieved albedo. Al-

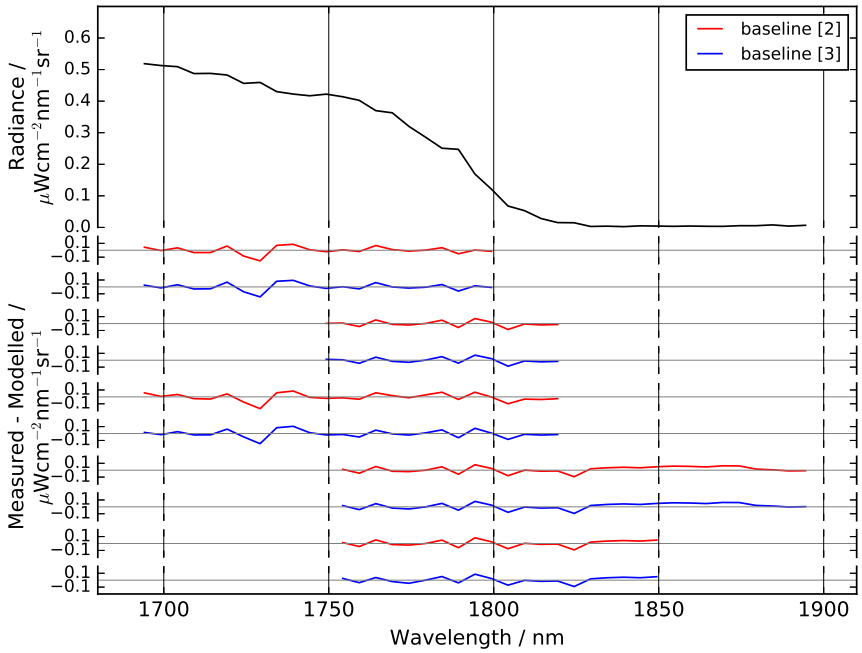

Figure 4.21: Averaged residuals of all test spectra that converged for the H_2O fit near 1.7 μm. Top: Example spectrum from the test ensemble, narrow panels: averaged residuals color coded for retrievals, where a second order polynomial (red) or third order polynomial (blue) was used for the baseline fit.

though "only" H_2O concentrations are adjusted in these retrievals, changes in the degree of the baseline polynomial strongly interfere with the water vapor/surface reflectance retrievals. XH_2O distributions are generally broader when the baseline is represented by a parabola than when a line fit is used. Some quadratic baseline fits (i.e. spectral windows $1,751-1,899$ nm, $1,751-1,852$ nm) also produce unrealistic albedo retrievals; see columns eight and ten in Fig. 4.20. This implies that a second order background polynomial may be a good choice. Further, spectral analysis revealed that the less opaque part of the water vapor band wing is affected by residual structures that persisted even when other spectroscopic databases (HITRAN08, HITRAN16) were used. These features, shown in Fig. 4.21 occur near $1,730$ nm and therefore this spectral range should be avoided. One can only speculate that an instrumental issue causes these spectral residuals.

The three retrieval configurations which did not cause amplified spectral residuals and which do not use a background polynomial of degree three are shown in columns three, seven and nine in Fig. 4.20 ($1,751-1,899$ nm [2], $1,751-1,852$ nm [2] and $1,749-1,820$ nm [2]). Of these remaining set-ups, the $1,749-1,820$ nm spectral window produced the lowest scatter XH_2O field ($\sigma = 0.1‰$) and additionally had the lowest correlation with surface reflectance (albeit still high at $R = 0.92$).

Thus, to increase the performance of H_2O retrievals and thereby increase CO_2 retrieval performance, it seems favorable to conduct dedicated water vapor fits between $1,749 - 1,820$ nm.

CO_2 retrieved from combinations of SWIR bands

The above sections have discussed the most favorable retrieval configurations for the ensemble of background spectra in the SWIR-1,2 and 1.8 μm ranges. Combinations of these configurations were used to investigate any added value that can be achieved by coupling several of these spectral windows. This paragraph concludes the present sensitivity study by selecting the retrieval with the most promising overall retrieval performance in terms of spectral residuals and scatter of CO_2 and H_2O.

Fig. 4.22 gives an overview of these retrieval tests. Although the SWIR-1 spectral range – by itself – only enabled low-performance retrievals, coupling the most favorable SWIR-1 retrieval configuration (spectral windows $1,550 - 1,597$ nm coupled with $1,585 - 1,639$ nm) to the SWIR-2 spectral range reduced the standard deviation of the retrieved XCO_2 field (see Table 4.3). This was observed regardless of whether the coupled SWIR-2 ($1,961 - 2,043$ nm coupled with $2,030 - 2,105$ nm) retrieval or only the strong band SWIR-2 set-up ($1,961 - 2,043$ nm) retrieval was used in combination with the SWIR-1.

In the previous analysis of the SWIR-2 spectral range, the coupled retrieval and the strong-band-retrieval both performed well. Here, retrieval tests where the SWIR-2 was coupled with other bands demonstrate that leaving out the weak CO_2 band in the SWIR-2 range slightly reduced both the scatter in XCO_2 and the mean value of the retrieved XCO_2 field. However, such retrievals that only use the strong SWIR-2 band also exhibit somewhat larger spectral residuals, when the water vapor or SWIR-1 spectral band is included in the retrieval. All differences between these configurations are too small to be statistically significant (see Table 4.3) and therefore the set-up including the additional weak band is regarded the optimized retrieval configuration due to a first principles approach that more CO_2 bands lead to better retrievals. Fig. 4.23 illustrates that the addition of the weak SWIR-2 CO_2 band impacts spectral residuals foremost in the neighboring strong CO_2 band. The Figure shows that changes in the spectral residuals follow the three other SWIR CO_2 band structures, which indicates that the weak band may provide added value in fitting CO_2 concentrations from AVIRIS-NG spectra.

Because no ground truth XCO_2 data are available for this flight, the absolute XCO_2 values can only be assessed from the present retrievals. Yet, since the goal of this work is to assess differences in the carbon dioxide columns across the spatial domain of the sensor, such offsets in the total column are not critical (offsets of more than 1 ppm are observed for different tests in Table 4.3).

When adding the dedicated water vapor retrieval window to the retrievals, an improvement in the standard deviation of the retrieved XH_2O field was observed. The water vapor concentrations were coupled across all windows, since uncoupling the water vapor lead to significant decreases in the convergence rate of RemoTeC. Both, Table 4.3 and Figure 4.22,

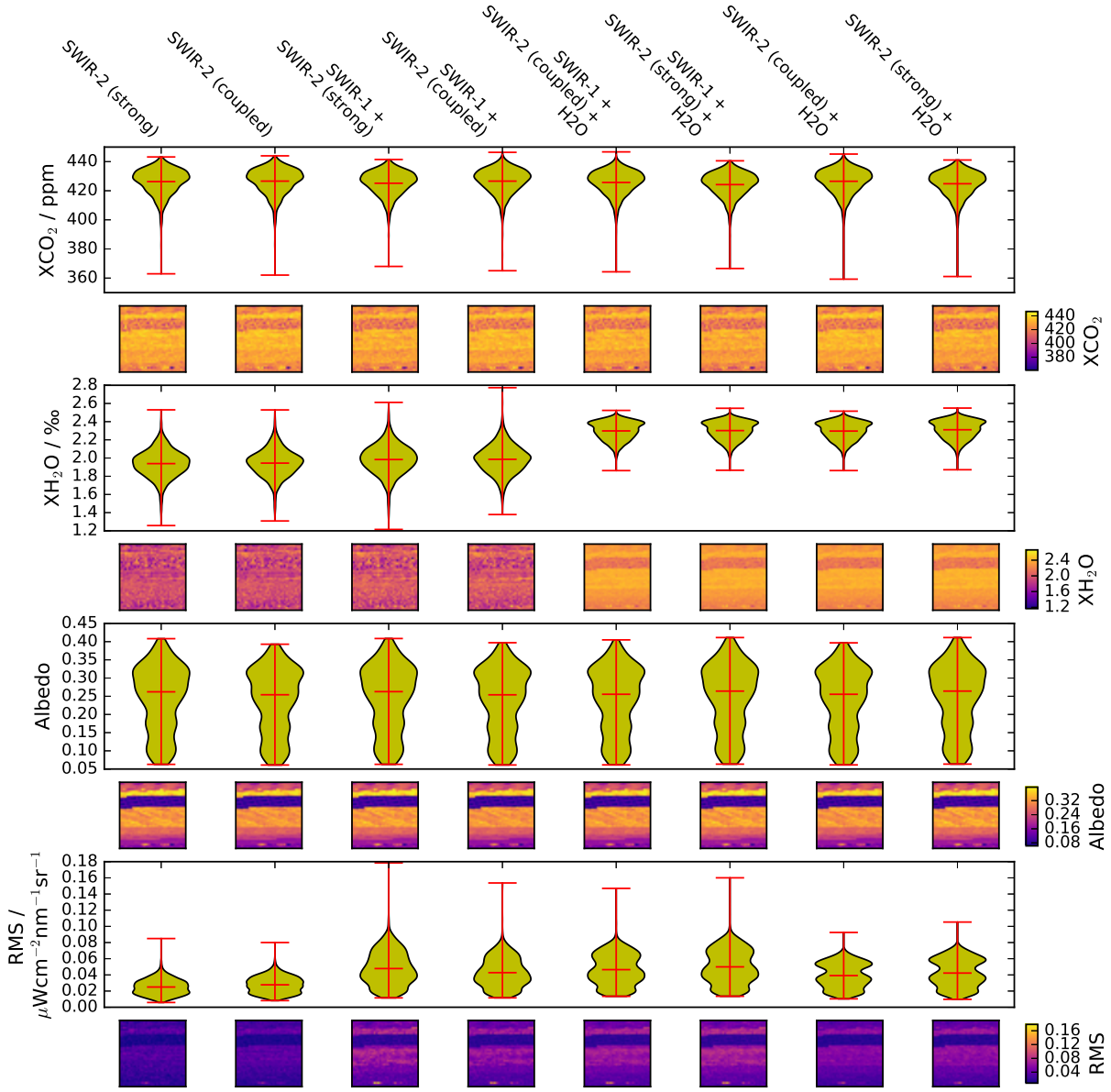

Figure 4.22: Performance of retrievals with XCO_2, XH_2O coupled across spectral bands. First column: reference single-band retrieval at the strong SWIR-2 band. Retrieval configurations are noted at the top of each column. SWIR-1: $1,550-1,597$ nm coupled with $1,585-1,639$ nm, SWIR-2 (coupled): $1,961-2,043$ nm coupled with $2,030-2,105$ nm, SWIR-2 (strong): $2,030-2,105$ nm, H2O: $1,749-1,820$ nm. The baseline fit used a quadratic polynomial in all bands except for the H_2O window (linear fit). Column 5 achieves an advantageous combination of low scatter in XCO_2, XH_2O and low spectral residuals.

Retrieval Configuration	∅XCO_2 /ppm	$\sigma(XCO_2)$ /ppm	∅XH_2O /‰	$\sigma(XH_2O)$ /‰	R_{ALB}^{H2O}	R_{ALB}^{CO2}	∅RMS /Radiance
SWIR-2 (strong)	426.26	8.74	1.94	0.15	0.25	0.71	0.025
SWIR-2 (coupled)	426.60	8.75	1.94	0.15	0.27	0.71	0.028
SWIR-1 + + SWIR-2 (strong)	425.14	8.32	1.98	0.16	0.32	0.69	0.048
SWIR-1 + + SWIR-2 (coupled)	426.59	8.46	1.99	0.16	0.37	0.69	0.043
SWIR-1 + H_2O + + SWIR-2 (coupled)	425.68	8.33	2.30	0.10	0.91	0.69	0.046
SWIR-1 + H_2O + + SWIR-2 (strong)	424.21	8.27	2.30	0.10	0.91	0.69	0.050
SWIR-2 (coupled) + + H_2O	426.50	8.64	2.30	0.10	0.91	0.72	0.039
SWIR-2 (strong) + + H_2O	424.81	8.60	2.31	0.10	0.91	0.71	0.042

Table 4.3: Overview of retrieval performance data for the most promising configurations tested in this thesis. The first column indicates the spectral retrieval windows (see text and Fig. 4.22 for more information). Remaining columns: average (∅) and standard deviation (σ) of the trace gas fields, correlation coefficients for correlations between CO_2 and H_2O (R_{H2O}^{CO2}) as well as between CO_2 and albedo (R_{ALB}^{CO2}) and average value of spectral RMS in units of absolute spectral radiances ($\mu Wcm^{-2}nm^{-1}sr^{-1}$). The yellow row marks the configuration that is considered a favorable set-up, because of both low scatter in XH_2O and XCO_2 as well as low spectral residuals and because it uses all available CO_2 bands.

show that the XH_2O scatter was significantly reduced with this extra spectral window and that the average values of the water vapor distribution were enhanced with respect to retrievals without this window. The average values of XH_2O retrieved in these coupled retrievals agree with the values reported previously for XH_2O retrievals solely using the 1.8 μm band to within their standard deviation. The inclusion of the dedicated water vapor retrieval window also decreased the standard deviation in the XCO_2 field in every case, although the effect is small (see Table 4.3). At the same time, the added water vapor window had the effect of increasing correlation between H_2O and the surface reflectance. This effect can be understood by looking at the square images of the XH_2O "tiles" in Fig. 4.22 (row four): these retrieval configurations retrieve XH_2O at high accuracy and therefore they display a similar retrieval correlation to ground albedo as observed for XCO_2. Both XCO_2 and XH_2O exhibit distributions with rather long tails towards low values, which in turn are associated with low ground reflectance. No retrieval solutions have been found which would remove the remaining correlations between trace gas columns and surface

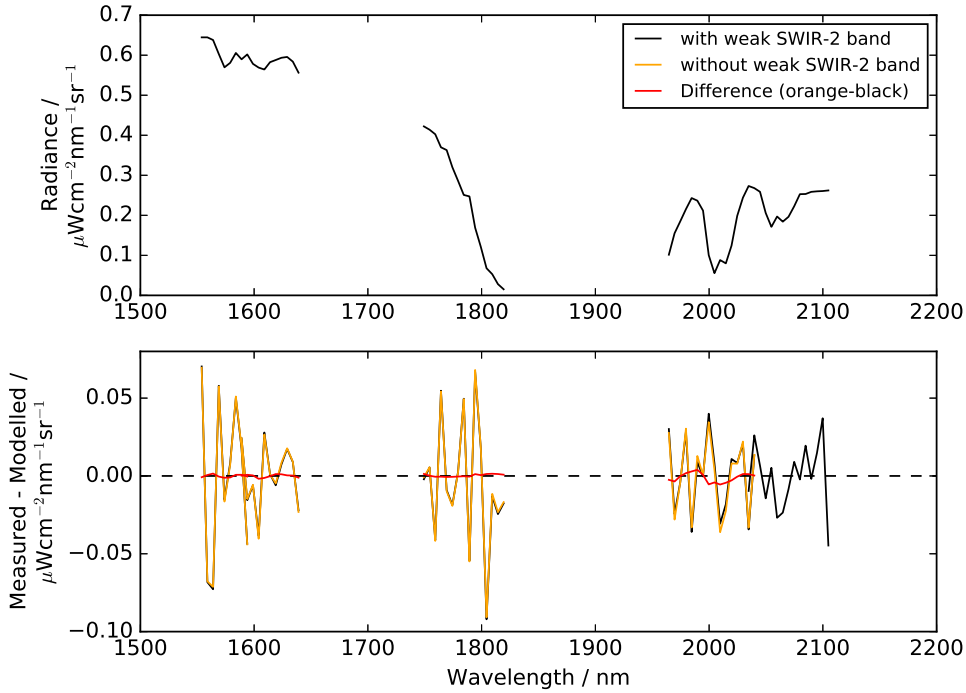

Figure 4.23: Adding the weak SWIR-2 CO_2 band to the coupled retrievals impacts averaged residuals in the other CO_2 bands. Top: An example spectrum from the test ensemble showing the spectral range used in the coupled retrievals. Bottom: averaged residuals from the retrievals in rows 5 and 6 of Table 4.3, (black and orange), i.e. the optimized configurations with and without the weak SWIR-2 CO_2 band. The red line shows the difference between these averaged residuals, which occur at the spectral locations of CO_2 absorption across the SWIR.

reflectance. Albedo correlations will be addressed in an *a posteriori* manner in chapter 4.2.5, where a bias correction is introduced.

To conclude, several retrieval configurations with favorable retrieval performance have been identified. Among these, the retrieval that coupled the SWIR-1, SWIR-2 bands and the dedicated water vapor band had enhanced overall performance (five spectral windows: $1,550 - 1,597$ nm, $1,585 - 1,639$ nm, $1,749 - 1,820$ nm, $1,961 - 2,043$ nm, $2,030 - 2,105$ nm).

O_2 Retrieval Attempts

The retrievals described above assume the geometric lightpath through the atmosphere. By retrieving the oxygen column number density from its spectral signature(s), changes in the lightpath can theoretically by detected so that a corrected dry air column mixing ratio of CO_2 can be obtained. O_2 absorption bands near 760 nm and $1,270$ nm were used in studies with the ensemble of AVIRIS-NG test spectra. In each test retrieval, oxygen as well as

collision induced absorption of oxygen (CIA, taken from Richard et al. (2012)) was adjusted together with a spectral shift parameter and a polynomial to fit the spectral baseline. In addition and only in the presence of water vapor absorption (i.e. in the $1,270$ nm window), the water column was retrieved as an interfering species. All retrievals attempted in this work provided such low accuracy and low precision that when the retrieved O_2 column number densities were used to calculate XCO_2, the standard deviation in the optimized XCO_2 field (previous section) increased at least by a factor of two in comparison to when the prior O_2 column was used. Oxygen column number density retrievals had standard deviations of at least 5 % of the total column in every set-up investigated. Since the test scenes are known to be free of haze or smoke, such large scatter in the oxygen column must be a result of inaccuracies in the retrieval.

In case of the oxygen retrievals that were tested in the spectral range $1,180-1,330$ nm, large and systematic spectral residuals were observed at $1,205$ nm and near $1,283$ nm, of which especially the latter structure interfered with oxygen absorption lines. Large spectral residuals also occurred for spectral retrieval configurations examined in the $730-790$ nm range, specifically in the off-band continuum. These spectral residuals seem the most obvious explanation for inaccurate oxygen retrievals from AVIRIS-NG measurements.

As a result of these relatively unsuccessful retrieval attempts, the following analysis will rely on oxygen columns derived from prior meteorology (not *retrieved* oxygen columns) to calculate XCO_2. While it is unfortunate, that the large spectral range of AVIRIS-NG could not be used to retrieve applicable O_2 columns simultaneously with the carbon dioxide concentration, using the prior O_2 is a well established retrieval approach (Butz et al., 2011).

4.2.4 Retrieval of Power Plant Plumes

The optimized retrieval configuration including all four CO_2 absorption bands near 1.6 and 2.0 μm was applied to two data sets that contain coal-fueled power plants in the flightline of AVIRIS-NG, namely the "Four Corners Power Plant" and the "San Juan Generating Station" (see page 43). The former is the same flightline from which the ensemble of test spectra was selected. The Four Corners Power Plant had an estimated emission rate of 8.8 $MtCO_2$ per year in 2019 (EPA, 2020). Reported emissions of the San Juan facility were 9.9 $MtCO_2$ in the year of the AVIRIS-NG measurement (EPA, 2020).

Four Corners Power Plant

Fig. 4.24 displays the retrieved XCO_2 in the vicinity of the Four Corners Power Plant as retrieved from the AVIRIS-NG measurement on June 21, 2019. The CO_2 exhaust plume is clearly visible in the retrieval and small turbulent eddies on the sub-plume scale are apparently resolved. In terms of plume morphology, XCO_2 enhancements of more than 200 ppm (i.e. total columns with $XCO_2 > 625$ ppm) can be observed for several pixels close to the stack and the plume appears rather stream-lined, which indicates a relatively high wind speed at the time of measurement. Significant correlations of the CO_2 column

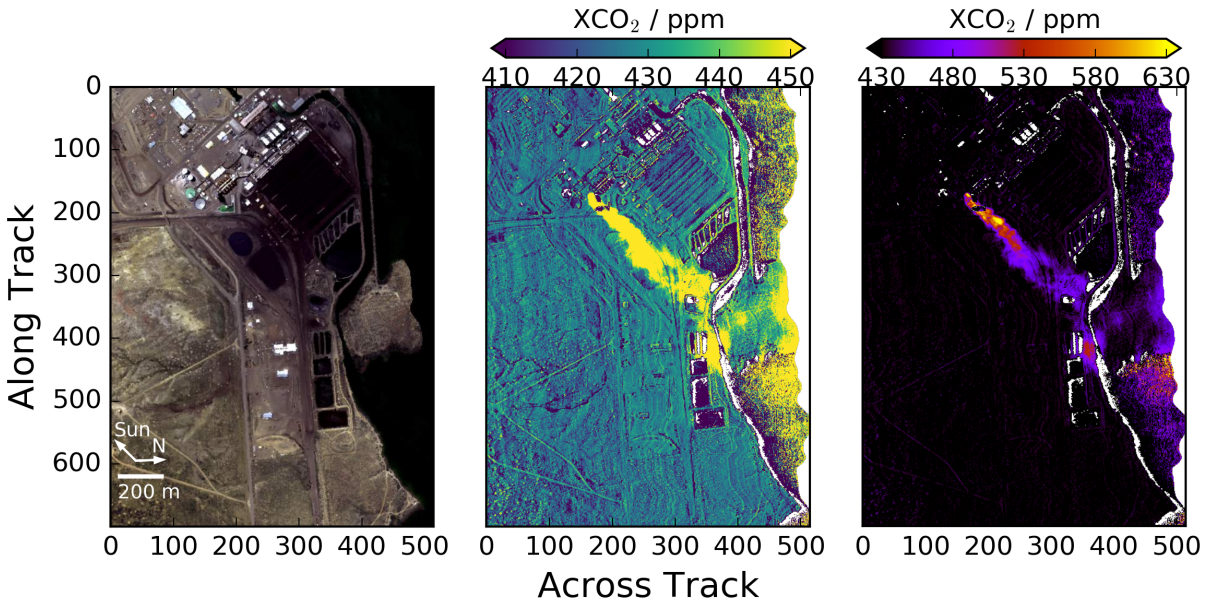

Figure 4.24: XCO_2 retrieval near the Four Corners Power Plant. Left: RGB image of the AVIRIS-NG measurement with scale and arrows indicating the solar location (Sun) and north (N) at the bottom. Center, right: XCO_2 retrieval with different color-maps illustrating two XCO_2 scales. A CO_2 plume can be observed emerging from an exhaust stack and the internal structure of the plume is resolved. White pixels indicate non-convergence of the retrieval.

to surface reflection features remain in Fig. 4.24. Notably, a number of pixels directly downwind of the point source are affected by shadow and there is a small water surface near the stack. These features result in very low XCO_2 retrievals, which are in strong contrast to the surrounding plume. Further retrieval biases correlated with the ground albedo can be observed throughout Fig. 4.24. The presence of water surfaces towards large across-track pixels leads to both non-convergence of the retrieval algorithm and large scatter in XCO_2. More subtle albedo effects are observed over land, where individual small-scale structures, e.g. roads, are reflected in small-scale XCO_2 biases. Additionally, the XCO_2 retrieval exhibits "stripes", i.e. small systematic biases between neighboring spatial pixels, which appear as faint lines, especially over homogeneous non-plume regions over land.

Fig. 4.25 illustrates other critical parameters of the retrieval near the power plant. Retrieved XH_2O displays a plume structure emanating from the power plant, which has the same shape as the XCO_2 plume but extends over a shorter spatial range. The water vapor plume is also hidden in the dark pixels near the stack. Strikingly, XH_2O values are strongly negatively biased over an oval ground area close to the plume (the surface material could not be identified, but it certainly is of a man-made nature). These spectra all exhibit increased spectral residuals that occurred in the 1.8 μm spectral window, i.e. the dedicated

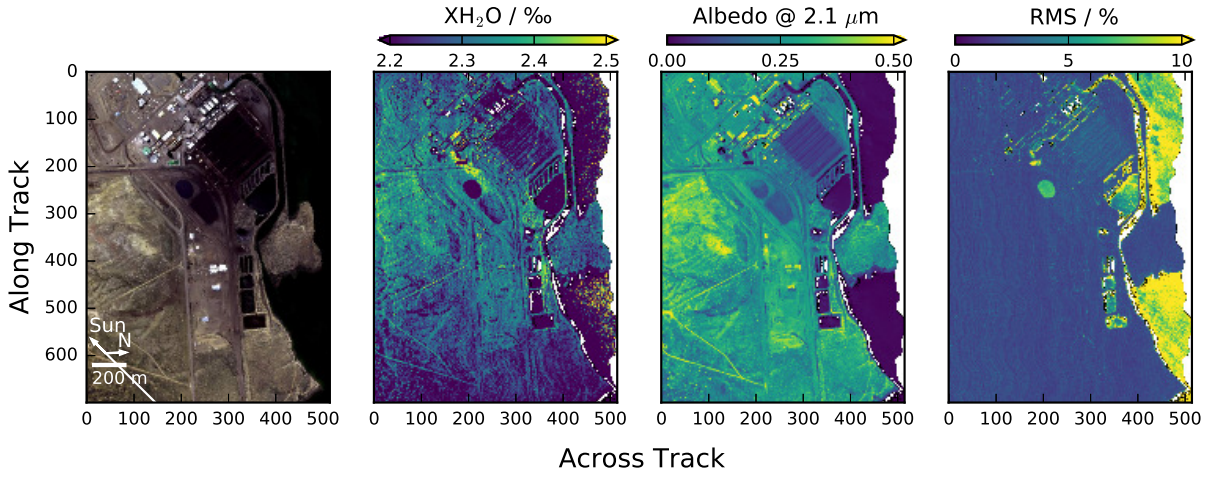

Figure 4.25: Four Corners Power Plant retrieval. Left: true color image of the AVIRIS-NG measurement with scale and arrows indicating the solar location (Sun) and north (N) at the bottom. Column two to four: retrieved XH_2O, albedo (at 2.1 μm) and spectral RMS. The exhaust plume is visible in the water vapor retrieval as well. Large RMS values for the oval surface in the top center of the flightline are caused by residuals in the 1.8 μm spectral window of the retrieval. Corresponding XH_2O values are significantly biased.

water vapor retrieval window. Such artifacts could be explained through albedo features that disturb the molecular (H_2O) absorption signal. Retrieved albedo values in the SWIR-2 exemplify that the measurement scene only contains few dark land pixels in the short wave infrared spectral range. In terms of spectral residuals, greater RMS error is generally associated with darker scenes (i.e. water surfaces). Pixel-to-pixel stripe signatures were observed both in the illustration of retrieved XH_2O and spectral residuals.

San Juan Generating Station

Retrievals conducted for the San Juan Generating Station, shown in Fig. 4.26, generally support the results of Thorpe et al. (2017) who also retrieved two separate plumes associated with two of the facility's units. The broader angular plume shape indicates slower wind speeds than the Four Corners observation (Jongaramrungruang et al., 2019). Water vapor condensate downwind of the two active stacks is visible in the true color image of the AVIRIS-NG observation. The retrieved XCO_2 field shows turbulent behavior of both plumes and retrieval biases driven by ground albedo are clearly visible. Such artifacts are most prominent for a range of brightly reflecting anthropogenic materials as well as for very dark scenes and pixels affected by shadow. What appears to be some kind of encased conveyor belt system (the bright, linear structures) lead to increased XCO_2 retrievals downwind of the stack to the right in Fig. 4.26 and the shadows that these structures cast strongly reduce XCO_2 in the present analysis. Scenes affected by shadow

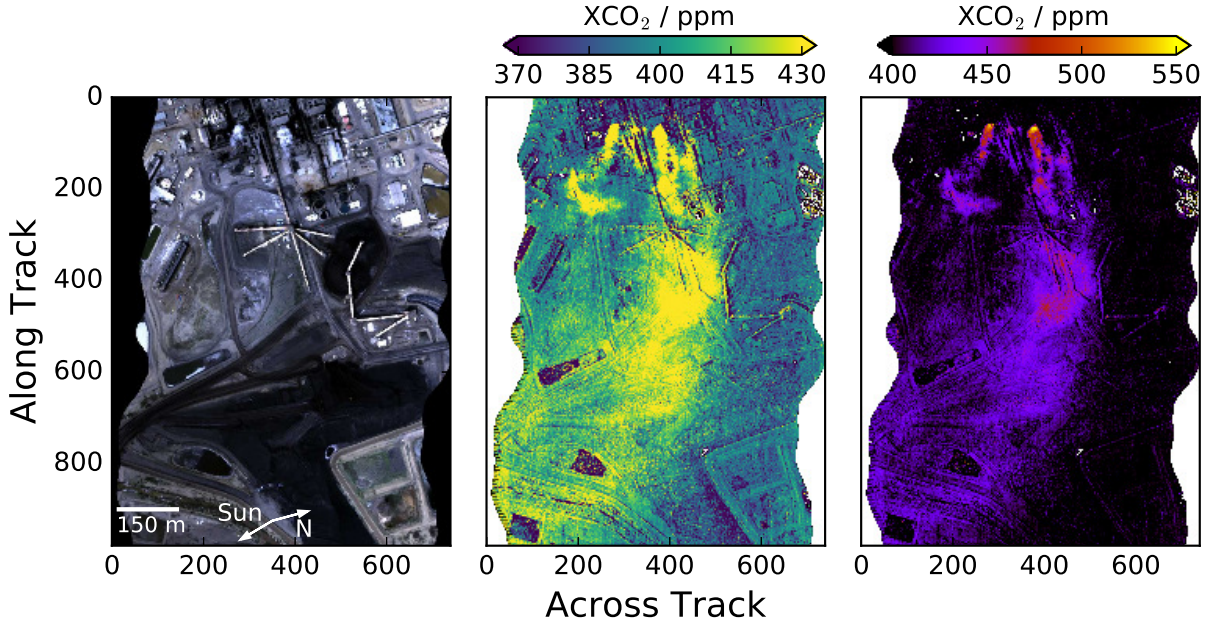

Figure 4.26: XCO_2 retrieval near the San Juan Generating Station. Left: RGB image of the AVIRIS-NG measurement, delimited to the left by the across-track dimension of the sensor's field of view (black area: no data) with scale and arrows indicating the solar location (Sun) and north (N) at the bottom. Center, right: XCO_2 retrieval with different color-maps. A CO_2 plume can be observed emerging from an exhaust stack, internal structure of the plume is resolved. White pixels indicate non-convergence in the retrieval.

exhibited radiance levels below 0.1 $\mu\mathrm{Wsr}^{-1}\mathrm{cm}^{-2}\mathrm{nm}^{-1}$ at 2,100 nm, as did the spectra collected over the surfaces that are heavily negatively biased in the retrieved XCO_2 field (e.g. near across-/along-track pixels 100/600 in Fig. 4.26, possibly water ponds).

Figure 4.27 illustrates the retrieved water vapor columns, albedo and spectral RMS error of the retrieval. Although XH_2O is increased in the water vapor condensate plumes emitted by the two stacks, no significant water vapor plume is visible further downwind of the power plant. Enhancements in XH_2O are sometimes, but not always, co-located to larger surface reflectance values. This hints at the presence of certain surface types that may interfere with the water vapor absorption signal. In general, the present scene is darker than the Four Corners Power Plant observation discussed above. As a result, spectral residuals are mostly lower in this flightline, except when bright man-made surface types are present. With the solar radiation coming from the left of the image, it may be possible that some surfaces reflect radiation in a specular fashion, introducing large RMS values specifically on the left sides of some anthropogenic structures.

The results obtained here indicate that the retrieval configuration that was derived earlier is applicable to a wide range of AVIRIS-NG observations, although caveats apply. Specifically, the retrieved CO_2 column has a pronounced correlation to the surface albedo

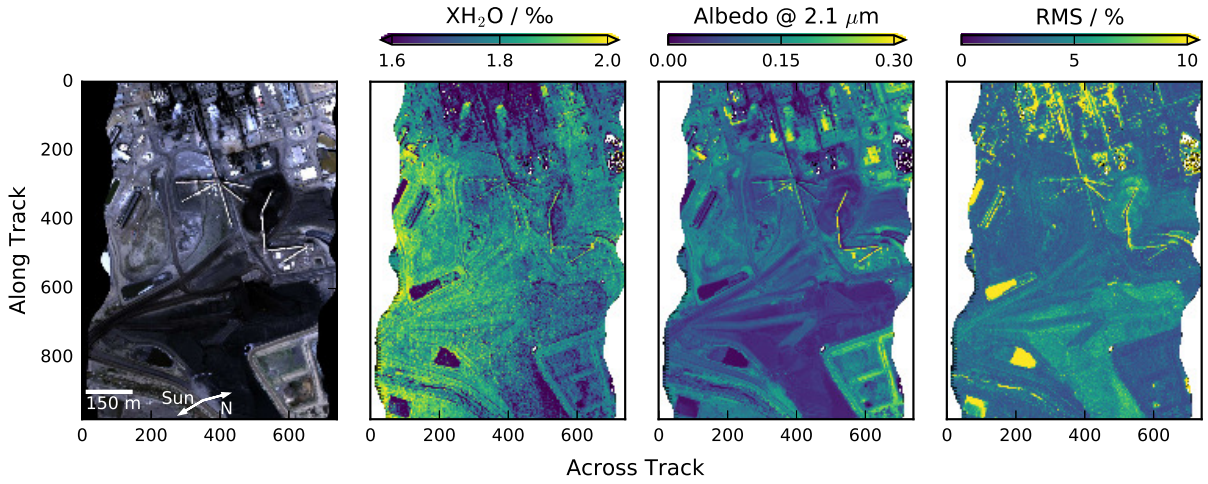

Figure 4.27: San Juan Generating Station retrieval. Left: true color image of the AVIRIS-NG measurement with scale and arrows indicating the solar location (Sun) and north (N) at the bottom. Column two to four: retrieved XH_2O, albedo (at 2.1 μm) and spectral RMS.

and low albedo pixels (water surfaces, shadows) introduce additional scatter and increased spectral residuals into the retrieval.

4.2.5 Posterior XCO_2 Correction

To improve the XCO_2 retrievals discussed above, a posterior correction was applied to the retrieved XCO_2 fields to address the strong albedo dependence of the XCO_2 retrieval. Historically, many trace gas retrievals have been corrected for spurious correlation of the trace gas column with respect to surface reflectance (Lorente et al., 2020, O'Dell et al., 2018, Wunch et al., 2011a). A linear correction with respect to albedo biases was carried out here according to eq. 4.1.

$$\mathrm{XCO_{2,corrected}} = \mathrm{XCO_{2,retrieved}} - m \cdot (\mathrm{albedo_{@2.1\mu m}} - \mathrm{mean(albedo_{@2.1\mu m})}) \,. \tag{4.1}$$

The correction term was found to be $m = 64.68 \pm 1.84$ ppm ($\pm 1\sigma$) and the average albedo at 2.1 μm was 0.238 with the retrieval results of the background test ensemble (using the SWIR-1+SWIR-2 +H_2O benchmark retrieval configuration). Fig. 4.28 illustrates the effect of the albedo bias correction on the XCO_2 results of the benchmark retrieval. In general, this linear correction significantly reduced the scatter of the retrieved XCO_2 fields as well as the correlation to surface albedo (see Table 4.4). The standard deviation of bias corrected XCO_2 values was reduced by over 2 ppm in every retrieval and correlation coefficients were reduced to R$<$ 0.1. Small changes in the mean value of XCO_2 were also observed when the bias correction was applied, which can be explained by slightly different albedo retrievals for some retrieval configurations. For instance, the average albedo at

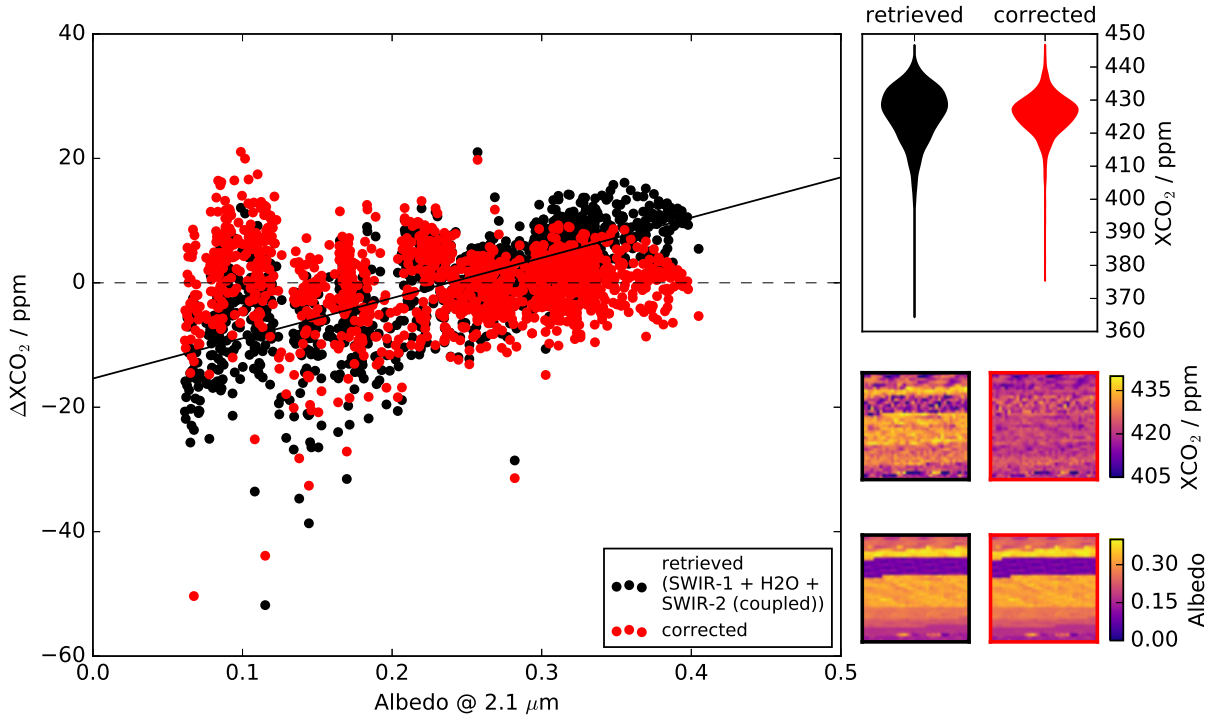

Figure 4.28: Bias Correction Derived from Test Ensemble. Left: linear correction of the retrieved XCO_2 using the test ensemble and the benchmark retrieval configuration according to eq. 4.1. Right: XCO_2 retrieval visualization for the test retrievals before and after bias correction (black and red violin plots and tiles, respectively). Albedo distribution in the test ensemble in the last row for reference.

2.0 μm was 0.244 in all retrievals that neglected the weak SWIR-2 band, i.e. greater than the average value used in eq. 4.1.

The applicability of the albedo bias correction to the Four Corners and San Juan plume data sets depends on the extrapolation of the correction towards albedo values that are not present in the test ensemble (i.e. below 0.06 and above 0.40). The analyses in previous sections have indicated that some surface types, especially those with low ground albedo, can introduce additional scatter and residuals into the XCO_2 retrieval. Figure 4.29 illustrates that local scatter in the retrieved XCO_2 field is greatly increased as the surface albedo decreases below 0.03. Since there was no access to the AVIRIS-NG noise vectors, the measurement noise could not be propagated into the retrieved CO_2 column. Hence, a local XCO_2 scatter metric was introduced to identify problematic retrieval regions. This metric ($\sigma(XCO_2)$) is the standard deviation of the local XCO_2 field with size 5×5

Retrieval Configuration	$\varnothing XCO_2$ /ppm	$\sigma(XCO_2)$ /ppm	R_{ALB}^{CO2}
SWIR-2 (strong)	425.96 (426.26)	6.16 (8.74)	0.07 (0.71)
SWIR-2 (coupled)	426.71 (426.60)	6.15 (8.75)	0.09 (0.71)
SWIR-1 + + SWIR-2 (strong)	424.82 (425.14)	6.05 (8.32)	-0.01 (0.69)
SWIR-1 + + SWIR-2 (coupled)	426.69 (426.59)	6.09 (8.46)	0.03 (0.69)
SWIR-1 + H_2O + + SWIR-2 (coupled)	425.68 (425.68)	6.04 (8.33)	0.00 (0.69)
SWIR-1 + H_2O + + SWIR-2 (strong)	423.79 (424.21)	6.02 (8.27)	-0.03 (0.69)
SWIR-2 (coupled) + + H_2O	426.54 (426.50)	6.04 (8.64)	0.08 (0.72)
SWIR-2 (strong) + + H_2O	424.39 (424.81)	6.09 (8.60)	0.04 (0.71)

Table 4.4: Performance data for the test retrievals after albedo bias correction. Table configuration as in Table 4.3. The corresponding data obtained before bias correction are given in parentheses for reference.

pixels around each spatial pixel of the power plant scenes[2]. Increases in local standard deviations point to systematic retrieval errors associated with surface albedo (if albedo can be assumed constant on these small spatial scales). Fig. 4.29 clearly shows that dark water surfaces and pixels affected by shadow (all with albedo below 0.03) dominate the local scatter statistics with regional XCO_2 standard deviations much greater than 20 ppm. At the same time, the majority of sufficiently bright spectra are located in low local standard deviation clusters, although the darker AVIRIS-NG flight scene above the San Juan generating station exhibits greater scatter in XCO_2. For a quantitative analysis of the albedo bias correction, the procedure was applied to non-plume spectra of both flight lines, selected from the lower left and lower right corners of the Four Corners and San Juan data sets, respectively. For these scenes, panels c) and g) of Fig. 4.29 resolve XCO_2 retrieval standard deviation as a function of albedo in bins of 0.03. In both cases, the per-spectrum XCO_2 retrieval scatter strongly trends towards greater values for lower albedo. In case of the Four Corners background spectra (Fig. 4.29 c)) the number of scenes

[2]The size of the field for local statistics must not be chosen too large in order to separate albedo effects from the plume structure. The present choice of 5×5 pixels (13.5×13.5 m^2) was considered reasonable, because it is mostly insensitive to the internal plume structures of both power plant data sets (except for the first downwind meters of the Four Corners facility which indicates larger in-plume XCO_2 variability for these scenes as well as a stronger contrast between plume and background).

with albedo below 0.1 is limited, as is representative for the non-water spectra of this flight. By applying the albedo correction to the retrievals, XCO_2 retrieval scatter is reduced in all albedo bins with a significant amount of scenes. It also appears that extrapolating the correction to albedo values present in the test ensemble leads to decreases in XCO_2 scatter. Additionally, Fig. 4.29 d) shows that the correction reduces the overall standard deviation from 7.5 to 6.0 ppm (similar to the result obtained in the test ensemble) for this set of spectra and that the correlation coefficient between albedo and XCO_2 is reduced as well. Some albedo correlation remains, however, this may be an artifact of the extrapolation process of the albedo correction, which should be investigated in a future study. For the San Juan power plant scene, one can observe that XCO_2 standard deviation per 0.03 albedo bin is strongly enhanced for low-albedo bins, with a scatter of 70 ppm observed in the 0-0.03 albedo bin. Such dark surfaces should therefore be excluded from all further analyses[3]. The San Juan scene generally exhibits greater local scatter as well as per-albedo-bin scatter in XCO_2, which is most likely due to the low surface reflectance across the scene (i.e. the more bright scenes are included the lower the scatter will be). However, the albedo bias correction brings down the overall standard deviation of the selected background spectra by more than 1 ppm and reduces the Pearson correlation coefficient between XCO_2 and albedo from 0.4 to 0.1. The inset in Fig. 4.29 g) shows that the per-albedo-bin difference between retrieved and corrected XCO_2 is comparable to what is found for the Four Corners scene, although some outliers exist. Even if the impact of the correction may be relatively small for this subset of spectra in albedo space, Fig. 4.29 h) demonstrates that the correction slightly improves the general retrieval performance.

It is worth noting, that when extrapolating the albedo correction towards brighter scenes than albedo=0.4 (limit in the testensemble) in the Four Corners case, it appears that there is a slight tendency of "over-correction" of the retrieved XCO_2 in bright scenes (Fig. 4.29 d)). Yet, some findings support the extrapolation of the bias correction to the albedo range between 0.03-0.8. Firstly, the low correlation coefficients between corrected XCO_2 and albedo suggest that the correction performs well. Secondly, not performing the bias correction above albedo=0.4 resulted in increased XCO_2 standard deviation and albedo correlation when compared with the full correction up to albedo=0.8. Thirdly, only 4.7% of all scenes in the Four Corners tile and only 0.1% of scenes in the San Juan tile have albedo greater than 0.4. Because these bright scenes are relatively rare in both flight lines, one can expect the improvements of the bias correction in low albedo scenes to greatly outweigh any potential degradation of the retrieval in the few bright scenes found in the regions of the XCO_2 plumes.

In summary, a linear bias correction derived with the ensemble of test spectra was shown to successfully reduce albedo correlation and XCO_2 scatter in both power plant flights analyzed in this work and thereby deliver a valuable improvement to the retrievals. The range of albedo values, for which the correction was found to be valid is $0.03<\text{albedo}<0.80$.

[3]Spectra with albedo greater than 0.8 should also be removed for downstream data products, such as the power plant emission rate estimate (see chapter 4.2.6), because such bright scenes may pose problems due to specular reflection, overexposure, non-linearity of the detector, etc.

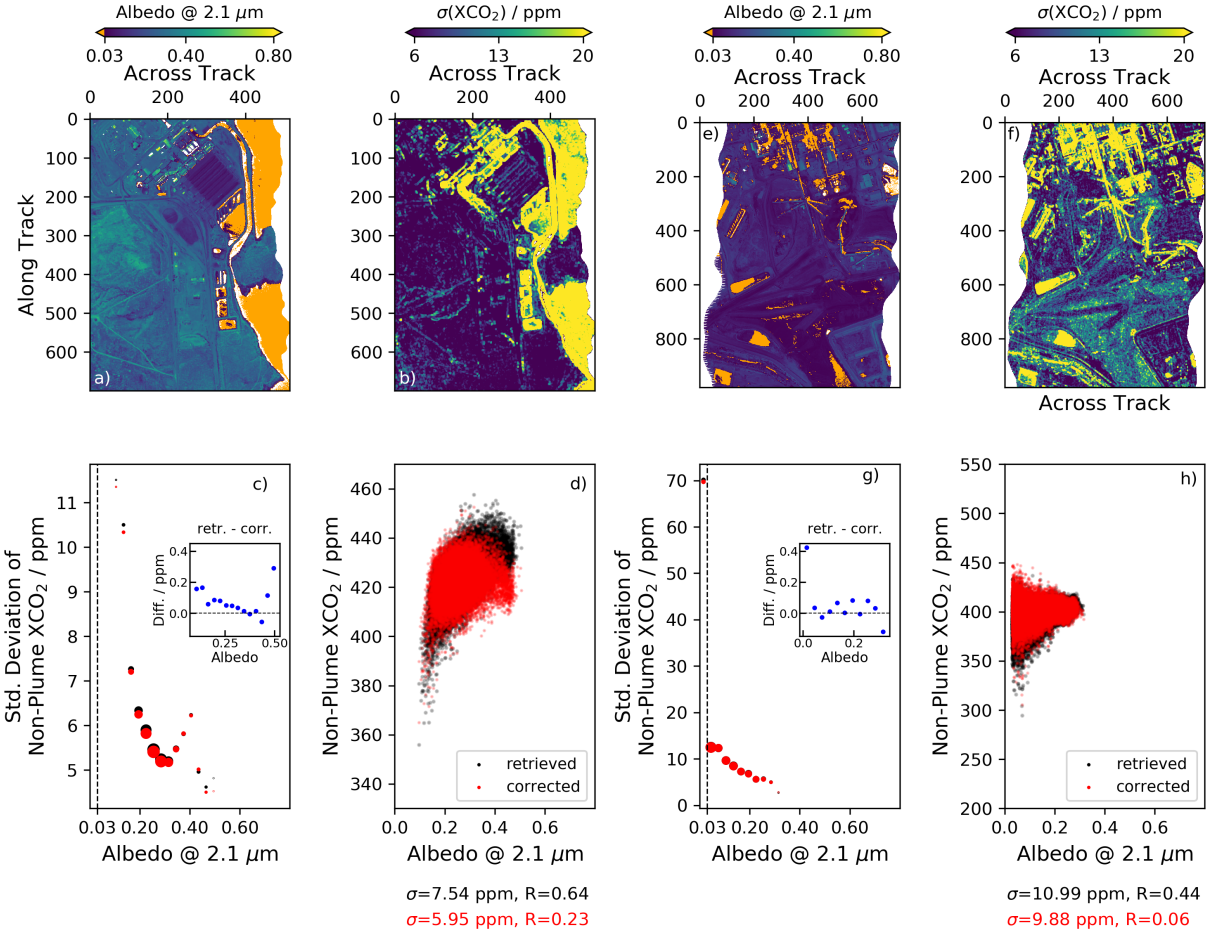

Figure 4.29: Limits and application of the bias correction method in the Four Corners (a)-d)) and San Juan (e)-h)) data sets. a) albedo distribution at 2.1 μm in the flight line, scenes with albedo below 0.03 in orange. b) local scatter of the retrieved XCO_2 field ($\sigma(XCO_2)$) over a 5×5 pixel box around each pixel. c) Standard deviation of retrieval results binned in increments of albedo (bin width=0.03) with marker size proportional to number of data per bin; inset shows the difference (blue dots) between retrieved (black) and bias corrected (red) retrievals per bin. d) Application of the linear bias correction to non-plume background scenes from the power plant flight line (same data as c)) filtered for albedo $\overset{!}{>}$ 0.03. Standard deviation, σ, and XCO_2-albedo-correlation coefficient, R, given below plot (black: retrieved, red: corrected). e)-h) same as a)-d) but for the San Juan flight. The non-plume pixels in c)-d) and g)-h) correspond to more than 45,000 spectra collected from the lower left and lower right regions of the Four Corners and San Juan flight tiles, respectively.

For further analysis, XCO_2 retrievals with surface albedo at 2.1 μm below 0.03 and above 0.8 should be removed from the data-sets. This approach is in line with the work of Ayasse

et al. (2018) and Borchardt et al. (2021) who have also filtered out the darkest AVIRIS-NG scenes for trace gas retrievals. In a future study, a bias correction could be derived from an ensemble of background spectra, which covers the entire dynamical range of surface albedo, so that more adequate corrections (possibly involving higher degree polynomials) can be applied. Alternatively, future research could explore the approach chosen by Foote et al. (2020) who correct for albedo effects in the retrieval by introducing an "albedo factor" with which they normalize the retrieved trace gas column.

4.2.6 Emission Rate Quantification

The exploration of methods enabling emission rate quantification from trace gas measurements is a very active area of research. A common struggle across the different techniques employed in the community is to obtain a reliable estimate of wind speeds, and wind profiles. Trace gas products, such as the (bias corrected) XCO_2 field in the vicinity of a source (see previous sections) must be coupled to the speed of the wind at the time of observation – either through a transport model, empirical relationships or measurements. The need for wind information is currently the greatest disadvantage in the remote sensing processing chain from spectroscopic measurements to emission rates. While in-situ measurements on board of aircrafts usually collect wind information along the flight path, remote sensing applications depend on external wind information, which often is not available for the exact location of the measurement. On the other hand, remote sensing can provide column information, while in-situ data may miss parts of the plume. Once wind information is available there are two methods that are predominantly discussed in the literature to retrieve emission rates from passive trace gas measurements: **a)** the mass balance or cross-sectional flux approach (e.g. Krings et al., 2013) and **b)** the integrated mass enhancement method (e.g. Varon et al., 2018). Other more idealized or exploratory methods have also been discussed (e.g. Bovensmann et al., 2010, Jacob et al., 2016, Jongaramrungruang et al., 2019, Nassar et al., 2017), but will not be employed here.

The cross-sectional flux method solves for the emission rate by postulating mass balance at a cross section downwind of the source. CO_2 emerging from the stack (per unit of time) must be equal to the product of wind speed, u, and the integral of plume enhancements, $\Delta\epsilon$, along an axis, y, orthogonal to the wind direction.

$$Q = \mathrm{u} \cdot C \qquad \text{with} \qquad C = \int_{-\infty}^{+\infty} \Delta\epsilon(x, y) dy \tag{4.2}$$

The integral C has units of kg/m, i.e. ppm enhancements need to be multiplied by the column airmass and the column dimension (pixel size). The mass balance method relies on a separation of plume and background scenes and has the advantage that the plume cross-section integral can be calculated several times along the plume which, by virtue of averaging, enables a more accurate estimate of Q (Klausner et al., 2020, Varon et al., 2018). This method assumes a constant wind speed and direction of the mean flow and it neglects turbulence of the plume.

The integrated mass enhancement (IME) method is based on observations of a linear correlation between source flux and the sum of all column enhancements within the remotely sensed plume (Frankenberg et al., 2016, Jongaramrungruang et al., 2019). Varon et al. (2018) argued that the IME within the entire detectable plume depends on the lifetime of trace gas molecules in the plume before they are blown out of the area that is characterized as the plume. This residence time can be calulated from the wind speed, u, divided by plume length or size, L. The emission rate of the source, Q, can be obtained through

$$Q = \frac{\mathrm{u}}{L} \cdot \mathrm{IME}, \tag{4.3}$$

where IME is calculated as the sum over the product of column mass enhancement, ϵ_i, times pixel area, A_i, for all N pixels of the plume:

$$\mathrm{IME} = \Sigma_{i=1}^{i=N} \Delta\epsilon_i \cdot A_i. \tag{4.4}$$

Mass enhancements have units kg CO_2/m^2 and they can be calculated by multiplying XCO_2 with the total column airmass. After deriving a plume mask, Varon et al. (2018) propose to use the square root of the mask area, $\sqrt{\mathrm{M_{area}}}$, as the length of the plume. The IME method has been shown to result in reliable emission estimates also in low-wind scenarios. On the other hand, this method requires a full image of the plume, which may not always be available.

Both the mass-balance and IME method are generally prone to errors under low wind speed conditions, as relative errors in wind speed translate into relative errors in the emission estimate. Before the applicability of these two methods to the AVIRIS-NG power plant data and the resulting challenges will be discussed, a plume mask for both power plant scenes will be constructed in the next section.

Construction of Plume Masks

In a first step, the scene background concentration was calculated from a histogram of the bias corrected XCO_2 distribution of the whole scene (or - in the case of the San Juan flight - from a plume-free subset of the scene) by computing the occurrence-weighted average of XCO_2 from the top 5% of histogram bins with the highest occurrence[4]. A weighted average concentration is suited to reflect potential asymmetries in XCO_2 around the mean and filtering for the most frequent XCO_2 signals ensures that the background is not calculated from pixels belonging to the plume (as the plume does not contribute to the top frequent XCO_2 values). Standard deviations of the corresponding XCO_2 retrieval results with highest occurrence are taken as the 1σ standard deviations of the background concentrations. For the Four Corners and San Juan data sets, the background concentrations were determined to be $XCO_2^{bg} = 423.3 \pm 7.5$ ppm and $XCO_2^{bg} = 398.9 \pm 12.5$ ppm, respectively. This result parallels the findings of Fig. 4.29 d) and h), where sub-samples from the Four Corners and San Juan flights had averages of 422.6 ± 6.0 ppm and 400.1 ± 9.9 ppm,

[4]The histograms span the range of retrieved XCO_2 values with bin size 0.5 ppm.

respectively. It is clear that the selection of background values is afflicted with uncertainty, the consequences of which are analyzed in a later section. However, given the large data set of spectra used here and the weighting of various XCO_2 contributions to the average calculation, the present statistics are considered robust.

To construct the plume mask, the procedure described by Varon et al. (2018) was adopted. Each spatial pixel of the scene was taken as the center of a 5×5 or 11×11 pixel square (Four Corners or San Juan, respectively) to perform a local Z-test between the local XCO_2 mean, XCO_2^{local}, with respect to the background concentration, XCO_2^{bg}, and the standard deviation of the background, σ:

$$\mathrm{Z} = \frac{\mathrm{XCO}_2^{\text{local}} - \mathrm{XCO}_2^{bg}}{2\sigma} \tag{4.5}$$

Different local square sizes were defined to reflect the difference in pixel size of the two measurements so that both local areas were on the order of 10-15 m^2. A Z-score confidence level of 95 % was used as the threshold to separate the plume from the background, as proposed by Varon et al. (2018). However, the 2σ standard deviation of the background concentration was employed in the denominator of eq. 4.5 (instead of the 1σ error as in Varon et al. (2018)). This has the effect of apparently making the Gaussian smoothing operation of the procedure of Varon et al. (2018) redundant. In fact, Gaussian smoothing with kernel sizes on the order of 2-5 pixels as suggested by Varon et al. (2018) deteriorated the mask performance, because narrow features, which clearly belonged to the plume, were removed. After the Z-test, the resulting plume mask was adjusted further with a median filter operated on the surrounding $5 \times 5/11 \times 11$ pixel square. This has the effect of smoothing the plume mask and removing false-classifications. For the San Juan scene, a simple cloud filter was applied; based on the observed radiances I in the 501.6 nm ("white"), 1,548.4 nm (SWIR-1, off-band) and 2,054.3 nm (SWIR-2, on-band) bands. Empirically, it appears that pixels with $I_{1,548}/I_{2,054} + I_{502}/1$ $\mu\mathrm{Wsr}^{-1}\mathrm{cm}^{-2}\mathrm{nm}^{-1}$ >11 match the true-color pixels which seem to contain condensate emanating from the two smoke-stacks (see also Fig. 4.33). This cloud mask should be tuned in a future study to minimize false detections of clouds minimized here by restricting the application of the cloud mask to the pixel range, where clouds are visible in the true color image.

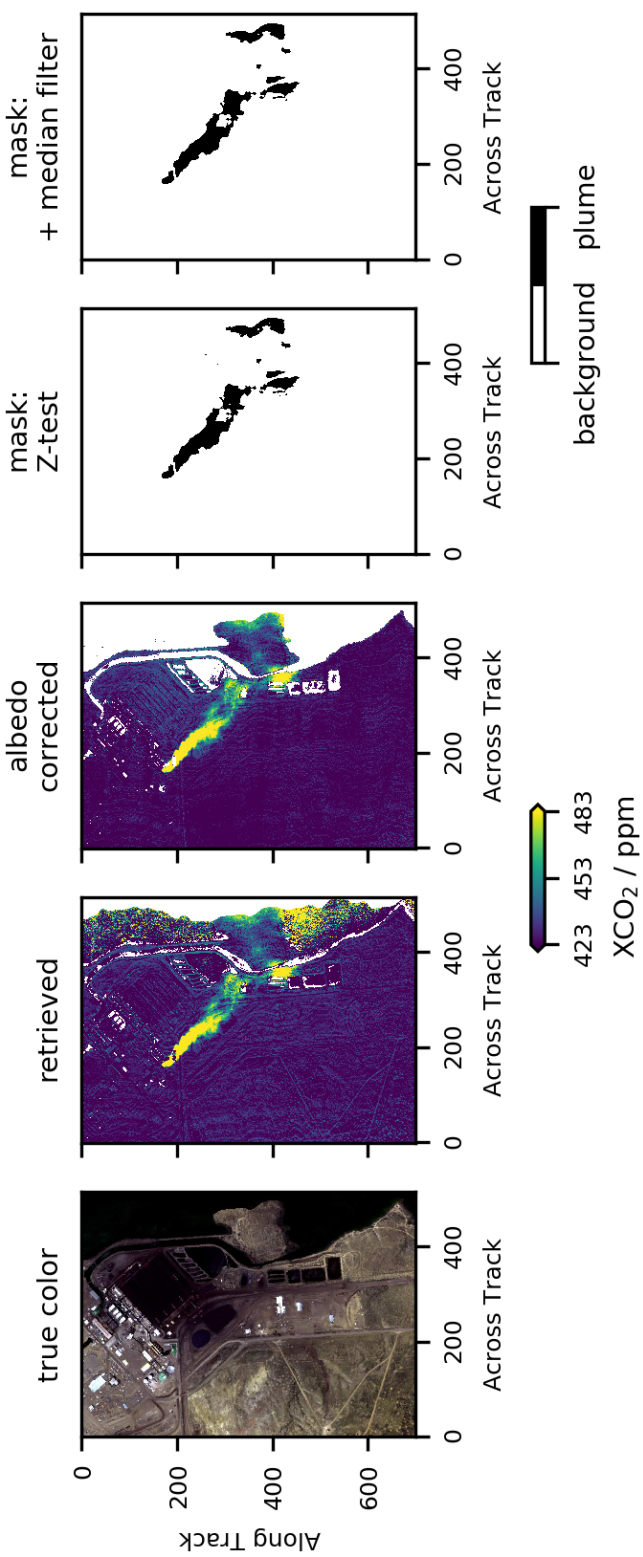

Figure 4.30: Construction of the plume mask for the Four Corners scene. The plume appears to have been cut off by the ground swath of the sensor.

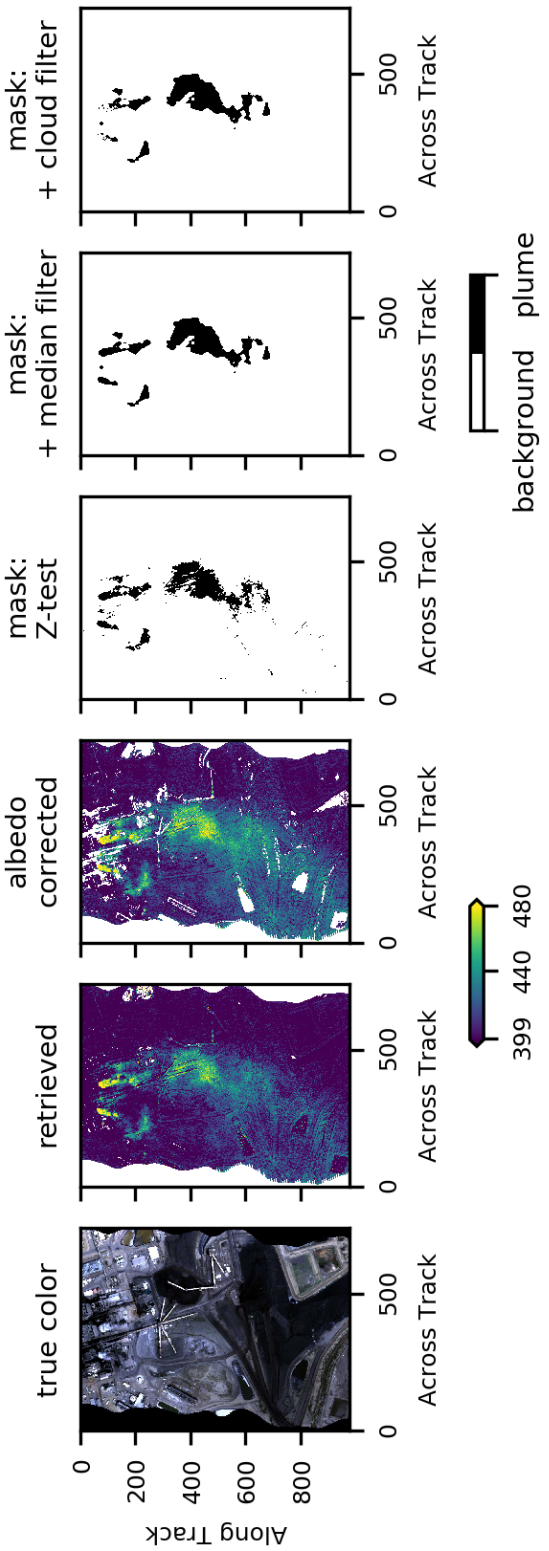

Figure 4.31: Construction of the plume mask for the San Juan scene.

The procedure to construct the masks is illustrated in Figs. 4.30 and 4.31. It appears that the plume of the Four Corners facility is cut off by the swath of AVIRIS-NG to the lower right of the scene. The San Juan flight line, conversely, seems to contain all significant enhancements emitted by the facility and the shape of the mask is similar to the observations of Thorpe et al. (2017) (Fig. 7b), although the current analysis detects additional plume enhancements farther away of the sources in along-track direction. The application of the median filter reduced the total plume mass by 0.4 % and 6.9 % in the Four Corners and San Juan data, respectively. In terms of plume dimension, the area of the plume was similarly decreased by 0.6 % (Four Corners) and 5.6 % (San Juan), indicating the median-filtering of XCO_2 is roughly proportional to the resulting loss of area (i.e. the median filter does not remove significant enhancement clusters, but rather false classifications). The cloud filter for the San Juan scene removes another 10.0 % of mass from the median-filtered plume while the plume area is only reduced by 5.7 %. As the pixels affected by condensate occur directly downwind of the two stacks, they are expected to contain large XCO_2 enhancements, so that one would expect a relatively large ratio between filtered mass and filtered area.

This section has shown that the Four Corners scene does not capture the entire plume, which is why the IME method is not suited for emission rate quantification in this case. The plume shape hints at a high wind speed and it thus seems adequate to retrieve the source rate with the mass-balance method. Conversely, the San Juan scene features two localized sources, presumably low wind speeds, the entire plume is captured by the swath of the sensor, and no large water surfaces prevent plume detection. As the two stacks seem to emit CO_2 in somewhat different directions, indicating local variability in wind direction and highly non-laminar flow, the integrated mass enhancement method was applied to this scene (because the mass balance approach requires perpendicular cross-sections of the plume, which were not readily available here).

Emission Rates

The two source rate estimation techniques applied here require the local wind speed, u, at the altitude of the stacks. Stack heights of the Four Corners and San Juan facilities have been reported previously by Weidner (2007) (Four Corners: 116 m, San Juan: 122 m). Local wind information at the respective altitudes is not available for the remote AVIRIS-NG measurements analyzed in this study. Three wind speed data sources are compared here: height-resolved ERA5 meteorological reanalysis data (Hersbach et al., 2020), 30 m reanalysis wind speeds from the North American Regional Reanalysis (NCEP, 2005) project and surface wind measurements obtained at the Four Corners Regional airport weather station, located roughly 25 km east of both power plants (data acquired from NOAA (2021)). ERA5 has a spatial resolution of 25×25 km^2, a height resolution of ~ 25 m in the lowermost levels of the troposphere, hourly temporal resolution and the two power plants are located within a 10 km radius next to a ERA5 grid point. NARR wind speeds were interpolated on its 32 km grid with a three-hourly resolution. The temporal

resolution of the local weather station is 2 hours and average wind speeds in the time of ±1 hour around the AVIRIS-NG measurements were used in this study. The terrain in the region around the power plants and the airport is a mesa landscape with no major topographic obstacles between the weather station and the power plants so that the wind conditions can be assumed to be similar at these locations. Borchardt et al. (2021) also used ERA5 and the regional airport to investigate wind speeds and noticed that ERA5 wind reanalyses had a systematic low bias with respect to the local wind measurements, which could reach differences of an order of a magnitude (Fig. A1 of their paper). Here, too, large differences between the ERA5 and weather station wind speeds were observed. The (weighted) average ERA5 wind speeds at the times of observation and at the altitude of the stacks were 0.6 and 1.2 m/s for the Four Corners and San Juan data sets, respectively, but wind speeds at the weather station are listed as 7.5 and 3.1 m/s during the Four Corners and San Juan flights, respectively. While ERA5 wind profiles indicate in both cases that the wind speed at 100-200 m was slightly lower than the surface wind, the very low values of ERA5 seem unrealistic for the two AVIRIS-NG observations of this study. The 30 m wind speeds of the NARR reanalysis are 6.1 and 4.3 m/s for the Four Corners and San Juan locations, respectively, supporting the finding that ERA5 underestimates the wind speed. While Borchardt et al. (2021) adopted the surface weather station wind speeds for their analysis of methane emissions at the surface, this work uses the 30 m wind speeds from NARR. It should be noted that a future study must address the derivation of effective 100-200 m wind speeds from surface (or 30 m) wind speed measurements or more suitable reanalysis products must be identified that contain 100-200 m winds. The large uncertainty in the wind speeds will be discussed in the next paragraphs.

Four Corners Power Plant Due to the fact that the plume of this power plant was not fully within the swath of AVIRIS-NG, the source rate was calculated with the mass-balance method. Fig. 4.32 illustrates the plume (from the median-filtering mask) rotated around its central axis, which separates the plume in two equal halves in terms of pixel enhancements. Angular and along-plume histograms of the plume enhancements are also shown in Fig. 4.32. The narrow angular distribution of the plume suggests that a high wind speed is present here (compare Fig. 9 of Jongaramrungruang et al. (2019)), although the actual angular distribution may be broader, since the plume is not fully captured in this measurement. By calculating the average cross-sectional enhancement integral for a contiguous part of the plume ($2,602.7 \pm 511.6$ ppm, see horizontal line in upper panel of Fig. 4.32) one can readily calculate the emission rate from eq. 4.2. Using a wind speed of 6.1 m/s, the estimated projected annual source rate is 16.9 $\mathrm{MtCO_2y^{-1}}$, while the emission rate reported by the U.S. Environmental Protection Agency (EPA) is 8.8 $\mathrm{MtCO_2y^{-1}}$ (EPA, 2020).

San Juan Generating Station $\mathrm{XCO_2}$ enhancements above the respective background levels, $\Delta\epsilon_i$, of the San Juan flight were used to calculate the integrated mass enhancement according to eqs. 4.3 and 4.4. The plume dimension, L, was taken to be the square root

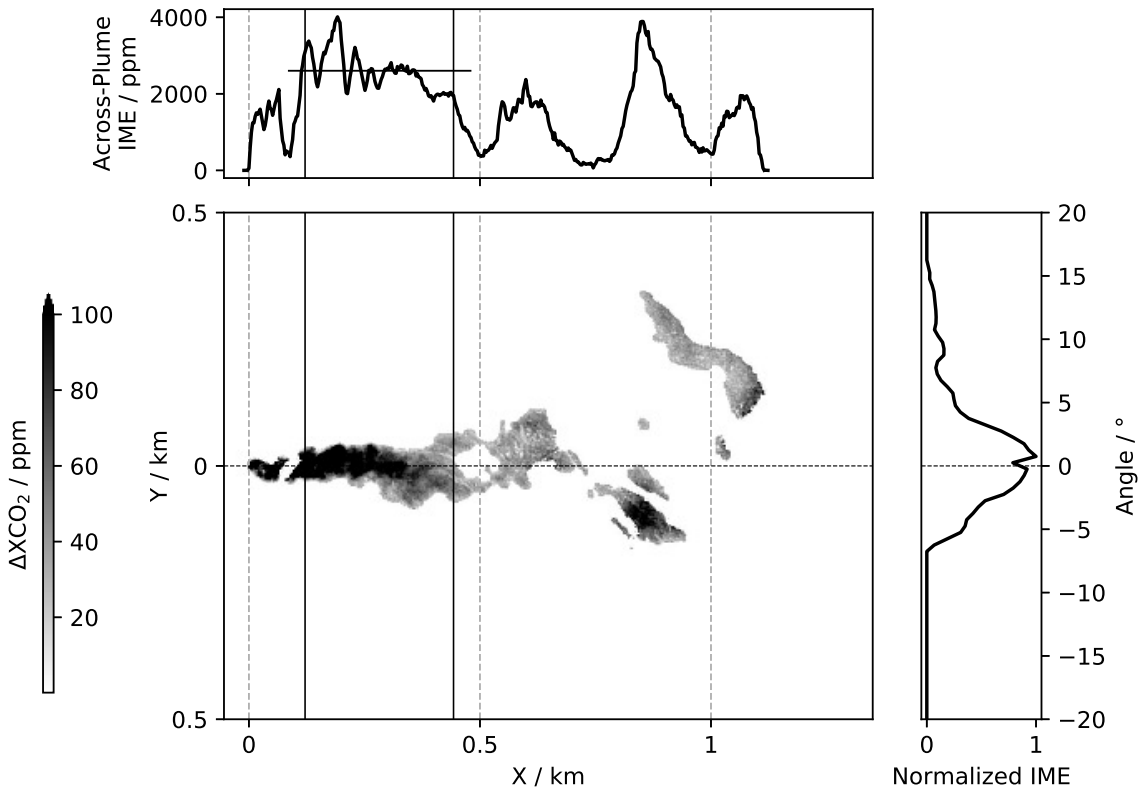

Figure 4.32: Morphology of the Four Corners plume. The image shows the plume rotated around its central axis, which divides the plume mass in half. The angular distribution of mass enhancements (IME, right panel) is created by sweeping a 0.5° slice (centered on the source) across the plume. Integrals of across-plume enhancements in the top panel visualize the effects of turbulence on the internal plume structure. Two solid lines indicate the contiguous plume section from which average across-plume integrals are derived.

of the area of the entire plume. Solution of eq. 4.3 – using the full plume masks and the interpolated NARR wind speed (4.3 m/s) – finally yields emission rates of 19.1 $\mathrm{MtCO_2y^{-1}}$ with the cloudy pixels and 17.8 $\mathrm{MtCO_2y^{-1}}$ without the cloudy pixels. As the reported EPA emission value is 9.9 $\mathrm{MtCO_2y^{-1}}$ for this facility (EPA, 2020), it may make sense to discard the cloudy pixels downwind of the stack as they may exaggerate the CO_2 enhancements through 3D radiative transfer effects. Fig. 4.33 illustrates the application of the cloud mask. To conclude, the uncertainties that affect the flux quantification will be discussed to constrain the accuracy of the present approach.

Flux Uncertainty The calculation of power plant emission rates must take into account the uncertainties of the upstream variables such as wind speed, u, the plume dimension, L, and the integrated mass enhancement of the plume, IME, or the across-plume enhancement integral, C.

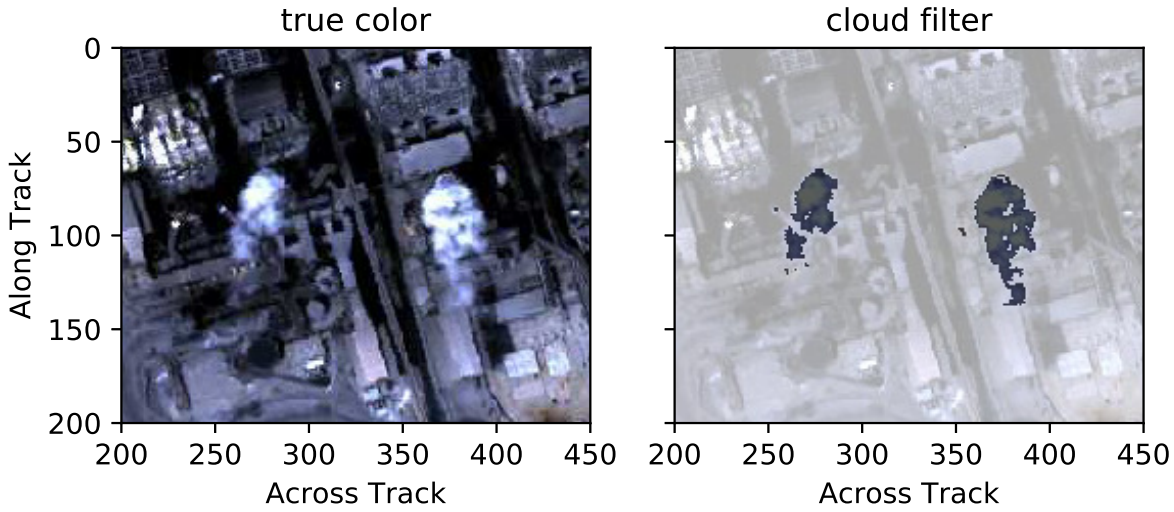

Figure 4.33: The cloud mask for the San Juan data set classifies scenes with $I_{1,548}/I_{2,054} + I_{502}/1$ μWsr^{-1}cm^{-2}nm^{-1} >11 as cloudy pixels. Left: True color image, right: cloud pixels darkened.

The previous discussion of wind speed data shows that wind information is associated with by far the largest uncertainty in these two case studies. In the Four Corners case, wind information from a meteorological reanalysis differs by roughly an order of magnitude from the data of a regional weather station; in the San Juan case, the difference in wind speed is "only" a factor of 2.6. The NARR reanalysis wind speeds that were subsequently employed for the flux inversion are in general agreement with the surface measurements and the observed shapes of the two plumes. Borchardt et al. (2021) faced a similar situation when working with ERA5 data and local wind measurements and assumed an uncertainty in wind speed of 1.5 m/s for the local wind data, which they justify with observations of typical (1σ) deviations between ERA5 surface wind speeds with weather stations. Varon et al. (2018) concluded that the error incurred on the 10 m effective wind speed from a meteorological reanalysis data base was 2 m/s for large plumes. In the present case, such an uncertainty seems an underestimation, because wind information in the NARR data set are reported at 30 m above ground, while the stacks release the CO_2 plumes at more than 100 m above ground. As a conservative approach the uncertainty that Borchardt et al. (2021) used for ground winds was doubled in this work, i.e. Δu=3 m/s. For the San Juan measurement, where the surface wind speed at the airport nearby was 4.3 m/s, this translates into a 70 % uncertainty in wind speed, whereas Δu/u=49 % for the Four Corners flight line. It seems crucial to derive techniques that will allow for an estimation of effective 100 or 200 m wind speeds in the future. The steps taken by Jongaramrungruang et al. (2019), who established a connection between plume angular width and wind speed could possibly be developed further to make wind speed estimation independent of external

information. Alternatively, flight patterns for upcoming measurement campaigns could be adapted to contain double fly-overs of the target to establish the wind speed from two subsequent measurements of the plume.

The uncertainties of the CO_2 enhancement sums (integral C in the mass balance approach and the normalized integrated mass enhancement of the IME technique) were determined by varying the background concentration, the Z-score confidence level of the plume classification scheme and the size of the smoothing kernel of the median filter plume mask within reasonable bounds (see Table 4.5). All of the variations applied here result in plume masks that closely resemble the shape of the masks discussed above (i.e. only reasonably small variations are applied, which leave the plume intact). This sensitivity study shows that the Four Corners plume is rather insensitive to small changes in the kernel of the median filter, which can be expected for such a streamlined plume with large enhancements. An erroneous overestimation of the background concentration could induce errors in C on the scale of 9 % for the Four Corners data, while the uncertainty in C from the Z-score confidence level is below 3 %. The value of IME/L of the San Juan plume, which is generally broader and exhibits many low-enhancement pixels, changes by 21 % if background XCO_2 is underestimated by 1 %. The San Juan observation is also more sensitive to changes in the confidence threshold of the mask, for which the test indicates an uncertainty of 24 % at most. Small variations in the median-mask kernel shape have a negligible influence on the total integrated mass of the plume.

Plume mask configuration	C / kg/m	IME/L / kg/m
Benchmark	**90.5**	**131.4**
XCO_2^{bg} +1 %	82.6	104.4
XCO_2^{bg} -1 %	95.5	149.2
Z-score level: 92 %	91.9	150.3
Z-score level: 98 %	87.7	100.0
Median-Filter Kernel = 7×7	90.4	
Median-Filter Kernel = 3×3	90.5	
Median-Filter Kernel = 15×15		130.8
Median-Filter Kernel = 11×11		132.1

Table 4.5: Impact of changes in plume mask variables on C and IME/L for the Four Corners and San Juan data sets, respectively. Benchmark denotes the result obtained with the plume mask as described in the previous sections and without the cloudy pixels in the case of the San Juan facility. Changes in background XCO_2 (XCO_2^{bg}) as well as variations in the confidence level of the Z-test of the plume mask (benchmark: 95 %) and variations in the dimension of the median filter smoothing kernel are investigated.

By adding the above errors in quadrature and propagating the errors of C and IME/L ($\Delta C/C = 0.11$, Δ (IME/L)/(IME/L)=0.37) into the source rate along with the wind speed

errors, one obtains emission rates of 17.4±8.8 $MtCO_2y^{-1}$ and 17.8±14.1 $MtCO_2y^{-1}$ for the Four Corners and San Juan scenes, respectively.

It is clear that the above discussion of flux uncertainties is only a starting point for future inverse studies of power plant emission strengths. While not all errors could be addressed here in their entirety (e.g. errors induced by XCO_2 "stripes" of individual detector pixels) and rather conservative uncertainty budgets have been chosen, it is clear that no reliable emission rate calculations can be performed without a good knowledge of the local wind speed.

The fact that the presented emission estimates differ from the EPA inventory by several $MtCO_2y^{-1}$ in both cases is not unusual, given that no information about seasonal changes in the activity of the two power plants is available here.

4.3 Air-Borne specMACS Observation of a Small Power Plant

This chapter summarizes the challenges encountered when retrieving XCO_2 from specMACS spectra while trying to resolve the XCO_2 plume of a small power plant. In contrast to the AVIRIS-NG sensor, specMACS has an even coarser spectral resolution (FWHM>7 nm; recall Fig. 3.2) and the instrument, which is targeted at cloud properties, has not been used for trace gas monitoring purposes before.

The specMACS measurement scene analyzed here is located near the town of Andernach in the western part of Germany, and it includes a small power and heat generating station with a source rate of about 0.18 $MtCO_2y^{-1}$ (EPRTR, 2021). At such low emission rates and given the spatial resolution of specMACS, CO_2 total column enhancements caused by the power plant are expected to be on the order of 1 ppm in a Gaussian plume model. Turbulence may create higher enhancements in confined areas, but nonetheless this facility is not expected to create a plume with enhancements of an order of magnitude greater than the retrieval noise (as in the two AVIRIS-NG cases in chapter 4.2). Previous chapters of this thesis have shown that decreased spectral resolution leads to decreased accuracy in XCO_2 retrievals and thus it would be a surprise if the present specMACS scene would actually resolve the plume of the small, local source. Yet, regardless of a plume detection, the present chapter will provide some insights into the performance of CO_2 retrievals at specMACS resolving powers below $\lambda/\text{FWHM} < 300$.

Fig. 4.34 gives an overview of the measurement scene around the power plant south of Andernach with an illustration of some exemplary specMACS spectra. Even for closely neighboring pixels, variations in the spectral shape of CO_2 absorption bands in the SWIR spectral range are observable. These variations manifest themselves both in the slope of the underlying spectral continuum as well as in the shape of the bands themselves. Two possible explanations for this observation seem likely. First, recall that the FWHM of specMACS varies across the spatial and the spectral dimensions of the sensor with changes on orders of roughly 1 nm every 50 spatial pixels and even greater variability along the spectral axis (see Fig. 3.2). These variations may induce visible differences even in spatial pixels that are relatively close to each other – a phenomenon which underscores the importance of an accurate ISRF characterization (and which may explain why AVIRIS-NG spectra appeared more homogeneous in shape for closely neighboring spatial pixels). Second, since the ground pixel size during this flight was on the order of $\sim 22 \times 46$ m^2 in this observation, it is possible that a non-negligible number of detector pixels suffer from inhomogeneous illumination due to the presence of mixed surfaces within each pixel, which may drive (small, but uncharacterized) changes in the instrumental spectral response function of the sensor (compare e.g. Hummel et al. (2021)). Note that the aircraft ground track has not been ortho-corrected for these measurements, so that each across-track column in Fig. 4.34 corresponds to one spatial focal plane array element.

A range of CO_2 retrieval configurations was tested that included retrievals from either

or both SWIR spectral regions (i.e. near 1.6 μm and/or 2.0 μm), but also retrievals from the oxygen band near 1.3 μm to constrain the airmass of the atmospheric column. These retrieval configurations differed mainly in the selection of (coupled/uncoupled) spectral windows and the parameterization of the surface albedo (through a polynomial of variable degree). Given the low source rate of the local CO_2 point source, it is not surprising that no retrieval set-up could be identified with which the CO_2 plume from the power station could be resolved in the specMACS imagery.

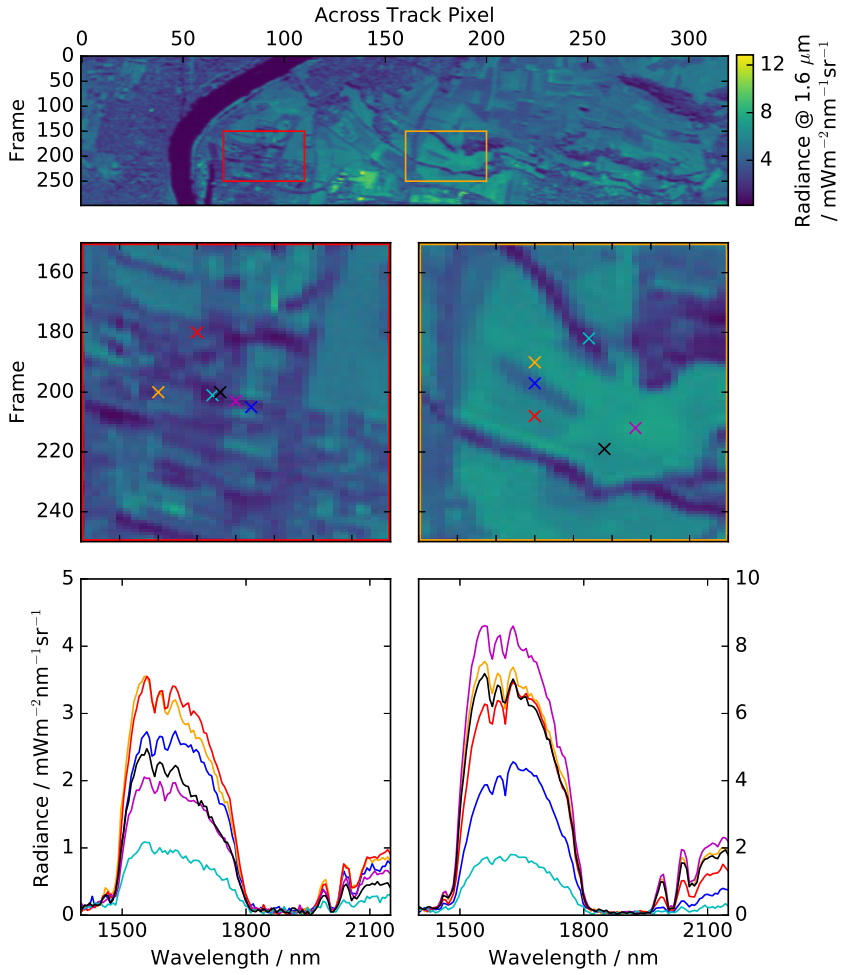

Figure 4.34: Overview of the flight scene south of Andernach, Germany, with the Rhine river visible as a dark structure between across-track pixels 50-100 (top). Zoom into areas containing an industrial area (red box) and nearby agricultural fields (orange box) (middle row). Example spectra in the SWIR spectral range (bottom), color coded to the selected pixels ('x') in the respective panels above.

However, the retrieval study with specMACS measurements revealed some more general properties of the sensor's CO_2 measurement abilities in the SWIR spectral range. To this end, only one spectral retrieval set-up is discussed here, which has been found to reduce

residuals, and provide high convergence rates. This configuration uses the spectral windows $1,538-1,639$ nm in the SWIR-1 coupled with the $1,961-2137$ nm band in the SWIR-2, as well as baseline parameterizations with third and second degree polynomials in the SWIR-1 and SWIR-2, respectively. The fit adjusts a spectral shift parameter in each spectral window. In the oxygen band between $1,181-1,333$ nm, the background was adjusted through a line fit and O_2-O_2 CIA was taken into account according to Tran and Hartmann (2008).

In contrast to AVIRIS-NG retrievals, convergence of the RemoTeC retrieval with specMACS spectra was strongly reduced when the individual CO_2 absorption bands were dealt with in individual fitting windows. Spectral residuals were significantly reduced when relatively large spectral windows were selected; specifically in the SWIR-1 range (e.g. a shorter spectral retrieval window between $1,538-1,626$ nm produced large residuals). Fig. 4.35 illustrates the average spectral fitting quality of more than $30,000$ spectra that converged in the specMACS scene near Andernach (selected from the upper 100 frames of the scene). It is striking that large systematic spectral residuals remain especially in the two CO_2 spectral ranges, where the average deviation between model and measurement seems greatest in between the two CO_2 bands. These residuals could not be reduced by changing the spectroscopic database, or by changing the configuration of the retrieval state vector (i.e. introducing an intensity offset, coupling or decoupling H_2O or CO_2, changing the degree of the polynomial to fit the spectral baseline). In contrast, residuals in the O_2 band are rather low, except for the short wave end of the retrieval window.

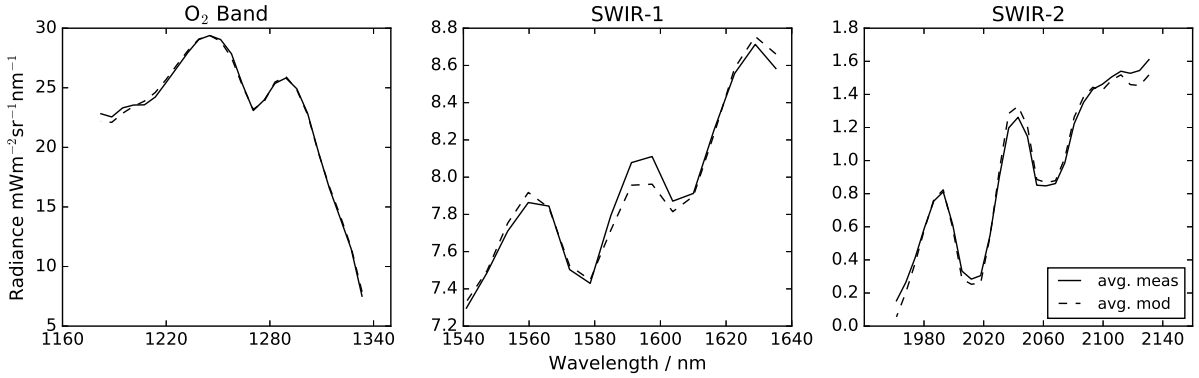

Figure 4.35: Averaged spectra (measured: solid line, modeled: dashed line) of specMACS retrievals in the SWIR spectral range covering the oxygen absorption band near 1.3 μm and the CO_2 bands near 1.6 and 2.0 μm.

To evaluate the XCO_2 retrieval performance, consider Fig. 4.36, which displays the retrieved XCO_2 field (total columns and column enhancements) along with the local scatter of the retrieval and the correlation of XCO_2 with albedo.

The overall standard deviation of retrieved XCO_2 in the specMACS scene is 39 ppm with an average XCO_2 of 358 ppm. As a result of this large scatter in the retrieval,

no plume could be detected in the scene. Note that XCO_2 retrieval scatter increases to over 60 ppm when retrieving XCO_2 from only one of the SWIR spectral ranges. Large standard deviations of ~ 20 % were also observed in the oxygen column retrieval from the 1.3 μm band (not shown here). As such, the present O_2 column retrievals are not suited to improve the XCO_2 retrieval by removing errors due to light scattering from the retrieved column as they would introduce even more variability into the retrieval – consequently, all subsequent XCO_2 values discussed here were calculated using airmass values derived from meteorological reanalyses.

There is a strong bias of the retrieved CO_2 column that is observed along the spatial detector axis (see Fig. 4.36 c)). The dependence of this bias on the spatial dimension of the sensor hints at an instrumental artifact that propagates into the XCO_2 retrieval. Several effects should be regarded possible causes of this effect. On the one hand, these biases could be caused by insufficiencies in the calibration of the SWIR sensor of specMACS. It is possible that the radiometric calibration obtained in the lab does not match the performance of the sensor in flight. The same could be true for the spectral calibration and the Gaussian approximation of the SRF may also introduce errors. To some degree, such spectral calibration issues could also cause the large residuals observed in Fig. 4.35. On the other hand, such effects could be partly driven by non-Lambertian reflectance at the ground (recall that there were hints of specular reflection induced retrieval issues in the previous analysis of AVIRIS-NG spectra) or an unknown dependence of the measured signal on the polarization state of the incident radiation. In future retrievals with detectable plumes, such biases could be removed by calculating the median XCO_2 concentration of each across-track detector element in a background observation and correcting the retrieval with these values. Similar "destriping" efforts have been explored, for example, by Borsdorff et al. (2019). It would also be desirable to obtain an in-flight characterization of the sensor or to renew the characterization that was carried out by Ewald et al. (2016) to check for changes in the sensor's calibration. Retrieval performance would surely increase were these issues corrected in some way.

Retrieving XCO_2 from either the SWIR-1 or the SWIR-2 bands alone resulted in standard deviations of 61 ppm in the SWIR-1 and 163 ppm in the SWIR-2. This shows that although the spectral resolution of specMACS is lower in the shortwave CO_2 bands than in the 2 μm range, the higher signal levels of the SWIR-1 apparently provide added value to the retrieval which out-competes the lower spectral resolution. Yet, coupling all CO_2 bands resulted in the lowest XCO_2 retrieval standard deviation ($\sigma = 39$ ppm), which mirrors the findings of the previous chapter. Further, as also observed in the previous chapters, a spurious dependence of XCO_2 with respect to the surface albedo remains visible in Fig. 4.36 b) and d). Although the XCO_2-albedo correlation coefficient is merely 0.18 across the scene, the pixels with lowest radiances also introduce the largest local standard deviation into XCO_2 and greater surface reflectance is associated with higher retrieval accuracy. Local retrieval standard deviation is defined as the standard deviation of a 5×5 pixel box around each spatial pixel in the scene, used here in lieu of proper retrieval errors, which would require full specMACS noise vectors that were not available in this study. This local

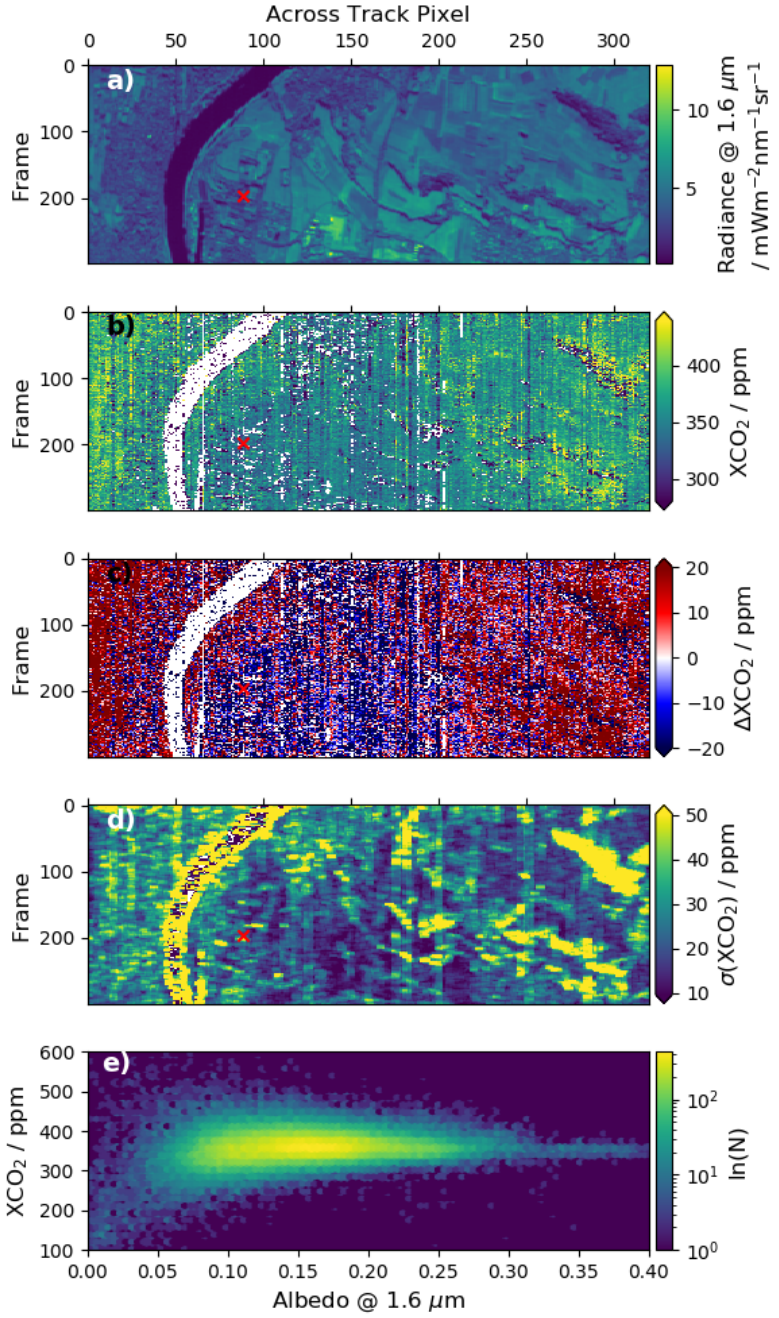

Figure 4.36: Overview of the specMACS retrieval with CO_2 coupled between the SWIR bands near Andernach, Germany. The red cross in a)-d) indicates the location of the power plant. a) Measured radiances at 1.6 μm. b) XCO_2 retrieval. c) Deviations of XCO_2 from the mean value (358 ppm). d) Local scatter metric calculated from the standard deviation in XCO_2 over the 5×5 pixels around each scene. e) XCO_2 versus albedo at 1.6 μm (note logarithmic color-scale).

scatter is greater over darker surfaces than over brighter ones, which is in line with the observation of the previous chapter.

While the plume of the facility in the present data set could not be resolved, it seems that large XCO_2 enhancements should principally be observable with specMACS, although this work cannot provide proof of this statement due to the lack of a sufficiently strong source within the archived specMACS data set. Therefore, the current work can only be regarded as a starting point for a future CO_2 retrieval study with specMACS, where the presented spectral set-up might serve as a first attempt to resolve the plume of a future measurement. Special care must be taken in the interpretation of retrievals over surfaces with low albedo, because it appears that these introduce systematic scatter and bias into the retrievals. Furthermore, the present study indicates that a re-calibration of the sensor may be beneficial in order to remove potential instrument artifacts that may arise from errors in the spectral or radiometric characterization of specMACS.

Chapter 5

Conclusions and Outlook

In this thesis XCO_2 retrievals were conducted across three orders of magnitude in spectral resolution space with the goal of enabling CO_2 emission monitoring techniques. A central conclusion from the three case studies presented in chapter 4 is that a spectral resolution of $\Delta\lambda$ =1.3 nm in the SWIR spectral range is the most promising spectral resolution for CO_2 emission monitoring purposes.

Finer spectral resolution (e.g. native GOSAT) may bring about moderate enhancements in XCO_2 retrieval performance, but at the cost of greatly increased spatial ground resolution, which in turn would prohibit the detection of emission signals from small facilities with emission rates below 10 $MtCO_2y^{-1}$.

Coarser spectral resolution (e.g. AVIRIS-NG, specMACS) can serve to qualitatively resolve emission plumes in higher spatial detail, but the mixing of information on CO_2 absorption (and H_2O absorption) and albedo features in the retrieval becomes a decisive factor against such sensors. Despite many attempts to separate molecular absorption signals and ground reflectance signals in the retrievals, no decoupling of albedo and XCO_2 was possible due to the low spectral resolution ($\Delta\lambda \sim 5$ nm for AVIRIS-NG and $\Delta\lambda \sim 10$ nm for specMACS) . Retrievals at such coarse spectral resolutions therefore require the application of posterior bias correction methods and they are also afflicted with significantly greater retrieval uncertainty than XCO_2 retrievals at $\Delta\lambda = 1.3$ nm.

A number of specific results from the present work are discussed in this chapter and the three XCO_2 retrieval case studies, namely chapters 4.1 to 4.3 are reflected upon.

Chapter 4.1 addresses the performance of a hypothetical satellite spectrometer at moderate spectral resolution ($\Delta\lambda \sim 1$ nm) in either the SWIR-1 (near 1.6 μm) or the SWIR-2 band (near 2.0 μm) with regard to XCO_2 retrievals from solar backscatter measurements. Retrievals of spectrally degraded GOSAT measurements were compared, without the addition of extra noise, with native GOSAT retrievals and the ground-based reference network TCCON. Retrieval performance was also discussed across a range of resolving powers that approximately bridges the gap between the AVIRIS-NG and CarbonSat instrument concepts, namely resolving powers between 8,100 and 760 for the SWIR-1 and between 6,500

and 700 for the SWIR-2.

Chapter 4.2 derives CO_2 emission rates from two AVIRIS-NG measurements of power plants by carrying out a retrieval study with an ensemble of the $\Delta\lambda \sim 5$ nm spectra of AVIRIS-NG selected from a background region and selected from different surface kinds. Favorable retrieval configurations were identified and the retrievals were subsequently corrected for albedo bias. Plume masks were created and flux rates were calculated from the mass balance and integrated mass enhancement methods as appropriate for different measurement scenarios.

In chapter 4.3 XCO_2 enhancements from air-borne specMACS measurements near a small power plant were retrieved. Retrieval performance in the SWIR-1 and SWIR-2 spectral ranges was discussed and challenges that induce large scatter in the retrieved XCO_2 field thereby masking the plume in this measurement were identified.

Loss of information content in the retrieval caused by the reduction of spectral resolution

It has been shown throughout chapter 4 that the information content of the retrieval parameters describing absorption and scattering processes in the atmosphere is gradually lost as spectral resolution is degraded.

In the first case study of this thesis, ch. 4.1, some sensitivity of SWIR-2 spectra at degraded spectral resolutions was observed with respect to three parameters that characterize light scattering through effective parameters (size, height, and amount of aerosol particles). However, the information content of this particle retrieval was limited to 0.38 degrees-of-freedom for the three parameters on average. The analysis indicates that, nonetheless, such a highly constrained aerosol fit significantly improves retrieval accuracy and precision when compared to a non-scattering XCO_2 retrieval in the SWIR-2. In case of the SWIR-1 spectral range, even lower average DFS for a particle retrieval was observed so that the target SWIR-1 retrieval set-up neglects lightpath modifications due to scattering events. As resolving power was decreased the XCO_2 retrieval scatter around TCCON was moderately enhanced. Below a resolving power of 1,000 a steep deterioration of retrieval performance was observed in the SWIR-2. Target resolving powers of 1,200 and 1,600 were identified in the SWIR-1 and SWIR-2, respectively, which were used as standard retrieval configurations throughout further analyses. At these resolving powers, scatter around TCCON measured 3.00 ppm (SWIR-1) and 3.28 ppm (SWIR-2), whereas the scatter of native GOSAT retrievals amounted to 2.43 ppm. The proposed SWIR configurations can be mapped onto a 256-spectral-pixel detector at a sampling ration of three per FWHM. Additional retrieval metrics in the TCCON comparison indicate that the degraded spectral resolution retrievals did not show significantly worse performance than the native GOSAT retrievals (i.e. bias or correlations with the aerosol parameters were mostly small). Global scale native GOSAT retrievals were used to evaluate the low-resolution SWIR runs, where differences in the range of 2 to 3 ppm were found, which, in case of the SWIR-1, evidently occured over desert areas. As opposed to the TCCON assessment the departures from na-

tive GOSAT for the two SWIR set-ups also exhibited correlations with the effective aerosol parameters (R frequently in the range 0.2-0.3 and up to 0.5). Given that native GOSAT retrievals fare better at capturing the truth the performance of both SWIR retrievals is expected to deteriorate in the presence of aerosols, which may induce regionally correlated errors.

By degrading spectral resolution from $\Delta\lambda \sim 0.1$ nm to $\Delta\lambda \sim 1$ nm in the first case study, individual CO_2 absorption lines were found to blend into a homogeneous band structure which apparently removes a large portion of the available information on atmospheric aerosol. When $\Delta\lambda$ is further increased to 5 nm as studied with the AVIRIS-NG sensor in ch. 4.2, it seems that the accuracy of XCO_2 retrievals deteriorates further. It has been demonstrated in this work that trace gas retrievals at such low resolving powers profit from including many spectral signatures into the retrieval windows. Specifically, the addition of a dedicated water vapor retrieval window near the opaque H_2O band at 1.9 μm reduced the scatter in the retrieved XH_2O field from 0.19‰(SWIR-2) to below 0.1‰ and simultaneously reduced albedo correlation. The scatter of background XCO_2 retrievals in the two AVIRIS-NG scenes had a variability of 7.5 ppm and 12.5 ppm for the relatively bright Four Corners and the darker San Juan scenes, respectively. This indicates that overall XCO_2 retrieval scatter is greater than in the previous study with the degraded GOSAT spectra at $\Delta\lambda \sim 1$ nm. In addition to increased XCO_2 scatter large correlations exist between trace gas columns and retrieved albedo values (correlation coefficients above 0.90 for XH_2O and above 0.60 for XCO_2). In fact the standard deviation of the retrieved XCO_2 can be regarded a function of surface albedo, where low albedo increases the retrieval scatter while bright scenes exhibit less scatter. For this reason the darkest scenes where the 2.1 μm albedo is below 0.03 must be excluded from all further analyses. The XCO_2 of the remaining scenes can be largely detrended from the surface albedo by means of a linear bias correction that was derived from the ensemble of test spectra. A linear correction was shown to reduce standard deviation in background XCO_2 retrievals by more than one ppm and to reduce albedo correlation coefficients from R=0.6 to R=0.2 (Four Corners data set) and from R=0.4 to R=0.1 (San Juan data set), so that correlated retrieval errors are weakened.

From the vantage point of XCO_2 retrievals there is a strong indication that the loss of spectral information to the levels of $\lambda/\Delta\lambda < 2,000$ (as proposed for the hypothetical 50×50 m^2 sensor in ch. 4.1 and as for AVIRIS-NG and specMACS) comes at the cost of losing the ability to resolve natural processes of the carbon cycle on a global scale with such instruments. Local scale retrieval accuracy may be sufficient to discriminate a plume from the background and quantify XCO_2 enhancements, but as these coarse-spectral-resolution measurements are not suited for a retrieval of particle scattering parameters, they will induce (albedo- and aerosol-related) biases between scenes captured around the globe. In terms of improving the assessment of the atmospheric lightpath by means of oxygen retrievals, large scatter was observed in O_2 retrievals carried out at coarse-spectral resolution with the AVIRIS-NG and specMACS sensors (both of which measure the 1.27 μm O_2 band). The specMACS XCO_2 retrievals appeared to be strongly biased along the spatial

axis of the detector of the instrument, which may hint at an instrument induced artifact in the retrieval. This underscores the importance of sensor characterization, which is key to a successful plume retrieval.

Spectral window selection: Optically thick absorption features and transparent regions enhance retrieval performance

Traditional CO_2 retrievals (e.g. native GOSAT) employ the "three-band" spectral set-up consisting of the O_2 A-band and the longwave SWIR-1 and SWIR-2 CO_2 bands. This thesis proposes spectral windows for CO_2 retrievals at coarse spectral resolutions.

The target retrieval configurations, SWIR-1 and SWIR-2 of chapter 4.1, contain tens of CO_2 spectral lines, and more H_2O lines, and the chosen retrieval windows all include transparent regions toward the longwave and shortwave limits to constrict surface albedo as well as its spectral variation. A major difference between the two retrieval set-ups is the generally lower absorption optical depth of CO_2 lines in the SWIR-1 compared to the SWIR-2. Additionally, the SWIR-1 range contains a methane absorption band.

The aim of this work is to examine the appropriateness of the SWIR-1 and SWIR-2 configurations for a proposed imaging spectrometer that targets localized CO_2 emission sources at high spatial resolution. It has been demonstrated here that, at least for errors that seem to be random in the TCCON and native GOSAT analyses, no substantial deterioration of XCO_2 retrieval performance is expected from confining spectral band coverage to a single SWIR band and decreasing spectral resolving power to 6,000 and 1,000.

Yet, the SWIR-1 and SWIR-2 retrieval configurations suffer from enhanced errors that are induced by particle scattering effects. With ground resolution of the order of $50 \times 50\,\mathrm{m}^2$, the hypothetical satellite sensor shall be focused on resolving plumes above the background on the scale of a few kilometers at most. Hence, the findings suggest that, in terms of random errors, a spectral set-up using a single SWIR band is promising. While this work has not dealt with the question of whether or not a compact, single-band SWIR spectrometer could reach a satisfactory signal-to-noise level, Strandgren et al. (2020) developed a detailed instrument noise model for the proposed sensor and demonstrated through simulations that random noise errors below 2 ppm are a reasonable assumption. At this noise level the non-scattering SWIR-2 configuration resolved simulated plumes of a source with an emission rate of 0.3 $\mathrm{MtCO_2\ y^{-1}}$ (Strandgren et al., 2020). Whether or not particle scattering induced errors play a greater role for the hypothetical sensor, depends on the homogeneity of the aerosol regime on the respective spatial scale of the CO_2 plume. Cusworth et al. (2019) have determined ground albedo as a critical driver of CH_4 retrieval precision and strong albedo correlation in XCO_2 retrievals with AVIRIS-NG have been observed in this study. However, it is possible that surface reflectance could be characterized in a straightforward fashion by independent measurements, as opposed to aerosols, which are perhaps less temporally consistent in the vicinity of a local source.

Although both SWIR spectral ranges individually seem suited for coarse-spectral resolution XCO_2 retrievals, the enhanced random noise observed in the SWIR-1 indicates that

the SWIR-2 may be the better choice. Increased noise levels in the SWIR-1 are likely due to the weak absorption lines of CO_2 found in this spectral range, so that a greater noise propagates into the retrieval there. In addition, the SWIR-2 range appears the better fit for the construction of a cloud mask, as its two CO_2 bands display strongly varying optical depths. It is common practice in GOSAT cloud filtering approaches to retrieve XCO_2 individually from the SWIR-2 bands and subsequently exclude scenes with large discrepancies. A similar approach has shown promising performance in removing cloudy scenes from AVIRIS-NG measurements, although future research should refine this technique.

The selection of retrieval windows in the AVIRIS-NG study showed that the SWIR-2 with its optically thick absorption bands fared better at retrieving low-standard-deviation XCO_2 fields from the measurements than the SWIR-1. Having the full SWIR spectral range available in the retrieval adds to the information content on XCO_2 and also enables cloud filtering techniques that employ, for example, radiances in the SWIR-1 and SWIR-2 and in the visible spectral range. Specifically, the radiance signals at 502 nm, 1,548 nm and 2,054 nm could be employed to construct a fast cloud mask by classifying $I_{1{,}548\ \mathrm{nm}}/I_{2{,}054\ \mathrm{nm}} + I_{502\ \mathrm{nm}}/1\ \mu\mathrm{Wsr}^{-1}\mathrm{cm}^{-2}\mathrm{nm}^{-1} > 11$ as cloudy pixels. Furthermore, retrieval advantages were observed that manifested themselves through decreased scatter and reduced spectral residuals, when each CO_2 absorption band was contained within an individual retrieval window, each of which included continuum radiance. One can conclude here that the strong bands in the SWIR-2 are crucial for a low-standard-deviation XCO_2 retrieval. The same seems to be true for the water vapor retrieval which benefited from including strong H_2O absorption near 1.8 μm. Additionally, the choice of small spectral retrieval windows emphasizes that retrievals at such coarse spectral resolution are prone to mixing information on albedo and trace gas signals and therefore, albedo must be characterized in small spectral intervals.

However, interference of particular surface types with molecular absorption signals cannot always be avoided, as for example in the case of a man-made surface structure which inhibits the water vapor retrieval from the 1.8 μm band in the Four Corners flight line. The retrieval study has also shown that surfaces with albedo below 0.03 are too dark for meaningful analyses. As a consequence, CO_2 plumes that are blown over water or very dark vegetation may systematically escape detection. To remedy the strong albedo dependence of XCO_2 retrievals in my AVIRIS-NG analysis, a linear bias correction was developed which was shown to reduce overall XCO_2 scatter and albedo correlations (R on the scale of 0.1-0.2).

The analysis of specMACS retrievals shows that large systematic spectral residuals are observed in the SWIR spectral ranges. A future study should try to minimize these residuals, and should then compare retrieval performance in the two SWIR bands. This study found a lower XCO_2 standard deviation for SWIR-1 retrievals than for SWIR-2-only retrievals, which is opposed to the expectation that the spectral range with finer spectral resolution should perform better ($\Delta\lambda = 12.4$ nm in SWIR-1 and $\Delta\lambda = 8.5$ nm in SWIR-2). This observation may hint at a retrieval advantage at the low spectral resolution of specMACS due to higher signal levels in the SWIR-1, which may be explored in another

study. It would be interesting to incorporate the actual noise vectors of AVIRIS-NG and specMACS in future studies with these sensors so that a more robust analysis of retrieval accuracy can be obtained.

Implications of local wind speed uncertainties on CO_2 monitoring capabilities

Once XCO_2 has been retrieved at a high spatial resolution near a localized carbon dioxide source, the CO_2 monitoring capability of such a measurement and retrieval ultimately depends on low uncertainties in the knowledge of the local wind speed. Chapter 4.2 has highlighted that the absence of reliable wind information will incur large uncertainties on any flux estimate from a remote measurement. As noted by Varon et al. (2018), flux rate errors in low wind speed scenarios quickly become dominated by wind speed errors, which was also observed in this work, where the San Juan emission rate has an error of 79 % due to the poor knowledge of the wind speed. Although poor knowledge of the local wind speed is a major impediment in CO_2 monitoring techniques with passive sensors, high spatial resolution is still necessary to detect plumes from weak sources and it reduces errors in the mass balance and IME flux inversion methods, because the plume shape is resolved. As opposed to methane, which is often released near the ground, power plants pose an additional challenge as their stacks can reach heights of 100 to 200 m, which has to be considered for an appropriate emission estimate (see also Brunner et al. (2019)). As a consequence, surface wind information from weather stations cannot readily be used for the flux inversion. NARR 30 m wind speed reanalyses were adopted here and an uncertainty of 3 m/s was applied, which is motivated by the study of Borchardt et al. (2021) who applied a 1.5 m/s uncertainty when working with regional surface measurements for methane sources near the surface. Doubling the uncertainty of Borchardt et al. (2021) seems like a conservative approach in the absence of established methods to estimate wind speed errors for tall emission stacks. Future studies should therefore investigate if there are relationships between surface winds and winds in the lowest 300 m of the troposphere. Alternatively, further studies could try to derive wind speed information from a proxy species, such as NO_2 (see e.g. Kuhlmann et al. (2019)), or from empirical relationships involving the plume angular distribution (Jongaramrungruang et al., 2019).

Outlook

The field of CO_2 (and CH_4) remote sensing from air- and space-borne instruments is evolving rapidly and the present study shows that XCO_2 retrievals can resolve localized XCO_2 enhancements at resolving powers as low as $\lambda/\Delta\lambda \sim 400$. While a significant effort is currently spent on designing sensors that are custom-built for trace gas imaging (e.g. ch. 4.1), the scientific community has started exploring CO_2 retrieval possibilities from sensors that were not originally built for gas detection, such as AVIRIS-NG. It appears that there is a trend to derive trace gas (especially CH_4) information from sensors that one would not intuitively associate with trace gas retrieval capability, e.g. the specMACS

cloud sensor (ch. 4.3), although no plume could be identified here. These developments include (Cusworth et al., 2019) trace gas retrievals from satellite sensors such as EMIT ($\Delta\lambda \sim 7 - 10$ nm, Green et al. (2020)), EnMAP ($\Delta\lambda \sim 10$ nm, Guanter et al. (2015)), PRISMA ($\Delta\lambda \sim 10$ nm, Loizzo et al. (2018)), or HyspIRI ($\Delta\lambda \sim 10$ nm, Hochberg et al. (2015)). In fact, even instruments like Sentinel-2 (Martimort et al., 2012), which do not measure continuous spectra, but rather collect radiation in several distinct spectral bands (each with bandwith on the order of $\Delta\lambda > 15$ nm) have been shown to be sensitive to large methane enhancements (Varon et al., 2021). It is possible that such monitoring opportunities will also be realized for CO_2 point sources (potentially using the same sensors) and that the ever expanding number of Earth-observing satellites will enable higher spatial and temporal coverage of large point sources through multi-satellite observations of the same sources (Cusworth et al., 2021).

The loss of spectral information content in measurements with degraded spectral resolution indicates that there are thresholds for CO_2 plume detection which were not derived here. Nonetheless it seems clear that the above mentioned case studies of methane plume detections at $\Delta\lambda > 5$ nm, which are carried out against a relatively small atmospheric CH_4 background, do not immediately translate into CO_2 monitoring capabilities with these sensors. Strandgren et al. (2020) illustrate that 64 % of worldwide CO_2 emissions from power plants originate from power plants with medium source strengths, i.e. facilities that emit 1-10 $MtCO_2y^{-1}$. Thus, it is crucial that CO_2 monitoring instruments can resolve plumes from relatively small sources so that their measurements are relevant to inform climate policies. Because of the high atmospheric CO_2 background, one can remain doubtful that such medium sized CO_2 sources can be monitored reliably and in a quantitative fashion with sensors that have resolutions on the scale of $\Delta\lambda \sim 10$ nm. This thesis shows that potential exists for coarse-spectral resolution sensors to resolve CO_2 plumes of localized sources, but in the case of specMACS, it would likely take a large source (as in the AVIRIS-NG examples) for a successful detection. One of the biggest sources of uncertainty, which was not addressed in this study, is the impact of particle scattering on the (mostly) non-scattering coarse-spectral-resolution XCO_2 retrievals carried out in this work. Work by Huang et al. (2020) hints at aerosol-scattering induced retrieval biases in methane inversions from AVIRIS-NG, which are on the order of ~ 5 % of the total column. A simulation study is necessary to approximate the influence of aerosols and clouds on CO_2 monitoring methods. Challenges that arise with complicated atmospheric aerosol scenarios may be overcome eventually by operating a dedicated aerosol sensor (e.g. the instrument proposed by Hasekamp et al. (2019)) in parallel to the CO_2 sensor. While the general feasibility of measuring XCO_2 at coarse spectral resolution has been demonstrated here, further studies should especially address the effects of aerosol scattering on the local error budget.

While the present study follows a rather traditional path of applying full-physics XCO_2 retrievals to spectra of high-spatial-resolution imagers, computationally less expensive retrieval approaches may become more important in the future when large amounts of imaging spectrometer data may be used synergetically and for a vast number of individual sources. To this end, it is conceivable that neural networks (e.g. David et al. (2021))

and matched filter retrievals (e.g. Foote et al. (2020)) will play a more visible role in CO_2 monitoring applications. Algorithms, which automate methane plume detection and plume mask generation already exist (Kumar et al., 2020) and future research will surely drive similar achievements for CO_2 monitoring, although it is unclear whether such techniques can replace the many steps involved in deriving the flux rate of a point source.

Finally, emission estimates may be optimized by sampling the plume at an early time of day, where turbulence is not as pronounced as during the midday flights of the AVIRIS-NG sensor of ch. 4.2. However, the sampling time must still allow for a sufficiently large solar zenith angle.

Appendix A

Does GOSAT Capture the Los Angeles XCO_2 Enhancement?

With its 10.5 km diameter ground footprint, the GOSAT satellite has enabled studies of greenhouse gas concentrations above major urban agglomerations. For instance, Kort et al. (2012) have studied XCO_2 enhancements above the Los Angeles (LA) megacity and found a systematic offset between the city center and the rural regions east and north of it. They reported an average offset between GOSAT measurements over urban and rural sites of $+3.2\pm1.5$ ppm. In connection with the spectral sizing effort for a high spatial resolution XCO_2 sensor (ch. 4.1), the work by Kort et al. (2012) would be well suited to illustrate the effect of decreased spectral resolution on the ability to retrieve XCO_2 gradients from GOSAT measurements. As it is not known which GOSAT observations Kort et al. (2012) have used for their study, this study tries to identify spectra measured above and near LA, that can be used to show the XCO_2 gradient between the megacity and its surroundings. To this end, GOSAT retrieval data of the Atmospheric CO_2 Observations from Space (ACOS) algorithm were used with which Kort et al. (2012) performed their analysis (JPL, 2018, O'Dell et al., 2012, 2018). These data correspond to build version 3.5 (B35) of the ACOS algorithm and the retrievals are not bias corrected.

The data were examined for soundings that were recorded within $0.5\,^\circ$ of downtown LA ("urban" observations) and soundings that were recorded at a distance $0.75\,^\circ < r < 2.5\,^\circ$ away from downtown LA ("rural" observations) and the soundings were specifically filtered for the temporal range of GOSAT measurements that Kort et al. (2012) used as well.

The left hand side plot of Fig. A.1 shows the result of this survey. The vast majority of the urban soundings shown here were obtained with the *target mode* pointing approach of GOSAT. Without filtering any of the downloaded data – neither at background or urban sites – one can reproduce a similar XCO_2 offset between the megacity and its surroundings, $\Delta XCO_2=4.3\pm3.9$ ppm, albeit with less statistical significance than in the original publication ($\Delta XCO_2 = 3.2 \pm 1.5$ ppm reported in Kort et al. (2012)). This difference may originate from a potential filtering of data in the rural background, since the supplementary material given by Kort et al. (2012, Fig. S2) show that the authors used only

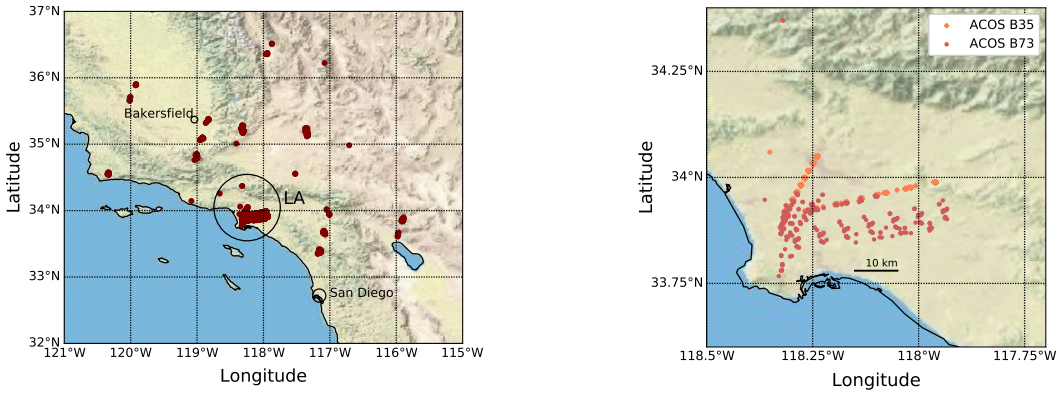

Figure A.1: GOSAT soundings near LA between June 2009 and August 2010 identified in ACOS data sets plotted on a physical map. The locations of the cities Bakersfield and San Diego are indicated with circles. Left: center locations of soundings that are found in the downloaded data. All soundings whose centers lie within the large circle around LA, were considered to be "urban" GOSAT measurements. Right: A zoom on the LA megacity basin shows that ACOS B35 (orange diamonds) and B73 (red circles) differ in the geolocation of the soundings (i.e. "original" (B35) vs. "best_estimated" (B73)).

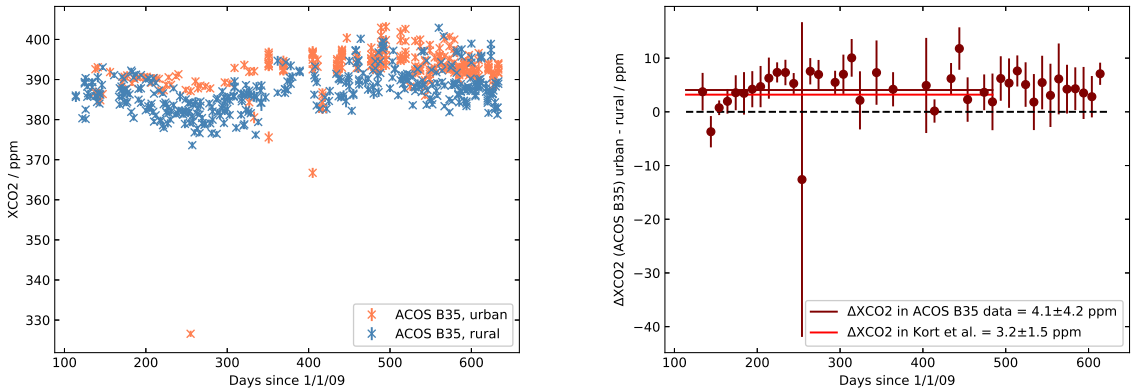

Figure A.2: Time series of ACOS B35 XCO_2 data. Qualitatively, results by Kort et al. (2012) can be retraced, albeit with decreased statistical significance. Left: downloaded ACOS B35 data, right: differences between urban and rural soundings in 10-day bins.

82 soundings in the desert whereas 280 rural soundings were considered here (Fig. A.1). It may make sense to discard certain soundings when the location of a sounding does not reflect typical conditions at the respective site. Although Kort et al. (2012) do not go into detail, they might have neglected some of the available background observations like the ones west of Los Angeles on days when the wind comes from the east so as to not use background spectra contaminated with the city plume.

The time series of differences for the ACOS B35 data product is shown in Fig. A.2. These results were obtained by binning differences of urban and rural XCO_2 concentrations in 10–day bins in the time between June 2009 and August 2010. Changing the width of the bins to 7 or 14 days respectively, changes the offset value to ΔXCO_2=4.0±4.6 ppm and ΔXCO_2=4.3±3.2 ppm, respectively.

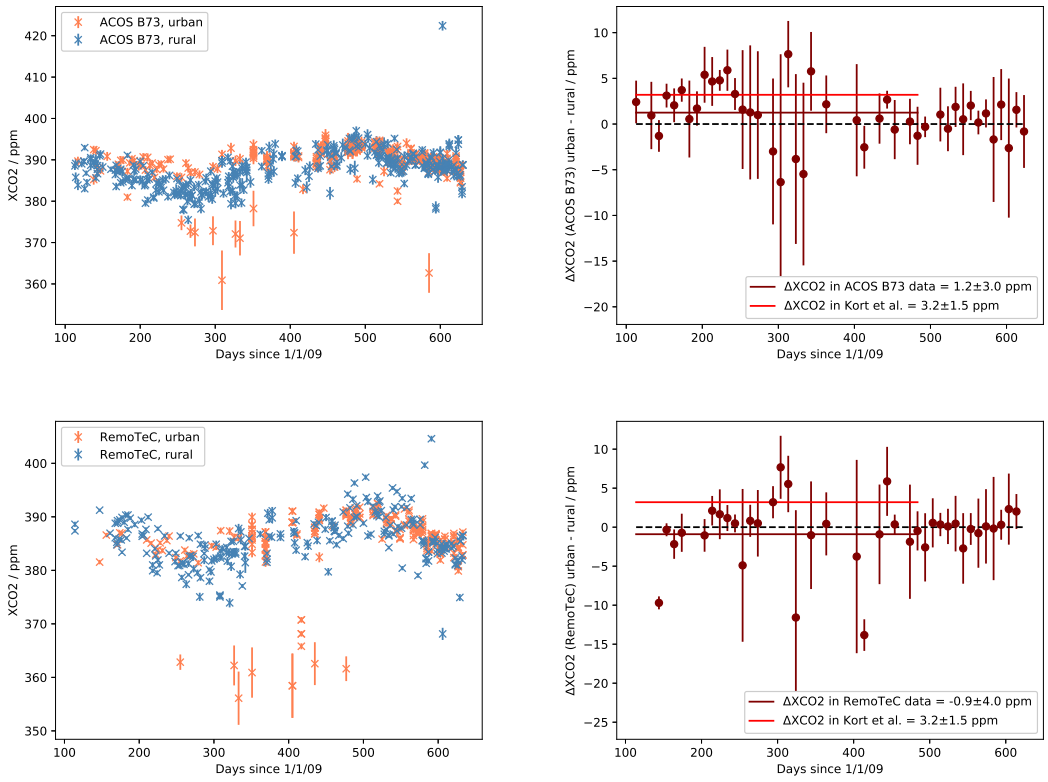

Figure A.3: Time series of XCO_2 concentrations around LA for ACOS B73 and RemoTeC calculations (top left and bottom left, respectively) and differences between urban and rural soundings in 10-day bins (right).

After the publication of Kort et al. (2012), GOSAT geolocations were revised in 2013, which affected all previous (and future) target mode measurements of GOSAT, because of inaccurate pointing of the instrument. This revision caused significant deviations of the sampling pattern over the urban area of Los Angeles in the time span considered by Kort et al. (2012). Fig. A.1 (right hand side) shows that the update in geolocations means that individual soundings over LA are corrected to ground spots as far as ∼10 km away from the originally assumed measurement location. Rural observation sites were not affected by the correction of geolocations, because they were not recorded in target pointing mode. The updated ACOS-GOSAT product corresponds to build 7.3 (B73) and was provided by H. Suto (Suto, 2018). Corrected geolocations of GOSAT are referred to as "best_estimated"

geolocations[1].

It is interesting to try to reproduce the study by Kort et al. (2012) once more with the newer ACOS B73 dataset as well as with RemoTeC to see if the XCO_2 signal above the city still exists when the new geolocations are applied.

Fig. A.3 shows that the XCO_2 offset observed between city and desert disappears in both ACOS and RemoTeC retrievals using the updated geolocations. The offsets observed between the city and the desert is ΔXCO_2=1.2±3.0 ppm (ACOS B73) and ΔXCO_2=-0.9± 4.0ppm (RemoTeC)[2]. In other words, the retrievals using updated geolocations do not exhibit a significant XCO_2 urban-rural gradient near LA.

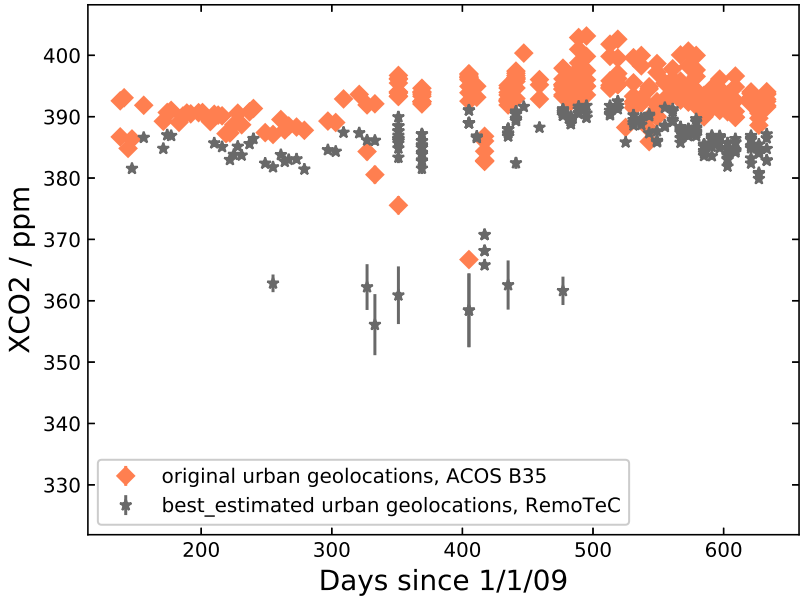

Figure A.4: Early versions of GOSAT data products (as in ACOS B35, orange diamonds) contain geolocations that may lead to XCO_2 concentrations above LA, which are in conflict with the values obtained with the "best_estimated" update of the sounding locations (as in RemoTeC, grey stars).

This change is caused by a variation in ground elevation that goes along with the change in geolocation. Similar observations have been discussed in detail by Kiel et al. (2019) who emphasized the impact of erroneous a priori surface pressure and elevation

[1]These are the geolocations used in all GOSAT analyses in this work and which are currently used with RemoTeC.

[2]When the size of the bin intervals is changed to 7 and 14 days, respectively, ACOS B73 ΔXCO_2 values become ΔXCO_2=1.3±3.2 ppm and ΔXCO_2=1.2±2.4 ppm, respectively. Likewise, RemoTeC offsets are not qualitatively affected by changing the bin size. ΔXCO_2 values become ΔXCO_2=-0.8±3.4 ppm and ΔXCO_2=-1.3±4.2 ppm for 7 and 14 day bins, respectively.

databases. The Los Angeles basin is bounded by a mountain range to the north and the basin consequently exhibits a steep elevation profile. As a result, satellite sounding locations over LA at distances of ∼10 km may have differences in elevations on the order of 100 m. Such differences in ground elevation have a strong impact on the calculation of XCO_2, because the spectroscopically determined CO_2 number density is divided by the airmass of the atmospheric column beneath the satellite sensor, to obtain XCO_2. The airmass will vary considerably depending on ground altitude. GOSAT observations above the "urban" region of LA were primarily affected. Changes in urban XCO_2 retrievals are presented in Fig. A.4, which highlights that the new geolocations systematically lead to lower XCO_2 retrievals.

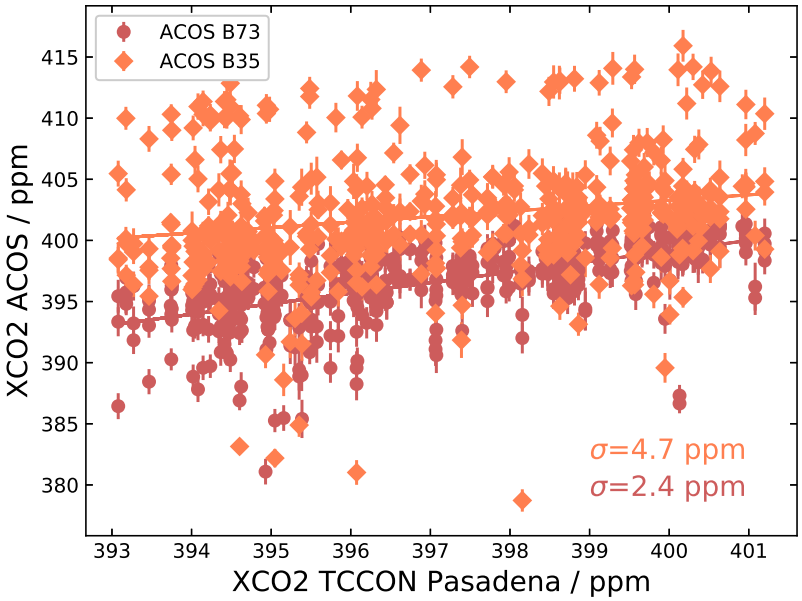

Figure A.5: Comparison of ACOS B35 and B73 XCO_2 data above the city of LA to colocated TCCON soundings at the nearby Pasadena station in 2013. ACOS B73 – built with the updated geolocations – exhibits a standard deviation about TCCON measurements of 2.4 ppm while ACOS B35 shows a greater scatter of 4.7 ppm around TCCON.

This finding implies that – given the geolocation update actually improved GOSAT sounding accuracy – the gradients resolved by Kort et al. (2012) may be regarded as artifacts of erroneous geolocations/poor knowledge of the actual satellite pointing. To test this hypothesis, one can compare XCO_2 values from the different ACOS versions B35 and B73 to XCO_2 measured at the TCCON station in Pasadena (within the Los Angeles basin). Fig. A.5 indicates that the newer dataset compares better to that TCCON site than the B35 product with old geolocations. The scatter around TCCON is decreased from 4.7 ppm (old geolocations) to 2.4 ppm when the updated, "best_estimated" geolocations are utilized.

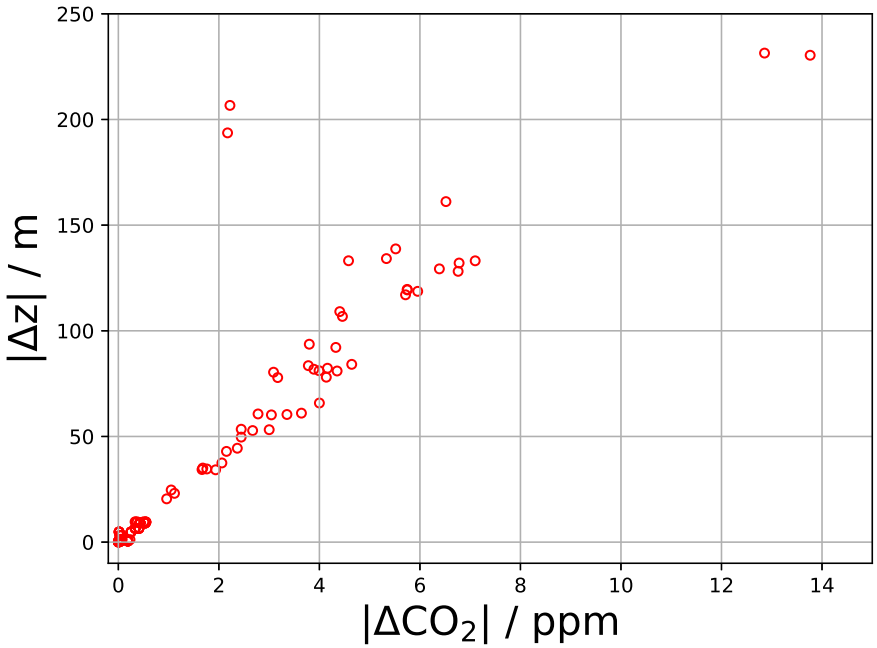

Figure A.6: Assuming erroneous ground elevation data for satellite remote sensing methods that rely on accurate knowledge of the airmass below the satellite introduces roughly 1 ppm XCO_2 error for every 20 m error.

Thus, one can conclude that the GOSAT geolocation correction truly improved the retrieved XCO_2 values and that the results of Kort et al. (2012) are a relic of erroneous sounding location data. The key message of this analysis is that the accuracy of a pointing system for a satellite sensor is absolutely crucial for the measurements to be useful. Especially over hilly terrain do pointing errors result in large uncertainties in the ground altitude of the observed ground spot. Such errors in height directly translate into errors in XCO_2, which add up to $\sim$1 ppm per 20 m. This correlation is shown in Fig. A.6, where the difference in XCO_2 of colocated ACOS B35 and B73 soundings is plotted with respect to the respective difference in ground altitude.

Hence, the LA megacity could not be used as a testbed to assess the impact of degraded spectral resolution retrievals on XCO_2 gradients, because even native GOSAT does not resolve such gradients over a measurement period of $\sim$ 500 days. In conclusion, accurate knowledge of the ground location of satellite soundings is essential to infer XCO_2 concentrations from such measurements. Sensors with especially small ground footprints will show an increased sensitivity to ground altitude. At the same time smaller ground pixels, and especially imaging information, may also help to assign a correct geolocation to the instrument, because of increased sensitivity to changes in surface reflectance on small spatial scales.

Appendix B

Supplemental Information for TCCON Analyses

This appendix lists two supplemental Tables providing traceability of the TCCON data used in this study (Table B.1) and additional details on inter-station-variability of native and degraded GOSAT retrievals (Table B.2). The latter contains the data displayed in Fig. 4.7.

TCCON station	Reference
Sodankyla	Kivi et al. (2014)
Lamont	Wennberg et al. (2016b)
Bialystok	Deutscher et al. (2015)
Anmeyondo	Goo et al. (2014)
Bremen	Notholt et al. (2014)
Tsukuba	Morino et al. (2018a)
Karlsruhe	Hase et al. (2015)
Edwards	Iraci et al. (2016a)
Paris	Té et al. (2014)
JPL	Wennberg et al. (2016a)
Orleans	Warneke et al. (2014)
Pasadena	Wennberg et al. (2015)
Garmisch	Sussmann and Rettinger (2018a)
Saga	Kawakami et al. (2014)
Zugspitze	Sussmann and Rettinger (2018b)
Hefei	Liu et al. (2018)
Park Falls	Wennberg et al. (2017)
Rikubetsu	Morino et al. (2018b)
Izana	Blumenstock et al. (2017)
Ascension Island	Feist et al. (2014)
Indianapolis	Iraci et al. (2016b)
Darwin	Griffith et al. (2014a)
Four Corners	Dubey et al. (2014), Lindenmaier et al. (2014)
Reunion	De Mazière et al. (2017)
Wollongong	Griffith et al. (2014b)
Lauder 1	Sherlock et al. (2014a)
Lauder 2	Sherlock et al. (2014b)

Table B.1: TCCON data sets utilized in this work. Adopted from the supplementary documentation of Wilzewski et al. (2020).

TCCON	N			Bias / ppm			σ / ppm		
station	FP	SWIR-1	SWIR-2	FP	SWIR-1	SWIR-2	FP	SWIR-1	SWIR-2
Sodankylä	217	211	217	-0.38	-0.83	2.55	2.08	2.71	3.47
Białystok	714	673	708	-0.76	-0.88	-0.6	2.14	2.82	3.46
Bremen	229	218	229	-0.28	-0.75	1.49	2.43	3.11	3.47
Karlsruhe	512	478	512	-0.82	-0.66	0.39	2.49	3.26	3.86
Paris01	215	211	214	-1.52	-1.37	-0.52	2.61	3.4	3.2
Orléans	740	712	736	-0.77	-1.02	0.28	2.06	3.13	3.52
Garmisch	493	462	493	-0.4	-0.47	0.39	2.14	2.93	3.7
Zugspitze	69	66	69	-1.47	-1.24	0.83	2.85	3.04	4.24
Park Falls	940	905	896	-0.53	-0.35	-0.21	2.09	2.84	3.41
Rikubetsu	68	60	68	-1.47	-1.52	-1.02	1.82	2.87	3.12
Indianapolis01	195	193	188	0.18	-0.15	1.24	1.84	2.62	2.99
Four Corners	45	30	34	-0.6	0.14	0.29	3.36	2.24	2.19
Lamont	5047	4939	4208	-0.62	-0.02	-1.15	1.98	2.83	2.62
Anmyeondo	9	9	9	-1.1	0.53	1.05	2.75	2.29	2.63
Tsukuba	837	731	830	1.15	0.16	0.63	2.81	3.38	3.83
Edwards	1666	1575	1462	1.98	2.07	2.31	2.64	2.95	3.0
JPL02	713	652	659	0.52	0.15	0.36	1.95	2.77	2.79
Pasadena01	2209	2084	1979	0.27	0.09	0.7	2.58	2.97	3.05
Saga	293	264	287	-0.2	-1.21	-0.96	2.29	3.31	3.53
Hefei	159	148	159	-0.96	-0.09	-0.77	2.24	3.2	3.0
Darwin	1521	1510	1404	1.07	0.63	-0.51	1.59	2.14	2.43
Wollongong	1029	975	974	-0.4	-1.05	-0.58	2.22	2.7	3.12
Lauder02	65	61	65	-2.22	-1.92	-0.06	2.04	2.61	3.48
Lauder01	17	15	17	-1.48	-3.11	-0.25	2.7	2.67	4.1

Table B.2: Performance of full-physics (FP), SWIR-1 and SWIR-2 retrievals for GOSAT scenes colocated with individual TCCON sites. Sites are ordered north to south (TCCON station). Number of GOSAT spectra (N), average differences between the current retrievals and TCCON (Bias) and standard deviation (σ) are shown. Table adopted from Wilzewski et al. (2020).

Acronyms

AERONET AErosol RObotic NETwork 64, 66, 67

AVIRIS-NG Next Generation Airborne Visible Infrared Spectrometer xi, 4, 33, 41–43, 49, 50, 69–71, 73, 75, 76, 81, 84–91, 94, 95, 99, 100, 105, 107, 108, 111–118, 131–133

CAI Cloud and Aerosol Imager 38, 40

CIA collision induced absorption 10, 34, 85, 107

DFS Degree of Freedom for Signal 31, 36, 53, 56–58, 61, 64, 112

ECMWF European Centre for Medium-Range Weather Forecasts 33, 38

FIR Far Infrared Radiation 11

FTS Fourier Transform Spectrometer 15, 17–19, 38–41, 46, 47

FWHM Full Width at Half Maximum 4, 17, 19, 39, 43, 45, 46, 51, 54–56, 105, 112, 133

GOSAT Greenhouse gases Observing SATellite xi, xiii, 3, 4, 37–41, 50–56, 58–67, 111–115, 119–125, 127, 131–133

HALO High Altitude LOng range research aircraft 44

HITRAN HIgh-resolution TRANsmission molecular absorption database 11, 55, 73, 77, 80, 131

HTP Hartmann-Tran-Profile 10

IME Integrated Mass Enhancement 95, 99, 101, 103, 116

IR Infrared Radiation 11, 21, 39

ISRF Instrumental Spectral Response Function 105

NIR Near Infrared (Radiation) 4, 50, 52, 56

OPD Optical Path Difference 15–18, 39

RMS Root-Mean-Square Error 73, 74, 83, 87–89

SNR Signal-to-Noise-Ratio 39, 42, 45, 46, 67

SOT Scattering Optical Thickness 60–62, 64, 66, 67

specMACS spectrometer of the Munich Aerosol and Cloud Scanner xii, xiv, 5, 33, 43–46, 49, 105–113, 115–117, 131–133

SRF Spectral Response Function 16, 17, 19, 21, 23, 24, 38, 43, 45, 56, 70, 108

SRTM Shuttle Radar Topography Mission 34, 38

SVD Singular Value Decomposition 29

SWIR Short Wave Infrared Radiation 4, 34, 38, 40, 41, 44–46, 50–67, 71–73, 75–78, 81–84, 87, 89–91, 96, 105–109, 111–115, 127, 131, 132

SZA Solar Zenith Angle 39, 40

TANSO Thermal And Near infrared Sensor for carbon Observations 38–41

TCCON Total Carbon Column Observing Network xi, xiii, 33, 46, 47, 50, 55–64, 67, 111, 112, 114, 123, 125–127, 131, 133

TIR Thermal Infrared Radiation 39–41, 51

TOA Top Of Atmosphere 26, 27

UV Ultraviolet Radiation 11, 12, 21

VIS Visible Radiation 11, 12, 21, 39

VNIR Visual and Near Infrared Radiation 44, 45

WMO World Meteorological Organization 47

List of Figures

List of Tables

Bibliography

ARIA Database, University of Oxford. Aerosol refractive index archive. http://eodg.atm.ox.ac.uk/ARIA/data, 2020. Last Accessed: 2021-01-04.

G. P. Asner, D. E. Knapp, J. Boardman, R. O. Green, T. Kennedy-Bowdoin, M. Eastwood, R. E. Martin, C. Anderson, and C. B. Field. Carnegie airborne observatory-2: Increasing science data dimensionality via high-fidelity multi-sensor fusion. *Remote Sensing of Environment*, 124:454 – 465, 2012. doi: https://doi.org/10.1016/j.rse.2012.06.012. URL http://www.sciencedirect.com/science/article/pii/S0034425712002489.

A. K. Ayasse, A. K. Thorpe, D. A. Roberts, C. C. Funk, P. E. Dennison, C. Frankenberg, A. Steffke, and A. D. Aubrey. Evaluating the effects of surface properties on methane retrievals using a synthetic airborne visible/infrared imaging spectrometer next generation (AVIRIS-NG) image. *Remote Sensing of Environment*, 215:386 – 397, 2018. doi: https://doi.org/10.1016/j.rse.2018.06.018. URL http://www.sciencedirect.com/science/article/pii/S0034425718302967.

A. K. Ayasse, P. E. Dennison, M. Foote, A. K. Thorpe, S. Joshi, R. O. Green, R. M. Duren, D. R. Thompson, and D. A. Roberts. Methane mapping with future satellite imaging spectrometers. *Remote Sensing*, 11(24), 2019. doi: 10.3390/rs11243054. URL https://www.mdpi.com/2072-4292/11/24/3054.

S. Baray, D. J. Jacob, J. D. Massakkers, J.-X. Sheng, M. P. Sulprizio, D. B. A. Jones, A. A. Bloom, and R. McLaren. Estimating 2010-2015 anthropogenic and natural methane emissions in Canada using ECCC surface and GOSAT satellite observations. *Atmospheric Chemistry and Physics Discussions*, 2021:1–40, 2021. doi: 10.5194/acp-2020-1195. URL https://acp.copernicus.org/preprints/acp-2020-1195/.

S. Basu, S. Guerlet, A. Butz, S. Houweling, O. Hasekamp, I. Aben, P. Krummel, P. Steele, R. Langenfelds, M. Torn, S. Biraud, B. Stephens, A. Andrews, and D. Worthy. Global co_2 fluxes estimated from gosat retrievals of total column co_2. *Atmospheric Chemistry and Physics*, 13(17):8695–8717, 2013. doi: 10.5194/acp-13-8695-2013. URL https://doi.org/10.5194/acp-13-8695-2013.

S. Basu, M. Krol, A. Butz, C. Clerbaux, Y. Sawa, T. Machida, H. Matsueda, C. Frankenberg, O. P. Hasekamp, and I. Aben. The seasonal variation of the CO2 flux over

tropical Asia estimated from GOSAT, CONTRAIL, and IASI. *Geophysical Research Letters*, 41(5):1809–1815, 2014. doi: https://doi.org/10.1002/2013GL059105. URL https://agupubs.onlinelibrary.wiley.com/doi/abs/10.1002/2013GL059105.

A. Baumgartner. Grating monochromator wavelength calibration using an echelle grating wavelength meter. *Opt. Express*, 27(10):13596–13610, May 2019. doi: 10.1364/OE.27.013596. URL http://www.opticsexpress.org/abstract.cfm?URI=oe-27-10-13596.

A. Baumgartner, P. Gege, C. Köhler, K. Lenhard, and T. Schwarzmaier. Characterisation methods for the hyperspectral sensor HySpex at DLR's calibration home base. In *Sensors, Systems, and Next-Generation Satellites XVI*, volume 8533, pages 371 – 378. International Society for Optics and Photonics, SPIE, 2012. doi: 10.1117/12.974664. URL https://doi.org/10.1117/12.974664.

S. Beirle, J. Lampel, C. Lerot, H. Sihler, and T. Wagner. Parameterizing the instrumental spectral response function and its changes by a super-gaussian and its derivatives. *Atmospheric Measurement Techniques*, 10(2):581–598, 2017. doi: 10.5194/amt-10-581-2017. URL https://www.atmos-meas-tech.net/10/581/2017/.

H. A. Bender, P. Z. Mouroulis, R. O. Green, and D. W. Wilson. Optical design, performance, and tolerancing of next-generation airborne imaging spectrometers. In *Imaging Spectrometry XV*, volume 7812, pages 212 – 223. International Society for Optics and Photonics, SPIE, 2010. doi: 10.1117/12.861331. URL https://doi.org/10.1117/12.861331.

P. Berrisford, D. Dee, P. Poli, R. Brugge, M. Fielding, M. Fuentes, P. Kållberg, S. Kobayashi, S. Uppala, and A. Simmons. The era-interim archive version 2.0. 2011. URL https://www.ecmwf.int/node/8174.

T. Blumenstock, F. Hase, M. Schneider, O. E. García, and E. Sepúlveda. TCCON data from Izana (ES), Release GGG2014.R1, 2017. URL https://doi.org/10.14291/tccon.ggg2014.izana01.r1.

J. Borchardt, K. Gerilowski, S. Krautwurst, H. Bovensmann, A. K. Thorpe, D. R. Thompson, C. Frankenberg, C. E. Miller, R. M. Duren, and J. P. Burrows. Detection and quantification of CH_4 plumes using the WFM-DOAS retrieval on AVIRIS-NG hyperspectral data. *Atmospheric Measurement Techniques*, 14(2):1267–1291, 2021. doi: 10.5194/amt-14-1267-2021. URL https://amt.copernicus.org/articles/14/1267/2021/.

T. Borsdorff, O. P. Hasekamp, A. Wassmann, and J. Landgraf. Insights into tikhonov regularization: application to trace gas column retrieval and the efficient calculation of total column averaging kernels. *Atmospheric Measurement Techniques*, 7(2):523–535, 2014. doi: 10.5194/amt-7-523-2014. URL https://amt.copernicus.org/articles/7/523/2014/.

T. Borsdorff, J. aan de Brugh, A. Schneider, A. Lorente, M. Birk, G. Wagner, R. Kivi, F. Hase, D. G. Feist, R. Sussmann, M. Rettinger, D. Wunch, T. Warneke, and J. Landgraf. Improving the TROPOMI CO data product: update of the spectroscopic database and destriping of single orbits. *Atmospheric Measurement Techniques*, 12(10):5443–5455, 2019. doi: 10.5194/amt-12-5443-2019. URL https://amt.copernicus.org/articles/12/5443/2019/.

H. Bovensmann, J. P. Burrows, M. Buchwitz, J. Frerick, S. Noël, V. V. Rozanov, K. V. Chance, and A. P. H. Goede. Sciamachy: Mission objectives and measurement modes. *Journal of the Atmospheric Sciences*, 56(2):127–150, 1999. doi: 10.1175/1520-0469(1999)056⟨0127:SMOAMM⟩2.0.CO;2. URL https://doi.org/10.1175/1520-0469(1999)056<0127:SMOAMM>2.0.CO;2.

H. Bovensmann, M. Buchwitz, J. P. Burrows, M. Reuter, T. Krings, K. Gerilowski, O. Schneising, J. Heymann, A. Tretner, and J. Erzinger. A remote sensing technique for global monitoring of power plant CO_2 emissions from space and related applications. *Atmospheric Measurement Techniques*, 3(4):781–811, 2010. doi: 10.5194/amt-3-781-2010. URL https://doi.org/10.5194/amt-3-781-2010.

G. Broquet, F. M. Bron, E. Renault, M. Buchwitz, M. Reuter, H. Bovensmann, F. Chevallier, L. Wu, and P. Ciais. The potential of satellite spectro-imagery for monitoring CO_2 emissions from large cities. *Atmospheric Measurement Techniques*, 11(2):681–708, 2018. doi: 10.5194/amt-11-681-2018. URL https://doi.org/10.5194/amt-11-681-2018.

C. J. Bruegge, J. E. Conel, J. S. Margolis, R. O. Green, G. C. Toon, V. Carrere, R. G. Holm, and G. Hoover. In-situ atmospheric water-vapor retrieval in support of AVIRIS validation. In *Imaging Spectroscopy of the Terrestrial Environment*, volume 1298, pages 150 – 163. International Society for Optics and Photonics, SPIE, 1990. doi: 10.1117/12.21346. URL https://doi.org/10.1117/12.21346.

D. Brunner, G. Kuhlmann, J. Marshall, V. Clément, O. Fuhrer, G. Broquet, A. Löscher, and Y. Meijer. Accounting for the vertical distribution of emissions in atmospheric co_2 simulations. *Atmospheric Chemistry and Physics*, 19(7):4541–4559, 2019. doi: 10.5194/acp-19-4541-2019. URL https://acp.copernicus.org/articles/19/4541/2019/.

M. Buchwitz, V. V. Rozanov, and J. P. Burrows. A near-infrared optimized DOAS method for the fast global retrieval of atmospheric CH4, CO, CO2, H2O, and N2O total column amounts from SCIAMACHY Envisat-1 nadir radiances. *Journal of Geophysical Research: Atmospheres*, 105(D12):15231–15245, 2000. doi: https://doi.org/10.1029/2000JD900191. URL https://agupubs.onlinelibrary.wiley.com/doi/abs/10.1029/2000JD900191.

M. Buchwitz, M. Reuter, O. Schneising, W. Hewson, R. Detmers, H. Boesch, O. Hasekamp, I. Aben, H. Bovensmann, J. Burrows, A. Butz, F. Chevallier, B. Dils, C. Frankenberg, J. Heymann, G. Lichtenberg, M. D. Maziere, J. Notholt, R. Parker, T. Warneke,

C. Zehner, D. Griffith, N. Deutscher, A. Kuze, H. Suto, and D. Wunch. Global satellite observations of column-averaged carbon dioxide and methane: The ghg-cci xco2 and xch4 crdp3 data set. *Remote Sensing of Environment*, 203:276 – 295, 2017. doi: 10.1016/j.rse.2016.12.027. URL https://doi.org/10.1016/j.rse.2016.12.027.

J. P. Burrows, E. Hölzle, A. P. Goede, H. Visser, and W. Fricke. SCIAMACHY-scanning imaging absorption spectrometer for atmospheric chartography. *Acta Astronautica*, 35 (7):445–451, 1995. doi: 10.1016/0094-5765(94)00278-T. URL https://doi.org/10.1016/0094-5765(94)00278-T.

A. Butz, O. P. Hasekamp, and I. Aben. Retrievals of atmospheric CO2 from simulated space-borne measurements of backscattered near-infrared sunlight: accounting for aerosol effects. *Applied Optics*, 48(18):3322–3336, 2009. doi: 10.1364/AO.48.003322. URL https://doi.org/10.1364/AO.48.003322.

A. Butz, O. P. Hasekamp, C. Frankenberg, J. Vidot, and I. Aben. CH_4 retrievals from space-based solar backscatter measurements: Performance evaluation against simulated aerosol and cirrus loaded scenes. *Journal of Geophysical Research Atmospheres*, 115(24):1–15, 2010. doi: 10.1029/2010JD014514. URL https://doi.org/10.1029/2010JD014514.

A. Butz, S. Guerlet, O. Hasekamp, D. Schepers, A. Galli, I. Aben, C. Frankenberg, J.-M. Hartmann, H. Tran, A. Kuze, G. Keppel-Aleks, G. Toon, D. Wunch, P. Wennberg, N. Deutscher, D. Griffith, R. Macatangay, J. Messerschmidt, J. Notholt, and T. Warneke. Toward accurate CO_2 and CH_4 observations from GOSAT. *Geophysical Research Letters*, 38(14):L14812, 2011. doi: 10.1029/2011GL047888. URL https://doi.org/10.1029/2011GL047888.

A. Butz, A. Galli, O. Hasekamp, J. Landgraf, P. Tol, and I. Aben. Tropomi aboard sentinel-5 precursor: Prospective performance of ch_4 retrievals for aerosol and cirrus loaded atmospheres. *Remote Sensing of Environment*, 120:267–276, 2012. doi: 10.1016/j.rse.2011.05.030. URL https://doi.org/10.1016/j.rse.2011.05.030.

A. Butz, S. Guerlet, O. P. Hasekamp, A. Kuze, and H. Suto. Using ocean-glint scattered sunlight as a diagnostic tool for satellite remote sensing of greenhouse gases. *Atmospheric Measurement Techniques*, 6(9):2509–2520, 2013. doi: 10.5194/amt-6-2509-2013. URL https://doi.org/10.5194/amt-6-2509-2013.

A. Butz, J. Orphal, R. Checa-Garcia, F. Friedl-Vallon, T. von Clarmann, H. Bovensmann, O. Hasekamp, J. Landgraf, T. Knigge, D. Weise, O. Sqalli-Houssini, and D. Kemper. Geostationary Emission Explorer for Europe (G3E): Mission concept and initial performance assessment. *Atmospheric Measurement Techniques*, 8(11):4719–4734, 2015. doi: 10.5194/amt-8-4719-2015. URL https://doi.org/10.5194/amt-8-4719-2015.

J. W. Chapman, D. R. Thompson, M. C. Helmlinger, B. D. Bue, R. O. Green, M. L. Eastwood, S. Geier, W. Olson-Duvall, and S. R. Lundeen. Spectral and radiometric

calibration of the next generation airborne visible infrared spectrometer (aviris-ng). *Remote Sensing*, 11(18), 2019. doi: 10.3390/rs11182129. URL https://www.mdpi.com/2072-4292/11/18/2129.

A. Chatterjee, M. M. Gierach, A. J. Sutton, R. A. Feely, D. Crisp, A. Eldering, M. R. Gunson, C. W. O'Dell, B. B. Stephens, and D. S. Schimel. Influence of El Niño on atmospheric CO_2 over the tropical Pacific Ocean: Findings from NASA's OCO-2 mission. *Science*, 358(6360), 2017. doi: 10.1126/science.aam5776. URL https://doi.org/10.1126/science.aam5776.

T. G. Chrien, R. O. Green, and M. L. Eastwood. Accuracy of the spectral and radiometric laboratory calibration of the Airborne Visible/Infrared Imaging Spectrometer. In G. Vane, editor, *Imaging Spectroscopy of the Terrestrial Environment*, volume 1298, pages 37 – 49. International Society for Optics and Photonics, SPIE, 1990. doi: 10.1117/12.21334. URL https://doi.org/10.1117/12.21334.

P. Ciais, A. J. Dolman, A. Bombelli, R. Duren, A. Peregon, P. J. Rayner, C. Miller, N. Gobron, G. Kinderman, G. Marland, N. Gruber, F. Chevallier, R. J. Andres, G. Balsamo, L. Bopp, F.-M. Bréon, G. Broquet, R. Dargaville, T. J. Battin, A. Borges, H. Bovensmann, M. Buchwitz, J. Butler, J. G. Canadell, R. B. Cook, R. DeFries, R. Engelen, K. R. Gurney, C. Heinze, M. Heimann, A. Held, M. Henry, B. Law, S. Luyssaert, J. Miller, T. Moriyama, C. Moulin, R. B. Myneni, C. Nussli, M. Obersteiner, D. Ojima, Y. Pan, J.-D. Paris, S. L. Piao, B. Poulter, S. Plummer, S. Quegan, P. Raymond, M. Reichstein, L. Rivier, C. Sabine, D. Schimel, O. Tarasova, R. Valentini, R. Wang, G. van der Werf, D. Wickland, M. Williams, and C. Zehner. Current systematic carbon-cycle observations and the need for implementing a policy-relevant carbon observing system. *Biogeosciences*, 11(13):3547–3602, 2014. doi: 10.5194/bg-11-3547-2014. URL https://bg.copernicus.org/articles/11/3547/2014/.

Copernicus Climate Change Service (C3S). ERA5: Fifth generation of ECMWF atmospheric reanalyses of the global climate. Copernicus climate change service Climate Data Store (CDS). https://cds.climate.copernicus.eu/cdsapp#!/home, 2017. Last Accessed: 2021-01-03.

D. Crisp, C. E. Miller, and P. L. DeCola. NASA Orbiting Carbon Observatory: measuring the column averaged carbon dioxide mole fraction from space. *Journal Of Applied Remote Sensing*, 2(March 2008):23508, 2008. doi: 10.1117/1.2898457. URL https://doi.org/10.1117/1.2898457.

D. Crisp, B. M. Fisher, C. O'Dell, C. Frankenberg, R. Basilio, H. Bösch, L. R. Brown, R. Castano, B. Connor, N. M. Deutscher, A. Eldering, D. Griffith, M. Gunson, A. Kuze, L. Mandrake, J. McDuffie, J. Messerschmidt, C. E. Miller, I. Morino, V. Natraj, J. Notholt, D. M. O'Brien, F. Oyafuso, I. Polonsky, J. Robinson, R. Salawitch, V. Sherlock, M. Smyth, H. Suto, T. E. Taylor, D. R. Thompson, P. O. Wennberg, D. Wunch,

and Y. L. Yung. The ACOS CO_2 retrieval algorithm – Part II: Global XCO_2 data characterization. *Atmospheric Measurement Techniques*, 5(4):687–707, 2012. doi: 10.5194/amt-5-687-2012. URL https://amt.copernicus.org/articles/5/687/2012/.

D. Crisp, H. Pollock, R. Rosenberg, L. Chapsky, R. Lee, F. Oyafuso, C. Frankenberg, C. Dell, C. Bruegge, G. Doran, A. Eldering, B. Fisher, D. Fu, M. Gunson, L. Mandrake, G. Osterman, F. Schwandner, K. Sun, T. Taylor, P. Wennberg, and D. Wunch. The on-orbit performance of the Orbiting Carbon Observatory-2 (OCO-2) instrument and its radiometrically calibrated products. *Atmospheric Measurement Techniques*, 10(1):59–81, 2017. doi: 10.5194/amt-10-59-2017. URL https://doi.org/10.5194/amt-10-59-2017.

D. H. Cusworth, D. J. Jacob, D. J. Varon, C. Chan Miller, X. Liu, K. Chance, A. K. Thorpe, R. M. Duren, C. E. Miller, D. R. Thompson, C. Frankenberg, L. Guanter, and C. A. Randles. Potential of next-generation imaging spectrometers to detect and quantify methane point sources from space. *Atmospheric Measurement Techniques Discussions*, 2019:1–29, 2019. doi: 10.5194/amt-2019-202. URL https://www.atmos-meas-tech-discuss.net/amt-2019-202/.

D. H. Cusworth, R. M. Duren, A. K. Thorpe, E. Tseng, D. Thompson, A. Guha, S. Newman, K. T. Foster, and C. E. Miller. Using remote sensing to detect, validate, and quantify methane emissions from california solid waste operations. *Environmental Research Letters*, 15(5):054012, may 2020. doi: 10.1088/1748-9326/ab7b99. URL https://doi.org/10.1088%2F1748-9326%2Fab7b99.

D. H. Cusworth, R. M. Duren, A. K. Thorpe, S. Pandey, J. D. Maasakkers, I. Aben, D. Jervis, D. J. Varon, D. J. Jacob, C. A. Randles, R. Gautam, M. Omara, G. W. Schade, P. E. Dennison, C. Frankenberg, D. Gordon, E. Lopinto, and C. E. Miller. Multisatellite imaging of a gas well blowout enables quantification of total methane emissions. *Geophysical Research Letters*, 48(2):e2020GL090864, 2021. doi: https://doi.org/10.1029/2020GL090864. URL https://agupubs.onlinelibrary.wiley.com/doi/abs/10.1029/2020GL090864.

A. Dahlback and K. Stamnes. A new spherical model for computing the radiation field available for photolysis and heating at twilight. *Planetary and Space Science*, 39(5):671 – 683, 1991. doi: https://doi.org/10.1016/0032-0633(91)90061-E. URL http://www.sciencedirect.com/science/article/pii/003206339190061E.

J. V. Dave and C. L. Mateer. A preliminary study on the possibility of estimating total atmospheric ozone from satellite measurements. *Journal of Atmospheric Sciences*, 24(4):414 – 427, 1967. doi: 10.1175/1520-0469(1967)024⟨0414:APSOTP⟩2.0.CO;2. URL https://journals.ametsoc.org/view/journals/atsc/24/4/1520-0469_1967_024_0414_apsotp_2_0_co_2.xml.

L. David, F.-M. Bréon, and F. Chevallier. Xco_2 estimates from the oco-2 measurements using a neural network approach. *Atmospheric Measurement Techniques*, 14(1):117–132, 2021. doi: 10.5194/amt-14-117-2021. URL https://amt.copernicus.org/articles/14/117/2021/.

A. de Lange and J. Landgraf. Methane profiles from gosat thermal infrared spectra. *Atmospheric Measurement Techniques*, 11(6):3815–3828, 2018. doi: 10.5194/amt-11-3815-2018. URL https://amt.copernicus.org/articles/11/3815/2018/.

M. De Mazière, M. K. Sha, F. Desmet, C. Hermans, F. Scolas, N. Kumps, J.-M. Metzger, V. Duflot, and J.-P. Cammas. TCCON data from Réunion Island (RE), Release GGG2014.R1, 2017. URL https://doi.org/10.14291/tccon.ggg2014.reunion01.r1.

P. E. Dennison, A. K. Thorpe, E. R. Pardyjak, D. A. Roberts, Y. Qi, R. O. Green, E. S. Bradley, and C. C. Funk. High spatial resolution mapping of elevated atmospheric carbon dioxide using airborne imaging spectroscopy: Radiative transfer modeling and power plant plume detection. *Remote Sensing of Environment*, 139:116 – 129, 2013. doi: https://doi.org/10.1016/j.rse.2013.08.001. URL http://www.sciencedirect.com/science/article/pii/S0034425713002599.

A. Deschamps, R. Marion, X. Briottet, P. Y. Foucher, and C. Lavigne. Simultaneous co2 and aerosol retrieval in a vegetation fire plume using aviris hyperspectral data. In *2011 3rd Workshop on Hyperspectral Image and Signal Processing: Evolution in Remote Sensing (WHISPERS)*, pages 1–4, 2011.

N. M. Deutscher, J. Notholt, J. Messerschmidt, C. Weinzierl, T. Warneke, C. Petri, and P. Grupe. TCCON data from Bialystok (PL), Release GGG2014.R1, 2015. URL https://doi.org/10.14291/tccon.ggg2014.bialystok01.r1/1183984.

M. K. Dubey, R. Lindenmaier, B. G. Henderson, D. Green, N. T. Allen, C. M. Roehl, J.-F. Blavier, Z. T. Butterfield, S. Love, J. D. Hamelmann, and D. Wunch. TCCON data from Four Corners (US), Release GGG2014.R0, 2014. URL https://doi.org/10.14291/tccon.ggg2014.fourcorners01.r0/1149272.

O. Dubovik, A. Sinyuk, T. Lapyonok, B. N. Holben, M. Mishchenko, P. Yang, T. F. Eck, H. Volten, O. Munoz, B. Veihelmann, W. J. van der Zande, J.-F. Leon, M. Sorokin, and I. Slutsker. Application of spheroid models to account for aerosol particle nonsphericity in remote sensing of desert dust. *Journal of Geophysical Research: Atmospheres*, 111 (D11), 2006. doi: https://doi.org/10.1029/2005JD006619. URL https://agupubs.onlinelibrary.wiley.com/doi/abs/10.1029/2005JD006619.

R. M. Duren, A. K. Thorpe, K. T. Foster, T. Rafiq, F. M. Hopkins, V. Yadav, B. D. Bue, D. R. Thompson, S. Conley, N. K. Colombi, C. Frankenberg, I. B. McCubbin, M. L. Eastwood, M. Falk, J. D. Herner, B. E. Croes, R. O. Green, and C. E. Miller.

California's methane super-emitters. *Nature*, 575(7781):180–184, 2019. URL https://www.nature.com/articles/s41586-019-1720-3.

A. Eldering, P. O. Wennberg, D. Crisp, D. S. Schimel, M. R. Gunson, A. Chatterjee, J. Liu, F. M. Schwandner, Y. Sun, C. W. O'Dell, C. Frankenberg, T. Taylor, B. Fisher, G. B. Osterman, D. Wunch, J. Hakkarainen, J. Tamminen, and B. Weir. The Orbiting Carbon Observatory-2 early science investigations of regional carbon dioxide fluxes. *Science*, 358(6360), 2017. doi: 10.1126/science.aam5745. URL https://doi.org/10.1126/science.aam5745.

A. Eldering, T. E. Taylor, C. W. O'Dell, and R. Pavlick. The oco-3 mission: measurement objectives and expected performance based on 1 year of simulated data. *Atmospheric Measurement Techniques*, 12(4):2341–2370, 2019. doi: 10.5194/amt-12-2341-2019. URL https://amt.copernicus.org/articles/12/2341/2019/.

EPA. US Environmental Protection Agency: Facility Level GHG Emission Data. https://ghgdata.epa.gov/ghgp/main.do, 2020. Last accessed: 2021-02-05.

G. P. Eppeldauer, H. W. Yoon, Y. Zong, T. C. Larason, A. Smith, and M. Racz. Radiometer standard for absolute responsivity calibrations from 950 nm to 1650 nm with 0.05% (k= 2) uncertainty. *Metrologia*, 46(4):S139–S145, jun 2009. doi: 10.1088/0026-1394/46/4/s01. URL https://doi.org/10.1088%2F0026-1394%2F46%2F4%2Fs01.

EPRTR. European Pollutant Release and Transfer Register (E-PRTR). https://prtr.eea.europa.eu/, 2021. Last Accessed: 2021-02-25.

F. Ewald, T. Kölling, A. Baumgartner, T. Zinner, and B. Mayer. Design and characterization of specMACS, a multipurpose hyperspectral cloud and sky imager. *Atmospheric Measurement Techniques*, 9(5):2015–2042, 2016. doi: 10.5194/amt-9-2015-2016. URL https://amt.copernicus.org/articles/9/2015/2016/.

F. Ewald, T. Zinner, T. Kölling, and B. Mayer. Remote sensing of cloud droplet radius profiles using solar reflectance from cloud sides – part 1: Retrieval development and characterization. *Atmospheric Measurement Techniques*, 12(2):1183–1206, 2019. doi: 10.5194/amt-12-1183-2019. URL https://www.atmos-meas-tech.net/12/1183/2019/.

D. G. Feist, S. G. Arnold, N. John, and M. C. Geibel. TCCON data from Ascension Island (SH), Release GGG2014.R0, 2014. URL https://doi.org/10.14291/tccon.ggg2014.ascension01.r0/1149285.

M. D. Foote, P. E. Dennison, A. K. Thorpe, D. R. Thompson, S. Jongaramrungruang, C. Frankenberg, and S. C. Joshi. Fast and accurate retrieval of methane concentration from imaging spectrometer data using sparsity prior. *IEEE Transactions on Geoscience and Remote Sensing*, pages 1–13, 2020. doi: 10.1109/TGRS.2020.2976888. URL https://arxiv.org/pdf/2003.02978.pdf.

C. Frankenberg, U. Platt, and T. Wagner. Iterative maximum a posteriori (IMAP)-DOAS for retrieval of strongly absorbing trace gases: Model studies for CH_4 and CO_2 retrieval from near infrared spectra of SCIAMACHY onboard ENVISAT. *Atmospheric Chemistry and Physics*, 5(1):9–22, 2005. doi: 10.5194/acp-5-9-2005. URL https://acp.copernicus.org/articles/5/9/2005/.

C. Frankenberg, J. B. Fisher, J. Worden, G. Badgley, S. S. Saatchi, J.-E. Lee, G. C. Toon, A. Butz, M. Jung, A. Kuze, and T. Yokota. New global observations of the terrestrial carbon cycle from gosat: Patterns of plant fluorescence with gross primary productivity. *Geophysical Research Letters*, 38(17), 2011. doi: https://doi.org/10.1029/2011GL048738. URL https://agupubs.onlinelibrary.wiley.com/doi/abs/10.1029/2011GL048738.

C. Frankenberg, A. K. Thorpe, D. R. Thompson, G. Hulley, E. A. Kort, N. Vance, J. Borchardt, T. Krings, K. Gerilowski, C. Sweeney, S. Conley, B. D. Bue, A. D. Aubrey, S. Hook, and R. O. Green. Airborne methane remote measurements reveal heavy-tail flux distribution in four corners region. *Proceedings of the National Academy of Sciences*, 113(35):9734–9739, 2016. doi: 10.1073/pnas.1605617113. URL https://www.pnas.org/content/113/35/9734.

M. Frey, M. K. Sha, F. Hase, M. Kiel, T. Blumenstock, R. Harig, G. Surawicz, N. M. Deutscher, K. Shiomi, J. E. Franklin, H. Bösch, J. Chen, M. Grutter, H. Ohyama, Y. Sun, A. Butz, G. Mengistu Tsidu, D. Ene, D. Wunch, Z. Cao, O. Garcia, M. Ramonet, F. Vogel, and J. Orphal. Building the COllaborative Carbon Column Observing Network (COCCON): long-term stability and ensemble performance of the EM27/SUN Fourier transform spectrometer. *Atmospheric Measurement Techniques*, 12(3):1513–1530, 2019. doi: 10.5194/amt-12-1513-2019. URL https://amt.copernicus.org/articles/12/1513/2019/.

C. C. Funk, J. Theiler, D. A. Roberts, and C. C. Borel. Clustering to improve matched filter detection of weak gas plumes in hyperspectral thermal imagery. *IEEE Transactions on Geoscience and Remote Sensing*, 39(7):1410–1420, 2001. doi: 10.1109/36.934073. URL https://ieeexplore.ieee.org/document/934073.

A. Galli, S. Guerlet, A. Butz, I. Aben, H. Suto, A. Kuze, N. M. Deutscher, J. Notholt, D. Wunch, P. O. Wennberg, D. W. Griffith, O. Hasekamp, and J. Landgraf. The impact of spectral resolution on satellite retrieval accuracy of CO2 and CH4. *Atmospheric Measurement Techniques*, 7(4):1105–1119, 2014. doi: 10.5194/amt-7-1105-2014. URL https://doi.org/10.5194/amt-7-1105-2014.

D. M. Giles, A. Sinyuk, M. G. Sorokin, J. S. Schafer, A. Smirnov, I. Slutsker, T. F. Eck, B. N. Holben, J. R. Lewis, J. R. Campbell, E. J. Welton, S. V. Korkin, and A. I. Lyapustin. Advancements in the Aerosol Robotic Network (AERONET) version 3 database – automated near-real-time quality control algorithm with improved

cloud screening for sun photometer aerosol optical depth (AOD) measurements. *Atmospheric Measurement Techniques*, 12(1):169–209, 2019. doi: 10.5194/amt-12-169-2019. URL https://www.atmos-meas-tech.net/12/169/2019/.

H. Goldstein, C. P. Poole, Jr., and J. L. Safko. *Klassische Mechanik*. Wiley-VCH, Weinheim, 3^{rd} edition, 2006. ISBN 978-3-527-40589-3.

T.-Y. Goo, Y.-S. Oh, and V. A. Velazco. TCCON data from Anmeyondo (KR), Release GGG2014.R0, 2014. URL https://doi.org/10.14291/tccon.ggg2014.anmeyondo01.r0/1149284.

I. E. Gordon, L. S. Rothman, C. Hill, R. V. Kochanov, Y. Tan, P. F. Bernath, M. Birk, V. Boudon, A. Campargue, K. V. Chance, B. J. Drouin, J. M. Flaud, R. R. Gamache, J. T. Hodges, D. Jacquemart, V. I. Perevalov, A. Perrin, K. P. Shine, M. A. Smith, J. Tennyson, G. C. Toon, H. Tran, V. G. Tyuterev, A. Barbe, A. G. Császár, V. M. Devi, T. Furtenbacher, J. J. Harrison, J. M. Hartmann, A. Jolly, T. J. Johnson, T. Karman, I. Kleiner, A. A. Kyuberis, J. Loos, O. M. Lyulin, S. T. Massie, S. N. Mikhailenko, N. Moazzen-Ahmadi, H. S. Müller, O. V. Naumenko, A. V. Nikitin, O. L. Polyansky, M. Rey, M. Rotger, S. W. Sharpe, K. Sung, E. Starikova, S. A. Tashkun, J. V. Auwera, G. Wagner, J. Wilzewski, P. Wcisło, S. Yu, and E. J. Zak. The HITRAN2016 molecular spectroscopic database. *Journal of Quantitative Spectroscopy and Radiative Transfer*, 203:3–69, 2017. doi: 10.1016/j.jqsrt.2017.06.038. URL https://doi.org/10.1016/j.jqsrt.2017.06.038.

R. O. Green. Initial Flights of the AVIRIS Next Generation Instrument and HyspIRI Concept Technology Validation. 2012 HyspIRI Science Workshop, URL https://hyspiri.jpl.nasa.gov/downloads/2012_Workshop/day3/16_pres_HyspIRI_AVIRIS_NG_121015a.pdf, 2012. Last accessed: 2021-01-18.

R. O. Green, M. L. Eastwood, C. M. Sarture, T. G. Chrien, M. Aronsson, B. J. Chippendale, J. A. Faust, B. E. Pavri, C. J. Chovit, M. Solis, M. R. Olah, and O. Williams. Imaging spectroscopy and the airborne visible/infrared imaging spectrometer (aviris). *Remote Sensing of Environment*, 65(3):227 – 248, 1998. doi: https://doi.org/10.1016/S0034-4257(98)00064-9. URL http://www.sciencedirect.com/science/article/pii/S0034425798000649.

R. O. Green, N. Mahowald, C. Ung, D. R. Thompson, L. Bator, M. Bennet, M. Bernas, N. Blackway, C. Bradley, J. Cha, P. Clark, R. Clark, D. Cloud, E. Diaz, E. Ben Dor, R. Duren, M. Eastwood, B. L. Ehlmann, L. Fuentes, P. Ginoux, J. Gross, Y. He, O. Kalashnikova, W. Kert, D. Keymeulen, M. Klimesh, D. Ku, H. Kwong-Fu, E. Liggett, L. Li, S. Lundeen, M. D. Makowski, A. Mazer, R. Miller, P. Mouroulis, B. Oaida, G. S. Okin, A. Ortega, A. Oyake, H. Nguyen, T. Pace, T. H. Painter, J. Pempejian, C. P. Garcia-Pando, T. Pham, B. Phillips, R. Pollock, R. Purcell, V. Realmuto, J. Schoolcraft, A. Sen, S. Shin, L. Shaw, M. Soriano, G. Swayze, E. Thingvold, A. Vaid, and

J. Zan. The earth surface mineral dust source investigation: An earth science imaging spectroscopy mission. In *2020 IEEE Aerospace Conference*, pages 1–15, 2020. doi: 10.1109/AERO47225.2020.9172731. URL https://ieeexplore.ieee.org/document/9172731.

D. W. Griffith, N. M. Deutscher, V. A. Velazco, P. O. Wennberg, Y. Yavin, G. Keppel-Aleks, R. A. Washenfelder, G. C. Toon, J.-F. Blavier, C. Paton-Walsh, N. B. Jones, G. C. Kettlewell, B. J. Connor, R. C. Macatangay, C. Roehl, M. Ryczek, J. Glowacki, T. Culgan, and G. W. Bryant. TCCON data from Darwin (AU), Release GGG2014.R0, 2014a. URL https://doi.org/10.14291/tccon.ggg2014.darwin01.r0/1149290.

D. W. Griffith, V. A. Velazco, N. M. Deutscher, C. Paton-Walsh, N. B. Jones, S. R. Wilson, R. C. Macatangay, G. C. Kettlewell, R. R. Buchholz, and M. O. Riggenbach. TCCON data from Wollongong (AU), Release GGG2014.R0, 2014b. URL https://doi.org/10.14291/tccon.ggg2014.wollongong01.r0/1149291.

L. Guanter, H. Kaufmann, K. Segl, S. Foerster, C. Rogass, S. Chabrillat, T. Kuester, A. Hollstein, G. Rossner, C. Chlebek, C. Straif, S. Fischer, S. Schrader, T. Storch, U. Heiden, A. Mueller, M. Bachmann, H. Mühle, R. Müller, M. Habermeyer, A. Ohndorf, J. Hill, H. Buddenbaum, P. Hostert, S. Van der Linden, P. J. Leitão, A. Rabe, R. Doerffer, H. Krasemann, H. Xi, W. Mauser, T. Hank, M. Locherer, M. Rast, K. Staenz, and B. Sang. The enmap spaceborne imaging spectroscopy mission for earth observation. *Remote Sensing*, 7(7):8830–8857, 2015. doi: 10.3390/rs70708830. URL https://www.mdpi.com/2072-4292/7/7/8830.

S. Guerlet, S. Basu, A. Butz, M. Krol, P. Hahne, S. Houweling, O. P. Hasekamp, and I. Aben. Reduced carbon uptake during the 2010 northern hemisphere summer from GOSAT. *Geophysical Research Letters*, 40(10):2378–2383, 2013a. doi: 10.1002/grl.50402. URL https://doi.org/10.1002/grl.50402.

S. Guerlet, A. Butz, D. Schepers, S. Basu, O. P. Hasekamp, A. Kuze, T. Yokota, J. F. Blavier, N. M. Deutscher, D. W. Griffith, F. Hase, E. Kyro, I. Morino, V. Sherlock, R. Sussmann, A. Galli, and I. Aben. Impact of aerosol and thin cirrus on retrieving and validating XCO_2 from GOSAT shortwave infrared measurements. *Journal of Geophysical Research Atmospheres*, 118(10):4887–4905, 2013b. doi: 10.1002/jgrd.50332. URL https://doi.org/10.1002/jgrd.50332.

J. Hakkarainen, I. Ialongo, and J. Tamminen. Direct space-based observations of anthropogenic CO_2 emission areas from OCO2. *Geophysical Research Letters*, 43(11):400–411, 2016. doi: 10.1002/2016GL070885. URL https://doi.org/10.1002/2016GL070885.

L. Hamlin, R. O. Green, P. Mouroulis, M. Eastwood, D. Wilson, M. Dudik, and C. Paine. Imaging spectrometer science measurements for terrestrial ecology: AVIRIS and new developments. In *2011 Aerospace Conference*, pages 1–7, 2011. doi: 10.1109/AERO.2011.5747395. URL https://ieeexplore.ieee.org/document/5747395.

J. E. Hansen and L. D. Travis. Light scattering in planetary atmospheres. *Space Science Reviews*, 16(4):527 – 610, 1974. doi: 10.1007/BF00168069. URL https://doi.org/10.1007/BF00168069.

P. C. Hansen. Analysis of discrete ill-posed problems by means of the L-curve. *SIAM Review*, 34(4):561–580, 1992. doi: 10.1137/1034115. URL https://doi.org/10.1137/1034115.

P. C. Hansen and D. P. O'Leary. The use of the L-curve in the regularization of discrete ill-posed problems. *SIAM Journal on Scientific Computing*, 14(6):1487–1503, 1993. doi: 10.1137/0914086. URL https://doi.org/10.1137/0914086.

F. Hase, T. Blumenstock, and C. Paton-Walsh. Analysis of the instrumental line shape of high-resolution fourier transform ir spectrometers with gas cell measurements and new retrieval software. *Applied Optics*, 38(15):3417–3422, May 1999. doi: 10.1364/AO.38.003417. URL http://ao.osa.org/abstract.cfm?URI=ao-38-15-3417.

F. Hase, T. Blumenstock, S. Dohe, J. Groß, and M. Kiel. TCCON data from Karlsruhe (DE), Release GGG2014.R1, 2015. URL https://doi.org/10.14291/tccon.ggg2014.karlsruhe01.r1/1182416.

O. Hasekamp and J. Landgraf. A linearized vector radiative transfer model for atmospheric trace gas retrieval. *Journal of Quantitative Spectroscopy and Radiative Transfer*, 75(2):221 – 238, 2002. doi: https://doi.org/10.1016/S0022-4073(01)00247-3. URL http://www.sciencedirect.com/science/article/pii/S0022407301002473.

O. P. Hasekamp, G. Fu, S. P. Rusli, L. Wu, A. D. Noia, J. aan de Brugh, J. Landgraf, J. M. Smit, J. Rietjens, and A. van Amerongen. Aerosol measurements by SPEXone on the NASA PACE mission: expected retrieval capabilities. *Journal of Quantitative Spectroscopy and Radiative Transfer*, 227:170 – 184, 2019. doi: 10.1016/j.jqsrt.2019.02.006. URL http://www.sciencedirect.com/science/article/pii/S0022407318308653.

T. A. Hennig, J. L. Kretsch, C. J. Pessagno, P. H. Salamonowicz, and W. Stein. The shuttle radar topography mission. In *Digital Earth Moving*, 2001.

H. Herbin, L. C. Labonnote, and P. Dubuisson. Multispectral information from TANSO-FTS instrument – Part 1: Application to greenhouse gases (CO_2 and CH_4) in clear sky conditions. *Atmospheric Measurement Techniques*, 6(11):3301–3311, 2013. doi: 10.5194/amt-6-3301-2013. URL https://amt.copernicus.org/articles/6/3301/2013/.

H. Hersbach, B. Bell, P. Berrisford, S. Hirahara, A. Horányi, J. Muñoz-Sabater, J. Nicolas, C. Peubey, R. Radu, D. Schepers, A. Simmons, C. Soci, S. Abdalla, X. Abellan, G. Balsamo, P. Bechtold, G. Biavati, J. Bidlot, M. Bonavita, G. De Chiara, P. Dahlgren, D. Dee, M. Diamantakis, R. Dragani, J. Flemming, R. Forbes, M. Fuentes, A. Geer, L. Haimberger, S. Healy, R. J. Hogan, E. Hólm, M. Janisková, S. Keeley, P. Laloyaux, P. Lopez, C. Lupu, G. Radnoti, P. de Rosnay, I. Rozum, F. Vamborg, S. Villaume, and

J.-N. Thépaut. The ERA5 global reanalysis. *Quarterly Journal of the Royal Meteorological Society*, 146(730):1999–2049, 2020. doi: https://doi.org/10.1002/qj.3803. URL https://rmets.onlinelibrary.wiley.com/doi/abs/10.1002/qj.3803.

E. J. Hochberg, D. A. Roberts, P. E. Dennison, and G. C. Hulley. Special issue on the Hyperspectral Infrared Imager (HyspIRI): Emerging science in terrestrial and aquatic ecology, radiation balance and hazards. *Remote Sensing of Environment*, 167:1–5, 2015. doi: https://doi.org/10.1016/j.rse.2015.06.011. URL https://www.sciencedirect.com/science/article/pii/S0034425715300420. Special Issue on the Hyperspectral Infrared Imager (HyspIRI).

L. Höppler, F. Gödde, M. Gutleben, T. Kölling, B. Mayer, and T. Zinner. Synergy of active- and passive remote sensing: An approach to reconstruct three-dimensional cloud macro- and microphysics. *Atmospheric Measurement Techniques Discussions*, 2020:1–37, 2020. doi: 10.5194/amt-2020-49. URL https://amt.copernicus.org/preprints/amt-2020-49/.

H. Hu, O. Hasekamp, A. Butz, A. Galli, J. Landgraf, J. Aan de Brugh, T. Borsdorff, R. Scheepmaker, and I. Aben. The operational methane retrieval algorithm for TROPOMI. *Atmospheric Measurement Techniques*, 9(11):5423–5440, 2016. doi: 10.5194/amt-9-5423-2016. URL https://amt.copernicus.org/articles/9/5423/2016/.

H. Hu, J. Landgraf, R. Detmers, T. Borsdorff, J. Aan de Brugh, I. Aben, A. Butz, and O. Hasekamp. Toward global mapping of methane with TROPOMI: first results and intersatellite comparison to GOSAT. *Geophysical Research Letters*, 45(8):3682–3689, 2018. doi: 10.1002/2018GL077259. URL https://doi.org/10.1002/2018GL077259.

Y. Huang, V. Natraj, Z.-C. Zeng, P. Kopparla, and Y. L. Yung. Quantifying the impact of aerosol scattering on the retrieval of methane from airborne remote sensing measurements. *Atmospheric Measurement Techniques*, 13(12):6755–6769, 2020. doi: 10.5194/amt-13-6755-2020. URL https://amt.copernicus.org/articles/13/6755/2020/.

J. Humlicek. Optimized computation of the voigt and complex probability functions. *Journal of Quantitative Spectroscopy and Radiative Transfer*, 27(4):437 – 444, 1982. doi: https://doi.org/10.1016/0022-4073(82)90078-4. URL http://www.sciencedirect.com/science/article/pii/0022407382900784.

T. Hummel, C. Meister, J. Krauser, and M. Wenig. Slit homogenizer introduced performance gain analysis based on Sentinel-5/UVNS spectrometer. *Atmospheric Measurement Techniques Discussions*, 2021:1–18, 2021. doi: 10.5194/amt-2021-15. URL https://amt.copernicus.org/preprints/amt-2021-15/.

International Energy Agency. Global energy and CO2 status report 2019. https://www.iea.org/reports/global-energy-co2-status-report-2019/emissions, 2021. Last accessed: 2021-03-16.

L. T. Iraci, J. R. Podolske, P. W. Hillyard, C. Roehl, P. O. Wennberg, J.-F. Blavier, J. Landeros, N. Allen, D. Wunch, J. Zavaleta, E. Quigley, G. B. Osterman, R. Albertson, K. Dunwoody, and H. Boyden. TCCON data from Edwards (US), Release GGG2014.R1, 2016a. URL https://doi.org/10.14291/tccon.ggg2014.edwards01.r1/1255068.

L. T. Iraci, J. R. Podolske, P. W. Hillyard, C. Roehl, P. O. Wennberg, J.-F. Blavier, J. Landeros, N. Allen, D. Wunch, J. Zavaleta, E. Quigley, G. B. Osterman, E. Barrow, and J. Barney. TCCON data from Indianapolis (US), Release GGG2014.R1, 2016b. URL https://doi.org/10.14291/tccon.ggg2014.indianapolis01.r1/1330094.

H. Ishida, T. Y. Nakjima, T. Yokota, N. Kikuchi, and H. Watanabe. Investigation of GOSAT TANSO-CAI cloud screening ability through an intersatellite comparison. *Journal of Applied Meteorology and Climatology*, 50(7):1571 – 1586, 2011. doi: 10.1175/2011JAMC2672.1. URL https://journals.ametsoc.org/view/journals/apme/50/7/2011jamc2672.1.xml.

R. G. Jaacks and H. Rippel. Double pendulum michelson interferometer with extended spectral resolution. *Appl. Opt.*, 28(1):29–30, 1989. doi: 10.1364/AO.28.0029_1. URL http://ao.osa.org/abstract.cfm?URI=ao-28-1-29_1.

D. J. Jacob, A. J. Turner, J. D. Maasakkers, J. Sheng, K. Sun, X. Liu, K. Chance, I. Aben, J. McKeever, and C. Frankenberg. Satellite observations of atmospheric methane and their value for quantifying methane emissions. *Atmospheric Chemistry and Physics*, 16(22):14371–14396, 2016. doi: 10.5194/acp-16-14371-2016. URL https://acp.copernicus.org/articles/16/14371/2016/.

E. Jäkel, M. Wendisch, T. C. Krisna, F. Ewald, T. Kölling, T. Jurkat, C. Voigt, M. A. Cecchini, L. A. T. Machado, A. Afchine, A. Costa, M. Krämer, M. O. Andreae, U. Pöschl, D. Rosenfeld, and T. Yuan. Vertical distribution of the particle phase in tropical deep convective clouds as derived from cloud-side reflected solar radiation measurements. *Atmospheric Chemistry and Physics*, 17(14):9049–9066, 2017. doi: 10.5194/acp-17-9049-2017. URL https://acp.copernicus.org/articles/17/9049/2017/.

J. Jia, Y. Wang, J. Chen, R. Guo, R. Shu, and J. Wang. Status and application of advanced airborne hyperspectral imaging technology: A review. *Infrared Physics & Technology*, 104:103115, 2020. doi: 10.1016/j.infrared.2019.103115. URL http://www.sciencedirect.com/science/article/pii/S1350449519307649.

F. Jiang, H. Wang, J. M. Chen, W. Ju, X. Tian, S. Feng, G. Li, Z. Chen, S. Zhang, X. Lu, J. Liu, H. Wang, J. Wang, W. He, and M. Wu. Regional co_2 fluxes from 2010 to 2015 inferred from gosat xco_2 retrievals using a new version of the global carbon assimilation system. *Atmospheric Chemistry and Physics*, 21(3):1963–1985, 2021. doi: 10.5194/acp-21-1963-2021. URL https://acp.copernicus.org/articles/21/1963/2021/.

S. Jongaramrungruang, C. Frankenberg, G. Matheou, A. K. Thorpe, D. R. Thompson, L. Kuai, and R. M. Duren. Towards accurate methane point-source quantification

from high-resolution 2-d plume imagery. *Atmospheric Measurement Techniques*, 12(12): 6667–6681, 2019. doi: 10.5194/amt-12-6667-2019. URL https://amt.copernicus.org/articles/12/6667/2019/.

JPL. *CO_2 virtual science data environment*, 2018. https://co2.jpl.nasa.gov/download/?dataset=ACOSv3.5&product=FULL, Last accessed: 2018-08-18.

S. Kawakami, H. Ohyama, K. Arai, H. Okumura, C. Taura, T. Fukamachi, and M. Sakashita. TCCON data from Saga (JP), Release GGG2014.R0, 2014. URL https://doi.org/10.14291/tccon.ggg2014.saga01.r0/1149283.

M. Kiel, C. W. O'Dell, B. Fisher, A. Eldering, R. Nassar, C. G. MacDonald, and P. O. Wennberg. How bias correction goes wrong: measurement of xco_2 affected by erroneous surface pressure estimates. *Atmospheric Measurement Techniques*, 12(4): 2241–2259, 2019. doi: 10.5194/amt-12-2241-2019. URL https://doi.org/10.5194/amt-12-2241-2019.

M. Kiel, A. Eldering, D. D. Roten, J. C. Lin, S. Feng, R. Lei, T. Lauvaux, T. Oda, C. M. Roehl, J.-F. Blavier, and L. T. Iraci. Urban-focused satellite co2 observations from the orbiting carbon observatory-3: A first look at the los angeles megacity. *Remote Sensing of Environment*, 258:112314, 2021. doi: https://doi.org/10.1016/j.rse.2021.112314. URL https://www.sciencedirect.com/science/article/pii/S0034425721000328.

R. Kivi, P. Heikkinen, and E. Kyrö. TCCON data from Sodankylä (FI), Release GGG2014.R0, 2014. URL https://doi.org/10.14291/tccon.ggg2014.sodankyla01.r0/1149280.

T. Klausner, M. Mertens, H. Huntrieser, M. Galkowski, G. Kuhlmann, R. Baumann, A. Fiehn, P. Joeckel, M. Puehl, and A. Roiger. Urban greenhouse gas emissions from the Berlin area: A case study using airborne CO2 and CH4 in situ observations in summer 2018. *Elementa-Science of the Anthropocene*, 8, 2020. doi: 10.1525/elementa.411. URL https://doi.org/10.1525/elementa.411.

M. Knapp, R. Kleinschek, F. Hase, A. Agustí-Panareda, A. Inness, J. Barré, J. Landgraf, T. Borsdorff, S. Kinne, and A. Butz. Shipborne measurements of XCO_2, XCH_4, and XCO above the pacific ocean and comparison to CAMS atmospheric analyses and S5P/TROPOMI. *Earth System Science Data*, 13(1):199–211, 2021. doi: 10.5194/essd-13-199-2021. URL https://essd.copernicus.org/articles/13/199/2021/.

R. Kochanov, I. Gordon, L. Rothman, P. Wcislo, C. Hill, and J. Wilzewski. HITRAN Application Programming Interface (HAPI): A comprehensive approach to working with spectroscopic data. *Journal of Quantitative Spectroscopy and Radiative Transfer*, 177: 15 – 30, 2016. doi: https://doi.org/10.1016/j.jqsrt.2016.03.005. URL http://www.sciencedirect.com/science/article/pii/S0022407315302466.

T. Kölling, T. Zinner, and B. Mayer. Aircraft-based stereographic reconstruction of 3-d cloud geometry. *Atmospheric Measurement Techniques*, 12(2):1155–1166, 2019. doi: 10.5194/amt-12-1155-2019. URL https://www.atmos-meas-tech.net/12/1155/2019/.

E. A. Kort, C. Frankenberg, C. E. Miller, and T. Oda. Space-based observations of megacity carbon dioxide. *Geophysical Research Letters*, 39(17), 2012. doi: 10.1029/2012GL052738. URL https://doi.org/10.1029/2012GL052738.

S. Krautwurst, K. Gerilowski, H. H. Jonsson, D. R. Thompson, R. W. Kolyer, L. T. Iraci, A. K. Thorpe, M. Horstjann, M. Eastwood, I. Leifer, S. A. Vigil, T. Krings, J. Borchardt, M. Buchwitz, M. M. Fladeland, J. P. Burrows, and H. Bovensmann. Methane emissions from a californian landfill, determined from airborne remote sensing and in situ measurements. *Atmospheric Measurement Techniques*, 10(9):3429–3452, 2017. doi: 10.5194/amt-10-3429-2017. URL https://amt.copernicus.org/articles/10/3429/2017/.

T. Krings, K. Gerilowski, M. Buchwitz, M. Reuter, A. Tretner, J. Erzinger, D. Heinze, U. Pflüger, J. P. Burrows, and H. Bovensmann. Mamap – a new spectrometer system for column-averaged methane and carbon dioxide observations from aircraft: retrieval algorithm and first inversions for point source emission rates. *Atmospheric Measurement Techniques*, 4(9):1735–1758, 2011. doi: 10.5194/amt-4-1735-2011. URL https://amt.copernicus.org/articles/4/1735/2011/.

T. Krings, K. Gerilowski, M. Buchwitz, J. Hartmann, T. Sachs, J. Erzinger, J. P. Burrows, and H. Bovensmann. Quantification of methane emission rates from coal mine ventilation shafts using airborne remote sensing data. *Atmospheric Measurement Techniques*, 6(1):151–166, 2013. doi: 10.5194/amt-6-151-2013. URL https://amt.copernicus.org/articles/6/151/2013/.

T. Krings, B. Neininger, K. Gerilowski, S. Krautwurst, M. Buchwitz, J. P. Burrows, C. Lindemann, T. Ruhtz, D. Schüttemeyer, and H. Bovensmann. Airborne remote sensing and in situ measurements of atmospheric CO_2 to quantify point source emissions. *Atmospheric Measurement Techniques*, 11(2):721–739, 2018. doi: 10.5194/amt-11-721-2018. URL https://doi.org/10.5194/amt-11-721-2018.

G. Kuhlmann, G. Broquet, J. Marshall, V. Clément, A. Löscher, Y. Meijer, and D. Brunner. Detectability of CO_2 emission plumes of cities and power plants with the Copernicus anthropogenic CO_2 monitoring (CO2M) mission. *Atmospheric Measurement Techniques*, 12(12):6695–6719, 2019. doi: 10.5194/amt-12-6695-2019. URL https://amt.copernicus.org/articles/12/6695/2019/.

G. Kuhlmann, D. Brunner, G. Broquet, and Y. Meijer. Quantifying CO_2 emissions of a city with the Copernicus anthropogenic CO_2 monitoring satellite mission. *Atmospheric Measurement Techniques*, 13(12):6733–6754, 2020. doi: 10.5194/amt-13-6733-2020. URL https://amt.copernicus.org/articles/13/6733/2020/.

S. S. Kulawik, C. O'Dell, V. H. Payne, L. Kuai, H. M. Worden, S. C. Biraud, C. Sweeney, B. Stephens, L. T. Iraci, E. L. Yates, and T. Tanaka. Lower-tropospheric co_2 from near-infrared acos-gosat observations. *Atmospheric Chemistry and Physics*, 17(8):5407–5438, 2017. doi: 10.5194/acp-17-5407-2017. URL https://acp.copernicus.org/articles/17/5407/2017/.

S. Kumar, C. Torres, O. Ulutan, A. Ayasse, D. Roberts, and B. S. Manjunath. Deep remote sensing methods for methane detection in overhead hyperspectral imagery. In *Proceedings of the IEEE/CVF Winter Conference on Applications of Computer Vision (WACV)*, March 2020. URL https://openaccess.thecvf.com/content_WACV_2020/html/Kumar_Deep_Remote_Sensing_Methods_for_Methane_Detection_in_Overhead_Hyperspectral_WACV_2020_paper.html. Last accessed: 2021-05-04.

A. Kuze, H. Suto, M. Nakajima, and T. Hamazaki. Thermal and near infrared sensor for carbon observation fourier-transform spectrometer on the greenhouse gases observing satellite for greenhouse gases monitoring. *Applied Optics*, 48(35):6716, 2009. doi: 10.1364/AO.48.006716. URL https://doi.org/10.1364/AO.48.006716.

A. Kuze, D. M. O'Brien, T. E. Taylor, J. O. Day, C. W. O'Dell, F. Kataoka, M. Yoshida, Y. Mitomi, C. J. Bruegge, H. Pollock, R. Basilio, M. Helmlinger, T. Matsunaga, S. Kawakami, K. Shiomi, T. Urabe, and H. Suto. Vicarious calibration of the gosat sensors using the railroad valley desert playa. *IEEE Transactions on Geoscience and Remote Sensing*, 49(5):1781–1795, 2011. doi: 10.1109/TGRS.2010.2089527. URL https://doi.org/10.1109/TGRS.2010.2089527.

A. Kuze, T. E. Taylor, F. Kataoka, C. J. Bruegge, D. Crisp, M. Harada, M. Helmlinger, M. Inoue, S. Kawakami, N. Kikuchi, Y. Mitomi, J. Murooka, M. Naitoh, D. M. O'Brien, C. W. O'Dell, H. Ohyama, H. Pollock, F. M. Schwandner, K. Shiomi, H. Suto, T. Takeda, T. Tanaka, T. Urabe, T. Yokota, and Y. Yoshida. Long-term vicarious calibration of GOSAT short-wave sensors: Techniques for error reduction and new estimates of radiometric degradation factors. *IEEE Transactions on Geoscience and Remote Sensing*, 52(7):3991–4004, 2014. doi: 10.1109/TGRS.2013.2278696. URL https://doi.org/10.1109/TGRS.2013.2278696.

A. Kuze, H. Suto, K. Shiomi, S. Kawakami, M. Tanaka, Y. Ueda, A. Deguchi, J. Yoshida, Y. Yamamoto, F. Kataoka, T. E. Taylor, and H. L. Buijs. Update on GOSAT TANSO-FTS performance, operations, and data products after more than 6 years in space. *Atmospheric Measurement Techniques*, 9(6):2445–2461, 2016. doi: 10.5194/amt-9-2445-2016. URL https://doi.org/10.5194/amt-9-2445-2016.

A. Kuze, N. Kikuchi, F. Kataoka, H. Suto, K. Shiomi, and Y. Kondo. Detection of methane emission from a local dource using GOSAT target observations. *Remote Sensing*, 12(2):267, 2020. doi: 10.3390/rs12020267. URL http://dx.doi.org/10.3390/rs12020267.

J. Lamouroux, H. Tran, A. L. Laraia, R. R. Gamache, L. S. Rothman, I. E. Gordon, and J. M. Hartmann. Updated database plus software for line-mixing in CO2 infrared spectra and their test using laboratory spectra in the 1.5-2.3γm region. *Journal of Quantitative Spectroscopy and Radiative Transfer*, 111(15):2321–2331, 2010. doi: 10.1016/j.jqsrt.2010.03.006. URL https://doi.org/10.1016/j.jqsrt.2010.03.006.

J. Landgraf, O. P. Hasekamp, M. A. Box, and T. Trautmann. A linearized radiative transfer model for ozone profile retrieval using the analytical forward-adjoint perturbation theory approach. *Journal of Geophysical Research: Atmospheres*, 106(D21):27291–27305, 2001. doi: 10.1029/2001JD000636. URL https://agupubs.onlinelibrary.wiley.com/doi/abs/10.1029/2001JD000636.

C. M. Lee, M. L. Cable, S. J. Hook, R. O. Green, S. L. Ustin, D. J. Mandl, and E. M. Middleton. An introduction to the NASA Hyperspectral InfraRed Imager (HyspIRI) mission and preparatory activities. *Remote Sensing of Environment*, 167:6 – 19, 2015. doi: https://doi.org/10.1016/j.rse.2015.06.012. URL http://www.sciencedirect.com/science/article/pii/S0034425715300419.

L. Li, M. Li, Z. Zhang, and Z.-L. Huang. Assessing low-light cameras with photon transfer curve method. *Journal of Innovative Optical Health Sciences*, 09(03):1630008, 2016. doi: 10.1142/S1793545816300081. URL https://doi.org/10.1142/S1793545816300081.

R. Lindenmaier, M. K. Dubey, B. G. Henderson, Z. T. Butterfield, J. R. Herman, T. Rahn, and S.-H. Lee. Multiscale observations of CO2, 13CO2, and pollutants at Four Corners for emission verification and attribution. *Proceedings of the National Academy of Sciences*, 111(23):8386–8391, 2014. doi: 10.1073/pnas.1321883111. URL https://www.pnas.org/content/111/23/8386.

H. Lindqvist, C. W. O'Dell, S. Basu, H. Boesch, F. Chevallier, N. Deutscher, L. Feng, B. Fisher, F. Hase, M. Inoue, R. Kivi, I. Morino, P. I. Palmer, R. Parker, M. Schneider, R. Sussmann, and Y. Yoshida. Does GOSAT capture the true seasonal cycle of carbon dioxide? *Atmospheric Chemistry and Physics*, 15(22):13023–13040, 2015. doi: 10.5194/acp-15-13023-2015. URL https://acp.copernicus.org/articles/15/13023/2015/.

K.-N. Liou. *An introduction to atmospheric radiation*. Academic Press, Inc., 1980.

C. Liu, W. Wang, Y. Sun, and ,. TCCON data from Hefei (PRC), Release GGG2014.R0, 2018. URL https://doi.org/10.14291/tccon.ggg2014.hefei01.r0.

J. Liu, K. W. Bowman, D. S. Schimel, N. C. Parazoo, Z. Jiang, M. Lee, A. A. Bloom, D. Wunch, C. Frankenberg, Y. Sun, C. W. O'Dell, K. R. Gurney, D. Menemenlis, M. Gierach, D. Crisp, and A. Eldering. Contrasting carbon cycle responses of the tropical continents to the 2015–2016 El Niño. *Science*, 358(6360), 2017. doi: 10.1126/science.aam5690. URL https://doi.org/10.1126/science.aam5690.

Y. Liu, X. Wang, M. Guo, and H. Tani. Comparison of GOSAT CAI and SPOT VGT NDVI data with different season and land cover in East Asia. *ISPRS - International Archives of the Photogrammetry, Remote Sensing and Spatial Information Sciences*, XXXVIII-4/W25:94–97, 2011. doi: 10.5194/isprsarchives-XXXVIII-4-W25-94-2011. URL https://www.int-arch-photogramm-remote-sens-spatial-inf-sci.net/XXXVIII-4-W25/94/2011/.

R. Loizzo, R. Guarini, F. Longo, T. Scopa, R. Formaro, C. Facchinetti, and G. Varacalli. Prisma: The italian hyperspectral mission. In *IGARSS 2018 - 2018 IEEE International Geoscience and Remote Sensing Symposium*, pages 175–178, 2018. doi: 10.1109/IGARSS.2018.8518512. URL https://ieeexplore.ieee.org/document/8518512.

A. Lorente, T. Borsdorff, A. Butz, O. Hasekamp, J. aan de Brugh, A. Schneider, F. Hase, R. Kivi, D. Wunch, D. F. Pollard, K. Shiomi, N. M. Deutscher, V. A. Velazco, C. M. Roehl, P. O. Wennberg, T. Warneke, and J. Landgraf. Methane retrieved from TROPOMI: improvement of the data product and validation of the first two years of measurements. *Atmospheric Measurement Techniques Discussions*, 2020:1–28, 2020. doi: 10.5194/amt-2020-281. URL https://amt.copernicus.org/preprints/amt-2020-281/.

A. Luther, R. Kleinschek, L. Scheidweiler, S. Defratyka, M. Stanisavljevic, A. Forstmaier, A. Dandocsi, S. Wolff, D. Dubravica, N. Wildmann, J. Kostinek, P. Jöckel, A.-L. Nickl, T. Klausner, F. Hase, M. Frey, J. Chen, F. Dietrich, J. Necki, J. Swolkien, A. Fix, A. Roiger, and A. Butz. Quantifying ch_4 emissions from hard coal mines using mobile sun-viewing fourier transform spectrometry. *Atmospheric Measurement Techniques*, 12 (10):5217–5230, 2019. doi: 10.5194/amt-12-5217-2019. URL https://amt.copernicus.org/articles/12/5217/2019/.

C. D. Mackay. Charge-coupled devices in astronomy. *Annual Review of Astronomy and Astrophysics*, 24(1):255–283, 1986. doi: 10.1146/annurev.aa.24.090186.001351. URL https://doi.org/10.1146/annurev.aa.24.090186.001351.

D. Manolakis, R. Lockwood, T. Cooley, and J. Jacobson. Robust matched filters for hyperspectral target detection. In *2006 IEEE International Symposium on Geoscience and Remote Sensing*, pages 368–370, 2006. doi: 10.1109/IGARSS.2006.99. URL https://ieeexplore.ieee.org/document/4241246.

D. Manolakis, R. Lockwood, T. Cooley, and J. Jacobson. Hyperspectral detection algorithms: use covariances or subspaces? In *Imaging Spectrometry XIV*, volume 7457, pages 200 – 207. International Society for Optics and Photonics, SPIE, 2009. doi: 10.1117/12.828397. URL https://doi.org/10.1117/12.828397.

R. Marion, R. Michel, and C. Faye. Measuring trace gases in plumes from hyperspectral remotely sensed data. *IEEE Transactions on Geoscience and Remote Sensing*, 42(4): 854–864, 2004. doi: 10.1109/TGRS.2003.820604. URL https://doi.org/10.1109/TGRS.2003.820604.

P. Martimort, V. Fernandez, V. Kirschner, C. Isola, and A. Meygret. Sentinel-2 multispectral imager (MSI) and calibration/validation. In *2012 IEEE International Geoscience and Remote Sensing Symposium*, pages 6999–7002, 2012. doi: 10.1109/IGARSS.2012.6351960. URL https://ieeexplore.ieee.org/document/6351960.

S. Mauceri, B. Kindel, S. Massie, and P. Pilewskie. Neural network for aerosol retrieval from hyperspectral imagery. *Atmospheric Measurement Techniques*, 12(11):6017–6036, 2019. doi: 10.5194/amt-12-6017-2019. URL https://amt.copernicus.org/articles/12/6017/2019/.

B. Mayer. Radiative transfer in the cloudy atmosphere. *EPJ Web of Conferences*, 1:75–99, 2009. doi: 10.1140/epjconf/e2009-00912-1. URL https://doi.org/10.1140/epjconf/e2009-00912-1.

J. Messerschmidt, M. C. Geibel, T. Blumenstock, H. Chen, N. M. Deutscher, A. Engel, D. G. Feist, C. Gerbig, M. Gisi, F. Hase, K. Katrynski, O. Kolle, J. V. Lavrič, J. Notholt, M. Palm, M. Ramonet, M. Rettinger, M. Schmidt, R. Sussmann, G. C. Toon, F. Truong, T. Warneke, P. O. Wennberg, D. Wunch, and I. Xueref-Remy. Calibration of TCCON column-averaged CO_2: the first aircraft campaign over European TCCON sites. *Atmospheric Chemistry and Physics*, 11(21):10765–10777, 2011. doi: 10.5194/acp-11-10765-2011. URL https://doi.org/10.5194/acp-11-10765-2011.

S. M. Miller, A. M. Michalak, R. G. Detmers, O. P. Hasekamp, L. M. P. Bruhwiler, and S. Schwietzke. China's coal mine methane regulations have not curbed growing emissions. *Nature Communications*, 10, 2019. doi: 10.1038/s41467-018-07891-7. URL https://doi.org/10.1038/s41467-018-07891-7.

I. Morino, T. Matsuzaki, and M. Horikawa. TCCON data from Tsukuba (JP), 125HR, Release GGG2014.R2, 2018a. URL https://doi.org/10.14291/tccon.ggg2014.tsukuba02.r2.

I. Morino, N. Yokozeki, T. Matsuzaki, and M. Horikawa. TCCON data from Rikubetsu (JP), Release GGG2014.R2, 2018b. URL https://doi.org/10.14291/tccon.ggg2014.rikubetsu01.r2.

P. Mouroulis and R. O. Green. Review of high fidelity imaging spectrometer design for remote sensing. *Optical Engineering*, 57(4):1 – 19, 2018. doi: 10.1117/1.OE.57.4.040901. URL https://doi.org/10.1117/1.OE.57.4.040901.

M. Nakajima, H. Suto, K. Yotsumoto, K. Shiomi, and T. Hirabayashi. Fourier transform spectrometer on GOSAT and GOSAT-2. In *International Conference on Space Optics — ICSO 2014*, volume 10563, pages 1354 – 1362. SPIE, 2017. doi: 10.1117/12.2304062. URL https://doi.org/10.1117/12.2304062.

R. Nassar, T. G. Hill, C. A. McLinden, D. Wunch, D. B. A. Jones, and D. Crisp. Quantifying CO2 emissions from individual power plants from space. *Geophysical Research Letters*, 44(19):10,045–10,053, oct 2017. doi: 10.1002/2017GL074702. URL https://doi.org/10.1002/2017GL074702.

NCEP. National centers for environmental prediction: North american regional reanalysis (narr), 2005. URL https://rda.ucar.edu/datasets/ds608.0/. Last Accessed: 2021-04-27.

NOAA. NNDC Climate Data Online. https://www7.ncdc.noaa.gov/CDO/cdoselect.cmd?datasetabbv=SUMMARIES&countryabbv=&georegionabbv=&resolution=0, 2021. Last Accessed: 2021-02-22.

J. Notholt, C. Petri, T. Warneke, N. M. Deutscher, M. Palm, M. Buschmann, C. Weinzierl, R. C. Macatangay, and P. Grupe. TCCON data from Bremen (DE), Release GGG2014.R0, 2014. URL https://doi.org/10.14291/tccon.ggg2014.bremen01.r0/1149275.

D. M. O'Brien, I. Polonsky, C. O'Dell, A. Kuze, N. Kikuchi, Y. Yoshida, and V. Natraj. Testing the polarization model for TANSO-FTS on GOSAT against clear-sky observations of sun glint over the ocean. *IEEE Transactions on Geoscience and Remote Sensing*, 51(12):5199–5209, 2013. doi: 10.1109/TGRS.2012.2232673.

C. W. O'Dell, B. Connor, H. Bösch, D. O'Brien, C. Frankenberg, R. Castano, M. Christi, D. Eldering, B. Fisher, M. Gunson, J. McDuffie, C. E. Miller, V. Natraj, F. Oyafuso, I. Polonsky, M. Smyth, T. Taylor, G. C. Toon, P. O. Wennberg, and D. Wunch. The ACOS CO_2 retrieval algorithm - Part 1: Description and validation against synthetic observations. *Atmospheric Measurement Techniques*, 5(1):99–121, 2012. doi: 10.5194/amt-5-99-2012. URL https://www.atmos-meas-tech.net/5/99/2012/.

C. W. O'Dell, A. Eldering, P. O. Wennberg, D. Crisp, M. R. Gunson, B. Fisher, C. Frankenberg, M. Kiel, H. Lindqvist, L. Mandrake, A. Merrelli, V. Natraj, R. R. Nelson, G. B. Osterman, V. H. Payne, T. E. Taylor, D. Wunch, B. J. Drouin, F. Oyafuso, A. Chang, J. McDuffie, M. Smyth, D. F. Baker, S. Basu, F. Chevallier, S. M. R. Crowell, L. Feng, P. I. Palmer, M. Dubey, O. E. García, D. W. T. Griffith, F. Hase, L. T. Iraci, R. Kivi, I. Morino, J. Notholt, H. Ohyama, C. Petri, C. M. Roehl, M. K. Sha, K. Strong, R. Sussmann, Y. Te, O. Uchino, and V. A. Velazco. Improved retrievals of carbon dioxide from orbiting carbon observatory-2 with the version 8 ACOS algorithm. *Atmospheric Measurement Techniques*, 11(12):6539–6576, 2018. doi: 10.5194/amt-11-6539-2018. URL https://amt.copernicus.org/articles/11/6539/2018/.

S. Oshchepkov, A. Bril, T. Yokota, P. O. Wennberg, N. M. Deutscher, D. Wunch, G. C. Toon, Y. Yoshida, C. W. O'Dell, D. Crisp, C. E. Miller, C. Frankenberg, A. Butz, I. Aben, S. Guerlet, O. Hasekamp, H. Boesch, A. Cogan, R. Parker, D. Griffith, R. Macatangay,

J. Notholt, R. Sussmann, M. Rettinger, V. Sherlock, J. Robinson, E. Kyrö, P. Heikkinen, D. G. Feist, I. Morino, N. Kadygrov, D. Belikov, S. Maksyutov, T. Matsunaga, O. Uchino, and H. Watanabe. Effects of atmospheric light scattering on spectroscopic observations of greenhouse gases from space. Part 2: Algorithm intercomparison in the GOSAT data processing for CO2 retrievals over TCCON sites. *Journal of Geophysical Research: Atmospheres*, 118(3):1493–1512, 2013. doi: 10.1002/jgrd.50146. URL https://agupubs.onlinelibrary.wiley.com/doi/abs/10.1002/jgrd.50146.

S. Pandey, S. Houweling, M. Krol, I. Aben, G. Monteil, N. Nechita-Banda, E. J. Dlugokencky, R. Detmers, O. Hasekamp, X. Xu, W. J. Riley, B. Poulter, Z. Zhang, K. C. McDonald, J. W. C. White, P. Bousquet, and T. Rockmann. Enhanced methane emissions from tropical wetlands during the 2011 La Niña. *Scientific Reports*, 7, 2017. doi: 10.1038/srep45759. URL https://doi.org/10.1038/srep45759.

N. C. Parazoo, K. Bowman, C. Frankenberg, J. E. Lee, J. B. Fisher, J. Worden, D. B. Jones, J. Berry, G. J. Collatz, I. T. Baker, M. Jung, J. Liu, G. Osterman, C. O'Dell, A. Sparks, A. Butz, S. Guerlet, Y. Yoshida, H. Chen, and C. Gerbig. Interpreting seasonal changes in the carbon balance of southern Amazonia using measurements of XCO2 and chlorophyll fluorescence from GOSAT. *Geophysical Research Letters*, 40(11): 2829–2833, 2013. doi: 10.1002/grl.50452. URL https://doi.org/10.1002/grl.50452.

R. J. Parker, A. Webb, H. Boesch, P. Somkuti, R. Barrio Guillo, A. Di Noia, N. Kalaitzi, J. S. Anand, P. Bergamaschi, F. Chevallier, P. I. Palmer, L. Feng, N. M. Deutscher, D. G. Feist, D. W. T. Griffith, F. Hase, R. Kivi, I. Morino, J. Notholt, Y.-S. Oh, H. Ohyama, C. Petri, D. F. Pollard, C. Roehl, M. K. Sha, K. Shiomi, K. Strong, R. Sussmann, Y. Té, V. A. Velazco, T. Warneke, P. O. Wennberg, and D. Wunch. A decade of GOSAT proxy satellite CH_4 observations. *Earth System Science Data*, 12(4):3383–3412, 2020. doi: 10.5194/essd-12-3383-2020. URL https://essd.copernicus.org/articles/12/3383/2020/.

H. J. Paus. *Physik in Experimenten und Beispielen*. Carl Hanser Verlag, 2007.

W. Peters, A. R. Jacobson, C. Sweeney, A. E. Andrews, T. J. Conway, K. Masarie, J. B. Miller, L. M. P. Bruhwiler, G. Pétron, A. I. Hirsch, D. E. J. Worthy, G. R. van der Werf, J. T. Randerson, P. O. Wennberg, M. C. Krol, and P. P. Tans. An atmospheric perspective on north american carbon dioxide exchange: Carbontracker. *Proceedings of the National Academy of Sciences*, 104(48):18925–18930, 2007. doi: 10.1073/pnas.0708986104. URL https://www.pnas.org/content/104/48/18925.

G. W. Petty. *A First Course in Atmospheric Radiation*. Sundog Publishing, 2006.

D. L. Phillips. A technique for the numerical solution of certain integral equations of the first kind. *J. ACM*, 9(1):84–97, Jan. 1962. doi: 10.1145/321105.321114. URL https://doi.org/10.1145/321105.321114.

D. Pillai, M. Buchwitz, C. Gerbig, T. Koch, M. Reuter, H. Bovensmann, J. Marshall, and J. P. Burrows. Tracking city CO_2 emissions from space using a high-resolution inverse modeling approach: A case study for Berlin, Germany. *Atmospheric Chemistry and Physics*, 16(15):9591–9610, 2016. doi: 10.5194/acp-16-9591-2016. URL `https://doi.org/10.5194/acp-16-9591-2016`.

U. Platt and J. Stutz. *Differential Optical Absorption Spectroscopy*. Springer, 2008.

S. Prahl. "miepython". *GitHub repository*, 2020. URL `https://github.com/scottprahl/miepython`.

B. Raychaudhuri, S. Chaurasia, and S. Roy. Spatial variation of atmospheric carbon dioxide concentration retrieved from AVIRIS-NG images including water vapor correction and spectroradiometric validation for two urban places of India. In *Remote Sensing of Clouds and the Atmosphere XXIV*, volume 11152, pages 98 – 105. International Society for Optics and Photonics, SPIE, 2019. doi: 10.1117/12.2532027. URL `https://doi.org/10.1117/12.2532027`.

M. Reuter, M. Buchwitz, O. Schneising, J. Heymann, H. Bovensmann, and J. P. Burrows. A method for improved SCIAMACHY CO_2 retrieval in the presence of optically thin clouds. *Atmospheric Measurement Techniques*, 3(1):209–232, 2010. doi: 10.5194/amt-3-209-2010. URL `https://doi.org/10.5194/amt-3-209-2010`.

M. Reuter, M. Buchwitz, M. Hilker, J. Heymann, O. Schneising, D. Pillai, H. Bovensmann, J. P. Burrows, H. Bösch, R. Parker, A. Butz, O. Hasekamp, C. W. O'Dell, Y. Yoshida, C. Gerbig, T. Nehrkorn, N. M. Deutscher, T. Warneke, J. Notholt, F. Hase, R. Kivi, R. Sussmann, T. Machida, H. Matsueda, and Y. Sawa. Satellite-inferred European carbon sink larger than expected. *Atmospheric Chemistry and Physics*, 14(24):13739–13753, 2014. doi: 10.5194/acp-14-13739-2014. URL `https://acp.copernicus.org/articles/14/13739/2014/`.

M. Reuter, M. Buchwitz, O. Schneising, S. Krautwurst, C. W. O'Dell, A. Richter, H. Bovensmann, and J. P. Burrows. Towards monitoring localized CO_2 emissions from space: co-located regional CO_2 and NO_2 enhancements observed by the OCO-2 and S5P satellites. *Atmospheric Chemistry and Physics Discussions*, 2019:1–19, 2019. doi: 10.5194/acp-2019-15. URL `https://doi.org/10.5194/acp-2019-15`.

C. Richard, I. Gordon, L. Rothman, M. Abel, L. Frommhold, M. Gustafsson, J.-M. Hartmann, C. Hermans, W. Lafferty, G. Orton, K. Smith, and H. Tran. New section of the HITRAN database: Collision-induced absorption (CIA). *Journal of Quantitative Spectroscopy and Radiative Transfer*, 113(11):1276–1285, 2012. doi: https://doi.org/10.1016/j.jqsrt.2011.11.004. URL `https://www.sciencedirect.com/science/article/pii/S0022407311003773`.

D. A. Roberts, E. S. Bradley, R. Cheung, I. Leifer, P. E. Dennison, and J. S. Margolis. Mapping methane emissions from a marine geological seep source using imaging

spectrometry. *Remote Sensing of Environment*, 114(3):592 – 606, 2010. doi: https://doi.org/10.1016/j.rse.2009.10.015. URL http://www.sciencedirect.com/science/article/pii/S0034425709003241.

C. D. Rodgers. *Inverse Methods for Atmospheric Sounding: Theory and Practice*, volume 2 of *Series on Atmospheric, Oceanic and Planetary Physics*. World Scientific Publishing, Singapore, 2008.

C. D. Rodgers and B. J. Connor. Intercomparison of remote sounding instruments. *Journal of Geophysical Research: Atmospheres*, 108(D3), 2003. doi: https://doi.org/10.1029/2002JD002299. URL https://agupubs.onlinelibrary.wiley.com/doi/abs/10.1029/2002JD002299.

L. S. Rothman and L. D. Young. Infrared energy levels and intensities of carbon dioxide – II. *Journal of Quantitative Spectroscopy and Radiative Transfer*, 25(6):505 – 524, 1981. doi: https://doi.org/10.1016/0022-4073(81)90026-1. URL http://www.sciencedirect.com/science/article/pii/0022407381900261.

L. S. Rothman, R. R. Gamache, A. Goldman, L. R. Brown, R. A. Toth, H. M. Pickett, R. L. Poynter, J.-M. Flaud, C. Camy-Peyret, A. Barbe, N. Husson, C. P. Rinsland, and M. A. H. Smith. The HITRAN database: 1986 edition. *Appl. Opt.*, 26(19):4058–4097, Oct 1987. doi: 10.1364/AO.26.004058. URL http://ao.osa.org/abstract.cfm?URI=ao-26-19-4058.

L. S. Rothman, I. E. Gordon, A. Barbe, D. C. Benner, P. F. Bernath, M. Birk, V. Boudon, L. R. Brown, A. Campargue, J. P. Champion, K. Chance, L. H. Coudert, V. Dana, V. M. Devi, S. Fally, J. M. Flaud, R. R. Gamache, A. Goldman, D. Jacquemart, I. Kleiner, N. Lacome, W. J. Lafferty, J. Y. Mandin, S. T. Massie, S. N. Mikhailenko, C. E. Miller, N. Moazzen-Ahmadi, O. V. Naumenko, A. V. Nikitin, J. Orphal, V. I. Perevalov, A. Perrin, A. Predoi-Cross, C. P. Rinsland, M. Rotger, M. Šimečková, M. A. H. Smith, K. Sung, S. A. Tashkun, J. Tennyson, R. A. Toth, A. C. Vandaele, and J. Vander Auwera. The HITRAN 2008 molecular spectroscopic database. *Journal of Quantitative Spectroscopy and Radiative Transfer*, 110(9-10):533–572, 2009. doi: 10.1016/j.jqsrt.2009.02.013. URL https://doi.org/10.1016/j.jqsrt.2009.02.013.

N. Saitoh, S. Kimoto, R. Sugimura, R. Imasu, S. Kawakami, K. Shiomi, A. Kuze, T. Machida, Y. Sawa, and H. Matsueda. Algorithm update of the GOSAT/TANSO-FTS thermal infrared CO_2 product (version 1) and validation of the UTLS CO_2 data using CONTRAIL measurements. *Atmospheric Measurement Techniques*, 9(5):2119–2134, 2016. doi: 10.5194/amt-9-2119-2016. URL https://amt.copernicus.org/articles/9/2119/2016/.

A. Schäfler, G. Craig, H. Wernli, P. Arbogast, J. D. Doyle, R. McTaggart-Cowan, J. Methven, G. Rivière, F. Ament, M. Boettcher, M. Bramberger, Q. Cazenave, R. Cotton, S. Crewell, J. Delanoe, A. Dörnbrack, A. Ehrlich, F. Ewald, A. Fix, C. M.

Grams, S. L. Gray, H. Grob, S. Groß, M. Hagen, B. Harvey, L. Hirsch, M. Jacob, T. Kölling, H. Konow, C. Lemmerz, O. Lux, L. Magnusson, B. Mayer, M. Mech, R. Moore, J. Pelon, J. Quinting, S. Rahm, M. Rapp, M. Rautenhaus, O. Reitebuch, C. A. Reynolds, H. Sodemann, T. Spengler, G. Vaughan, M. Wendisch, M. Wirth, B. Witschas, K. Wolf, and T. Zinner. The north atlantic waveguide and downstream impact experiment. *Bulletin of the American Meteorological Society*, 99(8):1607 – 1637, 2018. doi: 10.1175/BAMS-D-17-0003.1. URL https://journals.ametsoc.org/view/journals/bams/99/8/bams-d-17-0003.1.xml.

D. Schepers, J. aan de Brugh, P. Hahne, A. Butz, O. Hasekamp, and J. Landgraf. LINTRAN v2.0: A linearised vector radiative transfer model for efficient simulation of satellite-born nadir-viewing reflection measurements of cloudy atmospheres. *Journal of Quantitative Spectroscopy and Radiative Transfer*, 149:347 – 359, 2014. doi: https://doi.org/10.1016/j.jqsrt.2014.08.019. URL http://www.sciencedirect.com/science/article/pii/S002240731400363X.

O. Schneising, J. Heymann, M. Buchwitz, M. Reuter, H. Bovensmann, and J. P. Burrows. Anthropogenic carbon dioxide source areas observed from space: assessment of regional enhancements and trends. *Atmospheric Chemistry and Physics*, 13(5):2445–2454, 2013. doi: 10.5194/acp-13-2445-2013. URL https://doi.org/10.5194/acp-13-2445-2013.

F. M. Schwandner, M. R. Gunson, C. E. Miller, S. A. Carn, A. Eldering, T. Krings, K. R. Verhulst, D. S. Schimel, H. M. Nguyen, D. Crisp, C. W. O'Dell, G. B. Osterman, L. T. Iraci, and J. R. Podolske. Spaceborne detection of localized carbon dioxide sources. *Science*, 358(6360), 2017. doi: 10.1126/science.aam5782. URL https://doi.org/10.1126/science.aam5782.

V. Sherlock, B. Connor, J. Robinson, H. Shiona, D. Smale, and D. F. Pollard. TCCON data from Lauder (NZ), 120HR, Release GGG2014.R0, 2014a. URL https://doi.org/10.14291/tccon.ggg2014.lauder01.r0/1149293.

V. Sherlock, B. Connor, J. Robinson, H. Shiona, D. Smale, and D. F. Pollard. TCCON data from Lauder (NZ), 125HR, Release GGG2014.R0, 2014b. URL https://doi.org/10.14291/tccon.ggg2014.lauder02.r0/1149298.

B. Sierk, J.-L. Bézy, A. Löscher, and Y. Meijer. The European CO2 monitoring mission: Observing anthropogenic greenhouse gas emissions from space. In *International Conference on Space Optics – ICSO 2018*, volume 11180, pages 237 – 250. SPIE, 2019. doi: 10.1117/12.2535941. URL https://doi.org/10.1117/12.2535941.

M. Sneep, M. Pedergnana, J. van Geffen, J. Landgraf, I. D. Smedt, D. Loyola, R. Siddans, A. Apituley, and J. P. Veefkind. S5P/TROPOMI static input for level 2 processors. https://sentinel.esa.int/documents/247904/2474724/S5P-TROPOMI-Static-input-for-Level-2-processors.pdf, 2015. Last accessed: 2021-01-05.

Y. Someya, R. Imasu, K. Shiomi, and N. Saitoh. Atmospheric ammonia retrieval from the TANSO-FTS/GOSAT thermal infrared sounder. *Atmospheric Measurement Techniques*, 13(1):309–321, 2020. doi: 10.5194/amt-13-309-2020. URL `https://amt.copernicus.org/articles/13/309/2020/`.

B. Stevens, F. Ament, S. Bony, S. Crewell, F. Ewald, S. Gross, A. Hansen, L. Hirsch, M. Jacob, T. Kölling, H. Konow, B. Mayer, M. Wendisch, M. Wirth, K. Wolf, S. Bakan, M. Bauer-Pfundstein, M. Brueck, J. Delanoë, A. Ehrlich, D. Farrell, M. Forde, F. Gödde, H. Grob, M. Hagen, E. Jäkel, F. Jansen, C. Klepp, M. Klingebiel, M. Mech, G. Peters, M. Rapp, A. A. Wing, and T. Zinner. A high-altitude long-range aircraft configured as a cloud observatory: The narval expeditions. *Bulletin of the American Meteorological Society*, 100(6):1061 – 1077, 2019. doi: 10.1175/BAMS-D-18-0198.1. URL `https://journals.ametsoc.org/view/journals/bams/100/6/bams-d-18-0198.1.xml`.

J. Strandgren, D. Krutz, J. Wilzewski, C. Paproth, I. Sebastian, K. R. Gurney, J. Liang, A. Roiger, and A. Butz. Towards spaceborne monitoring of localized co_2 emissions: an instrument concept and first performance assessment. *Atmospheric Measurement Techniques*, 13(6):2887–2904, 2020. doi: 10.5194/amt-13-2887-2020. URL `https://amt.copernicus.org/articles/13/2887/2020/`.

R. Sussmann and M. Rettinger. TCCON data from Garmisch (DE), Release GGG2014.R2, 2018a. URL `https://doi.org/10.14291/tccon.ggg2014.garmisch01.r2`.

R. Sussmann and M. Rettinger. TCCON data from Zugspitze (DE), Release GGG2014.R1, 2018b. URL `https://doi.org/10.14291/tccon.ggg2014.zugspitze01.r1`.

H. Suto. Personal Communication, September 2018.

H. Suto, F. Kataoka, N. Kikuchi, R. O. Knuteson, A. Butz, M. Haun, H. Buijs, K. Shiomi, H. Imai, and A. Kuze. Thermal and near-infrared sensor for carbon observation Fourier-transform spectrometer-2 (TANSO-FTS-2) on the Greenhouse Gases Observing Satellite-2 (GOSAT-2) during its first year on orbit. *Atmospheric Measurement Techniques*, 14 (3):2013–2039, 2021. doi: 10.5194/amt-14-2013-2021. URL `https://amt.copernicus.org/articles/14/2013/2021/`.

H. Takagi, S. Houweling, R. J. Andres, D. Belikov, A. Bril, H. Boesch, A. Butz, S. Guerlet, O. Hasekamp, S. Maksyutov, I. Morino, T. Oda, C. W. O'Dell, S. Oshchepkov, R. Parker, M. Saito, O. Uchino, T. Yokota, Y. Yoshida, and V. Valsala. Influence of differences in current GOSAT XCO2 retrievals on surface flux estimation. *Geophysical Research Letters*, 41(7):2598–2605, 2014. doi: 10.1002/2013GL059174. URL `https://agupubs.onlinelibrary.wiley.com/doi/abs/10.1002/2013GL059174`.

D. R. Taubert, J. Hollandt, P. Sperfeld, S. Pape, A. Höpe, K.-O. Hauer, P. Gege, T. Schwarzmaier, K. Lenhard, and A. Baumgartner. Providing radiometric traceability for the calibration home base of DLR by PTB. *AIP Conference Proceedings*, 1531(1):

376–379, 2013. doi: 10.1063/1.4804785. URL https://aip.scitation.org/doi/abs/10.1063/1.4804785.

Y. Té, P. Jeseck, and C. Janssen. TCCON data from Paris (FR), Release GGG2014.R0, 2014. URL https://doi.org/10.14291/tccon.ggg2014.paris01.r0/1149279.

J. Tennyson, P. F. Bernath, A. Campargue, A. G. Császár, L. Daumont, R. R. Gamache, J. T. Hodges, D. Lisak, O. V. Naumenko, L. S. Rothman, H. Tran, N. F. Zobov, J. Buldyreva, C. D. Boone, M. D. D. Vizia, L. Gianfrani, J.-M. Hartmann, R. McPheat, D. Weidmann, J. Murray, N. H. Ngo, and O. L. Polyansky. Recommended isolated-line profile for representing high-resolution spectroscopic transitions (IUPAC Technical Report). *Pure and Applied Chemistry*, 86(12):1931 – 1943, 2014. doi: https://doi.org/10.1515/pac-2014-0208. URL https://www.degruyter.com/view/journals/pac/86/12/article-p1931.xml.

D. R. Thompson, I. Leifer, H. Bovensmann, M. Eastwood, M. Fladeland, C. Frankenberg, K. Gerilowski, R. O. Green, S. Kratwurst, T. Krings, B. Luna, and A. K. Thorpe. Real-time remote detection and measurement for airborne imaging spectroscopy: a case study with methane. *Atmospheric Measurement Techniques*, 8(10):4383–4397, 2015. doi: 10.5194/amt-8-4383-2015. URL https://amt.copernicus.org/articles/8/4383/2015/.

D. R. Thompson, A. K. Thorpe, C. Frankenberg, R. O. Green, R. Duren, L. Guanter, A. Hollstein, E. Middleton, L. Ong, and S. Ungar. Space-based remote imaging spectroscopy of the Aliso Canyon CH_4 superemitter. *Geophysical Research Letters*, 43 (12):6571–6578, 2016. doi: 10.1002/2016GL069079. URL https://doi.org/10.1002/2016GL069079.

D. R. Thompson, J. W. Boardman, M. L. Eastwood, R. O. Green, J. M. Haag, P. Mouroulis, and B. Van Gorp. Imaging spectrometer stray spectral response: In-flight characterization, correction, and validation. *Remote Sensing of Environment*, 204:850 – 860, 2018a. doi: https://doi.org/10.1016/j.rse.2017.09.015. URL http://www.sciencedirect.com/science/article/pii/S0034425717304261.

D. R. Thompson, V. Natraj, R. O. Green, M. C. Helmlinger, B.-C. Gao, and M. L. Eastwood. Optimal estimation for imaging spectrometer atmospheric correction. *Remote Sensing of Environment*, 216:355 – 373, 2018b. doi: https://doi.org/10.1016/j.rse.2018.07.003. URL http://www.sciencedirect.com/science/article/pii/S0034425718303304.

A. K. Thorpe, D. A. Roberts, E. S. Bradley, C. C. Funk, P. E. Dennison, and I. Leifer. High resolution mapping of methane emissions from marine and terrestrial sources using a cluster-tuned matched filter technique and imaging spectrometry. *Remote Sensing of Environment*, 134:305 – 318, 2013. doi: https://doi.org/10.1016/j.rse.2013.03.018. URL http://www.sciencedirect.com/science/article/pii/S0034425713000977.

A. K. Thorpe, C. Frankenberg, and D. A. Roberts. Retrieval techniques for airborne imaging of methane concentrations using high spatial and moderate spectral resolution: application to AVIRIS. *Atmospheric Measurement Techniques*, 7(2):491–506, 2014. doi: 10.5194/amt-7-491-2014. URL https://amt.copernicus.org/articles/7/491/2014/.

A. K. Thorpe, C. Frankenberg, A. D. Aubrey, D. A. Roberts, A. A. Nottrott, T. A. Rahn, J. A. Sauer, M. K. Dubey, K. R. Costigan, C. Arata, A. M. Steffke, S. Hills, C. Haselwimmer, D. Charlesworth, C. C. Funk, R. O. Green, S. R. Lundeen, J. W. Boardman, M. L. Eastwood, C. M. Sarture, S. H. Nolte, I. B. Mccubbin, D. R. Thompson, and J. P. McFadden. Mapping methane concentrations from a controlled release experiment using the next generation airborne visible/infrared imaging spectrometer (AVIRIS-NG). *Remote Sensing of Environment*, 179:104–115, 2016a. doi: 10.1016/j.rse.2016.03.032. URL https://doi.org/10.1016/j.rse.2016.03.032.

A. K. Thorpe, C. Frankenberg, R. O. Green, D. R. Thompson, A. D. Aubrey, P. Mouroulis, M. L. Eastwood, and G. Matheou. The Airborne Methane Plume Spectrometer (AMPS): Quantitative imaging of methane plumes in real time. In *IEEE Aerospace Conference Proceedings*, volume 2016-June, 2016b. ISBN 9781467376761. doi: 10.1109/AERO.2016.7500756. URL https://doi.org/10.1109/AERO.2016.7500756.

A. K. Thorpe, C. Frankenberg, D. R. Thompson, R. M. Duren, A. D. Aubrey, B. D. Bue, R. O. Green, K. Gerilowski, T. Krings, J. Borchardt, E. A. Kort, C. Sweeney, S. Conley, D. A. Roberts, and P. E. Dennison. Airborne DOAS retrievals of methane, carbon dioxide, and water vapor concentrations at high spatial resolution: application to AVIRIS-NG. *Atmospheric Measurement Techniques*, 10(10):3833–3850, 2017. doi: 10.5194/amt-10-3833-2017. URL https://amt.copernicus.org/articles/10/3833/2017/.

A. K. Thorpe, R. M. Duren, S. Conley, K. R. Prasad, B. D. Bue, V. Yadav, K. T. Foster, T. Rafiq, F. M. Hopkins, M. L. Smith, M. L. Fischer, D. R. Thompson, C. Frankenberg, I. B. McCubbin, M. L. Eastwood, R. O. Green, and C. E. Miller. Methane emissions from underground gas storage in California. *Environmental Research Letters*, 15(4):045005, 2020. doi: 10.1088/1748-9326/ab751d. URL https://doi.org/10.1088%2F1748-9326%2Fab751d.

H. Tran and J. M. Hartmann. An improved O_2 A band absorption model and its consequences for retrievals of photon paths and surface pressures. *Journal of Geophysical Research Atmospheres*, 113(18):1–10, 2008. doi: 10.1029/2008JD010011. URL https://doi.org/10.1029/2008JD010011.

M. K. Tripathi, H. Govil, and S. Chattoraj. Identification of hydrothermal altered/weathered and clay minerals through airborne AVIRIS-NG hyperspectral data in Jahajpur, India. *Heliyon*, 6(2):e03487, 2020. doi: 10.1016/j.heliyon.2020.e03487. URL http://www.sciencedirect.com/science/article/pii/S2405844020303327.

A. J. Turner, D. J. Jacob, K. J. Wecht, J. D. Maasakkers, E. Lundgren, A. E. Andrews, S. C. Biraud, H. Boesch, K. W. Bowman, N. M. Deutscher, M. K. Dubey, D. W. T. Griffith, F. Hase, A. Kuze, J. Notholt, H. Ohyama, R. Parker, V. H. Payne, R. Sussmann, C. Sweeney, V. A. Velazco, T. Warneke, P. O. Wennberg, and D. Wunch. Estimating global and North American methane emissions with high spatial resolution using GOSAT satellite data. *Atmospheric Chemistry and Physics*, 15(12):7049–7069, 2015. doi: 10.5194/acp-15-7049-2015. URL https://acp.copernicus.org/articles/15/7049/2015/.

S. Twomey. On the numerical solution of fredholm integral equations of the first kind by the inversion of the linear system produced by quadrature. *J. ACM*, 10(1):97–101, Jan. 1963. doi: 10.1145/321150.321157. URL https://doi.org/10.1145/321150.321157.

H. C. van de Hulst. *Light Scattering by Small Particles*. Dover, 1981.

D. J. Varon, D. J. Jacob, J. McKeever, D. Jervis, B. O. A. Durak, Y. Xia, and Y. Huang. Quantifying methane point sources from fine-scale satellite observations of atmospheric methane plumes. *Atmospheric Measurement Techniques*, 11(10):5673–5686, 2018. doi: 10.5194/amt-11-5673-2018. URL https://amt.copernicus.org/articles/11/5673/2018/.

D. J. Varon, J. McKeever, D. Jervis, J. D. Maasakkers, S. Pandey, S. Houweling, I. Aben, T. Scarpelli, and D. J. Jacob. Satellite discovery of anomalously large methane point sources from oil/gas production. *Geophysical Research Letters*, 46 (22):13507–13516, 2019. doi: https://doi.org/10.1029/2019GL083798. URL https://agupubs.onlinelibrary.wiley.com/doi/abs/10.1029/2019GL083798.

D. J. Varon, D. Jervis, J. McKeever, I. Spence, D. Gains, and D. J. Jacob. High-frequency monitoring of anomalous methane point sources with multispectral Sentinel-2 satellite observations. *Atmospheric Measurement Techniques*, 2020:1–21, 2021. doi: 10.5194/amt-2020-477. URL https://amt.copernicus.org/preprints/amt-2020-477/.

J. P. Veefkind, I. Aben, K. McMullan, H. Förster, J. de Vries, G. Otter, J. Claas, H. J. Eskes, J. F. de Haan, Q. Kleipool, M. van Weele, O. Hasekamp, R. Hoogeveen, J. Landgraf, R. Snel, P. Tol, P. Ingmann, R. Voors, B. Kruizinga, R. Vink, H. Visser, and P. F. Levelt. TROPOMI on the ESA Sentinel-5 Precursor: A GMES mission for global observations of the atmospheric composition for climate, air quality and ozone layer applications. *Remote Sensing of Environment*, 120(2012):70–83, 2012. doi: 10.1016/j.rse.2011.09.027. URL https://doi.org/10.1016/j.rse.2011.09.027.

J. M. Wallace and P. V. Hobbs. *Atmospheric Science, An Introductory Survey*. Academic Press, San Diego, second edition, 2006. doi: https://doi.org/10.1016/B978-0-12-732951-2.50018-1. URL http://www.sciencedirect.com/science/article/pii/B9780127329512500181.

T. Warneke, J. Messerschmidt, J. Notholt, C. Weinzierl, N. M. Deutscher, C. Petri, and P. Grupe. TCCON data from Orléans (FR), Release GGG2014.R0, 2014. URL https://doi.org/10.14291/tccon.ggg2014.orleans01.r0/1149276.

K. Weidner. Investigating the effects of mercury emissions in the Four Corners area on local deposition levels and ambient concentrations. Master's project, Duke University. Retrieved from https://hdl.handle.net/10161/407, 2007. Last Accessed: 2021-02-20.

P. O. Wennberg, D. Wunch, C. M. Roehl, J.-F. Blavier, G. C. Toon, and N. T. Allen. TCCON data from Caltech (US), Release GGG2014.R1, 2015. URL https://doi.org/10.14291/tccon.ggg2014.pasadena01.r1/1182415.

P. O. Wennberg, C. M. Roehl, J.-F. Blavier, D. Wunch, and N. T. Allen. TCCON data from Jet Propulsion Laboratory (US), 2011, Release GGG2014.R1, 2016a. URL https://doi.org/10.14291/tccon.ggg2014.jpl02.r1/1330096.

P. O. Wennberg, D. Wunch, C. M. Roehl, J.-F. Blavier, G. C. Toon, and N. T. Allen. TCCON data from Lamont (US), Release GGG2014.R1, 2016b. URL https://doi.org/10.14291/tccon.ggg2014.lamont01.r1/1255070.

P. O. Wennberg, C. M. Roehl, D. Wunch, G. C. Toon, J.-F. Blavier, R. Washenfelder, G. Keppel-Aleks, N. T. Allen, and J. Ayers. TCCON data from Park Falls (US), Release GGG2014.R1, 2017. URL https://doi.org/10.14291/tccon.ggg2014.parkfalls01.r1.

J. S. Wilzewski, A. Roiger, J. Strandgren, J. Landgraf, D. G. Feist, V. A. Velazco, N. M. Deutscher, I. Morino, H. Ohyama, Y. Té, R. Kivi, T. Warneke, J. Notholt, M. Dubey, R. Sussmann, M. Rettinger, F. Hase, K. Shiomi, and A. Butz. Spectral sizing of a coarse-spectral-resolution satellite sensor for XCO2. *Atmospheric Measurement Techniques*, 13(2):731–745, 2020. doi: 10.5194/amt-13-731-2020. URL https://www.atmos-meas-tech.net/13/731/2020/.

WMO. GOSAT-GW. Observing Systems Capability Analysis and Review Tool, https://www.wmo-sat.info/oscar/satellites/view/gosat_gw, 2020. Last accessed: 2021-01-08.

J. R. Worden, A. J. Turner, A. Bloom, S. S. Kulawik, J. Liu, M. Lee, R. Weidner, K. Bowman, C. Frankenberg, R. Parker, and V. H. Payne. Quantifying lower tropospheric methane concentrations using GOSAT near-IR and TES thermal IR measurements. *Atmospheric Measurement Techniques*, 8(8):3433–3445, 2015. doi: 10.5194/amt-8-3433-2015. URL https://amt.copernicus.org/articles/8/3433/2015/.

L. Wu, O. Hasekamp, H. Hu, J. Landgraf, A. Butz, J. aan de Brugh, I. Aben, D. F. Pollard, D. W. T. Griffith, D. G. Feist, D. Koshelev, F. Hase, G. C. Toon, H. Ohyama, I. Morino, J. Notholt, K. Shiomi, L. Iraci, M. Schneider, M. de Mazière, R. Sussmann, R. Kivi, T. Warneke, T.-Y. Goo, and Y. Té. Carbon dioxide retrieval from

OCO-2 satellite observations using the RemoTeC algorithm and validation with TCCON measurements. *Atmospheric Measurement Techniques*, 11(5):3111–3130, 2018. doi: 10.5194/amt-11-3111-2018. URL https://doi.org/10.5194/amt-11-3111-2018.

L. Wu, O. Hasekamp, H. Hu, J. aan de Brugh, J. Landgraf, A. Butz, and I. Aben. Full-physics carbon dioxide retrievals from the orbiting carbon observatory-2 (OCO-2) satellite by only using the 2.06 μm band. *Atmospheric Measurement Techniques*, 12(11): 6049–6058, 2019. doi: 10.5194/amt-12-6049-2019. URL https://amt.copernicus.org/articles/12/6049/2019/.

L. Wu, J. aan de Brugh, Y. Meijer, B. Sierk, O. Hasekamp, A. Butz, and J. Landgraf. XCO_2 observations using satellite measurements with moderate spectral resolution: investigation using GOSAT and OCO-2 measurements. *Atmospheric Measurement Techniques*, 13(2):713–729, 2020. doi: 10.5194/amt-13-713-2020. URL https://amt.copernicus.org/articles/13/713/2020/.

D. Wunch, G. C. Toon, J.-F. L. Blavier, R. A. Washenfelder, J. Notholt, B. J. Connor, D. W. T. Griffith, V. Sherlock, and P. O. Wennberg. The total carbon column observing network. *Philosophical Transactions of the Royal Society of London A: Mathematical, Physical and Engineering Sciences*, 369(1943):2087–2112, 2011a. doi: 10.1098/rsta.2010.0240. URL https://doi.org/10.1098/rsta.2010.0240.

D. Wunch, P. O. Wennberg, G. C. Toon, B. J. Connor, B. Fisher, G. B. Osterman, C. Frankenberg, L. Mandrake, C. O'Dell, P. Ahonen, S. C. Biraud, R. Castano, N. Cressie, D. Crisp, N. M. Deutscher, A. Eldering, M. L. Fisher, D. W. T. Griffith, M. Gunson, P. Heikkinen, G. Keppel-Aleks, E. Kyrö, R. Lindenmaier, R. Macatangay, J. Mendonca, J. Messerschmidt, C. E. Miller, I. Morino, J. Notholt, F. A. Oyafuso, M. Rettinger, J. Robinson, C. M. Roehl, R. J. Salawitch, V. Sherlock, K. Strong, R. Sussmann, T. Tanaka, D. R. Thompson, O. Uchino, T. Warneke, and S. C. Wofsy. A method for evaluating bias in global measurements of co_2 total columns from space. *Atmospheric Chemistry and Physics*, 11(23):12317–12337, 2011b. doi: 10.5194/acp-11-12317-2011. URL https://doi.org/10.5194/acp-11-12317-2011.

D. Yang, Y. Liu, Z. Cai, X. Chen, L. Yao, and D. Lu. First global carbon dioxide maps produced from TanSat measurements. *Advances in Atmospheric Sciences*, 35 (6):621–623, 2018. doi: 10.1007/s00376-018-7312-6. URL https://doi.org/10.1007/s00376-018-7312-6.

W. Zdunkowski, T. Trautmann, and A. Bott. *Radiation in the Atmosphere: A Course in Theoretical Meteorology*. Cambridge University Press, 2007.

M. Zhang, I. Leifer, and C. Hu. Challenges in methane column retrievals from AVIRIS-NG imagery over spectrally cluttered surfaces: A sensitivity analysis. *Remote Sensing*, 9(8), 2017. doi: 10.3390/rs9080835. URL https://www.mdpi.com/2072-4292/9/8/835.

Y. Zhang, R. Gautam, S. Pandey, M. Omara, J. D. Maasakkers, P. Sadavarte, D. Lyon, H. Nesser, M. P. Sulprizio, D. J. Varon, R. Zhang, S. Houweling, D. Zavala-Araiza, R. A. Alvarez, A. Lorente, S. P. Hamburg, I. Aben, and D. J. Jacob. Quantifying methane emissions from the largest oil-producing basin in the United States from space. *Science Advances*, 6(17), 2020. doi: 10.1126/sciadv.aaz5120. URL `https://advances.sciencemag.org/content/6/17/eaaz5120`.

C. L. Zhao and P. P. Tans. Estimating uncertainty of the wmo mole fraction scale for carbon dioxide in air. *Journal of Geophysical Research: Atmospheres*, 111(D8), 2006. doi: 10.1029/2005JD006003. URL `https://agupubs.onlinelibrary.wiley.com/doi/abs/10.1029/2005JD006003`.

T. Zinner, U. Schwarz, T. Kölling, F. Ewald, E. Jäkel, B. Mayer, and M. Wendisch. Cloud geometry from oxygen-a-band observations through an aircraft side window. *Atmospheric Measurement Techniques*, 12(2):1167–1181, 2019. doi: 10.5194/amt-12-1167-2019. URL `https://amt.copernicus.org/articles/12/1167/2019/`.

Acknowledgements

Carrying out a Ph.D. thesis in a stimulating research environment is essential to master the intellectual challenges of such a project. I am very grateful that I was able to work with outstanding academic teachers, who always supported me during the last years. Prof. Dr. André Butz, Institute of Environmental Physics, Heidelberg University, and Prof. Dr. Bernhard Mayer, Munich Institute of Meterology, Ludwig-Maximilians-University, have accompanied me scientifically throughout my Ph.D. time. Prof. Butz always gave me very precious "24/7" support, and Prof. Mayer's group was a place where I always felt at home. Furthermore, Dr. Anke Roiger, Institute of Atmospheric Physics, German Aerospace Center, was a very thoughtful advisor, who generously offered me a graduate research position in her group, and gave me the necessary leeway for carrying out my project. I am also very thankful to Dr. Manfred Birk and Dr. Andreas Luther for their helpful comments on drafts of this manuscript. Additionally, many colleagues at DLR and LMU have kindly taken the time to share some of their expertise with me, especially Dr. Johan Strandgren, Dr. Julian Kostinek, Dr. Georg Wagner, Dr. Andreas Baumgartner, Dr. Claas Köhler, Dr. Tobias Kölling, Dr. Tobias Zinner, Dr. Fabian Jakub and Dennis Piontek. I acknowledge the support from the German Climate Computing Center (DKRZ) who provided me with valuable computing resources within the project "bd1104". I also thank Dr. John W. Chapman and Dr. David R. Thompson for providing AVIRIS-NG data. Dr. Luis Guanter pointed me towards working with AVIRIS-NG measurements and Dr. Sourish Basu helped me find wind reanalysis products in New Mexico. I gratefully acknowledge travel support by the German Academic Exchange Service (DAAD) to the 2019 AGU fall meeting in San Francisco, CA, USA. I thank the German Aerospace Center for letting me enroll in and graduate from their great *DLR_Graduate_Program*. Moreover, I thank my Ph.D. defense committee, Prof. Dr. Ilka Brunner, Prof. Dr. Harald Weinfurter, Prof. Dr. Jörg Schreiber and Prof. Dr. Tim Liedl.

Last but not least a heartfelt thank you to Talisa Bühl, who always helped me stay on track while keeping a good balance. My parents, Marianne Lehnert-Wilzewski and Jürgen Wilzewski, were there from the beginning. Thank you all.

Jonas Wilzewski Munich, May 2021